Gust tailoring in a wind tunnel for bird and MAV flight experiments

S. Miñano González

LentinkLab.

TU Delft

Gust tailoring in a wind tunnel for bird and MAV flight experiments

by

S. Miñano González

to obtain the degree of Master of Science
at the Delft University of Technology,
to be defended publicly on Thursday February 23, 2017 at 14:00 PM.

Thesis registration number:	121#17#MT#FPP	
Student number:	4404327	
Thesis committee:	Dr. ir. B. W. van Oudheusden,	TU Delft, supervisor
	Dr. D. B. Quinn,	University of Virginia, supervisor
	Dr. ir. F. T. Muijres,	Wageningen University and Research
	Dr. M. Percin,	TU Delft
	Dr. D. Ragni,	TU Delft

An electronic version of this thesis is available at http://repository.tudelft.nl/

Cover picture: hummingbird taking off from cactus, at Arizona Cactus garden (Stanford University). High-speed video available at: Nimia LentinkLab ©Rivers Ingersoll/NIMIA.COM. Courtesy of *LentinkLab*.

TU Delft

Summary

The project presented in this thesis is the result of a six-month stay at the Lentink Lab, a research laboratory within the Mechanical Engineering department at Stanford University. At this lab researchers and students look into different aspects of bird flight as an inspiration for the design of the next flying robots, and address biological questions with engineering tools and methods. Projects range from flow visualization over a wingbeat, to *in vivo* measurements of aerodynamic forces in flight, to head stabilization models for swans. The larger aim is to narrow the gap between biological questions and current engineering design challenges, between animal flight and the future small aerial vehicles.

One of the research lines of interest at the lab focuses on the following question: ***what mechanisms do birds use to stabilize in turbulence?***. Every day we see pigeons and sparrows maneuvering with ease and flying stably in urban environments, in which wind conditions are highly variable. Current small and micro aerial vehicles (MAVs), which are predominantly rotorcraft, are really far from this level of stability. Actually, instability under gusts is often highlighted as one of the main operational limitations to further development of their applications. In this context it seems smart to look towards nature to analyze the benefits of its strategies, and try to translate them to our aerial robot designs. Flapping kinematic strategies, wing morphing techniques or bio-inspired control algorithms are some of the areas of interest for this reverse engineering approach.

The project presented here aims to contribute to this larger question by developing a tool to be used in wind tunnel experiments. This **Gust Design Tool** enables the design of destabilizing wind profiles in a wind tunnel; this is of interest for both bird and MAV stability experiments. For bird stability studies, it allows to independently analyze the stabilization mechanisms used by birds when encountering a certain wind disturbance. For MAV studies, it provides a framework for performance assessment and comparison across configurations.

In order to make the tool more applicable to this kind of experiments, an added requirement is considered: the **tracking capability**. This refers to the capability of generating destabilizing wind profiles that are able to follow a moving objective. This kind of profiles are called *dynamic gusts* in the present report. The profile designs of focus in this project are non-uniform profiles across the span of the test section. This is because perturbations in roll are particularly destabilizing for MAVs, and are of special interest for bird flight studies as well.

To fulfill these requirements different pieces of equipment have been combined. The tool itself is built around a closed-circuit wind tunnel especially built for animal and small vehicle flight experiments. More precisely, it is built around its test section (1.0m wide, 0.82m tall and 1.73m long), which thanks to a modular design allows the inclusion of a special section upstream of it: the **active turbulence grid**. This grid is made up of rows and columns of diamond-shaped vanes, whose angular position can be modified. Since the grid is placed perpendicular to the incoming flow, modifying the vanes' angular position varies the area open to the flow. Hence, tailored profiles can be generated in the test section downstream. This flow speed information is gathered by an **array of low-cost wind sensors** placed at the location where the bird or small aerial robot is expected to fly in. The mentioned tracking capability is made possible by including a **motion capture equipment**. This equipment consists on a set of four high-speed infrared cameras that by triangulation give the position of a retroreflective marker. This marker, that is fixed to a thin rod in our experiments, would be attached to the flying robot or bird in the real experimental application. By moving the marker laterally across the width of the test section (i.e., in spanwise direction), it is possible to generate destabilizing wind profiles that adapt to the marker's position.

The approach for the construction of this Gust Design Tool with tracking capability is the following. The system made up of the grid and the wind sensor array (with input vanes angular position and output flowspeed) is found to be non-linear on a preliminary open-loop analysis. An empirical non-linear controller for the system is then proposed, to generate the desired flow profiles in the wind tunnel. This controller is based on a **lookup table** used in open-loop, that provides the required vane angular positions for each type of destabilizing profile. In order to populate this lookup table, a **closed-loop controller** is used.

The construction of this closed-loop controller is done progressively, by gradually incorporating three main aspects: a closed-loop approach, a division of the test section in regions and the addition of the tracking capability. A first closed-loop controller is built, based on one region. This controller is referred to as the **1-region closed-loop controller** and it provides the required angular position of all the vanes to reach a median flow speed value in the wind sensors array. Once the parameters for this 1-region controller are tuned for a satisfactory response, a **4-region closed-loop controller** is built. This is done by dividing the test section space in four regions and setting up four controllers in parallel, one in each region. At this point, different gust designs are compared to analyze potential advantages in convergence of certain designs. These are referred to as *static gusts*, because they lack tracking capability. Finally, an **8-region closed-loop controller** is built over an 8-region division of the test section space. The motion tracking equipment is added to this controller, enabling the design of *dynamic gusts*, or profiles that adapt to a moving objective. This is achieved by modifying the definition of the reference profile: the user defines the desired gust type and extreme values, and the marker's lateral position defines the profile's spanwise location. Note that the further subdivision in regions is beneficial for the tracking capability, enabling a closer match to the marker's actual position.

Once the 8-region closed-loop controller with tracking capability is built, the lookup table is populated and the **open-loop lookup table** controller is tested. The two approaches for the 8-region division, closed-loop and open-loop, are compared. Additionally, a demo for firing a gust to the objective location is commented on. The Gust Design Tool, mainly limited by the flow response, is found not fast enough for birds' fast maneuvers (in the order of a couple of wingbeats, $\sim 0.1s$). However, at its level of proof-of-concept it is still applicable for certain experiments. These applications and recommendations for follow-up developments are discussed as a conclusion to the project.

In conclusion, a Gust Design Tool for wind tunnel experiments has been built, with application in flight stability studies for both birds and MAVs. With the addition of the tracking capability it enables the generation of a stimulus that adapts to the subject's response. As such constitutes, to our knowledge, the first manipulated-stimulus approach ever built in a wind tunnel. As a proof-of-concept study, this work provides valuable guidelines for the development of more sophisticated controllers and wind tunnel experimental setups; more importantly, it sets the path for a reliable systems-level characterization of the flight dynamics under gusts of both birds and current MAVs.

Acknowledgments

This thesis project has been an amazing experience for me, and I feel very grateful for all the people that have made it possible. I would especially like to thank Daniel Quinn, my daily supervisor, of whom I have learned so much about research work. Thank you for your patience, support and useful insight. It has been a pleasure to work with you. I would also like to thank David Lentink, for having me as part of his lab in the first place, for the useful feedback and the lessons learned regarding work in academia. Another big Thank you to the amazing group of people that constitutes the LentinkLab: from undergrads to postdocs, I always found a helping hand when I needed it. I feel very lucky of having first experienced the ways of research work in such an enthusiastic and determined group. Thanks especially to Ben Perlman, for his endeavour to expand my American vocabulary, for his smiling and supportive personality and for always caring to make me feel part of the group. Special thanks as well to Yous van Halder, super prompt and nice answering all kind of grid-related questions. Highlight as well to all the great people I met in California, that made it such a wonderful stay.

As for the TU Delft side, I would like to thank my supervisor Bas van Oudheusden, for his support since the beginning, when we got in touch for an interest in a bio-inspired project. Thanks for keeping track of the progress, for the support in the numerous applications, and for some nice talks regarding research and PhD work. Thanks as well to the Justus and Louise van Effen Foundation, and the Prof.dr.ir. H.J. van der Maas Fonds for the generous financial support.

Finally I would like to thank my family, of which I feel so proud. Thanks for your strong support. Thanks to my friends as well, both in Delft and in Madrid, for making me feel like home. Especially I would like to thank Julián and Wim, for their time spent clarifying the control jungle to me. Thanks as well to my roommates Lu and Laura, to the library team (for loosing our sanity all together), to the climbing people and of course to Juliente, for their valuable help in the design of the cover. As for the Madrid division, thanks for all the support and for keeping a strong friendship regardless of our different paths. All of them have made me learn and grow a lot in the past 2.5 years, and I am really looking forward to the next step.

Contents

List of Figures

List of Tables

1 Introduction

The project at hand is the result of a research work performed during a six-month stay at the LentinkLab, a laboratory within the Mechanical Engineering department at Stanford University. Researchers and students at the LentinkLab look into different aspects of bird flight as a design inspiration for the next micro-aerial vehicles (MAVs). Sample project developed at the lab range from studies on the unsteady aerodynamics of flapping flight (Gutierrez et al., 2016), to in-vivo measurements of aerodynamic forces (Lentink et al., 2015), to modeling head stabilization in swans (Pete et al., 2015). The larger goal is to address biological questions with engineering methods and apply nature's strategies to future flying robot designs. This bioinspired approach to design has already proven useful in many applications. Particularly in the design of small aerial vehicles, varied examples exist of flying robots inspired in dragonflies, maple seeds or hummingbirds, as shown in Figure 1.1. Sample projects developed at LentinkLab are shown in Figure 1.2.

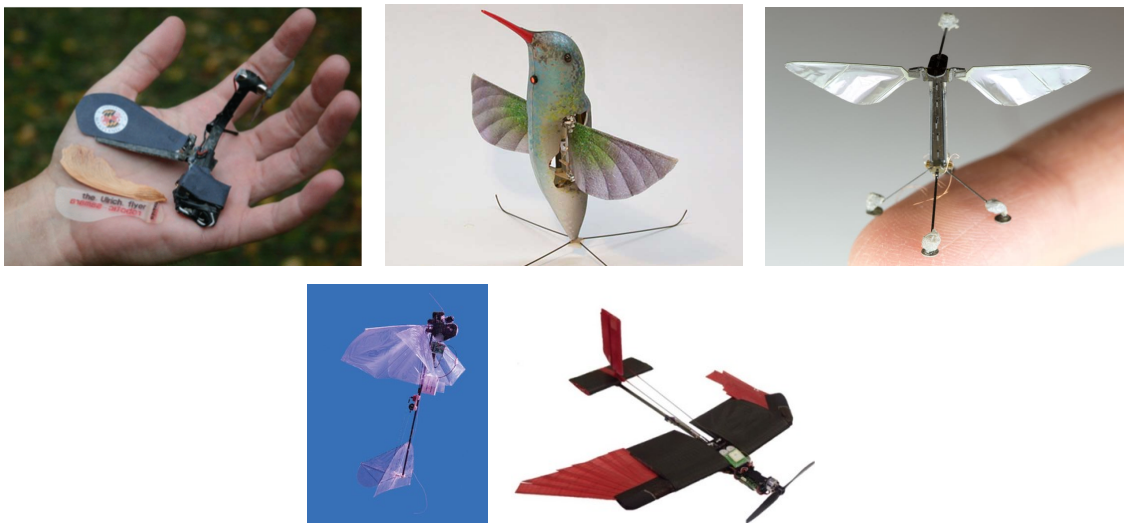

Figure 1.1: **Examples of bioinspired small aerial robots.** From left to right, first row: Ulrich Flier, developed at University of Maryland (Ulrich, 2012); Nano Hummingbird, developed by AeroVironment (Keennon et al., 2012); RoboBee developed at Harvard University (Ma et al., 2013). From left to right, second row: DelFly II, developed at Delft University of Technology (de Croon et al., 2012) and bio-inspired morphing wing, developed at École Polytechnique Fédérale de Lausanne (Di Luca et al., 2016)

Within this reverse engineering approach to biology, a relevant question is the following: ***what mechanisms do birds use to stabilize in turbulence?*** Indeed, this question is relevant not only for biologists interested in biomechanics of flight and motor control, but also for engineers seeking new design solutions for stabilization of flying robots. The present project contributes to further development in this area by introducing the design of a **Gust Design Tool**, a wind tunnel tool for use in both MAVs and bird flight stability

studies. The tool enables the design of destabilizing wind profiles in a wind tunnel, with an added motion tracking capability. That is, it allows the design of wind profiles that follow a moving objective. The project explores the performance of an experimental approach usually referred as *closed-loop*, in which the stimulus presented to the subject (in this case a bird) is manipulated according to the subject's response through some kind of feedback loop (Taylor et al. 2008, Altshuler et al. 2015). In this project this is nominatively applied in a wind tunnel. The tool construction process is addressed, as well as its performance. Note that in the following chapters, this concept of closed-loop is referred to as manipulated-stimuli approach, to avoid confusion with the closed-loop controller definition that is later used.

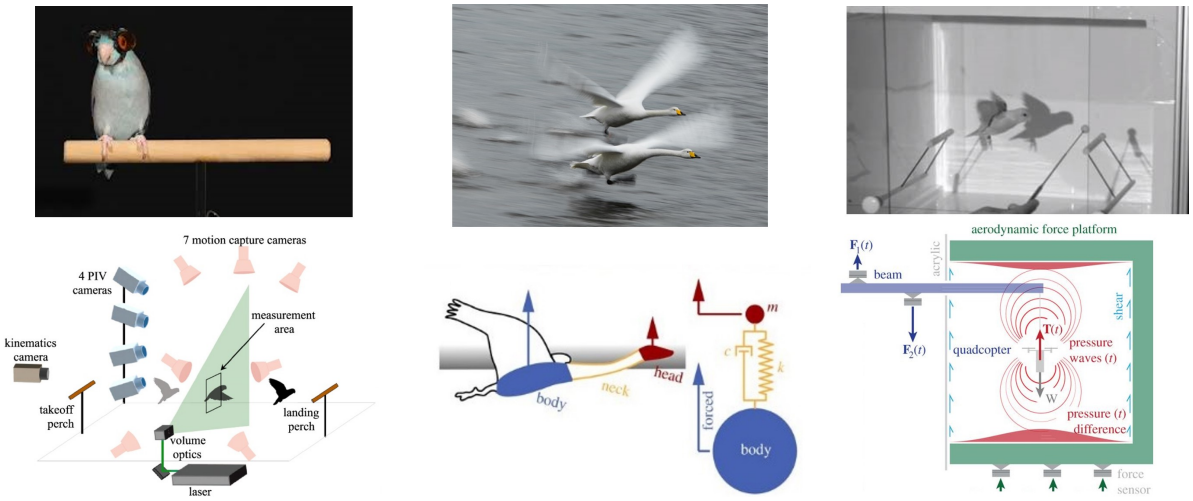

Figure 1.2: **Sample projects developed at LentinkLab.** From left to right, PIV flow visualization for bird flapping flight (Gutierrez et al., 2016), modeling of avian head stabilization (Pete et al., 2015) and development of an aerodynamic force platform (Lentink et al., 2015).

In the following sections the need and motivation for such a tool are presented, as well as the project outline and the research objective.

1.1. Research context and motivation

As mentioned, the interest on birds' stabilization mechanisms shows the multidisciplinary character of this area of research, being relevant from the biomechanics and zoology perspective, as well as for engineers and flying robots designers. Pigeons and sparrows fly with ease through turbulent urban environments, and birds of prey fly still under highly variable wind conditions. These are exceptional flight stability skills that current drones have not yet achieved. Actually, flying stably under gusts is often highlighted as the main factor preventing further development of UAV operations (Mohamed et al., 2014a). Small and micro aerial vehicles result especially sensitive to wind perturbations, due to their lower inertia and flying speeds. Moreover, the missions they are designed for often involve urban areas, in which the flow turbulence is considerably increased by city winds and building wakes (Watkins et al., 2013). The current attitude control problem for MAVs, considering its different factors and constraints, is precisely addressed in the review by Mohamed et al. 2014a. Figure 1.3 from that same work shows a schematic of the gust perturbation process, from the variation in the incident flow vector to the final effect on trajectory deviation.

Recent works on MAVs stability in gusty environments have stressed the need to consider these flight conditions as operating ones in the design process, and not as abnormal situations as it is generally done (Abdulrahim et al., 2010). To do so, two main required steps are identified. First, an adequate characterization of the atmospheric conditions at which these robots are meant to fly in is needed. That is the Atmospheric Boundary Layer, ABL, ranging from the ground to up to 400-1000m (Watkins et al., 2013). Second, the development of tools that enable the replication of representative destabilizing conditions from the ABL, in controlled environments, is needed. Only with full-scale wind tunnel experiments and a solid experimental framework it will be possible to properly assess the impact of wind turbulence and gusts on

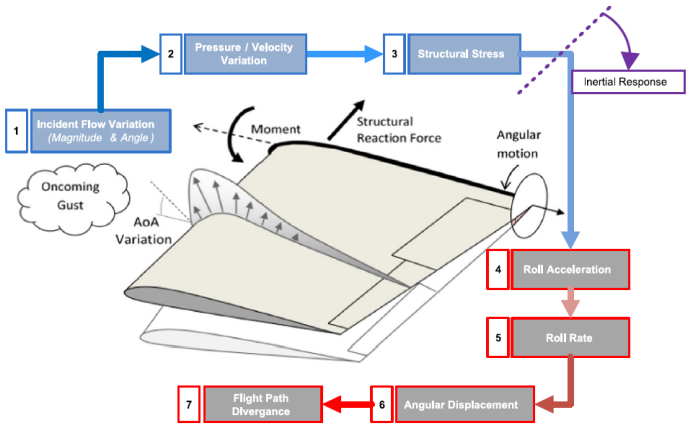

Figure 1.3: **Sequence of events upon encountering a gust.** Picture from Mohamed et al. 2014a.

MAV stability. This way it would be easier to incorporate it in the design process. Moreover, it would facilitate an objective comparison across studies and validation of models (Roadman and Mohseni, 2009a). The first steps in this direction have been carried out by Watkins (Watkins et al. 2006, Watkins et al. 2013, Watkins et al.2009) and Roadman (Roadman and Mohseni 2009a, Roadman and Mohseni 2009b); their works have been taken as reference for the gust design in this project.

The work by Watkins et al. (2006) aims to characterize the most destabilizing aspects of the atmospheric environment in which MAVs are meant to fly. The conclusions drawn have been taken as reference for the gust designs considered in this project. The authors consider pitch and roll as the two most relevant degrees of freedom to focus on, from a stick-fixed stability point of view (i.e., without control input). Indeed responses to these are a closely related to the lift distribution over the main wing and thus are very influenced by incident gusts on the leading edge. Linked to these two degrees of freedom, two main gust types are identified. First, an almost two-dimensional incoming gust with a uniform front, which will initially cause an increase in lift and a consequent pitch-up on the aircraft. When the gust passes and no longer influences the lift distribution over the wing, there will be a drop in lift and a pitch down of the aircraft. Second, an uneven front in the spanwise direction as a simplification of a gust that causes an uneven lift distribution over the wing, leading to a roll response (and most probably a coupling yaw). According to the work by Watkins et al. (2006) and Watkins et al. (2009), gusts that lead to roll inputs are the most challenging to stabilize in when piloting small remote-controlled aircraft in the ABL. As it will be later presented, uniform and especially uneven spanwise wind fronts are the main gust types looked into in the present study, considering them as well as the most representative regarding stability.

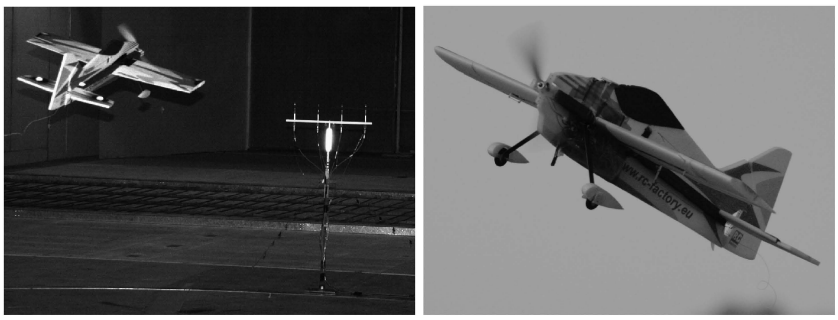

Figure 1.4: **Testing of fixed-wing unmanned aerial vehicle in wind tunnel and in open-air flight.** From the work by Abdulrahim et al. (2010). Picture on the left shows the fixed-wing UAV and the Cobra probes mounted in the wind-tunnel test section for flow measurement.

The work by Roadman and Mohseni (2009a) is also very relevant for this project: like the tool proposed in this project, their gust tunnel project is also based on an active grid. In their case the aim is to reproduce

full-scale ABL conditions in a wind tunnel, for full-scale Reynolds number testing on MAV. In this thesis the definition of *gust* given by Roadman and Mohseni (2009a) is applied, as *"any velocity deviation in either magnitude or direction from a uniform, steady, unidirectional flow field"*; additionally discrete gusts, as discussed in the same work, are the main focus of this project. More details on this work are included in Chapter 2. Figure 1.5 shows snapshots of a sequence proposed by Roadman and Mohseni (2009b).

As mentioned earlier, from the bio-inspired engineering point of view there is also an interest in further understanding the strategies used by animal fliers to stabilize under turbulence. Flapping flight has been suggested to benefit stability due to damping effects (Hedrick, 2011). Among biological fliers, birds may be particularly interesting due to their larger scale, matching MAV designs of larger size and payloads. However, research on aerodynamics, flight mechanics and stability and control have been mostly focused on insect flight, as noted by Paranjape et al. (2012). In any case, for small and large animal fliers, the link between external stimuli and the motor output is complex and still largely unknown (Altshuler et al., 2015). Both biologist and engineers would benefit from applying a systems-level analysis to their flight dynamics, as noted by Taylor et al. (2008). Further insight into the link between physics and physiology can be attained from a biologist perspective, and applications to drone design may be easily translated. In order to develop realistic flight dynamic models (or motor-sensor models in biology), experimental approaches based on manipulating stimuli through response feedback (such as virtual-reality or manipulated-stimuli setups) are of the utmost importance. The work presented in this thesis aims to contribute to further developments in this area, by proposing a wind tunnel tool that designs destabilizing wind profiles able to adapt to an objective's position. Note that this closed-loop approach may also be beneficial for autonomous MAV testing, facilitating a quantitative comparison. This is a very relevant niche currently in MAV turbulence testing, as highlighted by Watkins et al. (2009). Some approaches already go in this direction, such as the one in the work by Abdulrahim et al. (2010), in which turbulence sensitivity is compared across different aircraft configurations (Figure 1.4).

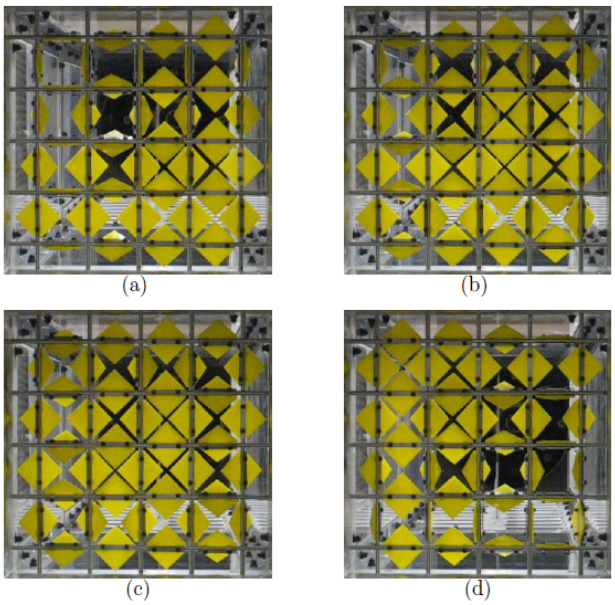

Figure 1.5: **Active grid used in gust tunnel.** Vanes rotational sequence proposed by Roadman and Mohseni (2009b) for the generation of large scale turbulence

From the presented overview, it is clear that a Gust Design Tool like the one proposed in this project would largely benefit current stability studies for both MAVs and bird flight experiments. In MAV testing, it provides a framework for objective comparison across configurations and disturbances. As for biomechanical studies on flight stability, the stimuli manipulation approach proposed is in line with current trends aiming for system's-level modeling of animal's flight dynamics. Additionally, the tailoring of profiles enables to focus on particularly destabilizing aspects.

1.2. Research objective

The objective of the present project can be now summarized as follows:

Build a tool to design destabilizing wind profiles in a wind tunnel, for experiments on bird or small aerial vehicle flight, with tracking capability.

To do so, an active grid fitted in a low-turbulence wind tunnel is used, along with an array of wind sensors disposed in the spanwise direction. The active grid is made up of eight columns of diamond-shape vanes disposed vertically and seven rows disposed horizontally (see Figure 1.6, and Chapter 3 for further details). Later, a motion tracking equipment is added to enable the *tracking capability*; this refers to the ability of designing destabilizing wind profiles that adapt to a moving objective (a flying bird or robot). The study is focused on the generation of horizontal two-dimensional profiles, as gust resulting in roll inputs have been identified as relevant for stability (Watkins et al., 2006). Thus, only the grid's vertical vanes are considered in the gust design, while horizontal vanes are kept fully open in order to limit the maximum wind tunnel blockage. The Gust Design Tool, its components and the tracking capability are shown in Figures 1.6 and 1.7.

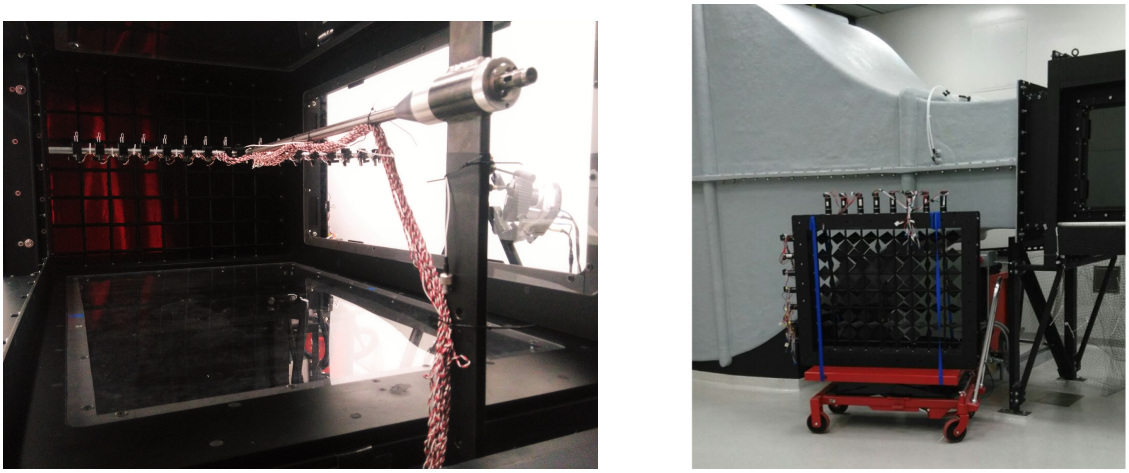

Figure 1.6: **Gust Design Tool setup and turbulence grid.** Figure on the left shows the view of the setup from downstream (accessible through a trapdoor, see section 3.2). Figure on the right shows the turbulence grid detached from the test section.

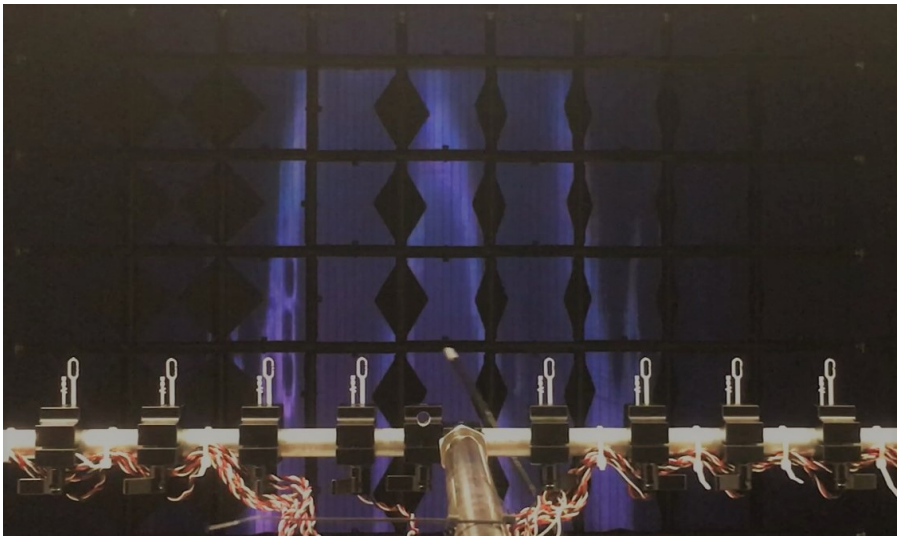

Figure 1.7: **Demo of tracking capability.** A thin rod with a retroreflective marker at the tip is translated sideways and the grid adapts to its position to generate the desired gust profile. The flow information is gathered by the array of wind sensors.

1.3. Methodology

The methodology for the construction of the Gust Design Tool is now described. The objective is to build a controller for the system made up of the grid and the wind sensor array, that enables the design of wind profiles with tracking capability. On a first open-loop analysis, the system is found to be non-linear. To control the profile design an empirical non-linear controller is then proposed. This controller is based on a **lookup table** to be used in open-loop. The table provides the required vane angular positions for each type of destabilizing profile. With a non-linear controller, controller specifications are satisfied in the whole range of operation. Additionally, since the controller is based on an empirical characterization, the complexity of identifying a mathematical model for a non-linear system is avoided. This approach is shown in Figure 1.8. The lookup table is populated with the desired profiles and corresponding vane positions by making use of a **closed-loop controller**.

This closed-loop controller is built by progressively incorporating three aspects: closed-loop approach, division in regions and tracking capability. The gradual inclusion of these three aspects results in three different closed-loop controllers. At each stage, the flow response is looked into and the system's performance is assessed. A first closed-loop controller is set up, based on one region. This controller is referred to as the **1-region closed-loop controller**. Once the parameters for this 1-region controller are tuned for a satisfactory response, a **4-region closed-loop controller** is defined. This is done by dividing the test section space in four regions and setting up four controllers in parallel, one in each region. At this point different gust designs are compared, to analyze potential advantages in convergence of certain designs. These profiles are referred to as *static gusts*, because they lack tracking capability. Finally, an **8-region closed-loop controller** is built over an 8-region division of the test section space. The motion tracking equipment is added to it, enabling the design of *dynamic gusts*, or profiles that adapt to a moving objective. This is accomplished by including the marker's lateral position in the definition of the reference profile. With this approach, the user defines the desired gust type and extreme flow speed values, and the marker's lateral position defines the profile's spanwise location. The progressive region subdivision leading to the 8-region closed-loop controller is shown in Figure 1.9.

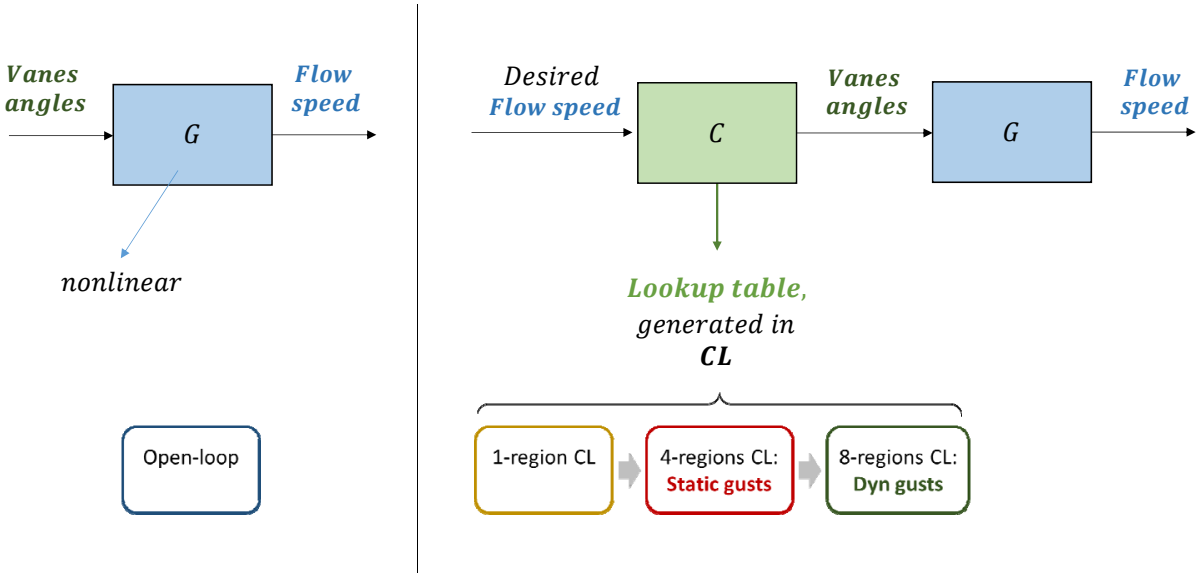

Figure 1.8: **Schematic of followed approach**. Figure to the left shows a schematic block diagram of the system made up of the active turbulence grid and wind sensors array (G); the system is found non-linear and thus a non-linear approach to its control is proposed. This is shown in the figure to the right: the non-linear controller C is based on a lookup table to be used in open-loop, that captures the inverse relation of the system. This lookup table is generated in closed-loop (CL), using the 8-region closed-loop controller. This controller is obtained in progressive steps.

The 8-region closed-loop controller is used to populate the lookup table. Next, the non-linear **open-loop lookup table** controller is developed. The two approaches for the 8-region division, closed-loop and open-loop lookup table, are compared. Additionally, a demo for firing a gust to the objective location is commented

on.

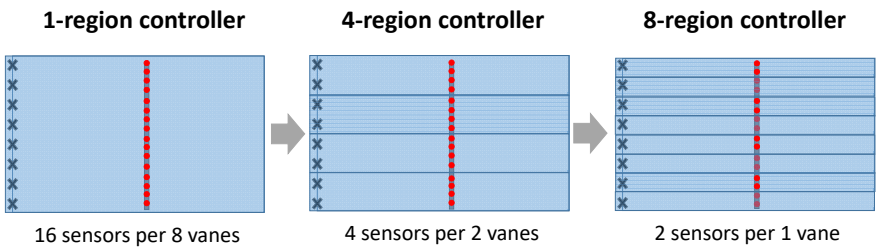

Figure 1.9: **Correspondence between sensors and vanes for the controllers used in the project**. The figure at the left shows a schematic of the one-region approach, which uses the median flow speed value across all sixteen sensors (dots) and one value for the angular position of the vanes (crosses). Figures at the center and right, show the next designs with the same approach in parallel: in the 4-region controller (center) the angular position of two contiguous vanes depends on the median flow speed value of the four sensors downstream of them; in the 8-region controller (right) the same occurs with one vane per two sensors. These last two designs are covered in Chapter 7 and Chapter 8

1.4. Project outline

The report structure follows the steps described in the methodology. First, for the design of the closed-loop controllers used to populate the lookup table, three main aspects are gradually incorporated: a closed-loop approach, a division of the test section in regions and the addition of the tracking capability. Once the 8-region closed-loop controller with tracking capability is set up, the lookup table is populated and the open-loop controller tested. Parallel to building this progressive controllers, the flow response is looked into at each stage, and the controller performance is assessed. The approach for the construction of the closed-loop controllers is shown in Figure 1.10.

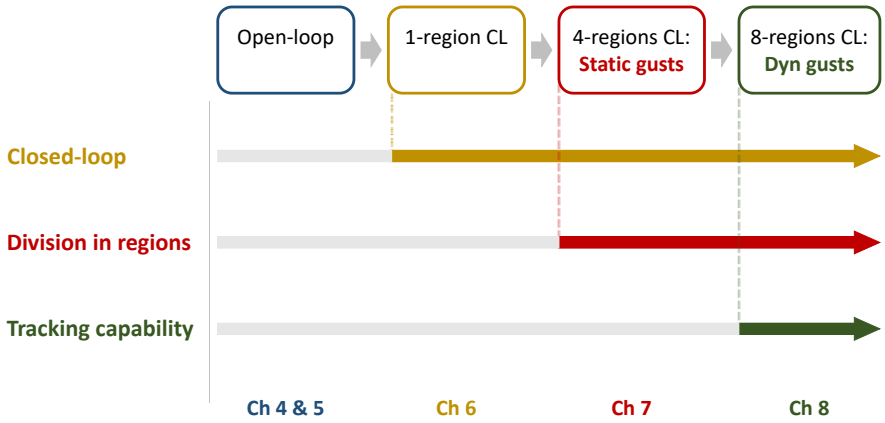

Figure 1.10: **Stages in the construction of the closed-loop controllers.** Closed-loop controllers are developed by progressively incorporating the three main aspects of the methodology: closed-loop approach, division in regions and tracking capability. *CL* stands for closed-loop; bottom labels indicate the chapters that correspond to each phase.

Each of the stages described correspond to a chapter in this report. First, the system made up of the grid and the sensor array is analyzed in open-loop, and the steady-state and transient step response are looked into in **Chapter 4** and **Chapter 5** respectively. Once the open-loop response has been explored, a closed-loop setup is approached in **Chapter 6**, in which a controller based on one region is built and tuned. Next, in **Chapter 7**, the selected controller configuration is set up in parallel as four independent controllers; each one controls the flow response in one of the four regions in which the test section has been divided in. The design of different gust profiles, referred to as *static gusts*, is carried out with this 4-region closed-loop controller. Differences in

the flow response across static gust designs are addressed. In **Chapter 8**, an 8-region closed-loop controller is presented, based on eight controllers set up in parallel, and the motion tracking system is added to the loop. The design of *dynamic gusts* in closed-loop is then addressed. Once the closed-loop control part is covered, the 8-region closed-loop setup is used to populate the lookup table, meant to be used as non-linear open-loop controller for the *dynamic gusts* design. Both 8-region setups, closed-loop and open-loop based on lookup table, are compared and a demo for firing a gust to the objective location is commented on. Finally, in **Chapter 9**, conclusions are drawn from the whole analysis and recommendations for future wind tunnel tools based on stimuli-manipulation are derived.

2

Literature review

The aim of this chapter is to present the state of the art on the three main research areas related to this project. These are identified as: (1) studies on flight of micro aerial vehicles (MAVs) in turbulence and gusts, (2) experiments with animal fliers under turbulence, and (3) applications of active turbulence grids. For each, the most relevant works to the project addressed in this thesis are presented and briefly discussed. Since one of the contributions of this project is its potential use in wind tunnel experiments, towards modeling both birds and MAVs dynamics when encountering atmospheric disturbances, a special focus is placed on model identification and manipulated-stimuli approaches, when discussing MAVs and animal fliers, respectively. The chapter closes with a summary of extracted conclusions, in which gaps are identified and the relevance of the project in its larger research context is highlighted.

2.1. Micro aerial vehicle flight in turbulence

Small flying robots are of interest in a wide variety of applications, ranging from defence tasks to civil ones, including transportation, communication, agriculture, environment conservation, industrial inspection, and search and rescue, among others. Research on these small drones over the past years has resulted in three main dominant platforms: fixed-wing, rotorcraft and flapping-wing, each of them more suitable for different missions and applications. Fixed-wing configurations are efficient in forward flight; this makes them well suited for covering large distances, as in agricultural photogrammetric mapping. Rotorcraft on the other hand are less efficient in forward flight, but present the advantage of hovering capability; this makes them useful for inspection applications (e.g., wind turbines or high voltage lines). However, these two configurations present a significant degradation of their performance when scaling them down. On the contrary, flapping-wing configurations scale down well (Lentink et al., 2009; Lentink and Dickinson, 2009), providing an alternative for small-scale propulsion based on unsteady force production (Floreano and Wood, 2015). Still, this comes at the cost of challenging aerodynamics and controls. This scaling characteristic, along with the evidences seen in nature of effective, stable and maneuverable flapping flight, make flapping-wing approaches particularly attractive for MAV designs. As an overview of the current state-of-the-art, a comparison of small aerial vehicle configurations in terms of mass and flight time is presented in Figure 2.1

The small scale of these MAVs also brings some challenges related to their operating environment. These aerial vehicles are meant for missions for which larger drones would be unsuitable or may result a hazard. This may be for example urban environments, confined spaces or areas in which drones operate close to people. Their operations then take place within the ABL (atmospheric boundary layer, which extends up to 400-1000m above the ground; Watkins et al., 2013), where flow is turbulent and winds are highly variable. These flow conditions especially affect MAVs, due to their lower speed and inertia (as shown in Figure 2.2, the lower the relative velocity the larger the perceived turbulence intensity; Watkins et al. 2006). An

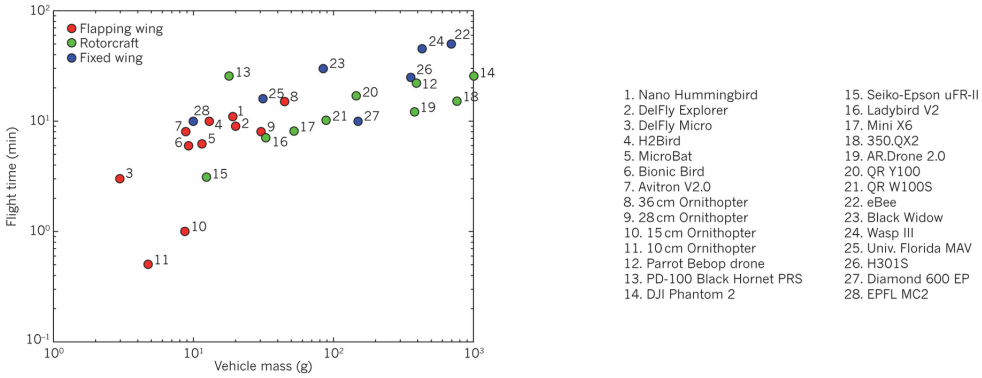

Figure 2.1: **Flight time against vehicle time**, for different small (< 1kg) aerial vehicle configurations, from (Floreano and Wood, 2015)

adequate characterization of this environment is therefore a must in order to design new platforms better suited to these conditions (Mohamed et al., 2014a; Watkins et al.).

The work started by Watkins et al. (2006), further completed in later works in 2010 and 2013, sets the path in describing the wind environment close to the ground, with a view to evaluate its influence on MAV flight. The strategy suggested by the authors is to characterize the ABL turbulent features and wind conditions, and identify the most relevant inputs for MAV flight. From their gathered data of the flow environment, they find large fluctuations in pitch angle in the spanwise direction, which would lead to roll inputs and which they identify as the most relevant for MAVs stability. The effect of turbulence on roll perturbations is also commented on by Mohamed et al. (2014a), on their review on the attitude control problem of MAVs, and further looked into in the work by Mohamed et al. (2014b): in it the correlation between pressure-related disturbances over the wing and subsequent roll perturbations is looked into, and the development of a bio-inspired pressure-based attitude controller is proposed. Watkins et al. (2006) suggest that flapping-wing configurations may pose an advantage for roll stabilization; this is later further supported with works such as the one by Fisher et al. (2016). Authors in Watkins et al. (2006) also highlight the importance of replicating these most relevant aspects of the ABL in a wind tunnel, in order to include this information in the design of MAV prototypes and in testing.

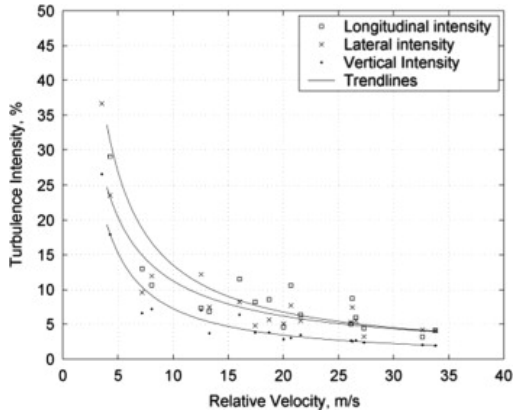

Figure 2.2: **Atmospheric turbulence intensity against relative velocity**, from Watkins et al. (2006)

The later work by Watkins et al. (2009) continues this approach, by reproducing ABL turbulence levels in a large wind engineering tunnel (through passive grids and other means), and testing different configurations of small remotely-piloted aircraft. Handling qualities (based on pilot ratings) are assessed for fixed-wing and rotorcraft, and preliminary results of a flapping-wing fixed to a force balance, under turbulence, are presented. Rotorcraft are found less sensitive to atmospheric turbulence than fixed-wing of similar scale. However, the challenge involved in an adequate comparison across configurations is emphasized (e.g., making rotor span and wingspan comparable overlooks the fact that the actual flow speed over spinning

blades is higher, and thus turbulence intensity relative to the moving blades is lower). In any case, the work results useful as a first attempt in defining test procedures and adequate parameters for comparison.

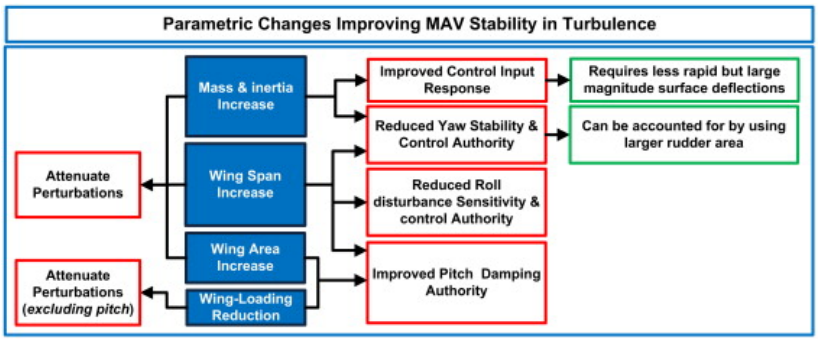

Figure 2.3: **Passive stabilization for MAVs**, from (Mohamed et al., 2014a)

This preliminary wind tunnel tests presented in Watkins et al. (2009) give way to a further defined testing procedure in the follow-up work by Abdulrahim et al. (2010). In it, the configuration of a fixed-wing aircraft is changed systematically and tested in a large wind engineering tunnel, in which turbulence levels proper of urban environments are replicated. In this way the role of parameters such as mass, wingspan or moment of inertia are related to turbulence sensitivity. An interesting methodology to address the effect of turbulence is proposed: the predicted behaviour of the aircraft, obtained through free flight test data and identification of the aircraft dynamics, is compared to the measured behaviour when flying the aircraft in the wind tunnel. The difference between both is used to estimate forces and moments generated on the aircraft due to turbulence, and these are expressed as equivalent control deflections. In this way disturbances due to turbulence are normalized with reference to aircraft controls.

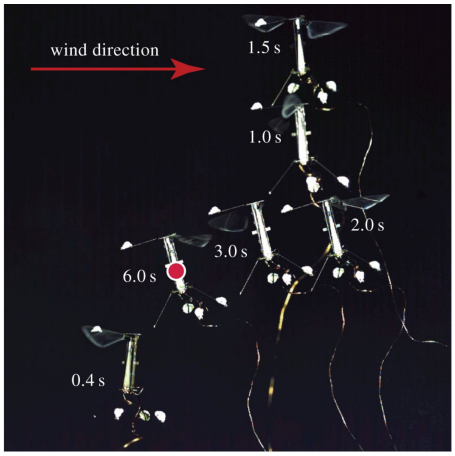

Figure 2.4: **Robobee under a gust at different instants, showing the performance of wind disturbance rejection scheme.** Shows the robot stabilizing under constant wind at 80 cm/s.; the red dot indicates the setpoint position. Image from Chirarattananon et al. (2017)

The larger problem of the attitude control in MAVs under turbulence and gusts is addressed by Mohamed et al. (2014a), who gather in their review both passive and active stabilization strategies. The former are mostly derived from the wind tunnel test results presented by Abdulrahim et al. (2010) and are summarized in Figure 2.3. Regarding the latter, the important role of active approaches in autonomy is highlighted, conferring stability without a loss in maneuverability. Two recent works on the implementation of active control for turbulence mitigation strategies are worth highlighting. In the first one, by Mohamed et al. (2016), a phased-advanced sensor inspired in feather mechanoreceptors is developed and tested. The second one, by Chirarattananon et al. (2017) and developed on RoboBee (see Figure 2.4), suggests a simplified model for the effect of wind disturbances on the flight dynamics of the robot, and proposes two schemes for wind disturbance rejection. Additionally, this work provides supporting evidence to the

potential advantage of flapping-wings on mitigation of atmospheric disturbances.

Improving the modeling of the effect of wind disturbances on the flight dynamics of a small flying robots is one of the applications that could be derived from the proposed Gust Design Tool. Examples of model identification studies on ornithopters include those by Caetano et al. (2013a) and Caetano et al. (2013b), in which the MAV DelFly II is programmed to automatically execute maneuvers for system identification; these works could be used as reference for identification of the dynamics in turbulence. Additionally the tracking capability of the gust tool may enable to do without clamps in this kind of experiments (supports can affect force measurements as noted by Caetano et al. (2015)); this would be in the line of the work by de Wagter et al. (2013), who develop a control scheme to enable untethered testing of the DelFly II.

To sum up, there is an evident need to improve the stability of micro aerial vehicles under variable wind conditions. Some steps have already been taken towards replicating relevant disturbing conditions in a wind tunnel, to characterize the response of MAV and for testing. This kind of approaches enable to include this more realistic conditions for MAV flight not only in prototyping and testing phases, but also in the extraction of flight dynamics models and in the design of mitigating control algorithms.

2.2. Experiments on animal flight in turbulence

Current knowledge on the flow conditions outdoors close to the ground, and on the effect these have on flight performance of both MAVs and animal fliers is still very limited. In nature we find solutions that cope well with this variable wind environment and clearly outperform current MAV designs in that respect. Flying animals need to forage in a variety of atmospheric conditions, and thus present mechanisms and strategies that might be of interest to translate to our flying robots designs. Observing animal flight performance in turbulence and gusts is therefore relevant not only as a piece of fundamental research, but also as a reverse engineering problem, with application in MAV design.

The review presented in this section focuses on animal flight experiments carried out in flow-controlled environments (such as wind tunnels or gust chambers), which address questions concerning flight in turbulence. Most experiments reviewed look into the effect of turbulence on the wingbeat kinematics and/or on the energetic cost it implies. A larger question that would encompass both aspects is whether flapping flight poses an advantage when flying in turbulent conditions. Note that this last question again shows the interdisciplinary nature of the topic, being of interest from an evolutionary biology perspective (Hedrick, 2011), and from a engineering design point of view (Fisher et al., 2016).

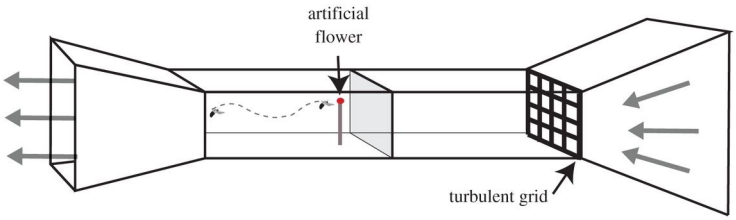

Figure 2.5: **Bee hovering in passive grid generated turbulence in a wind tunnel**, the insect is fed from an artificial flower downstream the grid. Image from (Crall et al., 2017)

Most literature on animal flight is centered on insect flight and that is also the case for studies in turbulence. Within insects, bumble bees are the focus of many of these works, presumably due to their "all-weather foragers" nature (Ravi et al., 2013). A recent work with bees is the one carried out by Crall et al. (2017), which combines outdoors and wind tunnel measurements, to evaluate the effect of turbulence in flight performance of bumble bees. Outdoors measurements show that windy conditions do not prevent bees from foraging. Wind tunnel measurements, in passive grid generated turbulence at environmentally relevant levels (see Figure 2.5), show that bees increase kinematic parameters such as wingbeat frequency and stroke amplitude, when increasing the turbulence in the flow. An increasing asymmetry between left and right wing stroke amplitude is also found for increasing turbulence; from these results authors suggest

that a wide variety of different mechanisms seem to be used by biological fliers to mitigate turbulence.

This suggestion appears to be supported by two previous works, also on bees in turbulence. The first one, by Combes and Dudley (2009), looks into orchid bees flying in fully mixed turbulent flow. Bees are set to fly in front of an outdoor air jet, by attracting them with an artificial scent. The objective is to analyze the effect of flow variability on maximum flight speed and flight stability. A particular sensitivity to roll instabilities is found, as well as an interesting mechanism to compensate it at large speeds: to increase roll stability, bees extended their hind legs, at the expense of a probable increase in drag and power costs. This supports the idea of a variety of strategies being used by animal fliers. As a complement to this work, the one by Ravi et al. (2013) also looks into bee flight in variable flow conditions, but now based on unsteady and unstructured vortices. By placing bees in a wind tunnel and feeding them from an artificial flower behind differently oriented cylinders, flight performance on the wake of the shed vortices is assessed. As in the work by Combes and Dudley (2009) bees are found to be most sensitive to roll disturbances, but additional evidence is presented on the fact that bees make use of their increased agility around their roll axis to compensate most lateral disturbances. An increase in the cost of flight due to being in this wake is also suggested, finding a decrease in forward speed when flying in unsteady flow.

The work by Ortega-Jimenez et al. (2013), now on hawkmoths, also looks into flight behind a von Kármán vortex street. In it kinematic wingbeat variables are compared when flying in the recirculating region behind the cylinder and when flying in the vortex-dominated region. Little qualitative difference is found between both, but a decrease of destabilizing effects occurs when going further downstream of the cylinder. Another work by the same group placed hawkmoths in a vortex chamber (Ortega-Jimenez et al., 2014a), previously characterized with PIV, to analyze the effect of whirlwinds of variable intensity on the flapping kinematics and body dynamics. Similar strategies as the ones observed in previous works are found, based on symmetric and asymmetric changes to wingbeat amplitude and stroke plane angle, as well as body orientation changes. However these tornado-like vortices seemed to destabilize flight at speeds much lower than what hawkmoths can adversely sustain in forward flight.

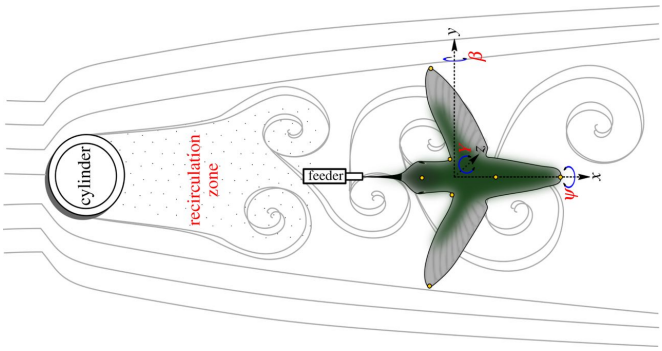

Figure 2.6: **Hummingbird hovering in a von Kármán vortex street**, generated from a cylinder. Image from (Ortega-Jimenez et al., 2014b)

Comparable studies on birds have focused mostly in hummingbirds. Ortega-Jimenez et al. (2014b) present an approach analogous to the one carried out in Ortega-Jimenez et al. (2013) with hawkmoths, but this time with hummingbirds (see Figure 2.6). The effect of variably sized vortices (shed behind cylinders of different diameters) on hummingbirds kinematics and metabolic cost is analyzed. Authors find that larger wakes that interact with both wings affect stability much more significantly, and lead to kinematic strategies that increase energetic costs of flight. Ravi et al. (2015) argue that von Kármán vortex streets are actually seldom found in natural environments and that a fully mixed flow is more realistic of what a hummingbird may encounter in their natural habitat. They replicate these conditions with a passive grid in a wind tunnel, and place downstream of it a hummingbird feeding from an artificial flower (analogously to the experiment with bees in the work by Crall et al., 2017). The kinematic strategies observed for mitigating turbulence-induced destabilizations are similar to those observed behind a von Kármán vortex street, and as in previous studies a particular sensitivity to roll instabilities is found. A novel contribution from this work is their analysis of the role of the tail: its mean fan angle is shown to increase and its orientation is shown to vary when flying in turbulence; this seems to aid in stabilization but probably increases energy expenditure due to drag.

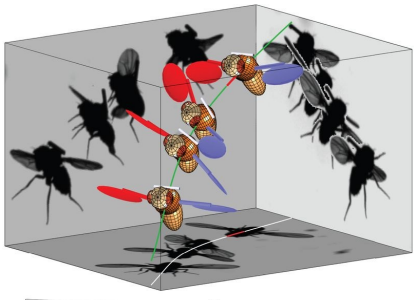

Figure 2.7: **Rendering showing roll perturbation and correction maneuver**. Rendering from measured kinematics. Green line shows trajectory of center of mass; over it red line indicates the perturbation location. Image from Beatus et al. (2015)

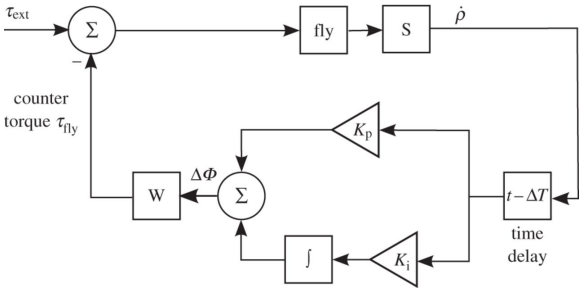

Figure 2.8: **PI-controller model for roll stabilization mechanism**, from corrections observed to perturbed fruit flies in roll. *Fly* block describes fly's dynamics; *S* block represents the haltere sensors, which measure roll velocity $\dot{\rho}$; $\dot{\rho}$ goes through a time-delay block (representing neuromuscular response time) and through a proportional-integral controller, the output of which is the wingstroke amplitude asymmetry $\Delta\phi$. This actuator signal $\Delta\phi$ is converted in the wings block *W* to the required counter-torque to be exerted by the fly τ_{fly} to overcome the external perturbation torque τ_{ext}. Image from Beatus et al. (2015)

Finally, two works are worth highlighting in this review, even though there are not performed in turbulent flow. The first one is relevant as an example of mechanisms used by birds at wing-body level: it is the work by Williams and Biewener (2015), which shows that pigeons execute different body and wing postures as obstacle-avoidance strategies, making trade-offs between stability and efficiency.

The second work is the one by Beatus et al. (2015) on fruit flies, and it is of interest due to its simple modeling of a stabilization mechanism. In it authors analyze stabilization strategies in roll (again identified as the most unstable and sensitive axis) by fixing a magnet to the insect's back and applying a short magnetic pulse. They find that for moderate destabilizations fruit flies perform a stroke-amplitude asymmetry, that can be modeled as a linear proportional-integral controller (see Figure 2.7 and 2.8). For more aggressive disturbances evidences are found for nonlinear control mechanisms. This work is in line with the suggestions given in the review by Taylor et al. (2008), regarding modeling of biological systems. In it it is suggested that in order to further refine flight dynamics and control models, experimental approaches in which stimuli can be varied separately or combined, such as virtual reality setups, should be used.

The experiments described on animal flight in turbulence seem to indicate that a wide variety of strategies are used by insects and birds to stabilize under atmospheric disturbances; however, the role of each of this kinematic strategies is still not well understood. Experimental approaches that allow independent stimulation of different stabilization mechanisms seem to be a smart next step: these would provide further insight into the observed strategies, enable the definition of realistic models, and translate the most relevant strategies to the design of future flying robots. The present project aims to contribute in this direction proposing a manipulated-stimuli setup built in a wind tunnel, that enables the analysis of separate effects by generating tailored destabilizing profiles.

2.3. Active grids for turbulence and gust generation

Generation of turbulence in a wind tunnel has been traditionally addressed by means of passive grids. These present a mesh-like geometry, made up of square bars or rods placed perpendicular to each other. By locating them at an adequate distance upstream the test section it is possible to obtain close to isotropic homogeneous flows. One classic work with passive grids, often used as as a baseline for results comparison, is the one by Comte-Bellot and Corrsin (1966). Another relevant review is the one by Roach (1987), who looks into the effect of different passive grid configurations on pressure drop, turbulence intensity and mean speed. As noted by Cekli and van de Water (2010), and Roadman and Mohseni (2009a), works with passive grids are well documented. The main inconvenience derived from using passive grids for turbulence

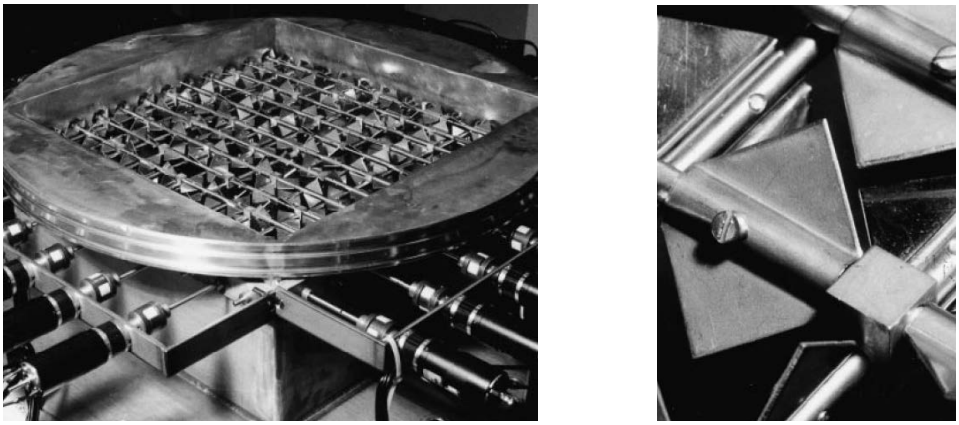

Figure 2.9: **Makita grid**, full grid and close-up to a vane. Image from (Roadman and Mohseni, 2009a)

generation is the limitation they impose to the maximum length scale attainable. Indeed the mesh size M determines the scale of the largest energy containing eddies (integral length scale). Additionally, with passive grids it takes a downstream distance of around $40M$ to reach isotropic and homogeneous conditions.

Active grids aim to overcome the drawbacks of passive grid generated turbulence. Although there are variations (see the grid with perforated plates by Mydlarski and Warhaft (1996)), the basic design follows the original one by Makita (1991), consisting on rods, distributed in rows and columns, with vanes attached (sometimes called wings). The rotation of each rod is controlled by servo motors, each one driving a complete row or column of vanes. Figure 2.9 shows Makita's grid. Recent most sophisticated setups, such as the one used by Cekli and van de Water (2010) and the one used in this project, allow the control of the initial position, speed and sense of rotation of each axis. With this arrangements active grids are able to generate near isotropic and homogeneous turbulence at much larger scales. Additionally, they require much shorter test section lengths, with good isotropy and homogeneity levels even at $10M$, as reviewed by Roadman and Mohseni (2009a). In this way, active grids enable the modulation of turbulence in both time and space (Cekli and van de Water, 2010).

The active grid used in this project is based on the design used by Cekli and van de Water (2010), developed at Eindhoven University of Technology. In his PhD thesis, Cekli (2011) uses the active grid for the generation of turbulence, to answer fundamental research questions from a fluid dynamics perspective. This is the case of one of his thesis derived publications, in which the tailoring capabilities of the grid are demonstrated, first by generating homogeneous shear turbulence (characterized by constant mean speed gradient and constant turbulence intensity); and secondly by producing a scaled ABL in a wind tunnel with tunable properties (Cekli and van de Water, 2010). An interesting aspect of their approach is the superposition of two techniques: by setting the initial angular position of the vanes the desired profile is designed, and by setting the vanes in flapping motion around these initial position the required turbulence intensity is injected. One of the earliest works on the characteristics of active grid generated turbulence is the one by Mydlarski and Warhaft (1996), often used as a reference. The work by Knebel et al. (2011) looks further into simulating atmospheric conditions in a wind tunnel using an active grid, and presents a replication of intermittent natural wind fields.

An active grid application that comes closer to that desired for MAV testing or experiments on animal flight is the one proposed in the two works by Roadman and Mohseni (2009a and 2009b). In them the development of a gust wind tunnel is proposed, able to replicate the characteristics of the ABL relevant for MAV flight, without downscaling. This would allow the most realistic comparison, being useful for testing as well as for model validations. Both papers describe the construction of a prototype gust tunnel, based on an active grid, which would serve as basis for the design of a future atmospheric gust tunnel.

In their first work on the topic, Roadman and Mohseni (2009a) present a short literature review on the modeling of atmospheric gusts and on its experimental simulation in wind tunnels. A distinction is presented between *discrete gusts*, understood as those generating *"a finite change in velocity occurring only*

once" , and *continuous gust*, associated with turbulence and a range of frequency content, usually addressed with an harmonic analysis. The theoretical relation between both models is described in detail in Zbrozek (1960). The experimental techniques used to simulate both types of theoretical gusts are also reviewed in Roadman and Mohseni (2009a): for the discrete type external jets and oscillating slats have been applied (see work on NACA Gust tunnel at Langley, Donely (1939); see schematic of Gust tunnel on Figure 2.10); for the continuous one mostly grids have been used.

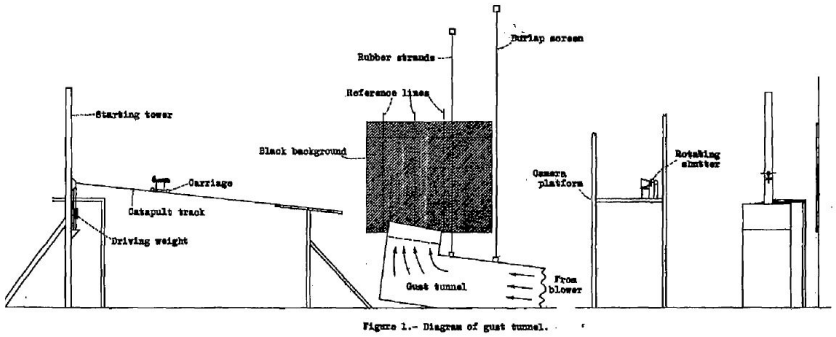

Figure 2.10: **Schematic of NASA Langley gust tunnel**, from Donely (1939)

On the follow-up work, Roadman and Mohseni (2009b) describe in further detail the construction of the prototype gust tunnel. Using an active grid, their objective is to replicate turbulence of the largest scale possible, with homogeneity and isotropy similar to atmospheric values. With an innovative vane twisting arrangement (see Figure 2.11) and the definition of a tip speed ratio based on wind tunnel width, they find an adequate operating point that leads to the generation of large length scales in a small wind tunnel (test section 0.34m wide, 0.91m long, length scales attained around 40%width) with higher levels of isotropy than those generated in previous studies.

Approaches like the ones followed by Roadman and Mohseni (2009b) and Cekli and van de Water (2010), in which the multiple degrees of freedom in active grids are used smartly to recreate realistic conditions, show the large potential of these tools. In the scope of this project, aiming mostly to prove a tracking capability, the active grid has not been used to its fullest potential; as a starting point for continuing projects in this line this short review is considered useful to inform about the active grid capabilities and inspire next developments.

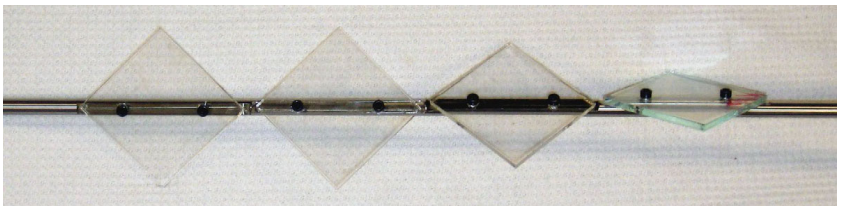

Figure 2.11: **Vane twisting arrangement proposed for gust tunnel**, from Roadman and Mohseni (2009b)

2.4. Conclusions and project relevance

The presented review has shown several gaps in the assessment of the stability problem of MAV under turbulence, and in the unraveling of stabilization mechanisms used by birds to overcome atmospheric upsets.

Regarding the first one, there is a need to replicate relevant destabilizing conditions in a wind tunnel, and to extract realistic models of its effects on MAV flight dynamics. This would facilitate the definition of improved designs, more robust against wind perturbations. As for bird stabilization mechanisms, approaches that enable independent manipulation of the stimuli may shed some light into the different roles of the

kinematic strategies observed. The present tool aims to contribute to both areas, developing at the level of proof-of-concept, a wind tunnel tool that allows the design of destabilizing wind profiles. These profiles are mostly oriented to generate roll perturbations (which has been shown to be a particularly sensitive axis) and yaw ones (relevant for example to unravel the role of the tail). The additional tracking capability is in line with recent proposals of systems-level approaches to the identification of biological systems.

3

Experimental setup

The experimental setup consists on four main elements: wind tunnel, active grid, wind sensors array and motion tracking system. In this chapter, each of these elements is discussed and main technical specifications are detailed. Since one of the proof-of-concept objectives of this project is to demonstrate the applicability of low-cost wind sensors in the design of gusts, a particular focus is made on them. Figure 3.1 shows a schematic of the setup.

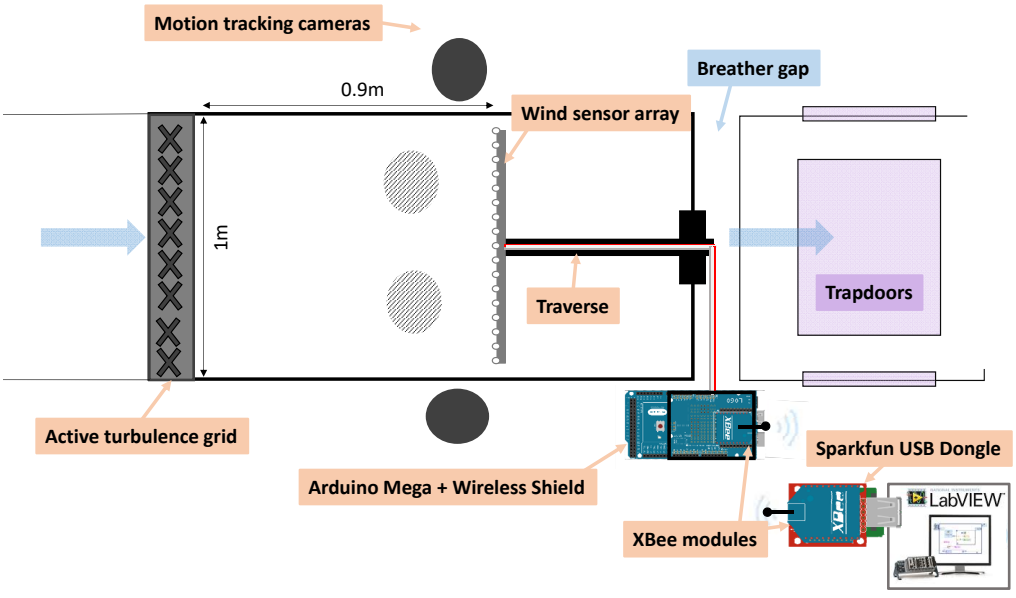

Figure 3.1: **Schematic top view of experimental setup.** Labels indicate the main parts discussed in the text. Light blue thick arrows indicate the flow direction, from left to right. The test section walls hold translucent acrylic panels (test section marked with orange contour). The whole set of four motion tracking cameras are marked with green contours; the ones located under the test section floor are marked with a texture fill. Note the breather gap downstream the test section, to ensure atmospheric pressure, and the trapdoors at the sections further donwstream (located on the floor and on the sidewalls), that allow access for training and experiments. Arduino, XBee and Sparkfun figures from Fritzing (2017); Labview figure from National Instruments (2017).

3.1. Chapter overview

The different pieces of equipment used to build up the Gust Design Tool are described. First, the **low-turbulence wind tunnel** is presented. Around its test section the tool is built. Next, the **active**

turbulence grid is introduced and its specifications are explained. The **wind sensor array** is then looked into: this section starts with a brief description of hot-element flow measurement techniques, then the two types of sensors used are discussed (low-cost wind sensors and hotwire probe); next the setting up of the array is commented, followed by the description of the data acquisition and display system; finally the calibration procedure is described. The chapter closes with the last piece of equipment added to the setup, the motion tracking equipment used to enable the tracking capability in the dynamic gust designs.

3.2. Low-turbulence wind tunnel

The wind tunnel in which the Gust Design Tool is built is a brand new low-turbulence wind tunnel especially designed for animal and small vehicle flight experiments (Figure 3.2). Officially inaugurated on April 22, 2016, its multipurpose design enables to study flight in the whole range of atmospheric conditions in which animals fly, from turbulent and gusty flow close to the ground (10-40%, Watkins et al. 2006), to quiet and laminar one at higher altitudes (<0.1%, Reeh 2014).

The wind tunnel configuration is closed-circuit: this allows to attain lower turbulence intensities than with open-circuit wind tunnels, as well as a quieter operation. However compared to an open-circuit tunnel, closed-circuit ones reach higher running temperatures. This requires the use of temperature control systems. In this wind tunnel, a water-chilled heat exchanger keeps the temperature steady (for the results presented in this thesis, temperature is kept at 20ºC).

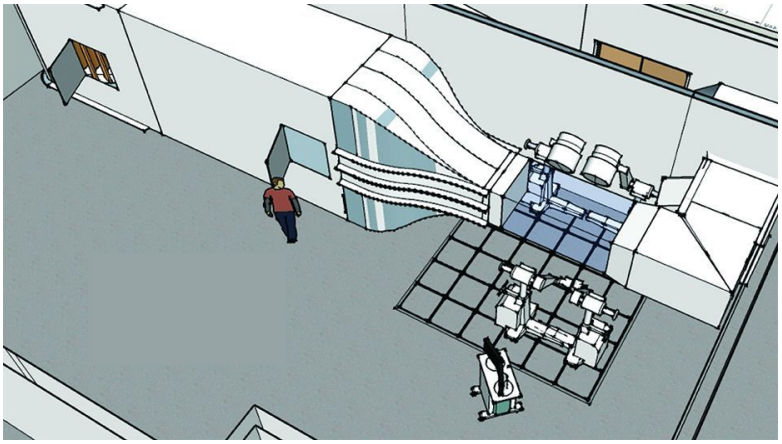

Figure 3.2: **Stanford low-turbulence wind tunnel,** for animal and small aerial vehicles flight studies. Preliminary schematic shows contraction and test section; fan and the rest of the closed-circuit are located at the other side of the acoustic wall. Image modified from LentinkLab (2016).

The wind tunnel can produce airspeeds up to 50 m/s in a rectangular test section that is 1m wide, 0.82m tall and 1.73m long. The test section walls diverge in the streamwise direction, accounting for boundary layer growth and minimizing streamwise pressure gradients (top and bottom walls, 0.5deg divergence; sidewalls divergence can be varied for different blockages). Downstream the test section a breather gap ensures testing pressures are close to atmospheric and enables easier access for probes supports. The traverse system used for the wind sensor array is fixed to the wind tunnel in this breather gap, as shown in Figure 3.1. The test section components are all matte black to facilitate motion tracking, high-speed videography and particle tracking. Additionally, each of its walls holds a translucent panel that can be removed for inside repairs or quick access. To facilitate access when installing supports or training with animals, side and floor trapdoors are present in the area downstream the test section (see Figure 3.1). From the floor trapdoor the test section is accessed for the dynamic gusts experiments in Chapter 8. In total the closed-circuit covers a projected area of 15.1m x 5.2 m, with a maximum height of 4m.

The flow is driven by a single stage, 18 blade, 1.5m diameter axial fan, powered by a 80 kW induction motor (max speed 891rpm, resolution +/- 0.1rpm). For the results presented in this thesis, the fan speed was set to

120 rpm. Uniformity in the flow is further achieved with a carefully designed 7:1 contraction upstream the test section and by incorporating seamless honeycomb and screens ahead of it. On normal wind tunnel operation (i.e., without active turbulence grid), turbulence intensities reached at the centerline of the test section, in both axial and transversal direction, are below 0.03% at all operating speeds. However, the tunnel's modular design allows the incorporation of an active grid just upstream the test section, which can generate highly turbulent flow (up to ~ 45% at the centerline). The grid enables the injection of turbulence in the flow, and can also be used in the design of nonuniform profiles downstream. In this work the latter capability is exploited.

3.3. Active turbulence grid

The active turbulence grid enables the definition of wind profiles downstream and the injection of turbulence in the flow. It is located just upstream of the test section (see Figure 3.4). As mentioned on section 2.3, the main advantage over passive grid setups is that active ones can produce large turbulence lengths scales and high turbulence intensity levels without requiring an excessively large test section (Roadman and Mohseni, 2009b; Cekli, 2011).

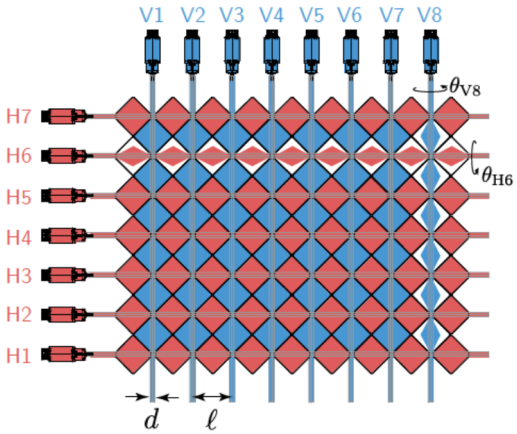

Figure 3.3: **Schematic of the active turbulence grid.** Dimensions l and d indicate the side of the diamond-shape vanes, and the rods' width, respectively: $l = 10$cm, $d = 2$cm. Degrees of freedom of each rod are also shown (θ_{V8} and θ_{H6}). Figure created by Daniel B. Quinn and Yous van Halder.

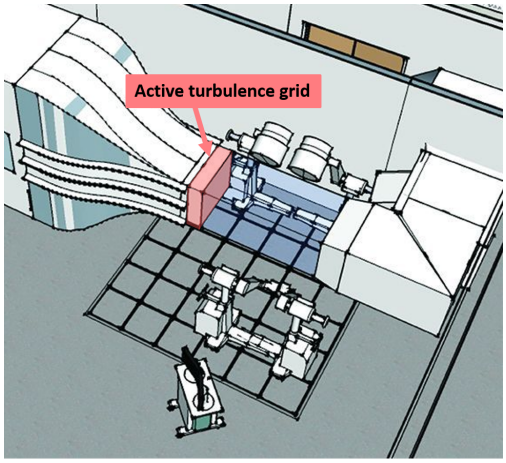

Figure 3.4: **Location of active grid when installed in the wind tunnel.** The grid is set up upstream the test section. Modified figure from LentinkLab (2016).

The active grid used is made up of seven rows and eight columns of diamond-shape vanes, as shown in Figure 3.3. Each row and column is controlled by a power assembly consisting on a motor (Maxon RE 40, diameter 40mm, Graphite Brushes, 150W Motor), a planetary gearhead (Maxon Planetary Gearhead GP 42C, diameter 42mm, 3-15Nm, Ceramic Version) and an encoder (Encoder HEDL 5540, 500 CPT, 3 Channels, with Line Driver RS 422). Motors are controlled with position controllers (Maxon EPOS2 70/10) each one with its individual power supply (Phoenix Contact QUINT Series 24V-20A). The grid design is based on the one built by Hakki Cekli and Willem van de Water (Cekli, 2011), from Eindhoven University of Technology.

The positive direction of rotation of the vanes is defined as the clockwise direction as seen from the motor. When inputting a certain vane angle, the vanes go to that position at maximum speed (12000rpm) The grid's state will be often characterized with the grid transparency parameter, that evaluates the ratio between the area at the grid section, at a certain vanes angular position, and the area at the grid section when all vanes are at 0deg. Taking into account the grid geometry (see Figure 3.3) the grid transparency parameter is defined as follows:

$$GT = \frac{250}{21} + \frac{100}{21}(8 - \sum_{i=1}^{8} \sin\theta_{v,i}) + \frac{150}{21}(7 - \sum_{i=1}^{7} \sin\theta_{h,i}); \qquad (\%) \tag{3.1}$$

where $\theta_{v,i}$ and $\theta_{h,i}$ are the vanes angles for each individual column or row, respectively. Note that there are eight vertical columns of vanes and seven horizontal rows of vanes. When all vanes, horizontal and vertical, are at 0deg position the grid state is referred as "fully-open". The grid was set up by previous visiting student Yous van Halder, who also defined several motion protocols for it (Turbulence Generation System Manual by van Halder, 2015). The resolution in the vanes angle is 1deg.

3.4. Wind sensor array

In this section the different aspects of the wind sensor array are discussed: first, the flow measurement technique common to the two types of sensors used in this project is introduced; next, each sensor type is discussed in more detail. Once the main specifications have been defined, the construction of the array is presented. The data acquisition setup is then discussed and finaly the calibration procedure is explained.

3.4.1. Sensors

Hot-element techniques for flow measurement are first discussed, and then the two wind sensor types used in this project are described: the low-cost wind sensor rev P (based on thermistors) and the hotwire probe.

Hot-element flow speed measurement techniques

Hot-element techniques determine flow speed from the convective heat transfer the flow causes on a hot element placed in it. The hot element is heated through Joule effect by an electrical current. It usually consists on a thin wire (hotwire anemometers) or a film (film probes, fiber-film proves), with typical diameters ranging from 0.5 - 5μm and lengths from 0.5 - 2mm. The length of the sensing element determines the minimum resolvable length scale in the flow, whereas the ratio wire length to diameter needs to be large enough, in order to assume negligible the heat transferred to the wire support (Cekli, 2011).

From the electrical point of view, the two most common approaches to design hotwire probes are Constant Temperature Anemometry (CTA) and Constant Current Anemometry (CCA); for both sensors used in this project the approach is CTA. Both CTA and CCA approaches rely on a Wheatsone bridge configuration, a circuit that enables the determination of an unknown electrical resistance with higher accuracy than a voltage divider. For the case of a hotwire probe, this unknown resistance corresponds to the wire's resistance R_w (see Figure 3.5). Applying Kirchhoff Laws, a relation between the voltage across the bridge V_G and the unknown wire resistance R_w can be derived:

$$V_G = \left(\frac{R_2}{R_1 + R_2} - \frac{R_w}{R_w + R_3}\right) V_s \tag{3.2}$$

where V_s is the supply voltage.

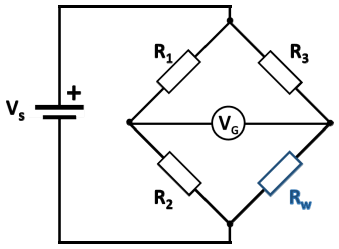

Figure 3.5: **Schematic wheatstone bridge.** V_G is the voltage across the bridge, V_S, the supply voltage; R_w the unknown resistance is marked in blue (the wire resistance for the hotwire case).

With a CTA approach the circuit aims to keep the wire's resistance R_w constant under changes in temperature (and thus, in resistance) imposed by the surrounding flow. It does so by feeding the output voltage from the bridge V_G to a servo amplifier G, which keeps the bridge in balance (i.e., V_G = 0) by supplying the necessary current to the resistance R_w(Figure 3.6). On the contrary a CCA approach relies on a balanced bridge at zero flow speed; this bridge then becomes unbalanced when an increase in flow speed varies the wire's resistance R_w. The unbalanced voltage directly relates to the resistance value R_w and the flow speed. Although in principle it is faster to read the bridge voltage than to balance the circuit, with a CTA approach the hot element temperature remains approximately constant and thus non-linearities related to thermal inertia are reduced (Dantec Dynamics, 2013a). Consequently CTA is often preferred for fast-changing fluctuations, whereas CCA is usually applied in resistance thermometers.

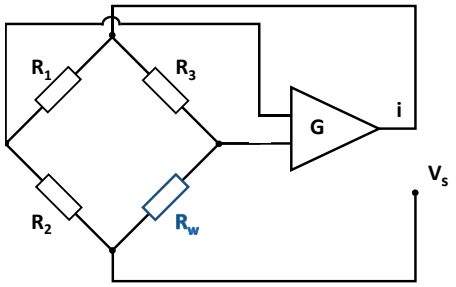

Figure 3.6: **Schematic for constant temperature approach (CTA)**. A servo amplifier G supplies the required current to keep the bridge in balance when R_w changes its resistance value due to flow speed variations that change its temperature.

These especial circuitry approaches, along with the thermal properties of the wire's selected material and its geometry (mainly its high surface-to-mass ratio, as indicated in the specifications by Dantec Dynamics (2013b)), make hotwire anemometry able to capture velocity fluctuations up to very high frequencies, with a relatively small spatial resolution (Roadman and Mohseni, 2009a). This makes it a reliable and widely used instrument for turbulence experimental research. However they are fragile and, most relevantly, quite expensive due to the manufacturing and calibration process (Roadman and Mohseni, 2009a). Their cost is indeed a strong limitation for experiments requiring multi-point simultaneous measurements (Prohasky and Watkins, 2014). A frequent approach to go around this limitation is to assume Taylor's frozen turbulence hypothesis, and derive spatial streamwise separation from temporal measurements (Wyngaard and Clifford, 1977; Cebeci, 2004). However in many applications it is desirable to make use of multiple sensors, for example for profiles evaluation when replicating atmospheric boundary layer flows or winds around buildings, as noted by Prohasky and Watkins (2014). An alternative option for multi-point measurements is to use optical methods such as Particle Image Velocimetry, but these are at least as expensive.

Wind sensor Modern Device rev P

Modern Device rev P wind sensor is the sensor type used to build up the array. These are low-cost hot-element anemometers that follow the same working principle as CTA hotwires. The sensor and its elements are shown in Figure 3.7 and a schematic of the circuit on Figure 3.8.

The schematic in Figure 3.8 shows that each wind sensor makes use of a Wheatstone bridge with controlled input voltage. On the bottom right prong it can be seen that a dedicated ambient temperature thermistor (10kΩ) is made part of the bridge as a hardware compensation for ambient temperature. On the opposite prong, a Microchip MCP9701A Linear Active Thermistor™ IC (an analog temperature sensor whose output voltage is directly proportional to the measured temperature) accounts for the hot element in the sensor. According to the manufacturer, its accuracy is of ±2°C from 0°C to +70°C when consuming 6 μA operating current (Microchip, 2016). Both of them are based on Positive Temperature Coefficient (PTC) thermistors, and so they increase their resistance with increasing temperatures.

The advantages of PTC versus Negative Temperature Coefficient (NTC) thermistors is that PTC are available at higher precisions, which enhances the accuracy attainable with the Wheatstone bridge. A disadvantage is

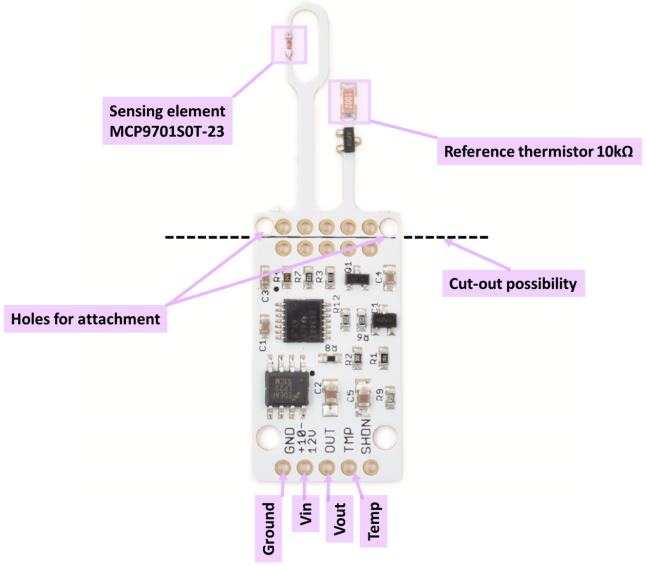

Figure 3.7: **Wind sensor Modern Device rev P.** Main elements are labeled and marked in purple. Note the holes that are used for attachment to the clamps and the possibility of splitting the PCB.

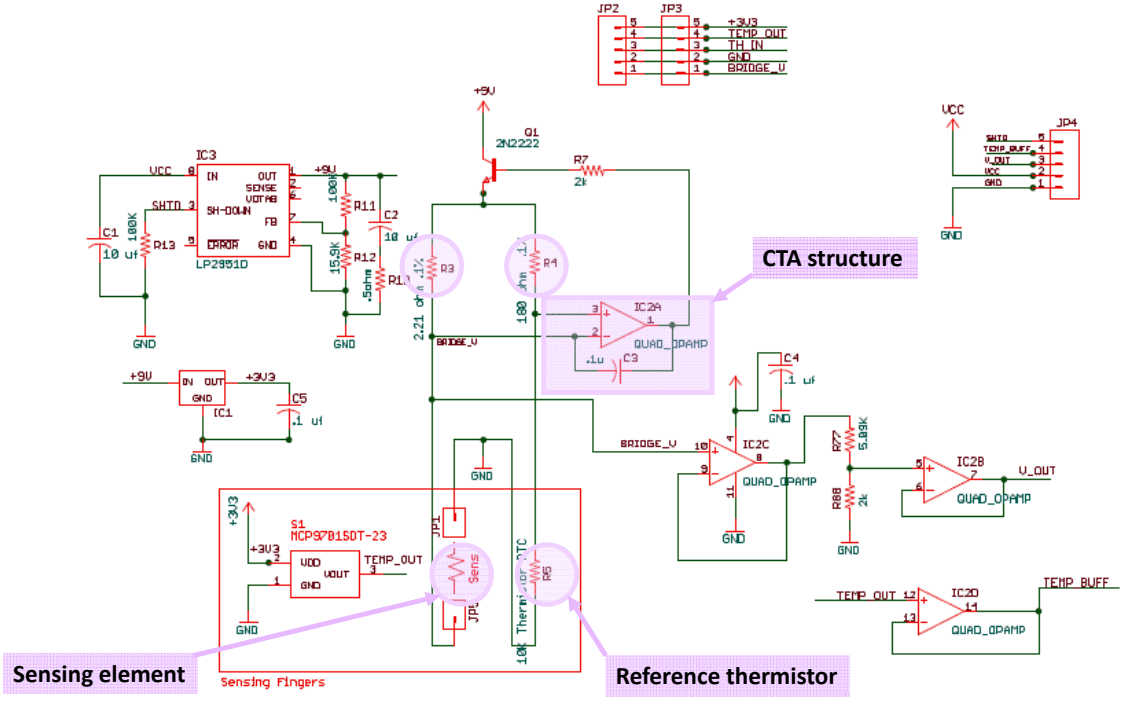

Figure 3.8: **Modern Device Wind sensor rev P circuit schematic.** Elements that make up the bridge are marked in purple circles; CTA structure is marked with a purple square. Sensing element and reference thermistor are labeled. Modified from schematic available at Badger (2014b).

that they are available only at high resistance values, and thus require larger supply voltages. However operating at a higher voltage may be beneficial for a faster cooling down of the hot element, being further away from ambient temperature. As shown in Figure 3.7, the sensing fingers are separated from the main body of the PCB, and the flow-sensing element is mounted in a loop with no board behind, in an effort to make it omnidirectional (Badger, 2014b). It should be noted that it is also possible to "cut-out" the sensing fingers from the board and use them separately, which can be very convenient for small setups.

This sensor was first released in June 2014 (Badger, 2014a); however they have been used scarcely in literature. Only one research group was found that used them, to develop a mini-wind tunnel and flow measuring tool with prototyping purposes, to preliminary assess wind effects around buildings (Prohasky and Watkins, 2014; Moya et al., 2014; Williams et al., 2015; Prohasky et al., 2014; the latter uses the predecessor of the rev P wind sensor). Their whole mini-wind tunnel setup is described in detail at the project's website, by Moya and Prohasky (2014). The work by Prohasky and Watkins (2014), the most relevant for the current project, presents a comparative study between Modern Device rev P wind sensors and the TFI Cobra probe, a multi-hole pressure probe that measures local static pressure and the three velocity components (Turbulent Flow Instrumentation, 2016). The former ones are 1/1000 of the price of the latter one. Both types are assessed in smooth and turbulent flow, replicating ABL conditions.

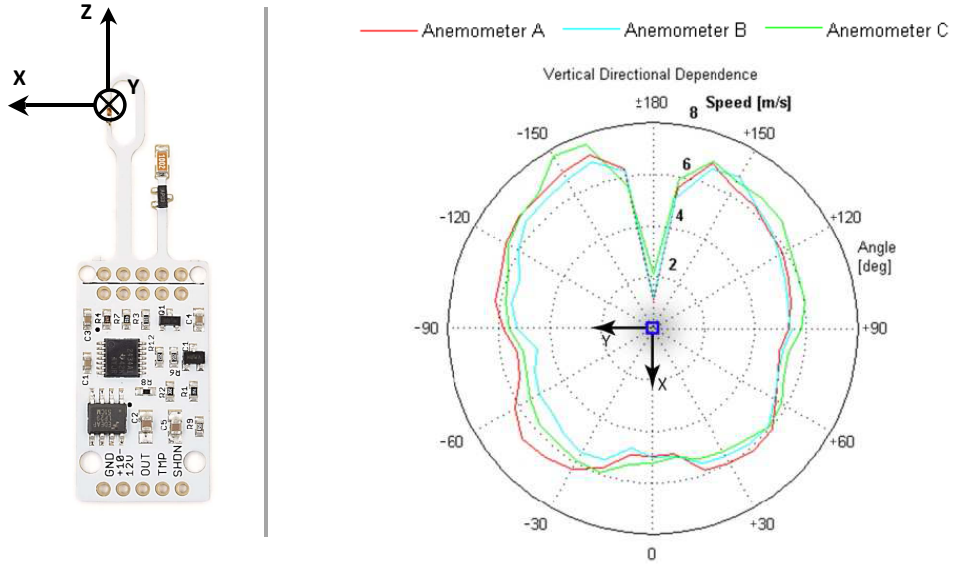

Figure 3.9: **Directional dependency results for three Modern Device rev P wind sensors, for yaw angle,** from Prohasky and Watkins (2014). Left figure shows the reference axis selected by the authors; note that they are defined in left-hand convention. Right figure show the directional dependency results. The sharp dip found at 180deg is attributed to the effect of the rotational rig. A close to omnidirectional response is found from +20deg to +160deg around the Z-axis; this is the region of operation in the present project.

Authors find that the sensors perform well in measuring average flow speeds (within ±0.5m/s), provided the ambient air temperature is controlled and kept constant; this is the case for the operating conditions in our wind tunnel. Additionally, some differences in response due to manufacturing variations are found; thus, the wind sensors used in our project are calibrated individually. Regarding directional dependency, a reasonable omnidirectionality in yaw is found from +20deg to +160deg, which is the range where we expect to work in (see Figure 3.9). The sharp dip in the yaw results at 180deg is attributed by the authors to rotational rig in which the sensor is set up. This seems to be the case by comparing the results to the preliminary analysis on yaw-angle dependency carried out early in this project (see Appendix E).

Prohasky and Watkins (2014) also assess the frequency response of the wind sensors. In passive grid-induced turbulent flow, the response is found to significantly reduce over 10Hz (Figure 3.10); this is taken into account when selecting the sampling frequency in our project. Additionally, the sensors are found

unsuitable for turbulence intensity measurements, yielding results larger than those given by the reference Cobra probe. The authors mention as possible causes the wind sensors' directional dependency, their reduced frequency range and the noise in the system during measurements (due to electrical inductance or temperature dependent responses), and suggest that a low-pass filter with cut-off frequency below 10Hz may improve the results.

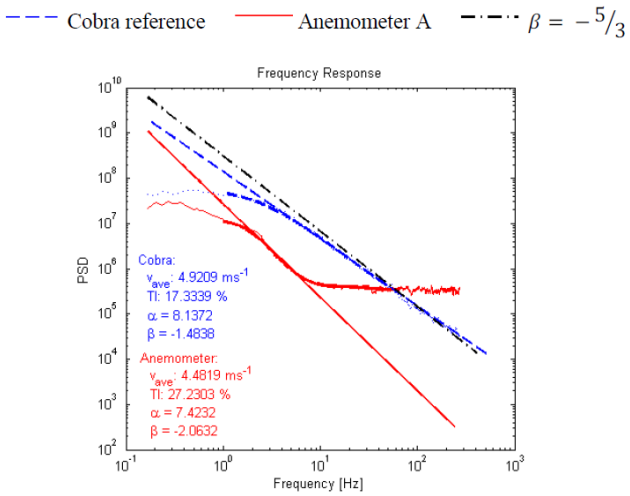

Figure 3.10: **Frequency response Cobra probe vs Modern Device wind sensor rev P (anemometer)**. β represents the slope of the log-log fit; α represents the intercept. Line with Kolmogorov slope -5/3 plotted as reference for inertial range in a fully developed turbulent flow. Image from Prohasky and Watkins (2014).

From this characterization study, Prohasky and Watkins (2014) conclude that these wind sensors are suitable for measuring average wind speeds when the flow direction is fairly well-known, and thus result useful for wind tunnel velocity profile measurements. They also emphasize their potential in prototyping applications, due to enabling close to real-time visualization. They also comment that their robustness make them good candidates for characterization field works in wind engineering, in a similar way to the Irwin probe (Irwin, 1981).

Hotwire probe Dantec CTA Miniature Wire Sensor 55P16

Apart from the low-cost wind sensors previously described, a hotwire probe is used in this project for performance comparison. The hotwire probe used is a Dantec CTA Miniature Wire Sensor 55P16, shown in Figure 3.11. The hot element in this case is a single wire of platinum-plated tungsten. Its working principle is also that of a Constant Temperature Anemometer (enabled via a Dantec miniCTA anemometer module (Dantec Dynamics, 2013c)). Its specifications are shown in Table 3.1.

Note that, although the circuitry working principle is the same for both types of sensors, their different materials and architectures affect their performance, with an important effect on their thermal inertia. The hotwire probe will present lower thermal lag due to its higher surface-to-mass ratio, that strongly enhances heat dissipation, and due to the thermal properties of its sensor material. Its lower density and heat capacity and its high temperature coefficient of resistance (which relates resistance and temperature of a metallic conductor) yield a smaller time constant, and thus a higher flow sensitivity (Dantec Dynamics, 2013b).

3.4.2. Array support

The array of wind sensors is made up of sixteen sensors: this amount of sensors matches the number of analog pins available in an Arduino Mega board (and avoid adding further multiplexing) and correspond each vertical column of vanes in the turbulence grid with two sensors. Seventeen round clamps from photographic equipment are used to support the sensors, and an additional rectangular clamp is used to fix the bar to the wind tunnel traverse (all clamps from SmallRig (2017), shown in Figure 3.12). An aluminum bar of 3ft (0.914m) and 15mm diameter, a short piece of threaded rod and an hexagonal nut complete the elements used in the setup (all purchased in McMaster-Carr (2016)). Images of the array support can be

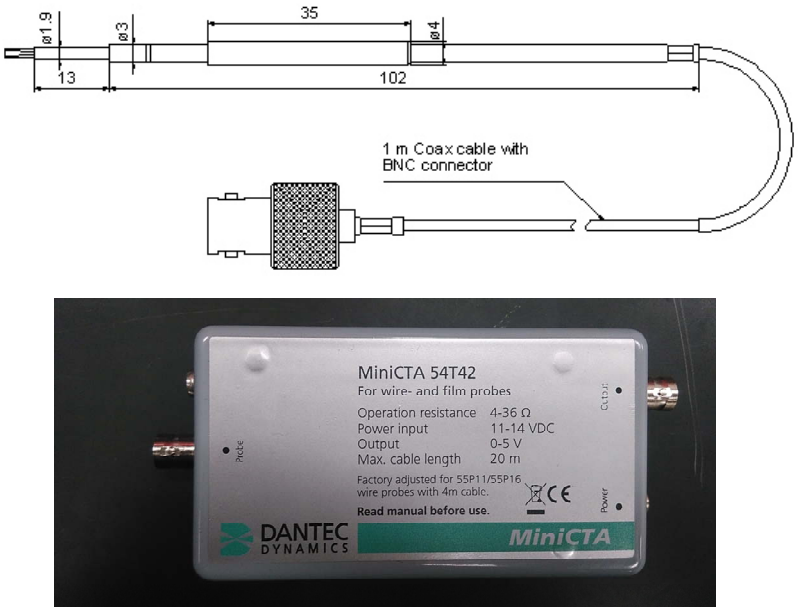

Figure 3.11: **Dantec CTA probe 55P16.** Top: technical drawing of hotwire probe, from Dantec Dynamics (2013d); bottom: mini CTA module

Table 3.1: Technical specifications for the probe used Dantec CTA probe 55P16, from (Dantec Dynamics, 2013b) and particular probe data sheet

Technical data for specific probe 55P16 used	
Medium	Air
Sensor material	Platinum-plated tungsten
Sensor dimensions	5μm dia, 1.25mm long
Sensor resistance at 20ºC (for specific probe)	3.45Ω
Leads resistance	0.9Ω
Temperature coefficient of resistance at 20ºC	0.36%/C
Max. sensor temperature	300žC
Max. ambient temperature	150žC
Max. ambient pressure	Depends on the type of mounting
Min. velocity*	0.05m/s
Max. velocity	500m/s
Frequency limit (CTA mode)	400kHz

* influence from natural convection up to approx. 0.20m/s

found in Appendix A.

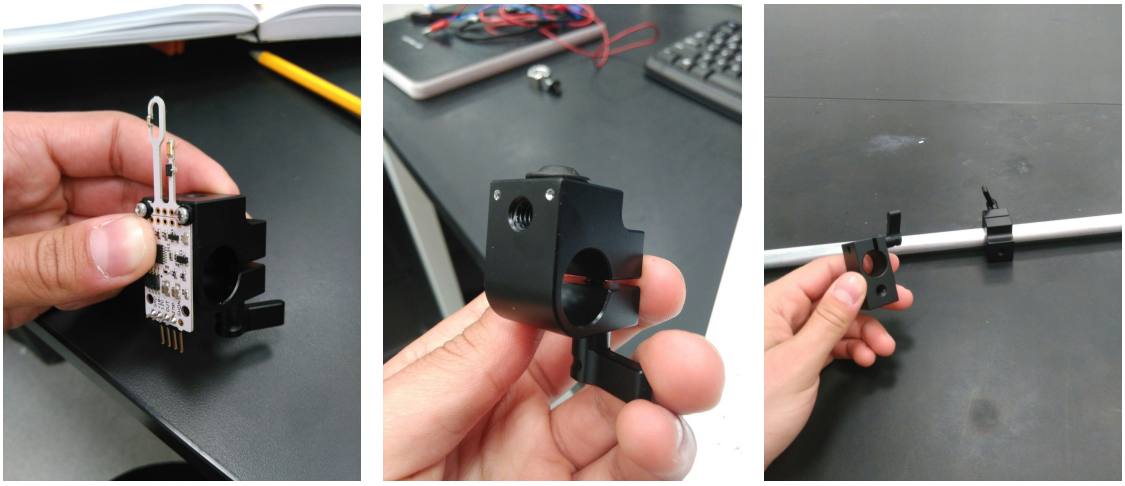

Figure 3.12: **Types of clamps used for the array setup.** Left: round clamp modified to support wind sensors. Center: round clamp modified to support hotwire probe; the pre-existing 1/4" - 20 thread was drilled through and the top one was use to fix the probe into place with a short screw. Right: rectangular clamp, later modified to attach the array to the wind tunnel traverse, and round clamp mounted on the rod.

The setup construction is now described. Each of the sensors is soldered to a connector housing, and three pieces of wire, of 3m each, are crimped and connected to the three relevant pins: ground, input voltage and output voltage. Each sensor is then attached to a clamp with two screws (using the available holes at the top of each PCB). All clamps with the sensors attached are slided in the aluminum bar, with a pitch between clamps of 5cm. Note that an extra clamp is added to support the hotwire probe, with a modified design to adapt to it. Additionally, the rectangular-type clamp is modified and located at the bar's midpoint to serve as attachment to the traverse. A bridging piece of roded bar is used to connect the modified rectangular clamp to the threaded end of the traverse. An hexagonal nut is added to make sure the bar does not roll. The wires from each of the sensors are tied to the traverse support with zip-ties and passed through the breather gap to be later connected to the Arduino Mega board. The array is finally located 0.9m downstream the grid. A schematic of the array setup is shown in Figure 3.13, including region division and sensor numbering.

3.4.3. Data acquisition system, display and processing software

The data acquisition is set up around an Arduino Mega board. Figure 3.14 shows an schematic of the setup and Figure 3.15 shows the breadboard connections. Wires coming from the sensors are connected to a breadboard. Input voltages and ground wires are connected to a power supply providing 12V and ground; the output voltage wires are connected to the analog pins of an Arduino Mega 2560 Rev3 board. To avoid floating ground issues, grounds from the Arduino board and the power supply are connected as well.

Additionally, pull-up $20k\Omega$ resistors embedded in the Arduino analog pins are enabled via software so that voltage drops are easily identified (the pull-up circuit "pulls" the pin to a high voltage reading when its not pulled down to a low reading by an external circuit). The Arduino board is powered by a 9V battery, or for practicality by connecting it to a laptop. The Arduino Mega board is fitted with an Arduino Wireless SD shield that enables the attachment of an XBee radio module. The other module of the XBee pair is connected to a Sparkfun USB dongle (Figure 3.16), that allows to connect it to the PC. This PC is equipped with Labview and contains the GUI for controlling the grid, developed by previous visiting student Yous van Halder.

Labview is selected as the software to process and display the sensor array data. This is due to its favorable integration with different pieces of hardware equipment and due to the grid controller being already implemented in Labview. The output voltage data from each sensor is acquired at the Arduino Mega board and transformed from analogue to digital, to be transmitted wirelessly to the XBee module connected to the PC. Through a VISA serial communication port in Labview, digital data is received, scaled to voltage data (5V

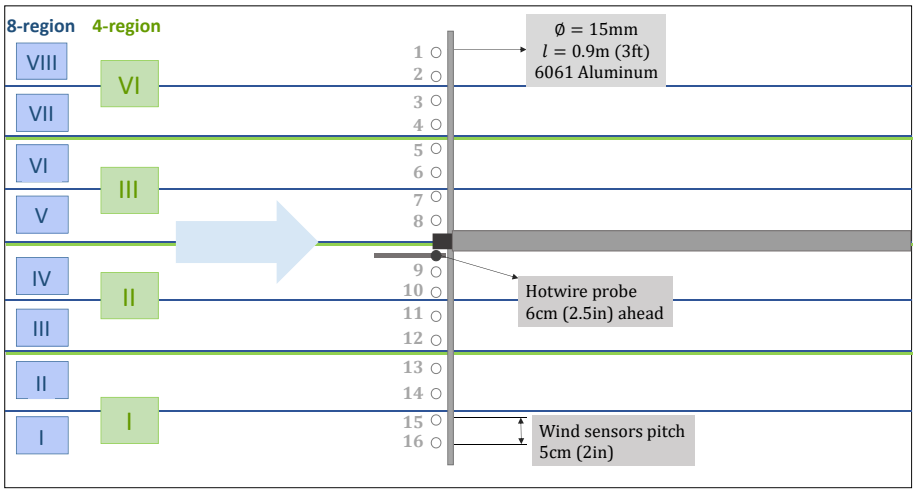

Figure 3.13: **Schematic top view of array support.** Wind sensor array and traverse support setup, as seen from the top, with flow going from left to right. Wind sensors are represented by round markers and accompanied by their assigned numbers. Pitch between sensors is 5cm, except for sensors 8 and 9, for which the distance in-between is 10cm (each of them is 5cm from the connecting traverse piece). The hotwire probe, when used, is located between the connecting piece to the traverse and sensor 9. Solid green lights indicate the limits for the 4-region approach, whereas solid blue lines indicate the limits for the 8-region approach. The numbering of the regions for each case is indicated to the left of the image.

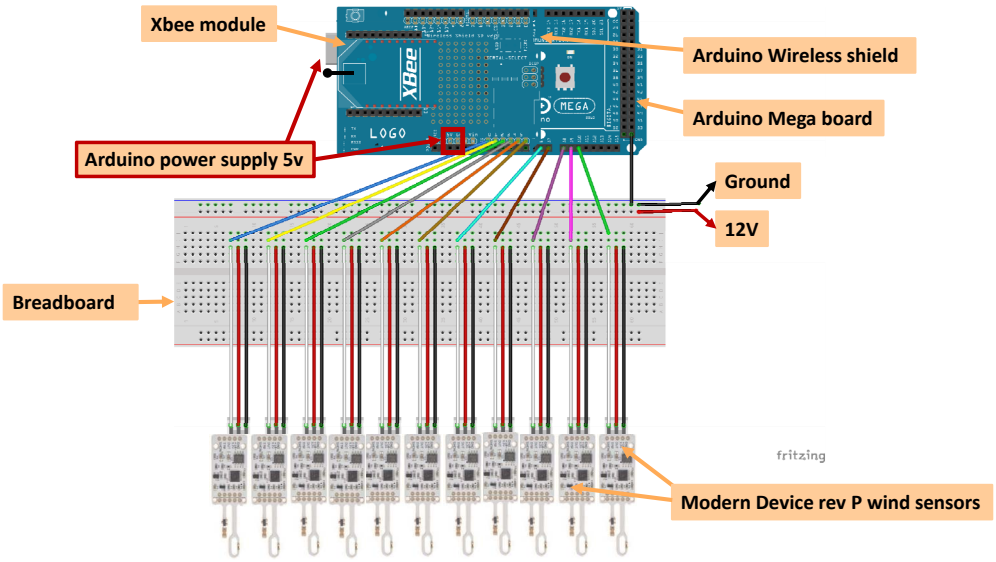

Figure 3.14: **Schematic of data acquisition system.** Connections between sensors, Arduino board with Wireless shield, and XBee module are shown. Note that the Arduino board can be powered with a battery, through the GND and 5V pins marked in a red square, or by powering it through a laptop via the USB connection.

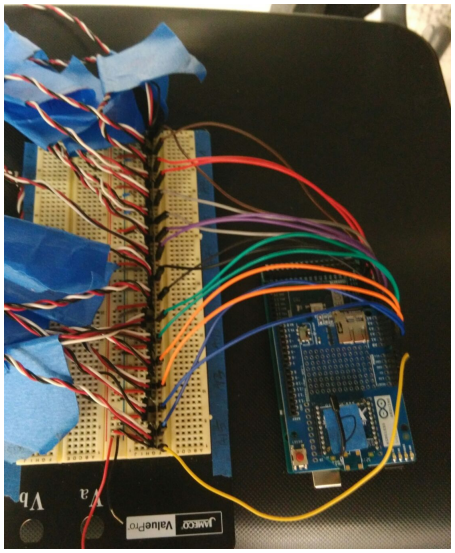

Figure 3.15: **Breadboard connections and Arduino board.** Note that the setup is not powered in the picture.

Figure 3.16: **XBee module connected through a USB Dongle to PC.** Wind sensors measurements are transmitted wirelessly to the PC with Labview.

= 1024bits), processed, displayed as flow speed measurements and saved. Baud rate (bits per second in the data reception) is set to 115200 and sampling frequency is set to 40Hz. This value is enough to capture the frequency range of the sensors, as noted by Prohasky and Watkins (2014). This approach also enables close to real-time visualization, an important advantage for experiment design and prototyping (Prohasky and Watkins, 2014).

Hotwire connection to the PC is more straightforward since Labview has dedicated VIs for interacting with certain hardware, such as the Dantec hotwire used here; The miniCTA module connects the probe to the PC, where the data is processed using a Data Acquisition configurable VI in Labview.

3.4.4. Array calibration

Each one of the wind sensors in the array is calibrated with the wind tunnel airspeed control. Fan rotating speed was gradually increased varying the setpoint speed in the wind tunnel control GUI, and data was gathered at each setpoint for 100s. Setpoint speeds were varied from 0 to 14 m/s, with increased data points acquired in the range from 1 - 6 m/s. From the voltage data registered at each sensor, at each setpoint speed, a trimmed mean is performed, removing outliers by not considering 1% of extreme values. For each sensor a calibration curve is thus obtained by fitting the trimmed mean voltage points to the corresponding flow speed values with a third-degree polynomial expression. Screenshots of the Labview VI codes are shown in Figure 3.17 and calibration coefficients used for each sensor are shown in Table 3.2.

The hotwire calibration curve used is the one defined by the previous visiting student Yous van Halder, also performed with temperature control at 20ºC. The expression applied is the following:

$$U_{hw} = 0.876\left(V_{out}^2 - 1.434\right)^{2.375} \tag{3.3}$$

where V_{out} is the voltage signal from the hotwire probe.

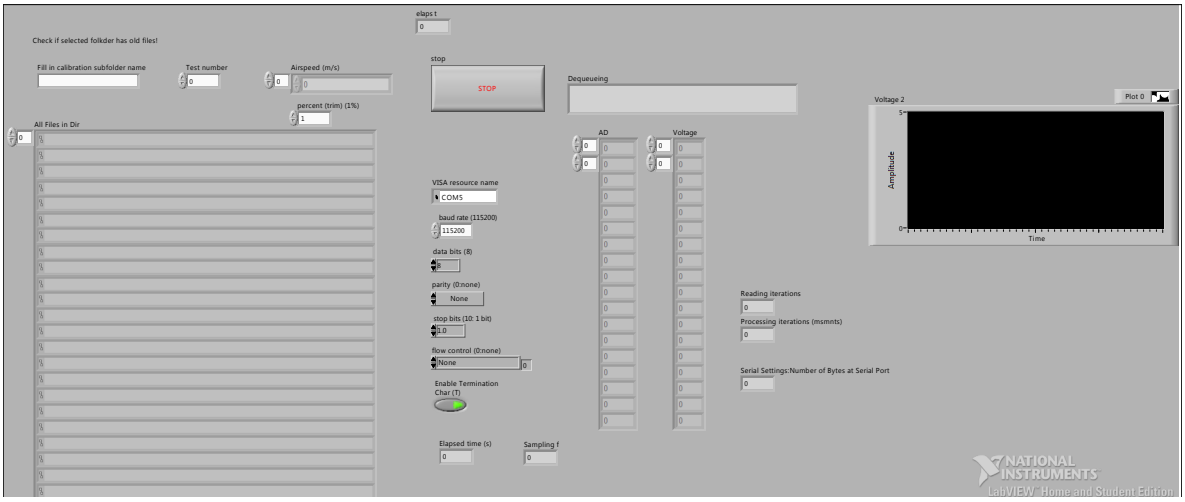

(a) **Data acquisition for calibration VI.**

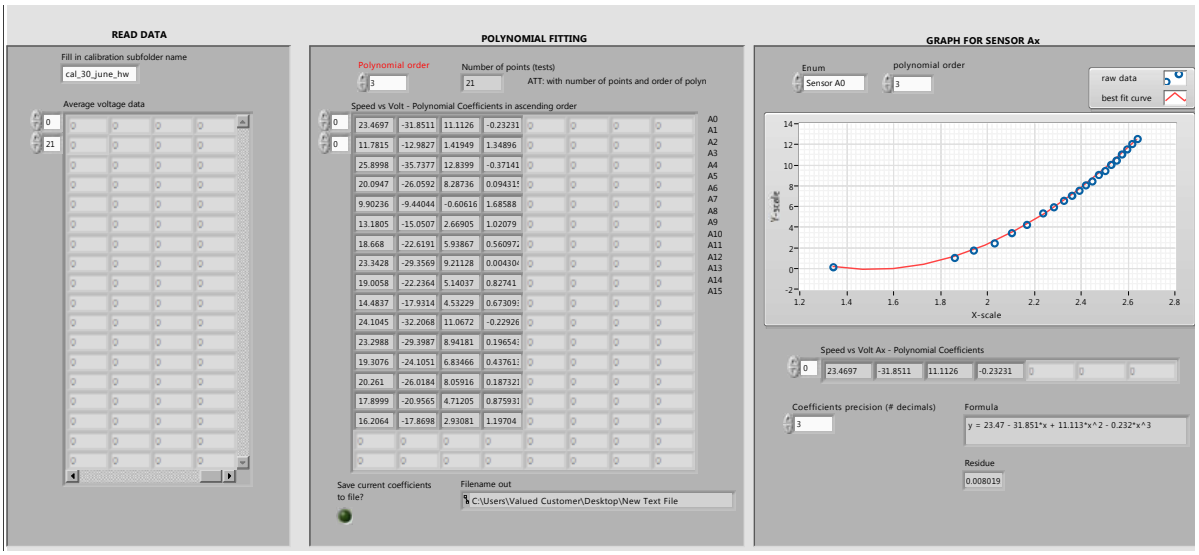

(b) **Calibration curves determination VI.** One curve is computed for each sensor. The curve fit tool developed enables the comparison of different fits; a 3rd order polynomial curve is considered a good choice.

Figure 3.17: **Screenshots of the developed VIs for calibration.** Top shows data acquisition procedure; bottom shows the determination of the fit curves.

Table 3.2: **Calibration coefficients for wind sensors.** General expression for calibration curve is shown on top, with airspeed U in m/s and output voltage V_{out} in V.

$$U = p_0 + p_1 V_{out} + p_2 {V_{out}}^2 + p_3 {V_{out}}^3$$

	p0	p1	p2	p3
Sensor A0	-11.473	31.565	-25.204	6.374
Sensor A1	-7.392	25.600	-22.581	6.048
Sensor A2	-0.940	17.110	-19.725	5.981
Sensor A3	5.895	4.628	-11.370	3.962
Sensor A4	-11.065	30.899	-24.582	6.146
Sensor A5	-21.381	47.121	-32.668	7.411
Sensor A6	-18.681	42.859	-30.404	6.995
Sensor A7	-9.881	29.316	-23.464	5.786
Sensor A8	-7.907	27.151	-23.273	6.009
Sensor A9	-0.408	12.862	-14.755	4.425
Sensor A10	4.723	6.552	-12.813	4.384
Sensor A11	-4.238	21.738	-20.824	5.677
Sensor A12	-10.361	30.049	-24.320	6.143
Sensor A13	-11.316	31.242	-24.683	6.136
Sensor A14	-20.157	46.552	-33.371	7.759
Sensor A15	-12.536	34.741	-27.480	6.797

3.5. Motion tracking system

For the dynamic gusts design on Chapter 8, a motion tracking equipment is introduced, which enables the design of gusts that adapt to a moving objective. The motion tracking setup used consists on four high-speed infrared cameras (Qualisys Oqus 7+) and one 4mm diameter retroreflective marker, fixed to the tip of a thin balsa wood rod (covered with black tape to avoid undesired reflections). Motion tracking cameras are largely used in biomechanical studies.

The equipment works as follows. The cameras emit light in the infrarred spectrum, and this is reflected back to the camera by the retroreflective marker. Through triangulation the coordinates of the marker's position are obtained, with respect to a reference frame set up during calibration. The data acquired is sent and made available in the Labview environment, facilitating interaction with other hardware. An important advantage of this equipment is its low latency, which enables real-time applications. Cameras are set to an update rate of 1000Hz, and the calibration results yield an accuracy below 1mm.

In the presented case the cameras are set around the test section, two on either side and two below it, all pointing upstream so that they covered a volume just ahead the active grid (pictures are included in Chapter 8, Figure 8.3). They are then calibrated following the manufacturer's instructions (Qualisys Motion Capture Systems, 2011), setting a retroreflective reference frame and covering the desired area with a retroreflective wand (see calibration equipment in Figure 3.18). Further details on the cameras setup are presented later in Chapter 8.

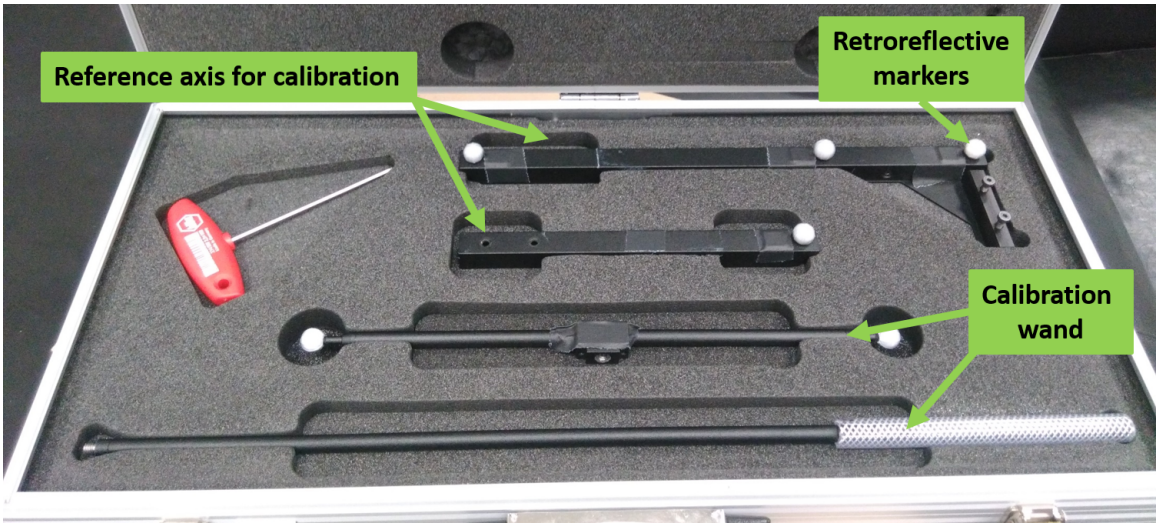

Figure 3.18: **Motion tracking system calibration equipment.** Two precisely manufactured pieces are assembled to make up the reference axis used for calibration. This reference is fixed at some desired position within the view of the cameras. Then, the calibration wand (also assembled by connecting the two pieces shown in the figure) is moved around the space covered by the cameras. The motion tracking software gathers the data and executes a calibration.

4

Open-loop response: steady-state analysis

The objective of this chapter is to address the steady-state open-loop response of the system, made up of the turbulence grid, the wind tunnel and the sensors array. Different angular positions are inputted to the vertical vanes in the grid and the flow response is observed after waiting a sufficient amount of time. This analysis is of interest for the later construction of a controller, as a first overview of the system's behaviour, providing insight into the governing physical phenomena. Moreover, the analysis enables the extraction of input-output relations in steady-state which can be benchmarked with results found in literature for similar systems. Two main aspects of the steady-state response are looked into: first, the effect of different vane positions on flow speed downstream; and second, the effect of different vane positions on the profile shape. Each one is addressed in the following sections.

4.1. Chapter overview

The steady-state analysis presented in this chapter is restricted to the generation of profiles based on one angular position input for all the vertical vanes (i.e., 1-region approach), while horizontal vanes are kept open at 0deg. As mentioned, two aspects are analyzed: the effect of different vane angular positions on flow speed downstream and on the profile shape. These two aspects provide insight into the physical phenomena related to the grid actuation. Each of them is briefly introduced below.

Regarding the **grid effect on flow speed**, it can be said that the primary steady-state effect of varying the vanes angles in the grid is the increase in total pressure drop across the grid section, and the subsequent decrease in speed in the test section. The total pressure drop across the grid section is usually assessed by the grid's blockage, or the ratio of streamwise-projected vanes area to total test section cross-sectional area. Conversely, the grid's transparency can be used, defined as the complementary to the blockage. As mentioned in Chapter 3, in this project the grid transparency parameter is used as a percentage and for our grid geometry the expression 3.1 is derived for it. Only in this chapter grid transparency is defined as a fraction over 1, as $\alpha = GT(\%)/100$, for a more convenient comparison with previous literature. Note that for all the cases in this chapter $\theta_h = 0$, and that for the grid setup shown in Figure 3.1, the total pressure drop is equivalent to a static pressure drop, since the flow is incompressible and the section area upstream and downstream the grid is constant.

Figure 4.1 shows the variation of grid transparency for a full 360deg change in vertical vane angles. Note that grid transparency is symmetrical with respect to 90deg and periodical every 180deg. For the sake of simplicity, in this project the vanes movement is limited to the range from 0 to 90deg. It can be seen in the figure that in that range of vane angles, grid transparency, which is a sinusoidal function, is close to a 3^{rd} order polynomial relation with vertical vanes angle.

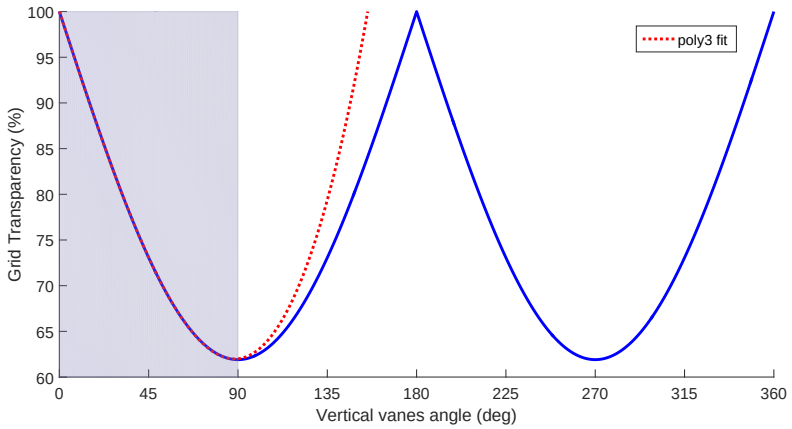

Figure 4.1: **Variation of grid transparency with vertical vanes angle.** Grid transparency variation is shown in blue, and the fit to a 3rd order polynomial in the shaded region is shown in dotted red. Note that only vertical vanes position is varied and horizontal vanes are kept at 0deg. This limits the minimum grid transparency achieved to 61.9%, at 90deg, leaving a large safety margin to prevent dangerous wind tunnel blockage. Goodness-of-fit parameters: summed square of residuals $SSE = 0.0997$, R-square $R^2 = 1.0000$, root mean square error $RMSE = 0.0338$.

As mentioned, grid transparency is often used to characterize grid effects. With an aim to derive a relation between steady-state flow speed downstream and grid transparency, two models for pressure loss are discussed. A first simple model for pressure losses, for incompressible flow across passive grids is the one used by **Corrsin and Gad-El-Hak (1974)**, who apply it to a uniform jet grid; it is also included in the review by Pinker and Herbert (1967) on pressure losses across square mesh wire gauzes. The model assumes that the grid behaves as an isentropic contraction up to the grid section, of area reduction factor α ($GT/100$), plus a sudden expansion downstream of it, of area expansion factor $1/\alpha$. This yields the following expression for the pressure loss coefficient across the grid λ:

$$\lambda = \frac{\Delta P_{\text{t,grid}}}{q_{us}} = \left(\frac{1}{\alpha} - 1\right)^2 \tag{4.1}$$

where $\Delta P_{\text{t,grid}}$ is the total pressure loss across the grid, q_{us} is dynamic pressure upstream the grid and α the grid transparency. Note that this pressure loss coefficient is dependent on grid geometry, Reynolds number and Mach number (Laws and Livesey, 1978). A second model, which presents a very good fit to experimental data for passive grids in incompressible flows, is the one analyzed and validated by **Roach (1987)**, on his work on generation of nearly isotropic turbulence. The model is also featured in the review work by Pinker and Herbert (1967) and in the work by Brundrett (1993). It provides the following total pressure loss coefficient across the grid:

$$\lambda = \frac{\Delta P_{\text{t,grid}}}{q_{us}} = A \cdot \left(\frac{1}{\alpha^2} - 1\right)^B \tag{4.2}$$

where A and B are empirical constants dependent on Reynolds number, Mach number and grid geometry. For the different passive grids geometries in incompressible flow analyzed by Roach (1987), constant A ranges from 0.52, for parallel rods and meshes of rods, to 0.94 for perforated plates, to 0.98, for parallel square bars and meshes of square bars. Roach (1987) notes that for mesh arrays of square bars, the dependency of constant A with Re based on mesh size is very low (this is also shown in the work on wire screens by Davis (1964), for Re beyond 200). Constant B on the other hand is close to 1 for most configurations analyzed by Roach (1987), except for perforated plates for which is higher, 1.28. Expression 4.2, with $A, B \simeq 1$, can be seen as an empirical correction to a model assuming the total pressure loss across the grid to be equal to the static pressure loss across an isentropic contraction of area reduction factor α.

Assuming that the pressure gradient driving the fluid downstream varies with grid transparency similarly as the pressure drop across the grid, it follows from the mechanical energy conservation in steady-state that the flow speed will vary approximately as the square-root of the pressure drop. Thus as a rough approximation,

the reduction in flow speed downstream the grid can be expected to vary with grid transparency as:

$$\Delta U_{ds,grid} \sim \left(\frac{1}{\alpha} - 1\right) \tag{4.3}$$

according to the pressure loss model used by Corrsin and Gad-El-Hak (1974); or according to Roach (1987) model with $A, B \simeq 1$ as:

$$\Delta U_{ds,grid} \sim \sqrt{\left(\frac{1}{\alpha^2} - 1\right)} \tag{4.4}$$

These two expressions will provide a qualitative benchmark for the obtained results. Note that these expressions, particularly the empirical correlation gathered by Roach (1987), successfully match pressure drop measurements across passive grids based on square-mesh geometries or parallel bars. Our grid however presents a more complicated geometry, with three-dimensional elements protruding from the grid plane, and thus it may deviate from the fits suggested.

A second effect that is anticipated when varying grid transparency with the active grid is the flow deviation introduced, due to fixing the vanes at a certain angle. This affects the obtained **profile shape**, since completely uniform profiles cannot be generated for a common vane angular position. In this section this is also assessed. It will be shown that the flow deviation observed justifies the use of a closed-loop controller divided in regions for the later wind profiles design. Note that the spanwise spread of the sensor array across the test section enables us to gather spatial information, as well as temporal data.

In the next section the procedure to obtain data used to assess the effect of the grid on flow speed and on the profile shape is described. Then, results for both effects are presented. The chapter closes with the *Conclusions* section, in which the main takeaways are summarized.

4.2. Experimental procedure

For the experiments in this chapter all the eight vertical vanes receive the same input to their angular position, while the horizontal vanes are held at the open position (0deg). Data is gathered at each of the 16 wind sensors in the array, at a frequency of 40Hz. The sensor array is located 90cm downstream the grid and wind tunnel setpoint temperature and speed are set to 5m/s and 20ºC respectively. Two sets of data are used: in the first one vanes angular position is varied in steps of 5deg, from 0deg to 90deg, holding each state for around 60s; in the second one, the same procedure is repeated varying vanes angular position in larger steps (10deg).

4.3. Results

In the following subsections the obtained results are presented. To assess the effect on flow speed downstream the grid, a collective value across the sensor array is computed. To address the effect on profile shape, individual sensor measurements are used.

4.3.1. Grid effect on flow speed

Variation of flow speed downstream the grid is assessed by the median flow speed value registered at the wind sensors, as shown in equation 4.5. Using the median value of the sensors' measurements is an effective way to gain insight into the steady-state response while removing outliers; therefore the median value will be used extensively throughout the project. It should be reminded that the wind sensors in the array are low-cost sensors based on thermistors, which were purposely selected to prove their applicability in gusts design and control, so outliers were expected. Flow speed downstream is therefore evaluated with the parameter:

$$\hat{U}_{med} = \frac{U_{med}}{U_{med,0deg}} = \frac{\text{median}(U,\ 16\ \text{sensors})}{\text{median}[\text{median}(U,\ 16\ \text{sensors}),\ 200\ \text{measurements at}\ \theta = 0deg]} \tag{4.5}$$

where U_{med} is the median speed across the sixteen sensors at each instant, and $U_{med,0deg}$ the median across

200 measurements of U_{med} values registered at fully open grid, at the beginning of the data acquisition.

Figure 4.2 shows in black dots the value of $\hat{U}_{med}$ at each instant, while keeping each angular position for 60s. Taking the median values at each angular position, the red dots are determined. It can be seen that these points, representing the steady-state response $\hat{U}_{med}$, are close to a 3rd degree polynomial fit with vanes angle P. It has been shown that grid transparency also varies close to a 3rd order polynomial with vertical vanes angles, from 0 to 90deg (see Figure 4.1). Thus, we expect $U_{med,0deg}$ to vary close to linearly with grid transparency, $U_{med}/U_{med,0deg} \sim \alpha$. Figure 4.3 shows that indeed there is a good fit to a linear relation (green dashed line). This linear fit is compared to the previously mentioned relations between both parameters (see equation 4.3 and equation 4.4), derived for passive grids. It can be seen that both fits are close to the results obtained, with the model derived from Corrsin (equation 4.3) providing a better approach overall, as indicate the goodness-of-fit parameters shown in Table 4.1

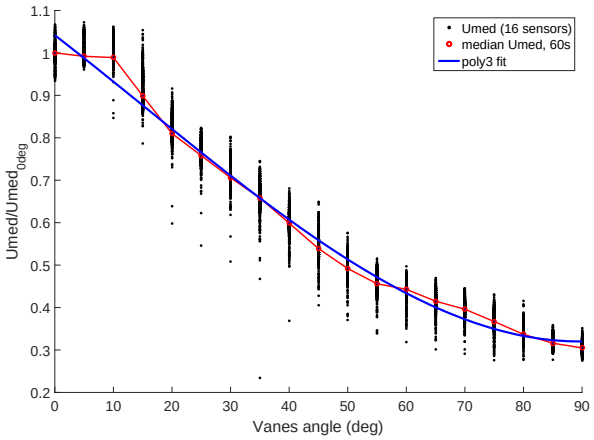

Figure 4.2: **Effect of different vane angles on flow speed downstream the grid.** In the plot, each black dot represents the $\hat{U}_{med}$ value registered for each profile during the 60s at the corresponding vane angle P. Red markers indicate the median $\hat{U}_{med}$ value for each vane angle. The blue line represents the 3rd degree polynomial fit to those median values. Further details of this fit can be found in Appendix B.

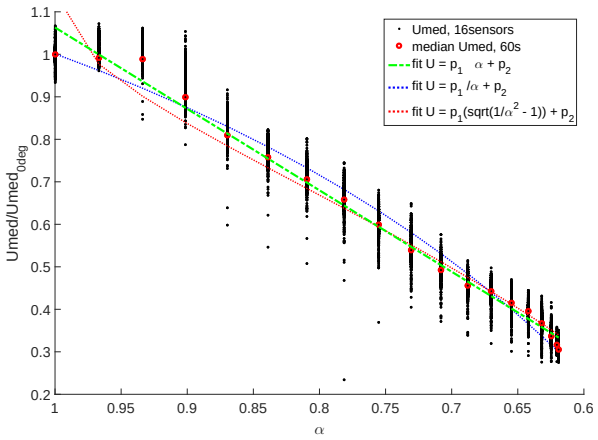

Figure 4.3: **Effect of varying grid transparency on flow speed downstream the grid.** Each black dot represents $\hat{U}_{med}$ value registered for each profile, during the 60s at the corresponding vane angle P. Red markers indicate the median $\hat{U}_{med}$ value for each vane angle P. The blue and red dotted line represent estimations from passive grid pressure loss models. The green dashed-dotted line represents a linear relation between the median of $\hat{U}_{med}$ values at each angle and α.

4.3.2. Grid effect on profile shape

Next, the effect of varying vanes angles on the shape of the uniform profiles is evaluated. In Figure 4.4 the effect of the vanes sense of rotation can be seen. Since the vanes rotate clockwise for increasing angles (seen from the top), flow is deviated to the left side of the test section, when increasing vane angle P. As a result there is an asymmetry in the registered wind profiles, with sensors closer to the left providing higher flow speed measurements than those to the right. In Figure 4.5 the distortion of the profile is evaluated with the spatial standard deviation $\sigma_{spatial}$. It can be seen that the median values (red dots) for the spatial standard deviations range from 0.04 to around 0.1 (expressed in the same units as the data, that is, fractions of $U_{med,0deg}$), and that values peak for a vane angle around 75deg. This can also be appreciated by inspecting the profiles shapes in Figure 4.4, in which we can see the largest deviation occuring around 70-80deg.

4.4. Conclusions

Some relevant conclusions are derived from the analysis presented on the steady-state response of the system.

First, the **effect of the vanes angular position on flow speed downstream** has been addressed. Steady-state flow speed downstream shows a third-order polynomial relation with vanes angular position, and a close to linear one with grid transparency. Comparing the linear relation obtained between flow speed and grid

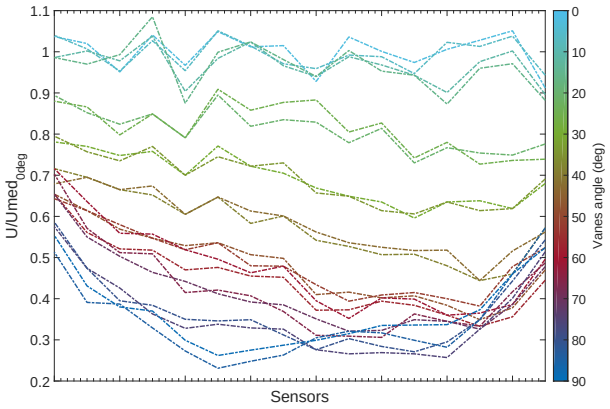

Figure 4.4: **Shape variation of uniform profiles at different vanes angles.** Profiles are made up of 16 measuring points, each one corresponding to one sensor. Each measurement is non-dimensionalized with $U_{med,0deg}$ the median value across all 16 sensors when the grid is fully open. Two profiles are shown for each vane position P, at instants corresponding to 25% and 50% of the step duration. Since the vanes angle sequence was inputted in time, color gradient corresponds to vanes position (varied in steps of 10deg) as well as time, so darker colors correspond to later instants in time.

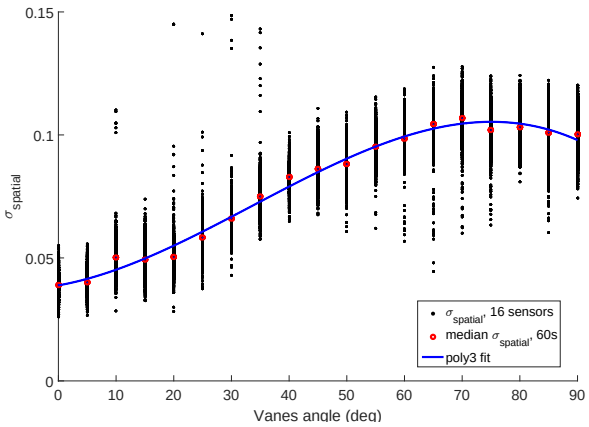

Figure 4.5: **Spatial standard deviation $\sigma_{spatial}$ for profiles at vane angles from 0deg to 90deg, in steps of 5deg.** Each black dot represents the $\sigma_{spatial}$ value for each profile registered during the 60s at the corresponding vane angle P. Red markers indicate the median of the $\sigma_{spatial}$ values obtained for the same vane position P. The blue line represents the 3rd degree polynomial fit to those median values.

Table 4.1: **Fit parameters for $\hat{U}$ vs grid transparency α**

	Linear $U = p_2 + p_1\alpha$	Corrsin and Gad-El-Hak derived $U = p_2 + p_1/\alpha$	Roach derived $U = p_2 + p_1\sqrt{(1/(\alpha)^2 - 1)}$
p_2	−0.8526	2.141	1.144
p_1	1.916	−1.140	−0.6343
Goodness-of-fit parameters			
SSE	0.01	0.0162	0.0376
R^2	0.9906	0.9848	0.9647
R_{adj}	0.99	0.9839	0.9626
RMSE	0.0243	0.0309	0.047

transparency, to estimated relations derived from static pressure drop models found in literature, it can be seen that trends are fairly close in the range of grid transparencies in which we operate (from $\alpha = 1$ up to a minimum of $\alpha \sim 0.6$). Differences may be due to the active grid presenting larger pressure drops than a passive grid with the same grid transparency at a certain range of vane positions, and lower at others, due to its quite different geometry and three-dimensional elements. However this results can only give qualitative assessments, and should be confirmed with a more detailed characterization of the pressure losses, with pressure measurements upstream and downstream the grid.

The fact that the system's response is close to linear with grid transparency variation makes grid transparency, in principle, a good candidate for manipulated variable in the next closed-loop controller design (see Chapter 6). However, this linear relation of flow speed with grid transparency holds for the steady-state response, which as it will be commented later can take $\sim 4s$ to settle in deceleration, and $\sim 16s$ in acceleration. For the dynamic gust design however, it would be required that the controller reference is updated at a higher rate. In this case choosing grid transparency as manipulated variable wouldn't provide a significant advantage. This point will be further discussed in Chapter 6.

The **effect of vanes angular position on profiles** downstream has also been assessed; this is the main justification for using a closed-loop approach for the wind profiles design. A possible solution to fix the asymmetry in the uniform profiles downstream may be to allow the vanes to rotate in both directions. A controller similar to the one developed in this project could be designed, which would allow vanes to rotate in either direction and would move them accordingly to obtain uniformity downstream. As a previous step, the 4-region and 8-region controllers designed in this project account for the flow deviation from neighbouring vanes, and enable uniform profiles downstream with little deviation (see Chapter 7 and Chapter 8). Note however that these vane motions introduce turbulence and recirculation in the flow, and thus may delay flow convergence to steady-state (see delays discussion on section 5.5, and discussion on non-uniform static gusts in subsection 7.3.2 and 7.3.3).

5

Open-loop response: transient analysis

The objective of this chapter is to analyze the transient response of the system made up of the turbulence grid, the wind tunnel and the sensors array, when reducing or increasing grid transparency. In this way, further insight is gained on the physical processes taking place when varying grid transparency.

To analyze this transient in the system's response, grid transparency is varied uniformly across the grid section (i.e., one region is assumed). A series of experiments are carried out, based on input steps to the vanes angular position of different amplitude and duration; the flow response is observed shortly after the input. The goal is, first, to gain further insight in the physical process of flow acceleration and deceleration during the instants just after varying the blockage; and second, to identify the sources of delay. A particular focus is made on identifying potential sensor-related delays; this is addressed by comparing the response of the wind sensor array with a hotwire anemometer.

5.1. Chapter overview

The chapter is structured as follows. First, a preliminary assessment of the sources of delays identified in the system is presented and an order of magnitude for each is given. Next, the experimental procedure for the three sets of data considered is described, and the objective of each of them is stated. In the following section, the results for these three sets of data are presented and discussed. At the end of each results subsection a brief conclusion summarizes the main observations. Finally, the main conclusions derived from the transient analysis and relevant for the controller design are collected.

5.2. Sources of delay

In this report it is considered a *source of delays* any contribution to the timespan between the instant the step input is given and the settlement of steady-state in the flow. On a preliminary analysis of the response, a *deadtime* (or deadband) has also been identified, that is, a timespan after the input in which the output does not change and keeps the same value as before the input. The concept of deadtime is further explained later in this chapter and its consequences for the controller design are discussed in Chapter 6; for now the focus is placed on the possible physical causes for this deadtime. The following sources of delay and deadtimes are identified in our system. Rough estimates for each delay are given to develop an intuition on their importance.

- ***propagation of the new pressure gradient in the wind tunnel***. In the transient regime, the sudden change in momentum introduced by a grid transparency variation generates pressure waves at the grid section that travel along the wind tunnel circuit and update the flow state to a new pressure gradient. For incompressible flows, these waves are sometimes called waterhammer waves (Manglik, 1997) due

to their link with the waterhammer effect. The time for a single pressure wave to travel across the wind tunnel length is estimated to be in the order of 0.1s (0.2s for an approximate tunnel length of 40m and speed of sound 340m/s).

- ***flow inertia in acceleration and deceleration***. The opposition of the flow to change its initial state of motion delays the settlement of a new steady-state condition. During the opening and closing of the grid, the fan speed in the wind tunnel is kept constant and so the variations in flow momentum (or equivalently, kinetic energy) are mainly driven by pressure differences, manipulated through changes in pressure drop due to grid transparency. The two opposing effects of the flow inertia and the flow speed change introduced by pressure waves are the main mechanisms driving the transient response. From a preliminary analysis the delay introduced due to this mechanism is estimated to be in the order of 1-10s. The flow inertia can be identified with the convective term in the momentum equation as explained in Chapter 6.

- ***sensor related delays***. Apart from the work by Prohasky and Watkins (2014), there is very little work on the performance of the Modern Device rev. P wind sensors. Reviewing the manufacturer's website (Badger, 2014a) comments were found (from both manufacturer and users) on the performance of this sensor and similar versions of it, and some characteristics were identified that may affect the measurements of the transient flow response. Some of these aspects frequently highlighted are that similar sensors tend to "latch on" low resistance (high speed) values, that they present higher thermal inertia compared to more accurate hotwires, or that they may present a higher lower-bound for flow speed sensitivity. All of these would increase the deadtime registered by the wind sensors, and affect the delay in reaching steady-state. From the frequency analysis carried out by (Prohasky and Watkins, 2014) on the wind sensors, delays in the order of 0.1s are considered.

- ***computational and communication delays***. As noted by Ogata (2002), computational and communication delays will also influence the system's response. Computational delays include the efficiency of the different codes' architectures (in our case, Labview and Arduino codes) or the memory usage. Communication delays include transmission of data between Arduino and XBee modules, between XBee modules wirelessly to the Labview PC, and between PC with Labview and the grid motors. They also include data saving and conversion (such as from analog to digital). Note that assessing each of these delay sources would require precise appropriate measurements, and it is challenging to estimate and verify an order of magnitude. In any case these delays are expected to affect similarly in all open-loop experiments conducted in this section, and therefore they will not be the focus of the analysis, being the comparison acceptable.

The first two delay sources mentioned relate closely to the physical phenomena that takes place when accelerating and decelerating the flow, whereas the last two are more related to the experimental setup. Although a precise characterization of each of these delay sources would require a more extensive study, the objective at this point is to estimate their influence and consequences and provide supporting theory. It should be reminded that when inputting a certain angular position to the vanes, these turn to the desired angle at maximum speed (12000rpm); the time scale for grid transparency change is therefore 5ms (see Chapter 3).

5.3. Experimental procedure

In order to gain further insight into the physical phenomena taking place during the transient response, and the sensor related effects, three experiments are considered. The procedure for each of them is specified below. In all of the cases horizontal vanes are kept open at 0deg. Sampling frequency for the wind sensors is 40Hz, while the hotwire probe samples at 10kHz. Wind tunnel temperature is kept at 20ºC in closed-loop control (see Chapter 3 for further details). Note that out of practicality the hotwire tip is located 6cm ahead of the hot elements of the wind sensors in the array, in the streamwise direction (see Figure 3.13 in Chapter 3).

1. **Wind sensors + hotwire, 5s 90deg step.** In this experiment a 90deg step (maximum blockage considered) for the vertical vanes angle is inputted and kept for 5.65s. Data is registered at all of the wind sensors in the sensor array and at the hotwire probe. The latter is located next to sensor 9 as shown in Figure 3.13 Chapter 3). The objective is to assess possible differences between the wind

sensor measurements and the hotwire's. Particularly, the aim is to identify whether the deadtime detected in the wind sensors response is a consequence of the sensors' higher thermal inertia (or other sensor-related particularities), or if it is indeed reflecting a physical phenomenon. The initial acceleration that occurs in the first phase of the response is also looked into, and measurements from both type of sensors are compared.

2. **Wind sensors array, 3 steps**. Three step responses to a 90deg input to the vertical vanes angle, of increasing duration (30.025s, 57.55s and 76.5s) are compared. Flow speed measurements at the sensors in the array are registered and their median flow speed value is used to analyze the transient response. One aspect of interest is whether the deadtime is affected by longer steps (because of the sensors potentially "latching" to low resistance values, or other particularities); another is the decelerations and accelerations registered. These are compared to the values registered by the hotwire on the previous set of experiments.

3. **Wind sensors array, sequence of steps**. The response to two sequences of steps in the vertical vanes angle is looked into. Each sequence alternates 20s duration states of fully-open with closed-grid ones of decreasing vertical vanes angle, in intervals of 10deg. The first sequence starts off with a step to 90deg and alternates with open grid states, until a 50deg step. The second sequence starts off with a step to 50deg and executes the same procedure until a step of 10deg. The objective is to assess the effect of steps of different amplitude, on the deceleration and acceleration process. Additionally, the effect on the deadtime is also analyzed, verifying whether there is an influence of the previous flow state or of the step amplitude. The effect of the initial state on the deceleration and acceleration slope is also commented.

The results for these three sets of experiments are presented and discussed in the next section.

5.4. Results

In this section the results for the three experiments considered are presented in separate subsections. Within each experiment, the main aspects discussed are introduced with subtitles in bold, for clarity.

5.4.1. Wind sensors + hotwire, 5s step

Flow speed measurements are assessed for each individual sensor and for the array as a whole, taking the median value across the sixteen sensors. Individual sensor measurements are first addressed, and deadtime values are estimated for each of them. Then the median response across the span is compared to the hotwire response and some conclusions for the comparison between sensors are drawn.

Individual sensors' measurements

Figure 5.1 shows the responses for all of the sensors in the wind sensor array, as well as for the hotwire probe, when inputting a 5s, 90deg step to the vertical vanes angular position. Speed data for each sensor $\hat{U}$ is non-dimensionalized with the median flow speed value over 200 measurements registered by the same sensor before data acquisition, when the grid is fully open ($\hat{U} = U/U_{0deg}$). Subfigure on the left on Figure 5.1 shows raw non-dimensional data for each sensor and for the hotwire probe, whereas postprocessed data is shown on the right. Wind sensor data is postprocessed with a moving average over a span of 0.2s to smoothen fluctuations. Hotwire data is filtered to obtain DC component, and so a low-pass rectangular filter with very low cutoff frequency (0.08Hz) is applied.

A first analysis in the sensors' response in Figure 5.1 shows that the deadband effect already seen for the wind sensors is also registered by the hotwire probe. Figure 5.1 also reveals a good match between the progression of the response registered by the hotwire and the wind sensors close to it spanwise (sensors 7, 8, 9). However there are differences across the spanwise direction. It can be seen that some sensors peak at deceleration whereas others peak at acceleration. This may be due to the vanes sense of rotation, clockwise when increasing angle and anticlockwise when decreasing. This effect may advect vortices downstream or deviate the flow towards sensors 8 to 16 when decelerating, and towards sensors 1-6 when accelerating. It can be seen in Figure 5.1 that these are the sensors that peak in the response just after the change in vanes angle. This asymmetry spanwise can be more clearly appreciated in Figure 5.2. Additionally Figure 5.3 shows

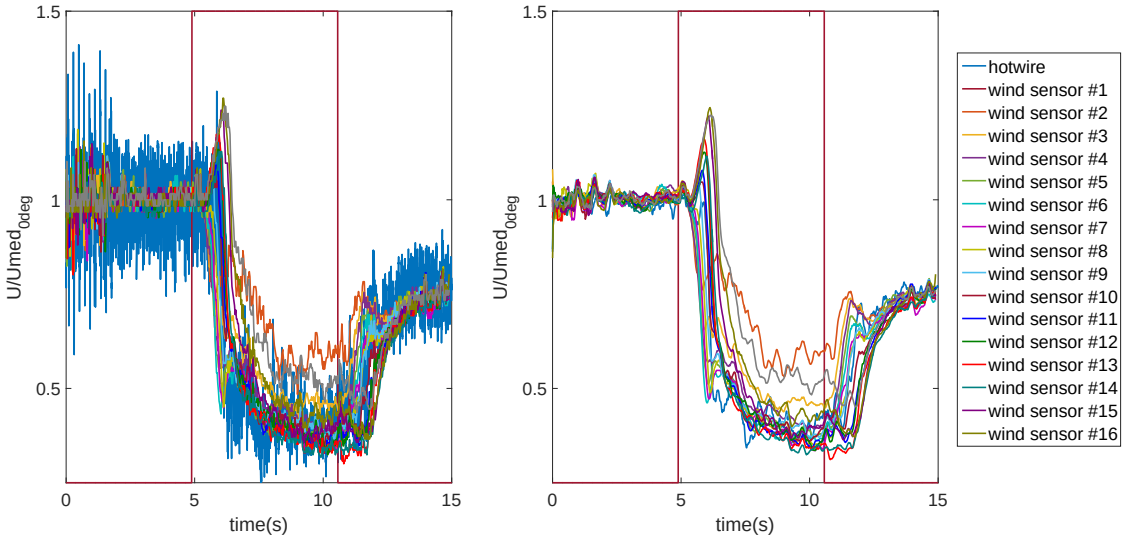

Figure 5.1: **Step response of each of the wind sensors in the array and of the hotwire probe**. Each sensor is assigned a color. Left plot shows raw data $\hat{U}$, non-dimensionalized with the corresponding median 0deg value for each sensor U_{0deg}. Right plot shows postprocessed data: wind sensor data is smoothed with a moving average over 0.2s, hotwire is low-pass filtered (cutoff frequency 0.08Hz) to obtain its DC component.

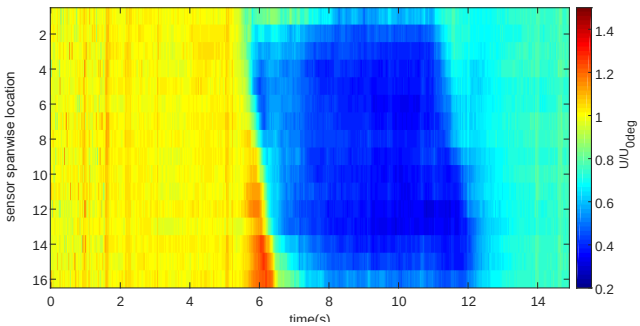

Figure 5.2: **Colormap of raw wind sensors measurements in time, when inputting a 5s step to the vertical vane angles, from 0deg to 90deg**. The y-axis of the plot shows the spanwise position of the sensors, from 1 to 16, and the x-axis shows evolution in time. The colorbar represents the value of the flow speed parameter $\hat{U} = U/U_{0deg}$.

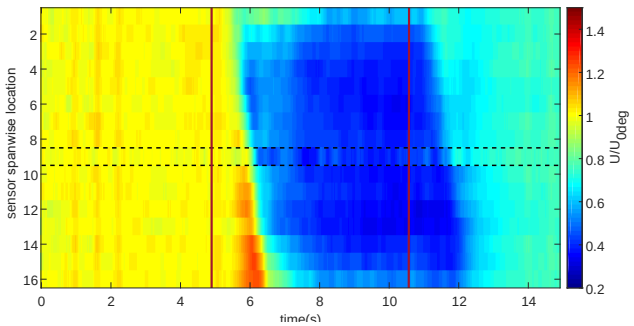

Figure 5.3: **Colormap of postprocessed wind sensors and hotwire measurements in time, when inputting a 5s step to the vertical vane angles, from 0deg to 90deg.** The vertical solid red lines indicate the input of the step from 0deg to 90deg, and from 90deg to 0deg. The dashed lines delimit the superimposed hotwire data. Results shown are postprocessed data: wind sensor data is smoothed with a moving average over 0.2s, hotwire is low-pass filtered (cutoff frequency 0.08Hz) to obtain its DC component.

the hotwire data superimposed in the wind sensors' colormap, showing a good match between the measurements.

Deadband parameters definition

Decelerating and accelerating responses are plotted separately and zoomed in for comparison in Figures 5.4 and 5.5. To characterize the evolution of the transient response, with a particular interest on characterizing the deadband time, two parameters are defined:

- **$DB_{5\%}$**, refers to the time it takes for the response to reach plus or minus 5% of its deadband value. This deadband value is defined for the deceleration step as the mean response value over the 0.5s after the inputted step, and for the acceleration step as the mean value over 0.7s. For the acceleration step only in this section, a variation of this parameter ($DB_{10\%}$, based on 10%) is used, since the response is found quite noisy when accelerating. Wherever used it is stated explicitly in the results. The increase in window and percentage for acceleration is thus done to obtain a more realistic estimation. The instant this condition occurs is indicated with a cross marker in the response graphs of Figures 5.4 and 5.5. The objective is to define a uniform parameter to compare across accelerating and decelerating cases.

- **$DB_{max,diff}$** refers to the time span from the instant the step is inputted until the point of maximum slope within a certain time window. This time window is set from visual inspection to cover the instant in which the response inflexes. The aim is to avoid detecting other fluctuations in the response. For the acceleration step, the window is set from 0.25 - 1.5s from the instant the step input is given, whereas for the deceleration response is set from 0.35s - 1s . This instant is indicated with a star marker in Figures 5.4 and 5.5. The objective is to define a parameter closer to the instant visually identified as the system starting to respond, keeping at the same time a common definition to compare across responses.

The fluctuations in the data make an accurate and standardized determination of the deadband quite challenging. However the aim is not a precise determination of the deadtime value, but a first estimate that enables comparison and discussion of potential causes and implications.

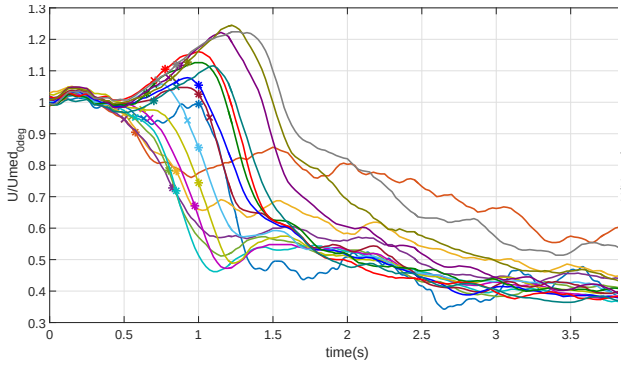

Figure 5.4: **Deceleration responses for hotwire and 16 wind sensors**. Evolution of the response for hotwire and wind sensors after the input of the step (at t= 0) from 0 to 90deg. The time instant for the $DB_{\text{max,diff}}$ is indicated with a star marker; the instant for $DB_{5\%}$ with a cross marker. Note the peak in response for sensors in the region of sensors 10-16, due to the vanes sense of rotation.

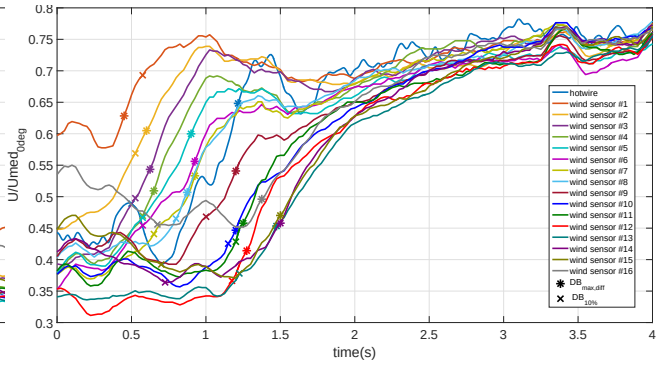

Figure 5.5: **Acceleration responses for hotwire and 16 wind sensors**. Evolution of the response for hotwire and wind sensors after the input of the step (at t= 0) from 90 to 0deg. The time instant for the $DB_{\text{max,diff}}$ is indicated with a star marker; the instant for $DB_{5\%}$ with a cross marker. Note the peak in response for sensors in the region of sensors 1-8, due to the vanes sense of rotation.

From the results shown in Figure 5.4 and 5.5, it can be seen that the $DB_{\text{max,diff}}$ parameter overestimates in most cases the value visually identified as the deadband; estimations from both parameters are compared in Figure 5.6. As for the $DB_{5\%}$, lower percentages were considered to define this parameter but the noisy responses made the comparison not very reliable. A 5% margin with the deadband sets a similar point in the progression of the response for all cases and thus it is used for comparison across the sensors. To visualize the deadband effect more clearly, the deadband timespan estimate given by $DB_{5\%}$ is superimposed on the wind sensors and hotwire colormap previously obtained, as shown on Figure 5.7. In this figure it can be seen that for the deceleration step the chosen parameter characterizes well the deadband timeframe. Also the hotwire deadband estimates are close to those obtained for adjacent sensors. For the acceleration step a

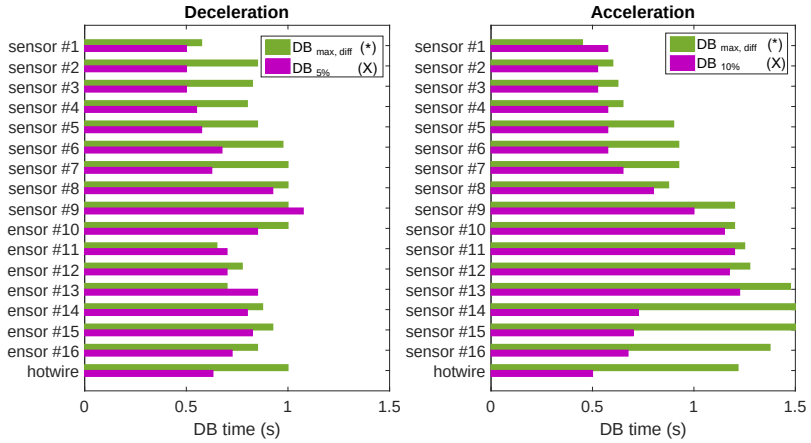

Figure 5.6: **Deadtime estimates for the 16 sensors and the hotwire probe, for a 5s 90deg step in vertical vanes angle.** Green bars represent values for $DB_{\text{max,diff}}$ parameter (corresponding to the star marker in the time responses); magenta bars represent values for $DB_{5\%}$ parameter (corresponding to the cross marker in the time responses). Note that although the hotwire estimates are shown at the bottom, its spanwise location was between sensor 8 and 9.

less close match can be seen, especially in the region of sensors 14-16. This may be again a consequence of the vanes sense of rotation, which increases flow speed in the region where sensors 1 - 8 are and delays convergence in the region around sensor 14. This region may also be affected by higher fluctuations in the flow, yielding a lower $DB_{5\%}$ value.

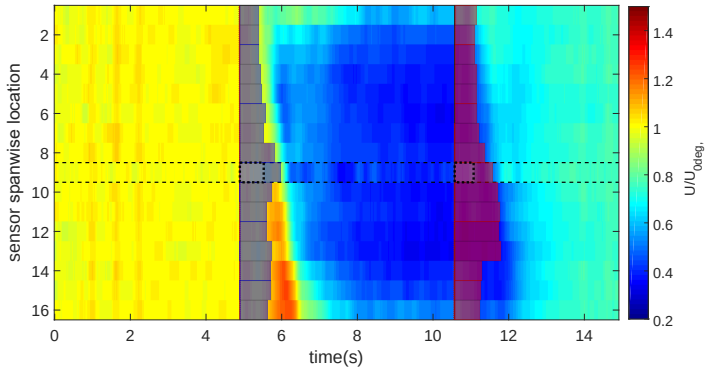

Figure 5.7: **Colormap of postprocessed wind sensors' and hotwire's readings in time, when inputting a 5s step in vane angles, from 0deg to 90deg, with deadband times overlaid.** Deadband estimations given by the parameter $DB_{5\%}$ are superimposed to the colormap with postprocessed wind sensors and hotwire results. Note that deadband estimations match well the color evolution in deceleration (indicated by solid red line to the left). For the acceleration step, the value given by the parameter $DB_{5\%}$ seems to not reflect well the behaviour of the flow, especially in the region around sensors 8-16. This is probably due to the higher turbulence in that area and the recirculation, which both delay the convergence to steady-state and generate peaks in the response (leading to underestimations of $DB_{5\%}$)

Median measurements across the array

It is now assessed how well the wind sensor array estimates the deceleration and acceleration in the flow. This is done by comparing the median value across the wind sensor array with the hotwire measurements. Figures 5.8 and 5.9 show the evolution of both responses. From visual inspection responses can be seen fairly similar, identifying in both of them some characteristic regions. For the deceleration step in Figure 5.8 one main deceleration region is observed (just after the deadband and until reaching steady-state), whereas two regions of acceleration can be seen in Figure 5.9, the first one with a higher slope. These last two regions appear more clearly in the experiments shown in the next section, in which a larger sampling time is considered. For now the aim is to verify whether the wind sensors provide a good estimate for these acceleration and deceleration rates.

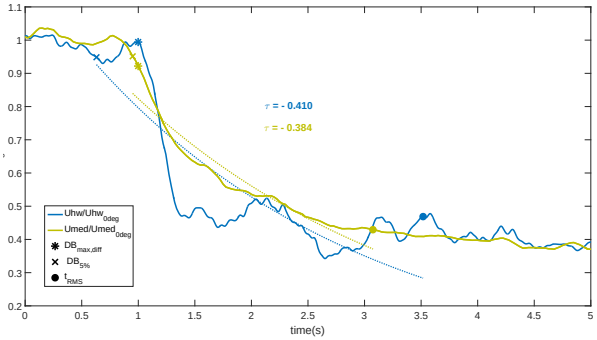

Figure 5.8: **Step decelerating response for hotwire probe and median response across the wind sensors' array**. Dotted lines show exponential fits $\hat{U} = a \cdot e^{\tau t}$, of which τ values are indicated in the plot. Subindex indicates whether the slope refers to the first or second region of acceleration.

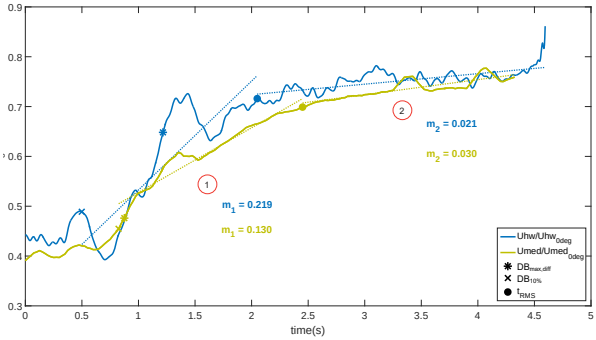

Figure 5.9: **Step accelerating response for hotwire probe and median response across the wind sensors' array**. Dotted lines show linear fits $\hat{U} = mt + n$, of which m values are indicated in the plot. Subindex indicates whether the slope refers to the first or second region of acceleration.

The aforementioned deadband parameters are computed as well for the median flow response across the array. In order to separate the identified decelerating and accelerating regions a new parameter is defined that will be used throughout the rest of the project. This is the $\mathbf{t_{RMS}}$ parameter, defined as the time instant in which the flow profile determined by the sixteen wind sensors has a root-mean-square error with the steady-state profile lower than 0.05. The steady-state profile is defined as the average profile over the last 1/6 samples. These definitios are later used for the gust designs (see **??**); the profiles used for its computation, for the case in this section are shown in Appendix C.

Having defined the t_{RMS} parameter, the slopes at the deceleration and acceleration region can now be characterized. For the deceleration phase the response is fitted to an exponential curve $a \cdot e^{\tau t}$, from the instant given by the $DB_{5\%}$ parameter until $t = t_{\text{RMS}}$ ($-\tau$ then represents the inverse of the time constant). It can be seen that although the wind sensors median response is influenced by spanwise variations there is a good match between the values of the exponential constant τ for hotwire and wind sensor array, with $\tau \sim 0.4 s^{-1}$ (time constant $\sim$ 2.5s) .

For the acceleration case, the two differentiated regions mentioned are characterized as follows: the first is considered as extending from the end of the deadtime (defined by the $DB_{10\%}$ parameter) until $t = t_{\text{RMS}}$, and the second one from $t = t_{\text{RMS}}$ until the end of the sampling time. In this case each of the regions is fitted to a linear relation and their slopes m are compared. It can be seen that for the first region, the wind sensors underestimate the acceleration by 40% (with $m_1 = 0.13 s^{-1}$), compared to the hotwire value ($m_1 = 0.219 s^{-1}$), whereas in the second region they overestimate it in a similar amount. This is thought to be because of taking the median across the span for the wind sensor case and because of the higher sensitivity to fluctuations of the hotwire probe; both factors affect the response and the location of the parameters that define the regions, $DB_{5\%}$ and t_{RMS}. In any case it is verified that the estimates are in the same order of magnitude and thus the wind sensors can be used to evaluate acceleration and deceleration rates and compare responses. An interesting aspect to highlight is the one order of magnitude difference between the two regions of the accelerating flow response. This will be further looked into in the next section, where the second region is analyzed with a larger sample.

Conclusions to comparison hotwire and wind sensors data

From this comparison between step response of wind sensors and hotwire the following points are concluded:

- The deadtime identified in the wind sensors' response also appears in the hotwire measurements. This suggests that this deadtime is not dominated by the wind sensors's higher thermal inertia or other sensor particularities as it was initially thought, and that it may actually indicate a physical phenomena related to the flow in the test section. It seems that is the case since for an identical step and initial flow conditions, the deadtime duration varies across sensors. It is suggested this is due to

flow deviation and turbulence affecting the flow non-uniformly across the span. Deadtimes in acceleration is also identified as being slightly larger, but in all cases large spread in the deadtime estimations can be seen, which suggests that other delay sources may also be affecting. Due to the system's configuration it is challenging to separate the influence of the delay sources, however from this results it can be concluded that wind sensor's characteristics are not the dominant reason behind it.

- Comparing the step response for the hotwire and for the wind sensors located nearby it can be seen that the evolution of the response, including the varying slopes and the deadtime values, are very similar. This indicates that the wind sensors' measurements can be used to characterize the system's transient response.

- Regarding the slopes in the response, two differentiatly sloped regions are identified in the accelerating step, and one in the decelerating case. The median flow speed value across the sensor array seems to provide a good estimate for the deceleration rate, being close to the one obtained with the hotwire. For the acceleration phase more differentiated values can be seen, which may be consequence of the spanwise asymmetry. However it seems that the median flow response of the wind sensors provides a reasonable estimate for the acceleration slope.

- Although the hotwire was located in a streamwise location 6cm ahead of the wind sensors' array, as shown in Figure 3.13, no significant differences are observed in the flow speed measurements with respect to adjacent wind sensors. It can be therefore concluded that any advection effects are overrun by the acceleration/deceleration due to pressure gradients.

Additionally, a first analysis on the acceleration and deceleration regions has been presented, which is looked further into in the next section. It should be mentioned that the strong asymmetry found spanwise in the flow measurements for this experiment is not seen as strongly in the results for similar tests. This may be due to the grid responding at a slightly slower pace for the particular experiment presented here, which may have enhanced the spanwise asymmetry observed. This was noted during the experiment. However since all measurements were taken in the same conditions the analysis is considered relevant, particularly for comparison with hotwire data. Other trials for the same step amplitude confirm there is an asymmetry in the response, especially in accelerating steps, but of less extent: this can be seen in Figure 5.10 and 5.11 (data shown is part of the set *Step 60s* analyzed in the next section).

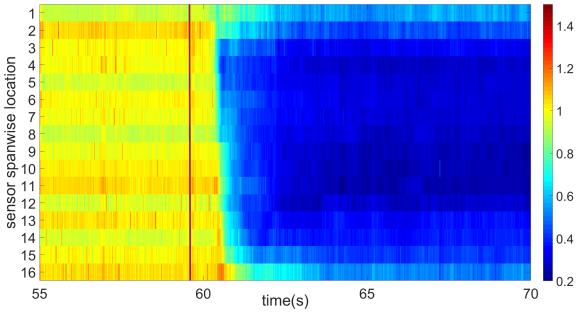

Figure 5.10: **Zoom in to decelerating step**, for wind sensor array measurements gathered during the *Step 60s* experiment.

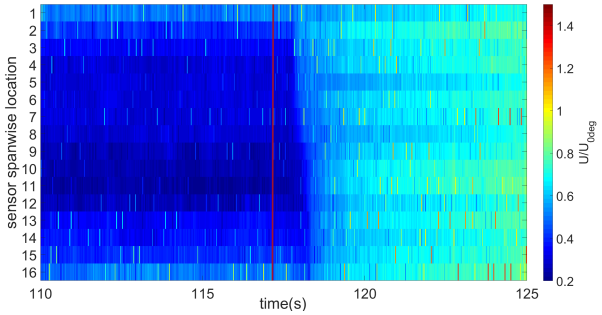

Figure 5.11: **Zoom in to accelerating step**, for wind sensor array measurements gathered during the *Step 60s* experiment.

5.4.2. Wind sensors, 3 steps

In this section the effect of inputting a 90deg step of increasing duration in the wind sensors' response is looked into. Figure 5.12 shows the median flow speed response, across the wind sensors array, for the three steps analyzed; note that the time axis have been scaled according to each step duration. Decelerating and accelerating steps are separated, deadtime parameters and time to reach steady-state are estimated, and slopes when accelerating and decelerating are obtained. Finally conclusions to this section are summarized.

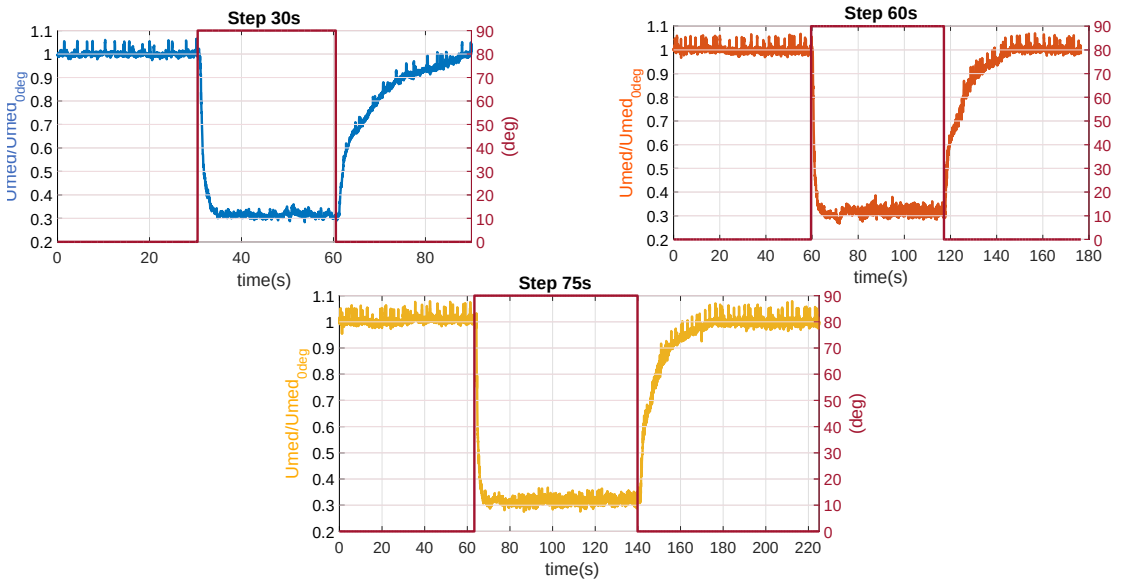

Figure 5.12: **Wind sensors array responses to 90deg steps of increasing duration.** The array response is assessed by the median flow speed value of its sensors. Steps 30s, 60s and 75s correspond to an actual duration of the 90deg phase of 30.025s, 57.55s and 76.5s respectively. Note that the time axis have been scaled according to each step duration.

Separation of decelerating and accelerating steps

From the raw data outliers are removed in the wind profiles following the procedure described in Chapter 7. As in the previous section, decelerating and accelerating responses are separated, taking the instant each step is inputted as $t = 0$. The median value is postprocessed with a moving average over 0.2s; this is done in order to reduce noise and facilitate the analysis and estimation of parameters.

Smoothed decelerating and accelerating responses are shown in Figures 5.13 and 5.14. It can be seen that the responses present variation in their deadtime values, but follow similar paths in their deceleration and acceleration to steady-state. The previously mentioned regions of higher slope are also identified: one for the deceleration case (from the end of the deadtime until $t \sim 3s$), and two differentiated ones for the acceleration case (between $t = 1$ and $t = 3$, and from $t = 3$ until around $t = 15s$). These last two can be more easily identified than in the previous section thanks to the larger timescale of this analysis (compare accelerating response on Figures 5.14 and 5.9).

Deadtime parameters and t_{RMS}

Deadtime is assessed through the two parameters mentioned before, now with a further focus on characterizing the deadtime more precisely. Note that these two have different objectives: with the $DB_{5\%}$ parameter the aim is to establish a uniform criteria to compare the flow responses, whereas with the $DB_{\text{max,diff}}$ the aim is to define a more flexible value that comes closer to the deadtime visually identified, while keeping a definition that allows comparison. The $DB_{\text{max,diff}}$ parameter is now constrained to the window were the change of slope occurs, from 0.1s to 0.975s in the deceleration step, and from 0.1s to 1.475s in the acceleration one. As for the $DB_{5\%}$ parameter, the deadband value, with respect to which the 5% variation is determined, is defined as extending from $t = 0s$ until $t = 0.5s$ for the deceleration phase, and from $t = 0s$ to $t = 0.7s$ in the acceleration phase. Note that in both cases the boundaries for the acceleration deadtime window are extended, since it is visually identified that it extends for a longer span. The results of computating these parameters on the median response, for each of the cases considered, are shown in

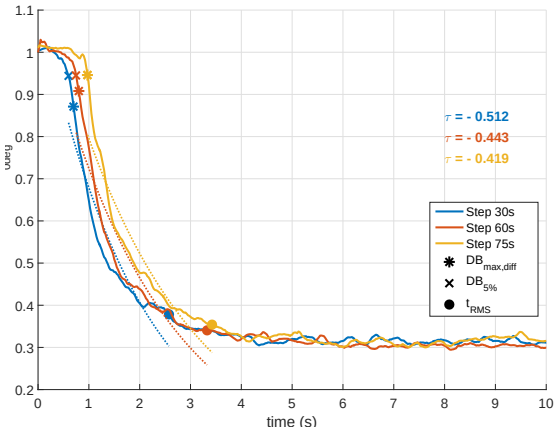

Figure 5.13: **Decelerating response for the three step durations analyzed**. Blue, red and yellow solid lines represent the smoothed median flow speed value for the cases 'step 30s', 'step 60s' and 'step 75s' respectively. The smoothing was done with a moving average over 0.2s. Star and cross markers indicate the instants corresponding to the deadband estimates $DB_{\text{max,diff}}$ and $DB_{5\%}$, respectively. Dot marker represents instant $t = t_{RMS}$. The region extending between the instants $DB_{5\%}$ and $t = t_{RMS}$ is fitted to an exponential curve in each case, of the form $y = ae^{\tau x}$, and the τ constant values are shown to the right. Note that although the responses show variation in the deadtime value, the evolution of the response through the deceleration phase and upon reaching steady-state is very similar in all three cases.

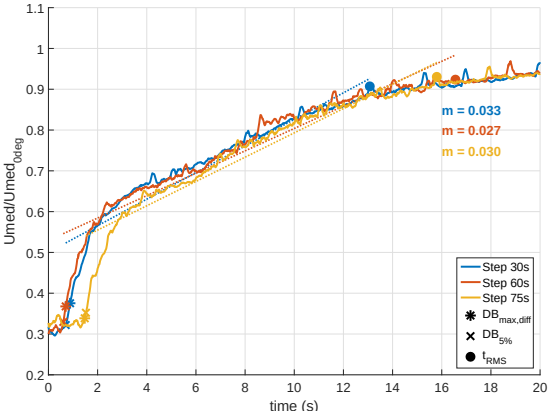

Figure 5.14: **Accelerating response for the three step durations analyzed**. Blue, red and yellow solid lines represent the smoothed median flow speed value for the cases 'step 30s', 'step 60s' and 'step 75s' respectively. The smoothing was done with a moving average over 0.2s. Star and cross markers indicate the instants corresponding to the deadband estimates $DB_{\text{max,diff}}$ and $DB_{5\%}$, respectively. Dot marker represents instant $t = t_{RMS}$. The region extending between the instants $DB_{5\%}$ and $t = t_{RMS}$ is fitted to a linear fit in each case, of the format $y = mx + n$, and the m constant values are shown to the right of the plot, representing the slope of the second acceleration region. Note that as for the deceleration case, although the responses show variation in the deadtime value, evolution of the response converges to a common behaviour towards reaching steady-state.

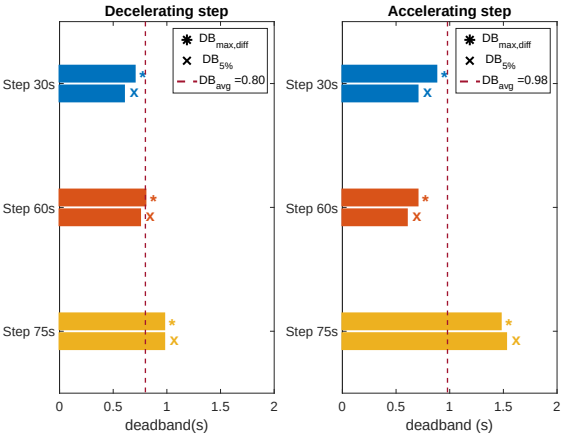

Figure 5.15: **Comparison of deadband parameter values for decelerating and accelerating steps.** Values for deadband parameters $DB_{\text{max,diff}}$ and $DB_{5\%}$ are plotted for each of the step cases analyzed. An avatar with the marker that represents each parameter is added at the end of each bar for clarity. The dashed red vertical line represent the average value across all parameters. The average value is shown in the legend box: for the decelerating case $\bar{DB} = 0.80$ whereas for the accelerating one $\bar{DB} = 0.98$

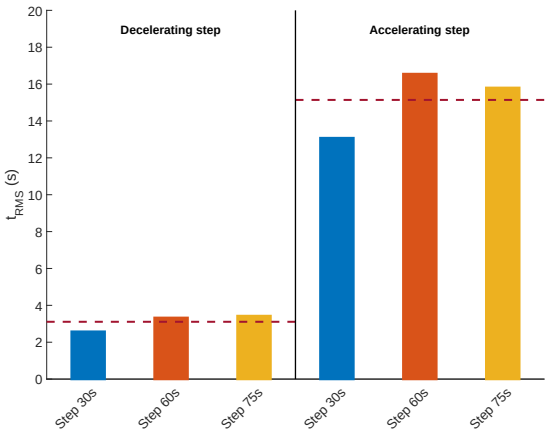

Figure 5.16: **Comparison of t_{RMS} parameter values for decelerating and accelerating steps.** Values for t_{RMS} are plotted for each of the step cases analyzed. The dashed red horizontal lines represent the average value across decelerating cases and accelerating ones. The average value for the decelerating cases is $\bar{t}_{RMS} = 3.108s$ whereas for the accelerating ones is $\bar{t}_{RMS} = 15.14s$

Figure 5.15.

From the results shown in Figure 5.15 it can be seen that the estimations given by both parameters for each case are close in value, and that they are also close to the instant visually identified as the response being no longer "flat" (see markers on Figure 5.13 and 5.14). However spread in the estimates across the different step cases can be seen, especially in the acceleration steps, as it was observed for the individual sensor's deadtime estimations of the previous section (see Figure 5.6). It can be verified as well that the values obtained stay within the same range as in the individual sensors' responses.

The parameter t_{RMS} is also computed for all three steps as in the previous section. This parameter refers to the time instant, from the input of the step, at which the wind speed profile is within a root-mean-square error equal or lower than 0.05, with respect to the steady-state profile. This steady-state profile is defined as the mean over the last 1/6 of the total samples considered. Figures 5.17 and 5.18 show the profiles evolution in time for the decelerating and accelerating response respectively, as well as the steady-state profile and the profile at $t = t_{RMS}$. Comparing both cases it can be seen that in all decelerating steps, the establishment of the steady-state occurs much earlier than in the accelerating cases: note that profiles are plotted with a timestep of 0.25s, and that in the accelerating case a much gradual progression can be seen. The value for the t_{RMS} parameter is indicated in the legend box.

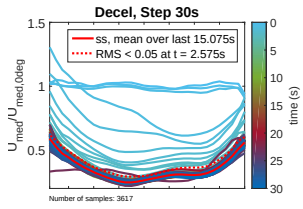

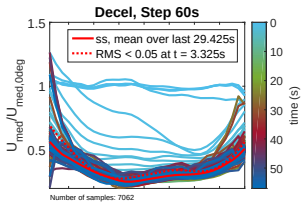

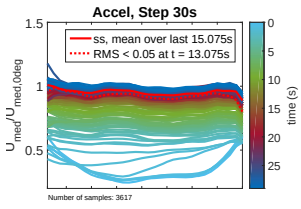

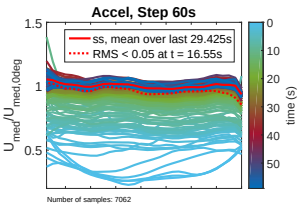

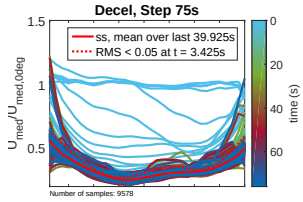

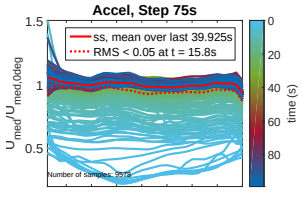

Figure 5.17: **Profiles evolution in time for decelerating 90deg step.** $U/Umed_{0deg}$ values for each sensor are plotted against the sensor spanwise location. Measurement points are resampled from 16 to 32 measurement points, and smoothed with a moving average over 8 points. The steady-state profile is indicated by a solid red line, obtained as average over last 1/6 samples. The profile at $t = t_{RMS}$ is indicated with a dotted red line; that is the profile that first deviates from steady state profile with a root-mean-square error less or equal than 0.05. Colorbar gradient represents evolution in time for each case.

Figure 5.18: **Profiles evolution in time for accelerating 90deg step.** $U/Umed_{0deg}$ values for each sensor are plotted against the sensor spanwise location. Measurement points are resampled from 16 to 32 measurement points, and smoothed with a moving average over 8 points. The steady-state profile is indicated by a solid red line, obtained as average over last 1/6 samples. The profile at $t = t_{RMS}$ is indicated with a dotted red line; that is the profile that first deviates from steady state profile with a root-mean-square error less or equal than 0.05. Colorbar gradient represents evolution in time for each case.

By analyzing the results obtained for the t_{RMS} parameter in Figure 5.16 it can be seen that although there is a large disparity between acceleration and deceleration cases, values obtained for all three decelerating steps and for all three accelerating ones are similar regardless of the step duration, suggesting that convergence to steady-state occurs at a similar pace for same step in amplitude (or grid transparency change) and flowspeed upstream. For decelerating cases t_{RMS} values average $\bar{t}_{RMS} = 3.108s$, and for accelerating cases, $\bar{t}_{RMS} = 15.14s$. Note the significant difference between acceleration and deceleration, being the acceleration average value $\bar{t}_{RMS}$ almost five times larger than the deceleration one.

Slopes in decelerating and accelerating

To gain further insight in the differences between acceleration and deceleration cases, the slopes of the responses are computed, from the instants $DB_{5\%}$ until $t = t_{RMS}$. For the decelerating cases that section of the response is fitted to an exponential relation $y = ae^{\tau x}$ and compare the values of the τ parameter.

Figure 5.13 shows that indeed the τ values are very close for all three decelerating cases, averaging $\tau = -0.458s^{-1}$ and that they closely match the results obtained in the previous section for hotwire ($\tau = -0.410s^{-1}$) and median wind sensors responses ($\tau = -0.384s^{-1}$).

Regarding the acceleration phases, the focus is now placed on the second accelerating region, which presents a shallower slope. The response from $DB_{5\%}$ until $t = t_{RMS}$ is fitted to a linear relation $y = mt + n$, and the values for the slope m are compared. In this way m now characterizes the second region. Note that in this case a larger sampling time is considered, and thus the $t = t_{RMS}$ instant corresponds more closely to the start of the steady-state phase. Indeed in the previous section the steady-state phase was not fully reached in acceleration, with $Umed/U_{med,0deg}$ value at the end of the sampling time being ~ 0.8 (see Figure 5.9). Again slope estimates for all three cases are very similar and average $m = 0.03s^{-1}$, with a reasonable match to the previous hotwire and median array values ($m_2 = 0.021s^{-1}$ and $m_2 = 0.03s^{-1}$ respectively). Considering the slope estimate for the first accelerating region of around $m_1 = 0.17s^{-1}$ from previous section, it can be seen there is a slope reduction of almost 18% between both regions. Moreover the reduction in slope is almost tenfold when going from region 1 to 2, if it is considered for region 1 the peak slope just after the deadtime, which averages to $m_1 = 0.34s^{-1}$ across the three cases.

Conclusions to deadtime estimations and decelerating/accelerating slopes
From the previous analysis the following conclusions can be extracted.

- Regarding the deadtime, not enough indications are found suggesting that steps applied for longer timespans affect the deadtime value. This could have been the case if the sensor thermal characteristics dominanted in the deadtime effect (latching on to low resistance values or degrading their performance due to heating up for example). Therefore it is concluded that sensor's particularities are probably not dominant in the deadtime length.

- For steps of identical amplitude and median flow speed upstream, it can be seen that deadtimes in deceleration are similar across the three cases, and the same occurs for acceleration. It was also observed that the deadtime was on average larger for acceleration cases, which also presented larger spread. This may be due to the flow being more turbulent just before the accelerating step: it may be that there are more variations in the flow with the vanes at 90deg than at 0deg, due to wake shedding of the vanes and the less uniform flow speed at the grid section. This may further extract kinetic energy from the flow and degrade its acceleration.

- As for the slopes in deceleration and acceleration, it is confirmed that these are not influenced either by steps of longer application. Estimates for the deceleration region closely match those obtained in the first section and again the response seems to fit well an exponential relation. Again, the fact that the slope values obtained are close to the hotwire values computed in the previous section suggests that they reflect mainly a flow phenomena and are not dominated by sensor characteristics. The two distinctive accelerating regions were also identified in these three cases; an estimate for the slope at the second region was also given and compared to that obtained for the first one. It was also highlighted the large difference between decelerating rate and accelerating one.

In these first two sections the focus has been placed on steps of same amplitude, applied in the same upstream flow conditions. In the final section of the chapter the effect of applying steps of different amplitudes is looked into, on deadtime and especially on the slope of the response.

5.4.3. Wind sensors, sequence 20s steps

In this final section of the transient response analysis the effect in the flow response of inputting steps of different amplitudes is looked into. By alternating decelerating and accelerating steps of decreasing amplitude, the impact on the deadtime value as well as the effect on the deceleration and acceleration slopes is qualitatively addressed.

Difference in decelerating and accelerating response
Figure 5.19a shows the evolution in the median flow speed response through the two sequences considered. It can be seen that the deceleration and acceleration regions identified earlier appear as well for the different amplitude steps. A noticeable aspect is again the asymmetry between acceleration and deceleration

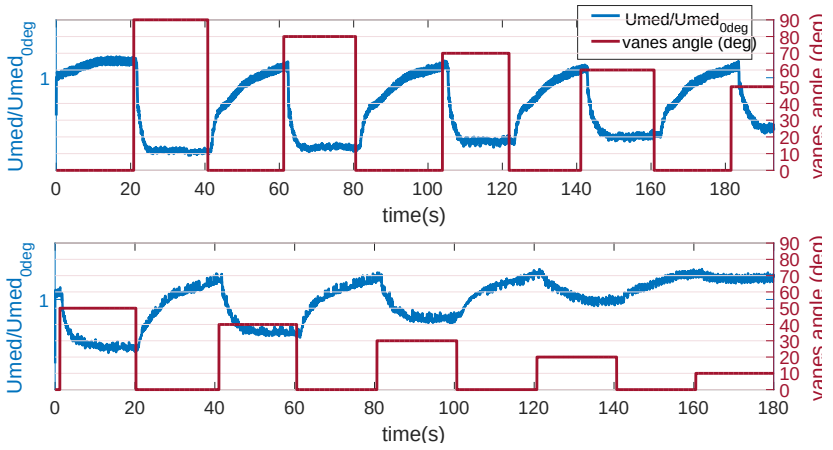

(a) **Sequences of decelerating and accelerating steps, of increasing amplitude**. Two sequences are carried out, the first one with steps from 90deg to 50deg, the second one from 50deg to 10deg.

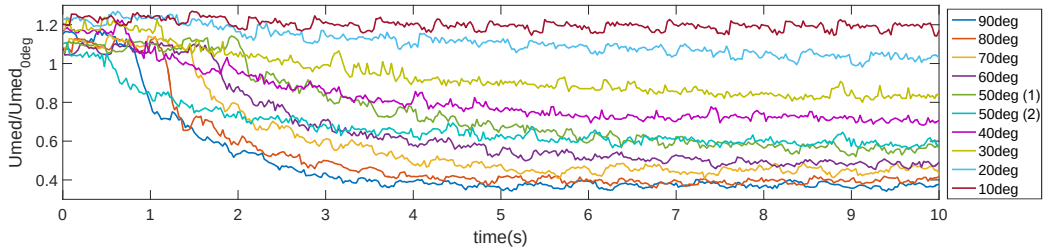

(b) **Response to decelerating steps of increasing amplitude.** Evolution of $\hat{U}_{med} = U_{med}/U_{med,0deg}$ in time, since the instant each step is commanded ($t = 0$). Notice the varying deadtime in the response.

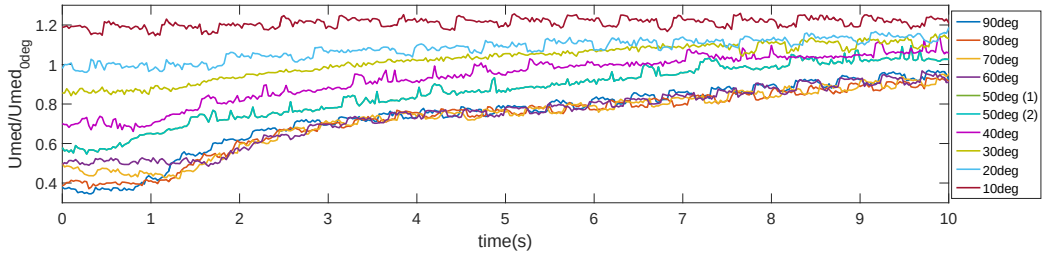

(c) **Response to accelerating steps of increasing amplitude.** Evolution of $\hat{U}_{med} = U_{med}/U_{med,0deg}$ in time, since the instant each step is commanded ($t = 0$). Notice the varying deadtime in the response.

Figure 5.19: **Wind sensor measurements for 20s steps sequences.** This set of data is later used in the uniform profiles in open-loop analysis in subsection 7.3.1

responses, when inputting through the grid transparency positive and negative changes in the pressure gradient. Indeed, for the decelerating steps, the flow reaches a steady-state condition within the 20s time frame, whereas for the accelerating steps the steady-state is less settled. From the work on the previous section it can be verified that around 20s into acceleration, the response has just reached steady-state (see Figure 5.14 and t_{RMS} values for acceleration on Figure 5.16). This may have consequences in the transient response and should be considered. As before, decelerating and accelerating responses are plotted separately for a better analysis. Figure 5.19b and Figure 5.19c show the decelerating and accelerating responses to the steps of increasing amplitude.

Decelerating slope with grid transparency change

Looking into the decelerating steps in Figure 5.19b, it can be seen that for decreasing amplitude (or decreasing grid transparency reduction), the slope of the response becomes shallower. This is thought to be a consequence of the strength of the decelerating pressure waves (induced by the grid transparency reduction), relative to the initial inertia in the flow. The result is an increasing time constant in the response for decreasing grid transparency change.

Additional data, only addressed qualitatively, seems to confirm the influence of the initial flow inertia as well. This is the flow response to a staircase input, shown in Figure 5.22, in which a varying time constant is also observed for the same step in angle, inputted sequentially. However this is also affected by the nonlinearity of the system: at low grid transparency states, the ratio amplitude of input to amplitude of output decreases (see steps around 90deg in Figure 5.22). This is due to the non-linearity in steady-state with vanes angular position. Since the varying time constant effect is expected to affect the response in closed-loop, it is further looked into in section 6.3.

The possible effect on the decelerating response of it starting from a not fully settled steady-state is also addressed. If the deadtime values are removed (as done in Chapter 7, for the same set of data) it can be seen that although decelerating responses do not start from fully established steady-state conditions, there is not much influence of this aspect in the value of the decelerating slope (see Figure 5.20). Indeed the final 50deg step of the first sequence (indicated as 50deg (1) in the figure), and the first 50deg step of the second sequence (indicated as 50deg (2) in the figure) present very similar slope values. This suggests that the decelerating slope is mostly dependent on the grid transparency change introduced.

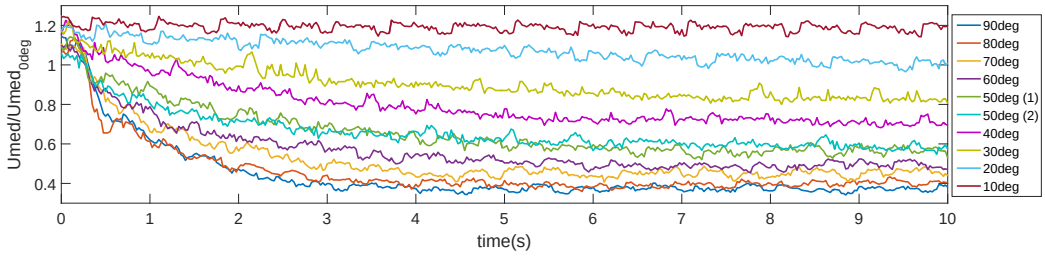

Figure 5.20: **Deceleration steps, deadband removed.** Deadband has been reomved as described in Chapter 7. Notice how both 50deg steps present very similar decelerating paths.

Accelerating slope with grid transparency change

Considering now the accelerating responses, it can be seen in Figure 5.19c that also for decreasing step amplitudes the slope for both accelerating regions becomes shallower. These two slopes also present a larger difference betweeen them for larger changes in grid transparency. This seems to indicate as well a dependence on the grid transparency change inputted. Reference lines have been plotted in Figure 5.21 to clarify this point.

Deadtime in decelerating and accelerating steps

Regarding the deadtime, decelerating steps are first looked into. For the different decelerating steps in the sequences it can be seen that deadtime increases as each sequence progresses (Figure 5.19b). Rather than a relation between the deadtime and the step amplitude, there seems to be an influence of the position of the step in the sequence. This seems to be the case if the deadtime values obtained for the two 50deg steps are

compared, one given at the end of the first sequence and the other at the start of the second sequence (see Figure 5.19b). For the accelerating steps, the deadtime does not seem to increase as much progressing in the sequence. This may be due to the flow being further into steady-state condition at the instant at which the accelerating step is inputted.

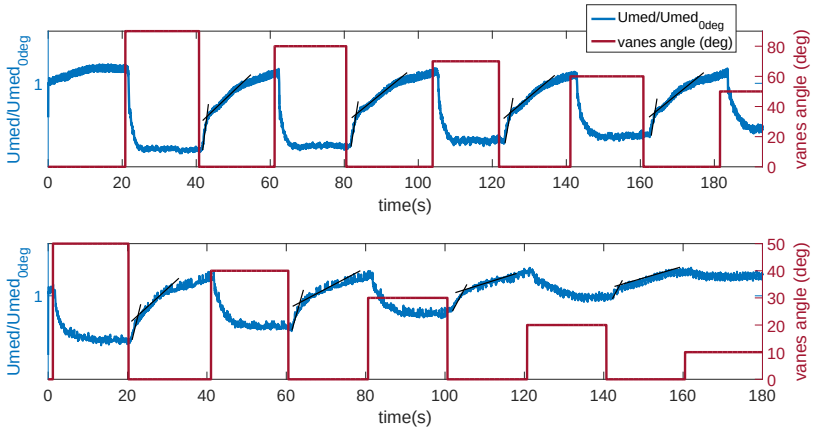

Figure 5.21: **Reference lines to accelerating steps show dependency with the step amplitude.** Note that these lines have been added manually and do not correspond to a computed fit.

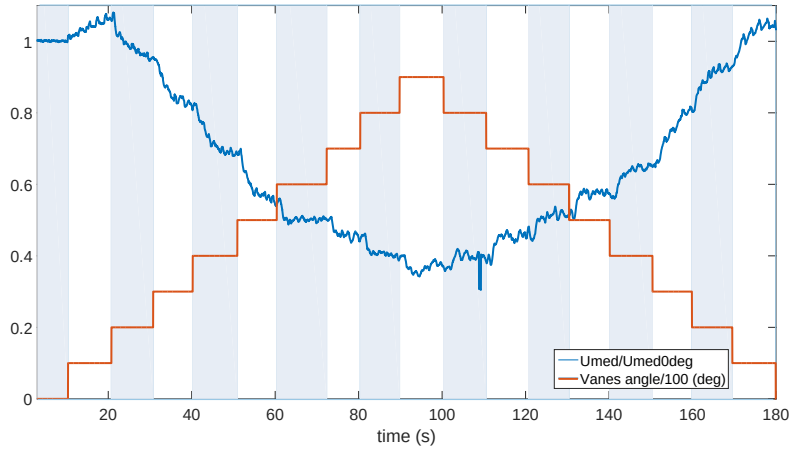

Figure 5.22: **Staircase response.** Steps are inputted sequentially increasing from fully-open grid state, by 10deg, until 90deg, and then decreasing. Further details on this plot can be found in Appendix C.

5.5. Conclusions

In this section the flow's step response in the transient phase has been looked into. A particular focus has been placed on the deadtime observed, the deceleration and acceleration slopes and the speed of response. The following conclusions from the previous discussions are the most relevant for the next chapters.

Regarding the **deadtime** observed, the possible factors affecting its variable magnitude have been commented. Sensor-related ones are not found as the main source of deadtime; flow speed phenomena in the grid transparency transition instead are suggested as an important factor. The turbulent state of the flow upstream before inputting the step, the flow recirculation induced due to changing grid positions or the vortex shedding could lead to a varying deadtime value. However, the variation of the deadtime value across the different cases analyzed seems to indicate contributions from diverse sources. The suggested approach to handle the deadtime, for the development of more sophisticated closed-loop controllers in follow-up projects, is to characterize it by averaging its value on a wide range of experiments. A more detailed analysis would provide further insight on the physical reasons for this effect.

As for **decelerating and accelerating slopes**, a good match of the response given by hotwire and windsensors was observed. A dependency of the slope in transient is found with the amplitude of the step (or equivalently, with grid transparency change). In both decelerating and accelerating cases, slopes become shallower for increasingly smaller steps in vanes angle, given from fully-open states (see Figure 5.19b and 5.19c). This results in a **varying time constant** for different input steps, and is expected to affect the closed-loop response. The physical reason behind this effect is thought to be in the mechanisms driving the transient response: the imbalance between the flow inertia and the strength of the pressure waves in the pressure gradient propagation. Additional results seem to confirm a dependency on the initial grid transparency state as well; however it is difficult to distinguish the effect from the reduced effectiveness, due to non-linearity with vanes angle. All these aspects are further explained in the next chapter.

Decelerating rates were found larger than accelerating ones for grid transparency changes of equal amplitude. It is suggested that this is due to the closing grid providing an additional mechanism to reduce kinetic energy of the flow when decelerating, through turbulent losses. This would yield a shallower slope when accelerating the flow.

One clear decelerating region was identified after reducing grid transparency, whereas **two slopes in the acceleration region** were found when inputting an increase in grid transparency. The first phase can be identified as in injection of momentum to the test section control volume due to suddenly opening to a lower pressure downstream the grid.

All in all, the system's response was found to be stable and well-damped in open-loop. However it is also very **slow**, with times to reach steady-state around 4s in decelerating steps and 16s in acceleration. These are time spans unsuitable for a real-time bird flight experiments, and this slow flow response will be the main limitation.

Finally, similitudes can be found between the process of varying grid transparency and a partial valve closure for incompressible flows, also known as water hammer. From the Joukowsky equation, derived from the momentum equation applied to a wavefront, the intensity of the wave for a sudden change in speed can be estimated (Manglik, 1997). The intensity is identified with the pressure change induced by the wave ΔP :

$$\Delta p = -\rho a \Delta U \tag{5.1}$$

where ρ is the fluid's density, ΔU the change in flow speed and a the sonic velocity of the pressure wave in the fluid. For the case considered, the larger grid transparency reduction, the larger the intensity of the pressure wave generated and the higher deceleration value. This indeed matches the observations (see Figure 5.19b). The pressure change given by equation 5.1 would be the maximum pressure rise or drop across the pressure wave, but this value can be largely reduced by reflections of the original wave, due to area changes, open or close ends.

6

Construction and tuning of 1-region closed-loop controller

Having looked into the response of the system in open-loop, our aim now is to build a controller for it. In the two previous chapters, it has been shown that this system with input P and output $\hat{U}_{med}$ is non-linear. A non-linear controller would better control a non-linear system, since the latter guarantees that all controller specifications are fulfilled at any operating point. Indeed, a linear controller approximates a linear relation around a certain operating point, and away from it, controller specifications are not exactly fulfilled. In this project the non-linear controller is obtained empirically, in the form of a lookup table. This table defines the relationship between desired profiles and required vanes angular position, and avoids the need of extracting a non-linear model for the system. To populate this lookup table, that is, to obtain the required vanes angular positions for a certain flow profile, a closed-loop controller is used. Since its purpose is to tailor flow profiles, the only requirement for this controller is to guarantee zero steady-state error. This chapter concerns the first step towards building this closed-loop controller, presenting the construction of the 1-region approach.

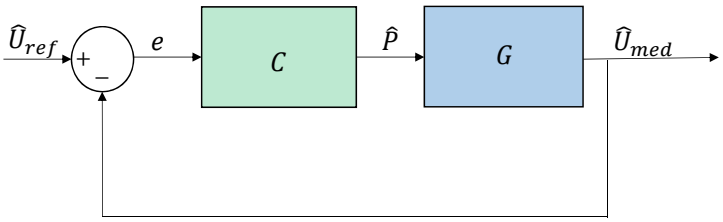

Figure 6.1: **Block diagram for the 1-region closed-loop controller.** The plant or system G (blue box) represents the turbulence grid + wind sensors array. The input variable for the system is the non-dimensional vertical vanes angular position $\hat{P} = P/90deg$, with P being the dimensional vertical vanes angular position. The output is the non-dimensional median flow speed of the sixteen wind sensors in the array $\hat{U}_{med} = U_{med}/U_{med,0deg}$. The green box C represents the closed-loop controller to be designed, whose main objective is to serve as a profile design tool. The error signal e is the difference between the reference input value $\hat{U}_{ref}$ and the system's output $\hat{U}_{med}$. Note that although a block diagram has been used for clarity, the plant G is nonlinear.

The choice of developing an empirical non-linear controller reflects a preference for fulfilling the specifications in the whole operating range, over aiming for a faster response of the system. This is based on the observations from the previous chapters: the slow flow response limits the attainable speed of response with a closed-loop controller, and it would be challenging to develop one that meets the fast speed of response requirements for adapting to quick bird maneuvers. These would require a timescale for profiles switching in the order of a wingbeat period (Quinn et al., 2015 [Manuscript submitted for publication]). As

an indication, flapping frequency for lovebirds is around 17Hz, so flapping period results around 0.06s (Kress et al., 2015), and for parrotlets is around 23Hz, resulting in a flapping period of 0.04s approximately (Gutierrez et al., 2016); a takeoff maneuver can take around 5 wingbeats. In contrast the time for flow to accelerate and decelerate in the wind tunnel when modifying the grid's transparency is in the order of 10s (as it has already been seen in Chapter **??**). For this exploratory project obtaining precisely tailored profiles is then primed over aiming for the fastest response in the system.

As an overview of the next steps in the project, once this 1-region controller is tuned, it will be replicated as 4 controllers in parallel in the 4- and 8-region approaches (see Figure 1.9). Using the 8-region closed-loop controller the lookup table is populated, enabling its use in open-loop as an empirically obtained non-linear controller. The 4-region controller developed in between is used for comparison across gust designs; since generating a lookup table for all the gust designs would be quite extensive, the 4-region controller is used, assuming the comparison would similarly translate in open-loop.

The objective of this chapter is then to build and tune a closed-loop controller for the system made up of the turbulence grid and the sensors array, assuming one region in the test section. Thus a single-input single-output (SISO) system is considered, with input variable the non-dimensional vertical vanes angular position $\hat{P}$ and output variable the non-dimensional median flow speed across the sixteen sensors in the array $\hat{U}_{med}$ (see Figure 6.1). In this way all the eight vertical vanes are commanded the same angle, aiming to reproduce uniform profiles downstream the grid. The closed-loop approach is used as a design tool, enabling convenient tailoring of different profiles, and the 1-region approach is the base for the controllers developed in Chapter 7 and Chapter 8.

6.1. Chapter overview

This chapter covers the procedure followed for the design of the 1-region closed-loop controller. First, a background for classical control theory is included, defining relevant concepts later used in the chapter. Next, some characteristics found in the open-loop response (analyzed in Chapter **??**), and relevant to the controller design are reviewed. Once this has been covered, the closed-loop controller design is discussed, defining its requirements, architecture and tuning procedure. The tuning of the controller's parameters is carried out manually, aiming for a fast response within stability. As an experimental assessment of the developed controller, two sets of experiments are presented, in which the tuning parameters are varied and the response at different parameter values are compared. Finally, conclusions of the closed-loop response, relevant for the next chapters, are drawn.

For this chapter the main objective is then to build a functioning closed-loop 1-region controller for the present nonlinear system, that guarantees zero steady-state error with an architecture as simple as possible, that will serve as a basis for the follow-up controllers developed later on.

6.2. Background in classical control theory

Following the definitions given by Ogata (2002), some classical control theory concepts that will be dealt with in this chapter are presented below. Note that classical control theory deals with single-input single-output (SISO) systems only .

A ***system*** can be defined as "*a combination of components that act together and perform a certain objective*". In the present case, the system is made up of the active turbulence grid, the sensors array, and all the supporting setup for their communication and operation. These include the Arduino board, the XBee radio modules and the PC with the LabVIEW code (see Chapter 3 for further details). From the physical objects that make up the system, the one (or the group of ones) that is to be controlled is the ***plant***. For the case at hand, the plant would be the combination of the active turbulence grid and the wind sensors array (blue block G in Figures 6.1 and 6.2). Note that although there are slight differences in their meaning (*system* is a broader concept), in the following *system* and *plant* are used as equivalent terms.

Feedback control is a method of limiting or correcting the output of a system subject to disturbances. It is based on operations aimed to minimize the difference between a reference value and a fed-back value. The fed-back value may be a function of the system's output or its derivatives or integrals. For the SISO case presented, the fed-back signal is directly the system's output $\hat{U}_{med}$. The difference between reference and fed-back values is the ***error signal*** e; in the case of analysis, the error signal $e = \hat{U}_{ref} - \hat{U}_{med}$ (see Figure 6.1). As shown in the closed-loop diagram on Figures 6.1 and 6.2, the operations aimed to control the system are indeed a function of this error signal.

When dealing with feedback control, the output of the system is the ***controlled variable***, defined as the *quantity or condition* being monitored and controlled. For the system considered here, the controlled variable is the non-dimensional median speed value, $\hat{U}_{med}$. The ***manipulated variable*** is the *quantity or condition* modified by the controller to steer the controlled variable towards the reference. In the present case, it is the non-dimensional vertical vanes angular position $\hat{P}$, obtained as $\hat{P} = \frac{P}{90deg}$, with P being the dimensional vertical vanes angular position.

Opposing closed-loop approaches there is ***open-loop control***, in which the system's output is not fed-back and thus it has no influence on the control operations (see Figure 6.2). Since there is no comparison of the system's state with a reference, open-loop control requires the relationship input-output to be known precisely. The performance of the system relies heavily on a careful calibration and on highly accurate components. Additionally, the system controlled in open-loop will not perform well under disturbances.

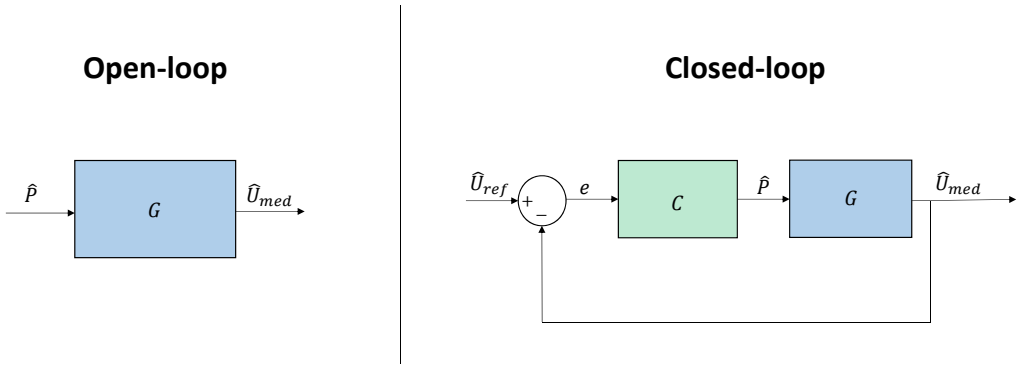

Figure 6.2: **Comparison of input and output variables for the system in open-loop and in closed-loop.** Input and output variables in open-loop are non-dimensional vanes angular position $\hat{P}$ and $\hat{U}_{med}$, respectively. Input and output variables considered for the closed-loop case are $\hat{U}_{ref}$ and $\hat{U}_{med}$, respectively.

The main problem when dealing with closed-loop systems is the potential destabilizations and oscillations due to overcorrections. However the use of closed-loop systems is necessary to correct unpredictable variations, both due to external disturbances or internal, due to unmodeled or uncertain dynamics. Since the aim is to build a tool that designs profiles from user-defined flow speed parameters (static gusts) and following a marker (dynamic gusts), a closed-loop setup is in principle convenient. A closed-loop approach is also required considering this controller serves as a basis for the follow-up ones (see Figure 1.9): when dividing the controlled space in regions, a closed-loop approach will account for the flow deviation generated by neighbouring regions.

In the following sections it is shown that the simplest controller architecture that satisfies the requirements for the 1-region closed-loop controller is a ***discrete integral controller***, in which the controller output is modified at a rate proportional to the error signal. In the case at hand, the controller gives a correction to the current angular position $\Delta\hat{P}$ that is proportional to the current error e. Since the controller is discrete, this correction $\Delta\hat{P}$ will be applied with a certain timestep Δt. The manipulated variable $\hat{P}$ then results from the accumulated increments in the control signal $\Delta\hat{P}$ of every discrete step. This is further explained in subsection 6.4.2.

6.3. Open-loop characteristics relevant for closed-loop controller design

Two main aspects of the open-loop response are identified in Chapter 5 as potentially affecting the closed-loop controller design. The first one is the varying time constant of the response, which showed a dependency with the amplitude of the input step in angular position (or equivalently, the grid transparency change inputted) and with the initial grid transparency state (see Figures 5.19b and 5.22). The second nonlinear effect is the presence of a deadtime (see Figure 6.3). Some aspects of these have already been commented on in the previous chapter. In this section these two effects are further looked into.

An estimation of the orders of magnitude of the different terms in the Navier-Stokes momentum equation provides information on the physical phenomena related to the **varying time constant** effect. In its conservative form this equation is:

$$\rho \frac{\partial \vec{u}}{\partial t} + \rho \vec{u} \cdot \nabla \vec{u} = -\nabla p + \mu \nabla^2 \vec{u} \tag{6.1}$$

From left to right, the terms in the equation are the unsteady term, the convective term, the pressure gradient term and the viscous term (taking $\nabla \cdot \tau' = \mu \nabla^2 \vec{u}$). Note that incompressibility has been assumed, and gravity forces are neglected. In non-dimensional form the equation results:

$$\frac{l_c}{t_c U_c} \frac{\partial \vec{u^*}}{\partial t^*} + \vec{u^*} \cdot \nabla^* \vec{u^*} = -\frac{\Delta P}{\rho {U_c}^2} \nabla^* p^* + \frac{\mu}{\rho U_c l_c} \nabla^{*2} \vec{u^*} \tag{6.2}$$

with superscript * indicating non-dimensional variables, obtained by adequately scaling with characteristic length l_c, flow speed U_c, time t_c and pressure difference ΔP (with $l_c / t_c U_c \sim 1$). Noting that the parameters by the viscosity term represent $1/Re$, equation 6.2 reveals that at the Reynolds number considered ($Re \simeq 10^4$) the viscosity effects are less relevant than the other terms. This yields the pressure term as the one leading the motion and the convective term as its main opposing force in the transient regime. The convective term represents what has been referred in the previous chapter as the flow inertia.

The non-dimensional form of the equation also shows that the ratio $\Delta P / \rho {U_c}^2$ determines the magnitude of the motor term. This ratio is the *Euler number* and represents how large the pressure change is relative to the flow kinetic energy in the volume. In this case this ratio can be related to how effective a certain change in grid transparency is in decelerating or accelerating the flow, given at a certain flow state. Indeed this matches previous observations: the amplitude of the grid transparency change affects the ΔP value (larger grid transparency reduction, larger intensity of the pressure waves, larger pressure change across the characteristic length l_c); and the initial grid transparency state relates to the initial flow inertia $\rho {U_c}^2$. This is thought to explain the varying time constant effect.

The second effect observed in the open-loop response and relevant for a closed-loop controller is the presence of a **deadtime**, of varying value (see Figure 6.3). The possible sources for this deadtime have been discussed in Chapter 5. Regarding the design of a controller, systems with deadtimes make the design of a satisfactory controller more challenging, since the instability introduced, due to the imbalance between the system lags and the intensity of the correction, forces to largely decrease controller gains in order to achieve stability (Craig, 2002). A consequence of this reduction in gain is a sluggish response, which largely limits the achievable response time.

A solution typically applied for a first-order system with deadtime is the construction of a structure called *Smith predictor* (Warwick and Rees, 1988). This scheme is based on building an additional loop in the block diagram, resulting in a closed-loop response of the system identical to that of the system without deadtime, but delayed an amount equal to the deadtime value. This is the most common strategy used to overcome deadtime effects in linear time-invariant processes, but its implementation can be complex (Ingimundarson, 2000). Since the objective now is to build a functioning prototype of the tool, the construction of such a scheme has not been considered. However it is recommended that this possibility is further analyzed for future applications and developments of the tool. More information on the model of a first order system with a deadtime can be found in Appendix D.

Having clarified the main control theory concepts and some relevant aspects observed in the open-loop

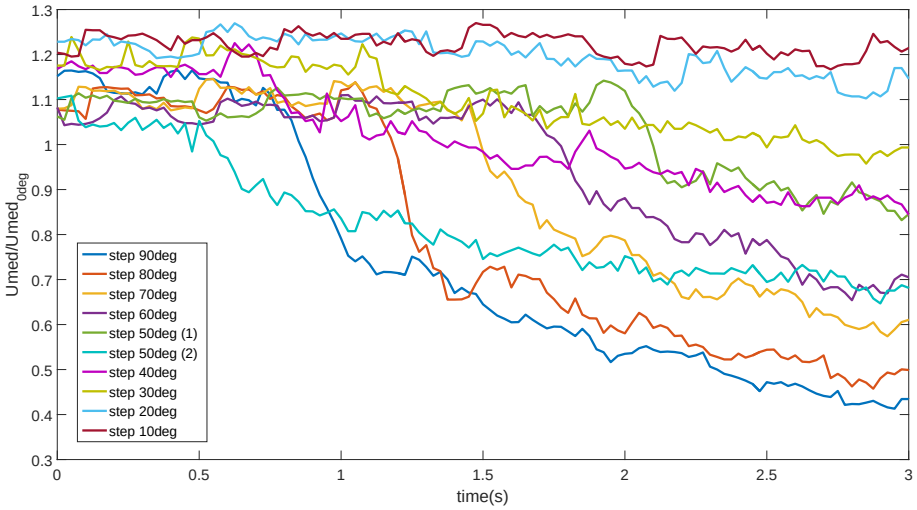

Figure 6.3: **Deadtime for steps in vanes angle of increasing amplitude, in open-loop.** Its varying value is clearly seen in the response. Zoom-in from results presented in subsection 5.4.3.

response, the design of the 1-region closed-loop controller is addressed in the next sections.

6.4. Controller design

The design of the closed-loop controller starts with the definition of the initial requirements. Next, the controller's architecture is selected, considering the previously set requirements and finally the controller's parameters are manually tuned. Once the closed-loop controller is tuned, experiments are carried out to assess its performance.

6.4.1. Controller requirements

The initial requirements for the closed-loop controller are the following:

1. *Simplicity of the design.* Since later on several controllers will be set up in parallel, a simple structure is prioritized at this stage.
2. *Zero steady-state error.* In order to obtain the desired profile designs, the goal is to reach zero steady-state error with the reference flow speed values.
3. *Stable response.* The response of the system in open-loop is slow but stable. In principle a closed-loop arrangement could introduce instabilities. Therefore, preserving stability is an important requirement.
4. *Minimal oscillations and minimal initial overshoots in the response.*
5. *Minimal oscillations in vanes angular position*, in order to preserve life of actuators and motors.

Note that vanes angular position $\hat{P}$ is chosen as manipulated variable, since it corresponds to the physical variable for interaction with the grid. In the previous open-loop analysis Chapter 4 however it has been shown that median flow speed presents a relation very close to linear with grid transparency GT (Figure 4.3); thus this would be a good choice for manipulated variable. For simplicity and to avoid an extra conversion in the loop, vanes angular position is $\hat{P}$ selected for our proof-of-concept approach, but exploration with using GT as manipulated variable would be recommended for future developments. Note that although GT would make the system linear, the requirement of having a controller that fulfills its specifications in the whole range of operation would be lost with a linear controller (even defining linearizations at different operating points). In appendix D, some linear models are briefly commented on.

6.4.2. Controller architecture

A **discrete integral controller** is the simplest architecture that fulfills the requirements set in the previous section. It should be reminded that the main goal with the integral controller is to use it as a design tool (to

later populate the lookup table that works as non-linear controller), and that its main requirement is then to guarantee zero steady-state error. An integral controller is the simplest arrangement that satisfies this requirement.

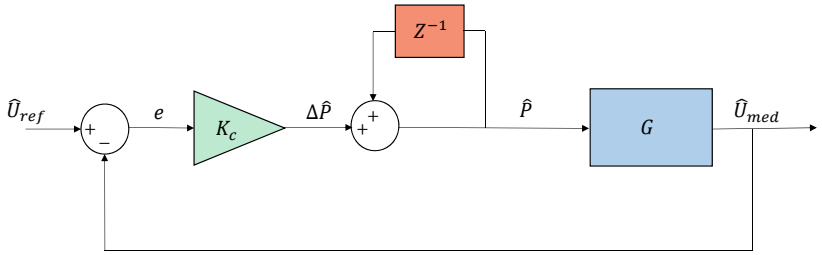

Figure 6.4: **Schematic of discrete integral controller.** The block Z^{-1} represents the integral action in the discrete domain: the previous angular position $\hat{P}$ is added to the corrective $\Delta\hat{P}$. Note that the controller corrective action in that iteration $\Delta\hat{P}$ is proportional to the error $e(k)$ in that iteration, through the constant K_c

With the discrete integral controller, the controller output is proportional to the integral of the error signal. As shown in the block diagram in Figure 6.4, the vanes current angular position is steered with corrections in angle proportional to the current error, in order to reach the desired $\hat{U}_{ref}$. As a reference, the open-loop response to a staircase is presented in in Figure 6.5, in which vanes angular position is changed gradually.

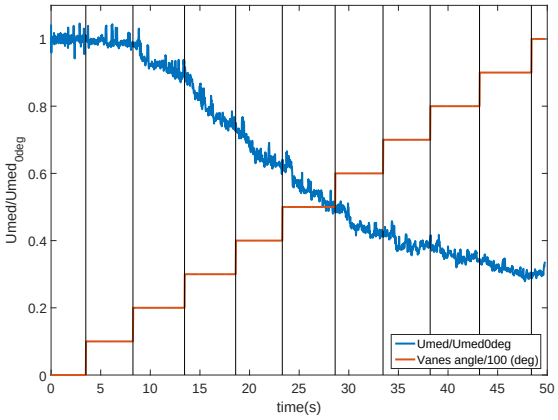

Figure 6.5: **Open-loop response of the system when inputting a gradual decrease in grid transparency.** This decrease is obtained by manually increasing the vanes angular position in steps of 10deg every 5s approximately.

6.4.3. Manual tuning

Regarding the tuning of the controller's parameters, it can be seen in Figure 6.6 that the discrete integral controller suggested is analogous to a continuous one with integral gain K_c/dt, when sampling time tends to zero. Thus, for this controller an adequate value of K_c/dt that provides stable control over a wide range of step amplitudes $\Delta\hat{P}$ is sought. Note the interrelation between both parameters: the gain value K_c now sets the maximum $\Delta\hat{P}$ given in every control-loop iteration and the timestep Δt sets the time left for the system to adapt to the new state. By making $\Delta\hat{P}$ dependent on the error the system is guaranteed to stay at the reference value once reached. From manual tuning it is found that an integral gain of $\mathbf{K_c/dt \sim 0.48s^{-1}}$ provides a stable behaviour across different $\hat{U}_{ref}$ values inputed. Keeping within that ratio, both design parameters are then tuned, aiming for the smallest Δt that gives a stable response. A small value of Δt is desirable so that if the external user (or eventually, the motion tracking marker) changes the reference value to follow $\hat{U}_{ref}$, the system reads it as soon as possible and starts moving towards it.

With these added requirements, a good performance is found across a wide range of $\hat{U}_{ref}$ inputs with $\mathbf{K_c = -0.12}$ and $\mathbf{dt = 0.25s}$. It is believed that this small value for the gain K_c is influenced by the deadtime in the response. The chosen gain value leads to a maximum correction of around $\Delta\hat{P} = 7deg$ (for an error

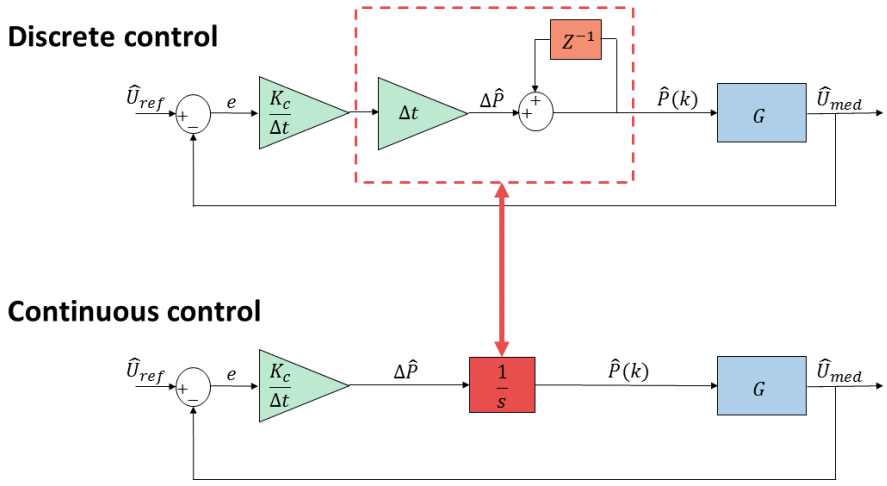

Figure 6.6: **Equivalence between discrete and continuous integral controller**, when sampling time tends to zero.

$e = -0.65$, when going from $\hat{U}_{ref} = 1$ to $\hat{U}_{ref} = 0.35$) and corrects deviations larger than $e = 0.09$ (with minimum corrections being $\Delta\hat{P} = 1deg$ due to rounding by the grid interface).

In order to gain further insight into the relation between the selected parameters, and into the system's response in closed-loop, a variation around the values selected for K_c and Δt is carried out and the differences in the response for the same $\hat{U}_{ref}$ inputs are analyzed. Two sets of experiments are presented for this purpose: $\mathbf{K_c}$ ***variation*** and Δ**t** ***variation***. Additionally, open-loop and closed-loop performance of the system will be compared making use of that same data. The procedure to obtain this data is discussed in the next section.

6.5. Experimental procedure

For all the experiments in this chapter the sixteen sensors in the array are used, set up in the traverse as described in Chapter 3. The wind sensors sampling frequency is 40Hz. Vertical vanes angles range from 0 to 90deg, rotating clockwise when increasing the angle, and anti-clockwise when decreasing it (seen from the top of the test section). When modifying the controller's parameters, variables are registered at the frequency the controller reads them, for for $\hat{U}_{med}$, or generates them, for $\Delta\hat{P}$. For all cases, the wind tunnel setpoint speed is 5m/s and the temperature of the test section is controlled and maintained at 20ºC. The parameter $U_{med,0deg}$ (used for non-dimensionalizing the registered U_{med} values) is obtained as the median of 200 data points of U_{med} registered at the start of every experimental procedure, while grid is kept at 0deg. The horizontal vanes are kept at 0deg throughout all experiments presented in this chapter.

6.5.1. $\mathbf{K_c}$ variation

For the analysis of the effect of the gain K_c variation, a representative sequence in $\hat{U}_{ref}$ is inputted for different values of K_c and the responses are compared to the previously established requirements. The controller timestep Δt is kept constant and equal to the value obtained in manual tuning $\Delta t = 0.25$. The sequence in $\hat{U}_{ref}$ was inputted manually, and chosen such that different step sizes at different total speeds were commanded. Figure 6.7 and Figure 6.8 show the values of K_c considered and the $\hat{U}_{ref}$ sequence.

6.5.2. Δt variation

For the exploration of the controller timestep values Δt around the selected value, a closed-loop sequence of steps in $\hat{U}_{ref}$ is inputted at different Δt values, keeping the controller gain constant $K_c = -0.12$. The steps $\Delta\hat{U}_{ref}$ are applied sequentially as decelerating and accelerating steps, as shown in Figure 6.10. The fully-open grid state is forced by inputting $U_{ref} = 1.5$ and the lowest grid transparency by inputting $U_{ref} = 0$. The sequence is split in two parts of 200s each, for practical reasons. With this approach the closed-loop response can be compared with comparable step-responses from the open-loop experiments. The sequence

Figure 6.7: Controller gain $\mathbf{K_c}$ values analyzed

K_c
-1.1
-0.65
-0.25
-0.16
-0.12
-0.08

Figure 6.8: $\hat{U}_{ref}$ input sequence for varying $\mathbf{K_c}$ analysis, first (top) and second (bottom) sequence. Time intervals for each $\hat{U}_{ref}$ setting are: 90s, 30s, 40s, 20s, 20s, 20s

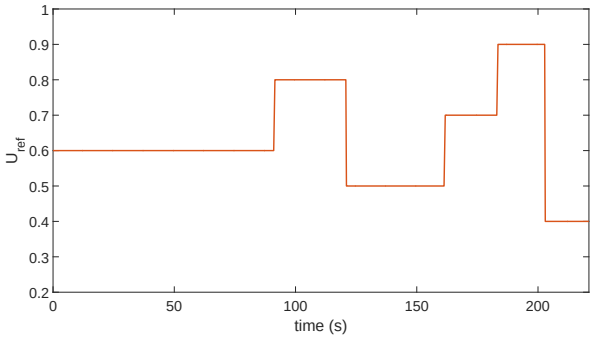

Figure 6.9: Controller timestep $\Delta\mathbf{t}$ values analyzed, in ms

$\Delta\mathbf{t}$
1
10
25
50
100
250
500
600
800
1000
2000

Figure 6.10: $\hat{U}_{ref}$ input sequence for varying $\Delta\mathbf{t}$ analysis

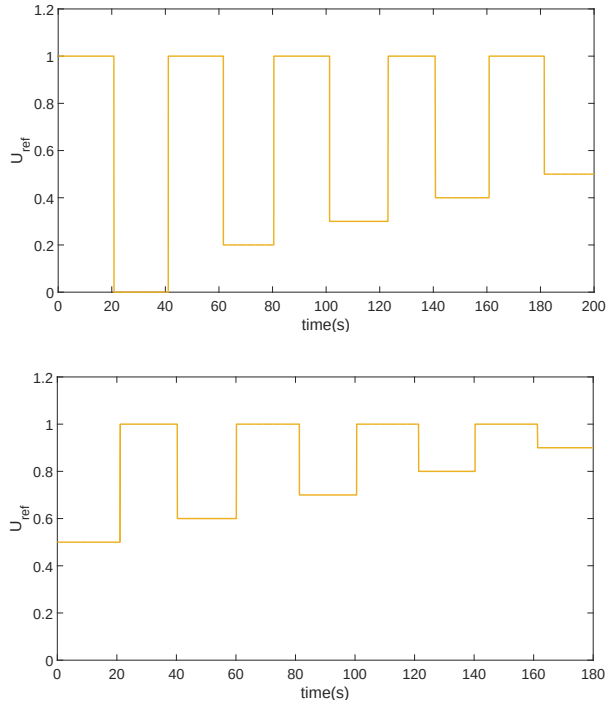

in $\hat{U}_{ref}$ was inputted manually by an external user, keeping each value for a certain timespan. The Δt values considered in the analysis are shown in Figure 6.9.

6.5.3. Varying time constant effect

For the open-loop analysis, the set of data used in Chapter 5 is considered. It is obtained by inputting a sequence of decelerating and accelerating steps in vanes angles, with amplitudes from 10 to 90 deg, by tens, holding each step for 20s (see Figure 5.19a). The open-loop response in terms of $\hat{U}_{med}$ is shown for decelerating and accelerating steps in Figure 5.19b and 5.19c respectively. The closed-loop data used for comparison is the same set used for the *varying* K_c analysis.

6.6. Results

6.6.1. K_c variation

Figure 6.11 shows the closed-loop response of the system with different K_c values. In each case the amplitude of each step correction $\Delta\hat{P}$ is modified (changing its scaling with the error) but keeping the same frequency of application. It is know from the open-loop analysis that the flow acceleration (the slope in the transient response) varies with the step amplitude and sign: in Figures 5.19b and 5.19c it can be seen that flow acceleration and deceleration is larger for larger steps in vanes angular position P, and that it is slower for accelerating steps. It has been shown that this is actually related to the varying grid effectiveness, and thus it is also dependent on the initial grid transparency state. We aim for the scale factor with the error in which the range of $\Delta\hat{P}$ given are close to linear.

From the response at $K_c = -1.1$ it can be seen that the $\Delta\hat{P}$ step given at each iteration is excessive in relation to the frequency at which it is applied. After a first $\Delta\hat{P}$ is applied, the following one is defined with a state of the flow that has changed little (or nothing if this new state is read on the deadtime) and the correction quickly accumulates and leads to oscillation between saturation values. The saturation can be clearly seen in the evolution of P.

Decreasing K_c by 40% it can be seen that oscillations in the response are smaller when setting $\hat{U}_{ref}$ to low grid transparency states (where the effectiveness is larger), but still problematic when $\hat{U}_{ref}$ is around larger grid transparencies. It is indeed expected that these steps to present larger time constants and thus prone to give oscillations in this closed-loop configuration. In any case even in the responses with less oscillation large initial overshoots are seen. Note that oscillations of low amplitude are not desirable since they can amplify with perturbations as seen around $t = 60$s with $\hat{U}_{ref} = 0.6$, in Figure 6.11b.

The trend observed for this two cases continues for $K_c = -0.25$ and $K_c = -0.16$. For these it can be seen more clearly that the initial convergence to the reference is slower for lower values of gains, which is consistent with the grid opening being more gradual. However in exchange stability in the response is gained. Note that $\hat{U}_{ref}$ around high grid transparencies are still oscillatory at $K_c = -0.25$, and overshooting at $K_c = -0.16$. Halving the gain value to $K_c = 0.08$ (Figure 6.11f) largely decreases the amplitude of the overshooting peaks, but makes the response much slower and sluggish, taking around 20s to first reach the reference value. The selected value $K_c = -0.12$ (Figure 6.11e) is a good trade-off between these last two cases, with enough speed of response and reduced overshoots. Additionally, the gain value $K_c = -0.12$ provides small oscillations in the vanes angular position and thus the life of actuators and motors is preserved.

6.6.2. Δt variation

The effect of modifying the frequency of application of each $\Delta\hat{P}$ is now looked into, keeping its scaling with the magnitude of the error signal $K_c = -0.12$. In Figure 6.12 cases from $\Delta t = 1$ms to $\Delta t = 250$ms are shown. Since the gain value is kept constant, these cases progressively decrease their K_c/dt ratio (i.e., their K_i gain), until the selected value (Figure 6.12f). An interesting behaviour is observed: when increasing Δt towards $\Delta t = 250$ms (and thus decreasing K_i) the response is faster and the amplitude of the overshoot increases. For $\hat{U}_{ref}$ inputs around large grid transparencies it can be seen the loss of damping effect mentioned in the previous section.

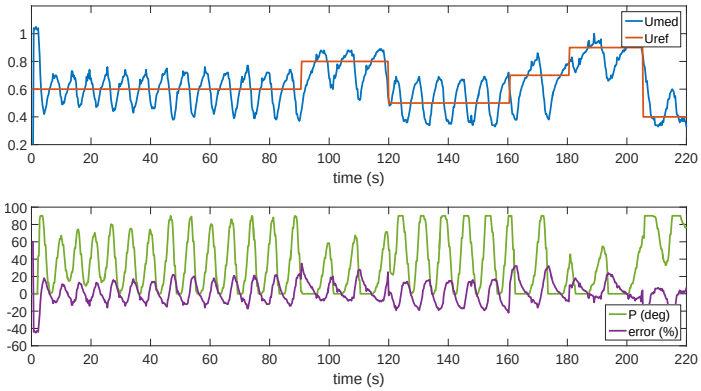

(a) **Response for $\mathbf{K_c} = -\mathbf{1.1}$.** ($K_i = -4.4$)

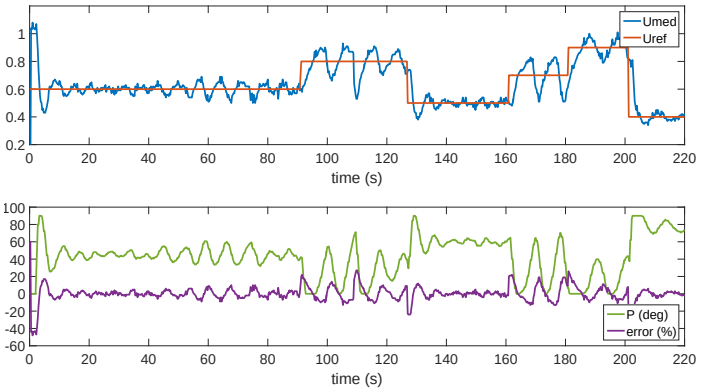

(b) **Response for $\mathbf{K_c} = -\mathbf{0.65}$.** ($K_i = -2.6$)

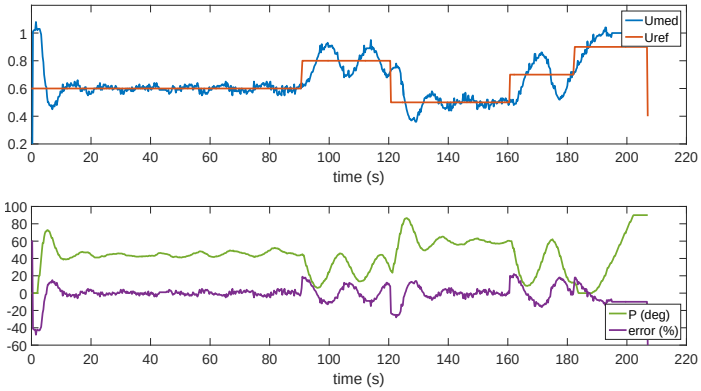

(c) **Response for $\mathbf{K_c} = -\mathbf{0.25}$.** ($K_i = -1$)

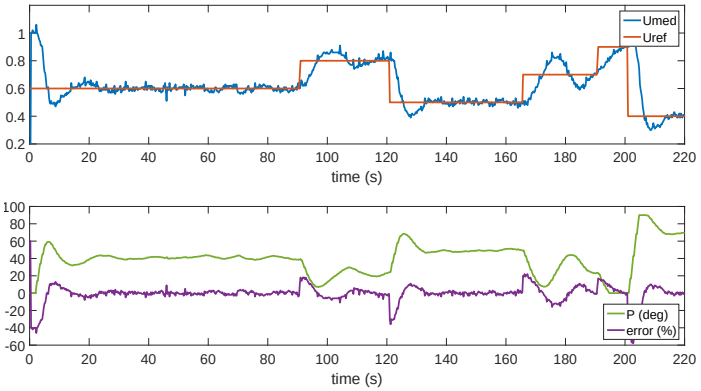

(d) **Response for $\mathbf{K_c} = -\mathbf{0.16}$.** ($K_i = -0.64$)

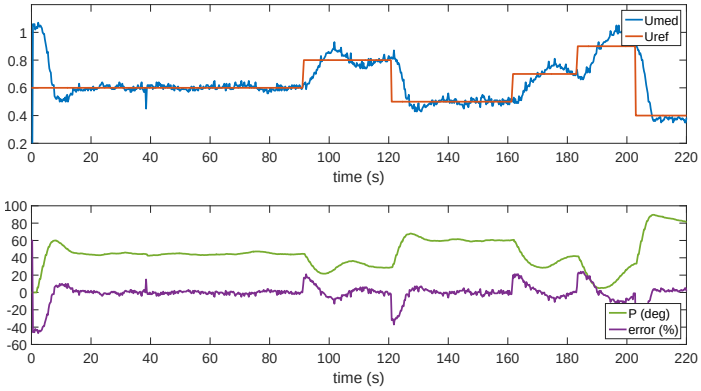

(e) **Response for $\mathbf{K_c} = -\mathbf{0.12}$.** ($K_i = -0.48$)

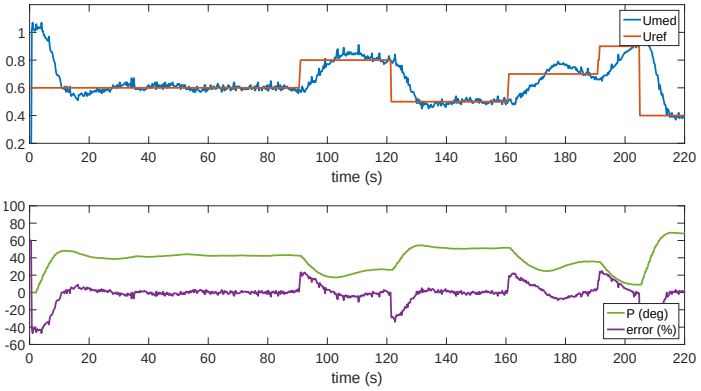

(f) **Response for $\mathbf{K_c} = -\mathbf{0.08}$.** ($K_i = -0.32$)

Figure 6.11: **Variation of controller gain K_c.** For each figure, top subplot shows the evolution in time of $\hat{U}_{med}$ (dark blue), for the $\hat{U}_{ref}$ sequence inputted (red). Bottom plot shows evolution of vanes angular position P in degrees (green) and the error signal e as a percentage (purple). For all cases shown $\Delta t = 25$ms.

Figure 6.13 shows the cases from Δt = 500ms to Δt = 2000ms, in which the integrator gain is reduced. It can be seen the opposite effect as before: as the gain decreases, a slower and more sluggish response appears. It can be seen as well that overshoots and oscillations decrease, but a loss in stability for small steps in $\hat{U}_{ref}$ is still observed. The selected configuration Δt = 250ms is again a good trade-off between speed of response and acceptable oscillations in small $\hat{U}_{ref}$ steps.

In conclusion, higher K_i values than the selected one (obtained with more frequently applied corrections; that is, with lower Δt) as well lower K_i values than the selected one (obtained with less frequently applied corrections, or higher Δt) present slower closed-loop responses, with less overshoot and oscillations, than the selected K_i value. It is suggested that this difference in varying K_i by modifying K_c or Δt and the particular well behaviour at Δt = 250ms is a consequence of the deadtime in the response, but a more detailed analysis would be required. Note that the first three cases (Figures 6.12a, 6.12b and 6.12c) present the same flow response, since the sensors sampling frequency limits flow data to a timestep of 25ms.

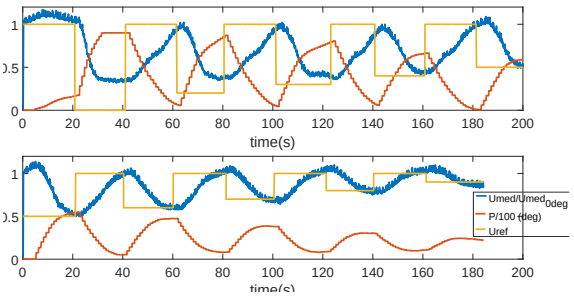

(a) **Response for dt = 1ms.**($K_i = -120$)

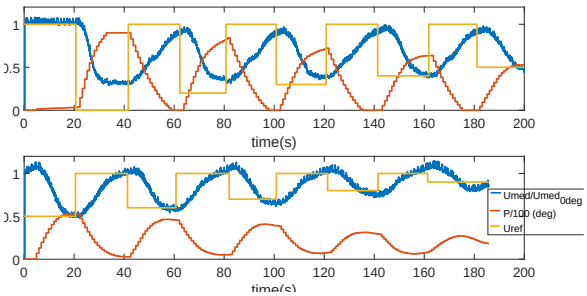

(b) **Response for dt = 10ms.** ($K_i = -12$)

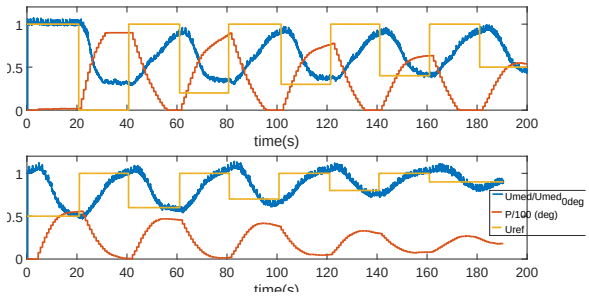

(c) **Response for dt = 25ms.** ($K_i = -4.8$)

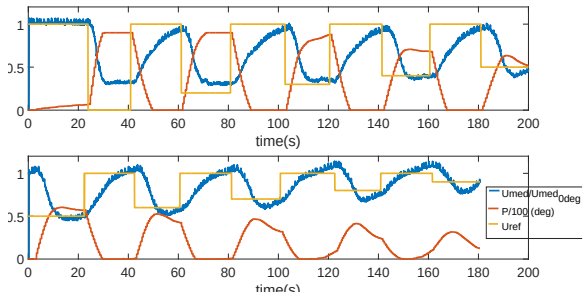

(d) **Response for dt = 50ms.** ($K_i = -2.4$)

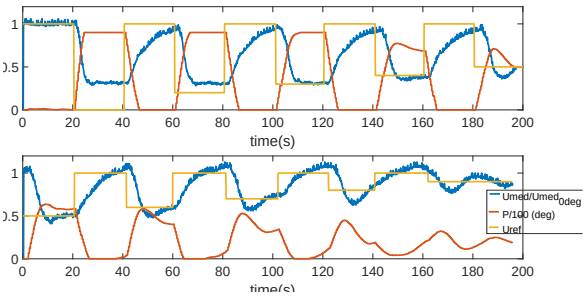

(e) **Response for dt = 100ms.** ($K_i = -1.2$)

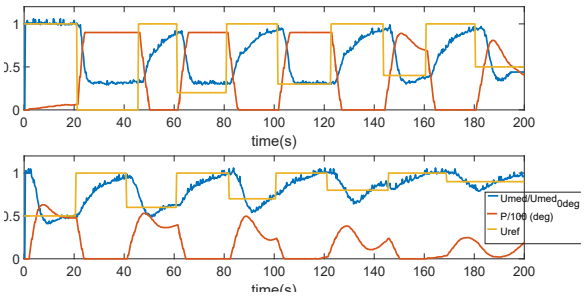

(f) **Response for dt = 250ms.** ($K_i = -0.48$)

Figure 6.12: **Variation of controller timestep Δt, from 1ms to 250ms.** For each figure, top subplot shows the first part of the sequence, and bottom plot shows the second part. It is shown the evolution in time of $\hat{U}_{med}$ (dark blue), for the $\hat{U}_{ref}$ sequence inputted (yellow), as well as the change in vanes angular position in degrees (red), as a fraction of 100, $P/100$. Note that the data shown is as read by the controller, and thus sampled at the rate specified by Δt. For all cases shown $K_c = -0.12$

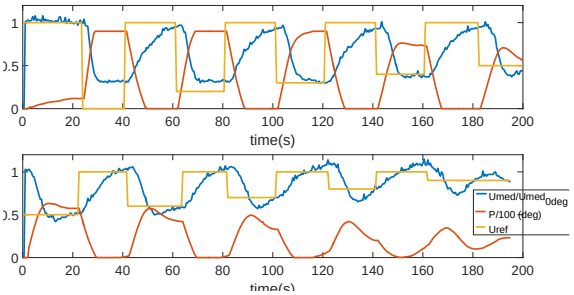

(a) **Response for dt = 500ms**. ($K_i = -0.24$)

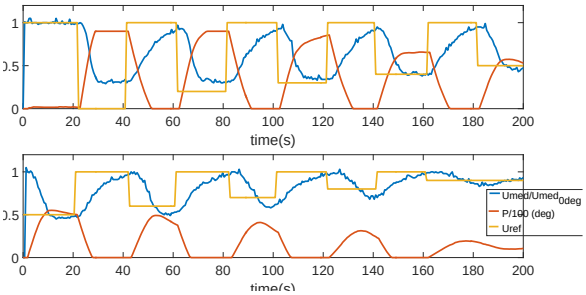

(b) **Response for dt = 600ms**. ($K_i = -0.20$)

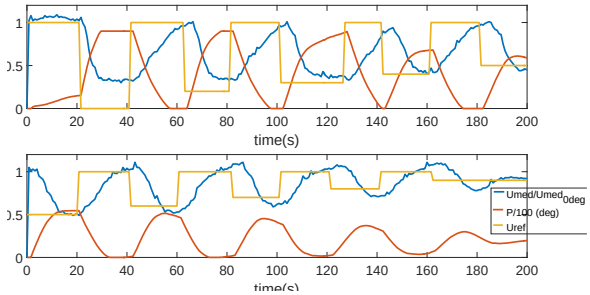

(c) **Response for dt = 800ms**. ($K_i = -0.15$)

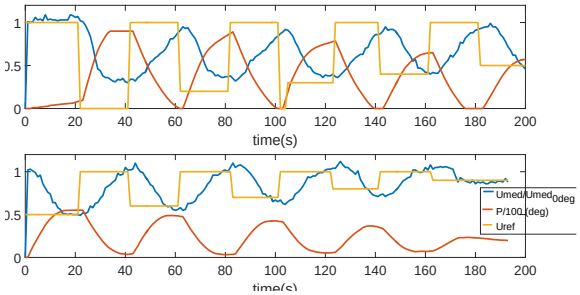

(d) **Response for dt = 1000ms**. ($K_i = -0.12$)

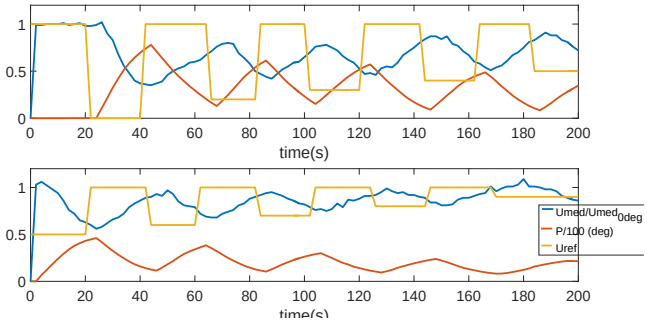

(e) **Response for dt = 2000ms**. ($K_i = -0.06$)

Figure 6.13: **Variation of controller timestep Δt, from 500ms to 2000ms.** For each figure, top subplot shows the first part of the sequence, and bottom plot shows the second part. It is shown the evolution in time of $\hat{U}_{med}$ (dark blue), for the $\hat{U}_{ref}$ sequence inputted (yellow), as well as the change in vanes angular position in degrees (red), as a fraction of 100, $P/100$. Note that the data shown is as read by the controller, and thus sampled at the rate specified by Δt. For all cases shown $K_c = -0.12$.

6.6.3. Varying time constant effect

The response of the system in open and closed-loop is now briefly compared in order to address the varying time constant effect. In closed-loop, data from K_c *variation* analysis for the selected configuration ($\mathbf{K_c = -0.12, dt = 250ms}$) is considered (line colors correspond to the same color shaded regions in Figure 6.14). For a clearer comparison, each step response is referred to its initial state, and thus relative changes $\hat{U}_{med,rel}$ and $\hat{P}_{rel}$ are plotted. These responses are then compared to the ones obtained in open-loop, when inputting the vane angle that the closed-loop controller gets closest to by the end of its $\hat{U}_{ref}$ step. Figure 6.15 shows the comparison between both cases, with input signals plotted on top and responses on the bottom.

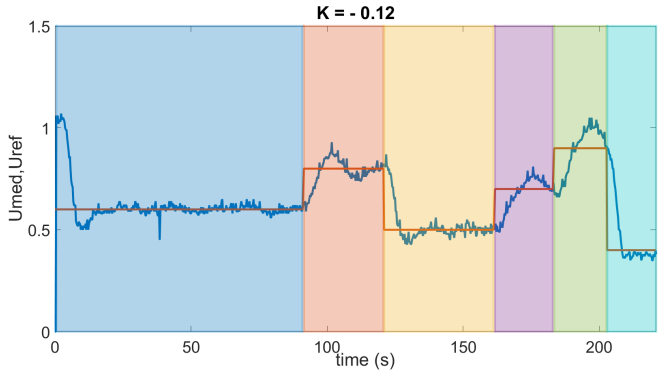

Figure 6.14: **Division into regions for closed-loop open-loop comparison**. Color shaded regions correspond to the same colors for the plots in the following figure.

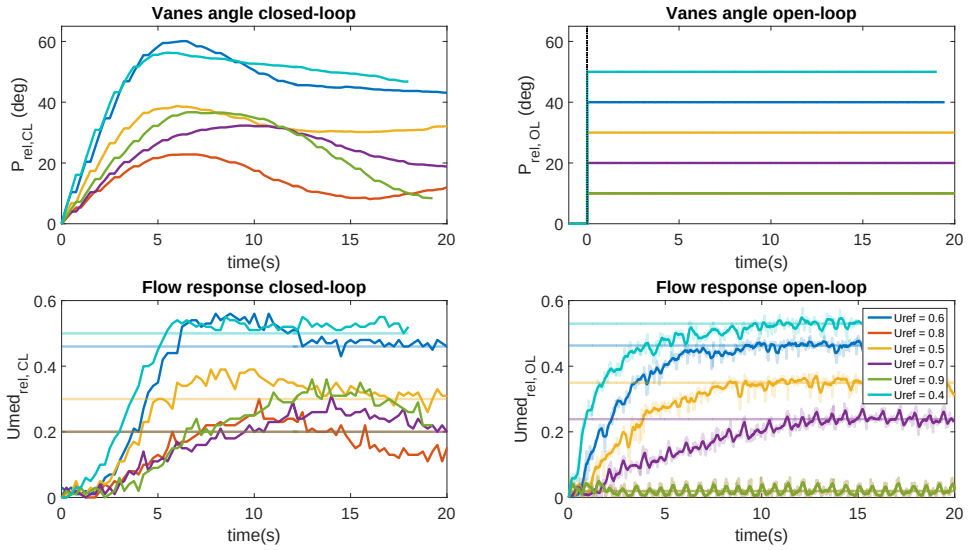

Figure 6.15: **Closed-loop and open-loop comparison**. Plots to the left show the evolution in vanes angle (top) and the flow response (bottom) when using the tuned integral controller; data is taken from the experiments on K_c *variation*. Values are referred to the initial values at the step for a clearer comparison. It should be however reminded that the flow initial state also influences the response. Plots to the right show the open-loop response for an instant turning of the vanes to a position close to the one reached in closed-loop. These responses are referred to an initial fully-open grid state. It can be seen that smaller steps indeed present a larger time constant. The legend and colors shown corresponds to the region considered

For the closed-loop controller it can be seen the effect already mentioned in previous sections: for small steps in $\hat{U}_{ref}$ there is a **loss of damping**. It is suggested that the reason for this loss of damping at large grid transparencies is linked to the increased time constant of the response when inputting small steps in angle at large grid transparencies. This can be seen more clearly by assimilating one of the system's open-loop responses to a 1st order linear system response and modeling our controller in the continuous domain as:

$$C(s) = \frac{K_c}{dt}\frac{1}{s} = \frac{K_i}{s} \tag{6.3}$$

where K_i represents the integral gain. The closed-loop transfer function results (with K and τ the plant's gain and time constant respectively):

$$H_{CL} = \frac{\frac{K_i}{s}\frac{K}{\tau s+1}}{1+\frac{K_i}{s}\frac{K}{\tau s+1}} = \frac{\frac{K_i K}{\tau}}{s^2+\frac{1}{\tau}s+\frac{K_i K}{\tau}} \tag{6.4}$$

Identifying terms of the denominator with the general characteristic equation for a second order system the following relation for the damping ratio is obtained:

$$\zeta = \frac{1}{2}\frac{1}{\sqrt{\tau K_i K}} \tag{6.5}$$

The damping ratio characterizes the shape of the response of a second order system (in terms of existence of overshoot and its oscillatory pattern). For values of ζ within $0 < \zeta < 1$ the response is characterized by the existence of damped oscillations. For this range of ζ values the response is called *underdamped*. For $\zeta = 1$ the response is said to be *critically damped*, the fastest response without overshoot or oscillations. For $\zeta > 1$ the response does not present oscillations but is slow and sluggish. It can be seen from expression 6.5 that a higher value of open-loop time constant τ would yield a lower value of ζ, and thus a loss in stability. It seems reasonable then that for our nonlinear system, when the controller inputs are small steps at high grid transparencies and yield a larger time constant, the damping of the controlled response decreases and an underdamped, oscillatory behaviour appears.

6.7. Conclusions

From the previous analysis in open-loop the system to control has been found non-linear and the flow response very slow. An empirical non-linear controller is proposed for the design of flow profiles, based on a lookup table. To build this lookup table, a closed-loop controller is built with the only purpose of designing reference profiles with zero steady-state error. The simplest architecture that fulfills this requirement is a **discrete integral controller**. As a first step towards building this final closed-loop controller a 1-region closed-loop controller is addressed (this controller is later replicated in the different regions for the 4-region and 8-region approaches). In this chapter the construction of this 1-region closed-loop controller has been discussed.
The manual tuning of the proposed discrete integral controller has raised interesting aspects regarding the system's response both in open and closed-loop. The main design decisions and conclusions are summarized below.

Once the controller architecture is chosen, the design parameter K_i (defined as the ratio between gain K_c and timestep Δt) is **manually tuned** until a satisfactory response is obtained. The manual tuning results yields $K_i = -0.48s^{-1}$, with $K_c = -0.12$ and $\Delta t = 250$ms. The low value of gain is thought to be a consequence of the deadtime. Indeed a deadtime in a linear system introduces instabilities already at low gains, forcing to largely decrease gain values in order to achieve stability, at the expense of a limited overall performance.

The closed-loop response is experimentally analyzed around the selected value of integral gain K_i: first K_c is modified while keeping Δt with the manually tuned value, and then Δt is modified, keeping the manually tuned K_c. For **varying $\mathbf{K_c}$** the response is as expected: higher values of K_i (obtained with a K_c value larger than the selected one) led to a faster response, but more oscillatory and with overshoots, whereas a lower K_i, (obtained with a lower K_c) led to an increasingly slow and sluggish response. However, when **varying Δt** a different trend was observed: higher K_i values than the selected one (obtained with more frequently applied corrections; that is, with lower Δt) as well lower K_i values than the selected one (obtained with less frequently applied corrections, or higher Δt) presented slower closed-loop responses, with less overshoot and oscillations, than the selected K_i value. This effect is surprising and seems to be affected by the way the controller has been implemented; however it is difficult to clarify due to the setup being no longer accessible. More experiments would be required to understand it fully. In any case the selected design

parameters are found as a good trade-off between fast response, and moderate oscillations and overshoots.

Additionally it was observed that in most cases (not only the selected one) the closed-loop response presents **a loss of damping** when inputting small (< 0.3) steps in $\hat{U}_{ref}$, especially when starting from high grid transparency states. This seems to be related to the varying time constant observed in open-loop, which appears larger for small $\Delta\hat{P}$ inputs at high grid transparency states. A suggested improvement to increase damping throughout the whole range of steps in $\hat{U}_{ref}$ would be to design an integral controller with variable integral gain, or to add a derivative term. In any case it is estimated that this effect, for small steps in $\hat{U}_{ref}$ at large grid transparencies will not pose a significant problem, since in the future gusts designs only large differences in $\hat{U}_{ref}$ (> 0.3) are of interest, since these lead to large gradients, which are expected to be more destabilizing.

Taking all of the above into account, the performance of the 1-region controller design is found satisfactory for a proof-of-concept approach: the closed-loop response is stable and fulfills the requirements to proceed with the setup of duplicated controllers in parallel and thus further explore the design of different gust profiles. Since it has been seen that the slow flow response is a large limitation, and it is suspected that a faster flow response may be dependent on the grid transparency change, the influence of this parameter is further looked into in the following chapters.

As for recommendations on future controllers developments, a suggested starting point for a closed-loop approach aiming for fast response would be to design a linear controller based on different operating points; this prioritizes speed of response over guaranteed fulfillment of requirements in the whole operating range. It would be interesting to assess how fast can the response be with this approach, although it is thought it would not be able to adapt to bird fast maneuvers (wingbeat period is in the order of 0.05s; a takeoff maneuver can take around 5 wingbeats). Regarding the development of more sophisticated non-linear controllers (analytic ones, instead of the empirical approach followed here), the extraction of a non-linear model of the system would be the first recommended step. Further recommendations are presented in Chapter 9.

7

Static gusts with 4-region controller

In this chapter the generation of static gusts is looked into. The concept of *Static gusts* is used in this project referring to profile designs that are not translated spanwise with a motion tracking system. Thus in this chapter the objective is to analyze the design of these static gusts, looking into potential differences in convergence across designs. For the design of tailored gust profiles a closed-loop controller based in a 4-region division is used. It consists of four 1-region closed-loop controllers working in parallel, each of them analogous to the one described in Chapter 6, but in this case controlling just two vanes with information gathered from four sensors (see Figure 7.1).

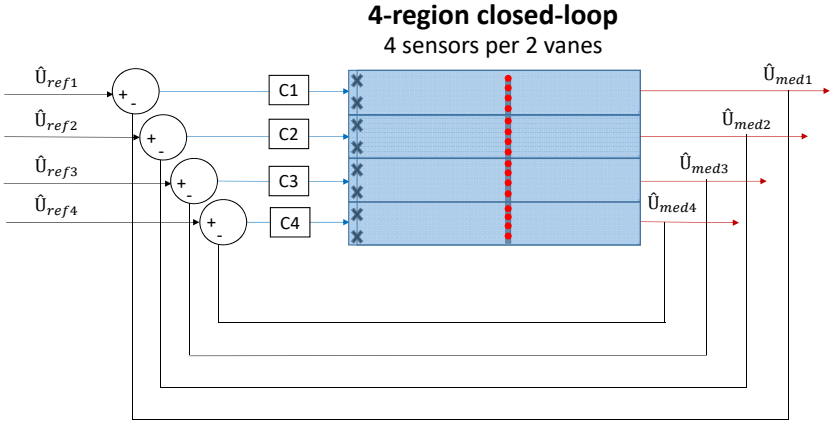

Figure 7.1: **Schematic of 4-region closed-loop controller.** The test section is divided in four regions.The information of the four sensors in each of the regions is fed back to each controller ($C1$, $C2$, $C3$, $C4$) to determine the required position of the vanes in that same region.

7.1. Chapter overview

In this section, the profile types considered for the static gusts analysis, and the parameters used to characterize the grid, are presented. A more specific set of subobjectives is also included, and the chapter structure is outlined.

Analyzed flow profiles

In this chapter the goal is to address differences in convergence across static gust designs. With an aim to adequately distinguish different flow related effects, and in order to easily compare open- and closed-loop approaches, a variety of profiles are analyzed. These result from the combination of the following conditions:

- ***uniform and non-uniform profiles***. Uniform profiles are those with the same $\hat{U}_{ref}$ setting for all the regions. In contrastnon-uniform profiles present different values for $\hat{U}_{ref}$ in their different regions. Comparing both cases the effect of grid transparency reductions differently distributed spanwise is assessed. For non-uniform profiles five types of profiles, deemed relevant for stability experiments, are defined: *step, shear, jet, wake* and *sawtooth* (see Figure 7.2).

- ***closed-loop and open-loop profiles***. Profiles generated in open-loop (i.e., directly inputting the vanes' angle required to obtain a certain profile) and in closed-loop (making use of the 4-region closed-loop controller) are additionally compared. Profiles in open-loop will present a reduction in computational delay, and thus the focus is placed on the physical wind tunnel delays due to grid transparency variation. Conclusions derived from this open-loop analysis are used to explain the physical phenomena contributing to the differences in convergence in the equivalent closed-loop profiles. Closed-loop profiles are obtained with a gradual variation of the grid transparency (vanes move at a rate determined by the controller and the flow response, through the error). In contrast, in open-loop vanes go to the set position instantly. As seen in the previous chapter closed-loop enables to account for the influence of flow deviated from neighbouring regions, but also restricts the speed of the response.

- ***saturated and unsaturated profiles***. Saturated profiles are those in which vanes are positioned either at 0deg or at 90deg; note that vanes angular position has been restricted to the range $P_i \in [0,90]deg$. The main advantage of using saturated profiles is that they are easily repeatable in closed-loop. This is done by forcing saturation of the controller (hence the name), inputting extreme $\hat{U}_{ref}$ values; $\hat{U}_{ref} = 0$ and $\hat{U}_{ref} = 1.5$ are used to force saturation. Using saturated profiles is also a very useful way to compare profiles with the same grid transparency reduction, but differently distributed spanwise. On the other hand, unsaturated profiles are more representative of the capabilities of the 4-regions controller as a wind profile design tool. With unsaturated profiles the aim is to assess the precision in reproducing the reference profile, for different designs. Among these, the ability to generate an homogeneous shear profile (i.e., a flow profile with a uniform velocity gradient, as done in the work by Cekli and van de Water (2010)) would be particularly interesting.

The main flow profile designs considered in this chapter are shown in Figure 7.2.

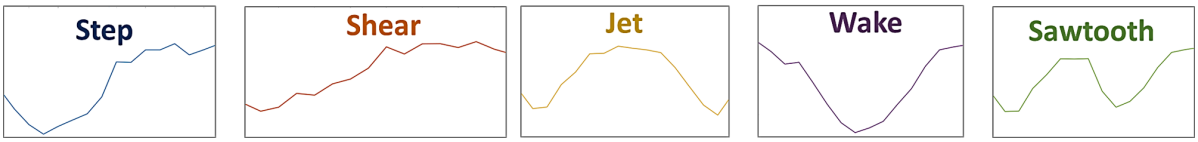

Figure 7.2: **Non-uniform profiles considered for static gusts design.** Adapted from snapshots of real-time measurements of non-uniform profiles

Grid parameters

The parameters used to characterize the grid are its inpiut, vanes angular position **P**, and its grid transparency. The influence of grid transparency on the response has already been mentioned in previous chapters. Since for the static gust designs the initial state is always fully-open grid, a special focus is placed on the grid transparency reduction $\Delta\mathbf{GT_{red}}$, as the amplitude of the reduction from fully-open grid state:

$$\Delta GT_{red} = 100 - GT \qquad (\%); \tag{7.1}$$

Additionally, the parameters grid transparency per region $\mathbf{GT_{reg}}$ and grid transparency reduction per region $\Delta\mathbf{GT_{red,reg}}$ are used, defined as follows (from the grid transparency definition given in Chapter 3, section 3.3):

$$GT_{reg} = \frac{250}{21} + \frac{400}{21}(2 - \sum_{i=1}^{2} \sin\theta_{v,i}) + \frac{150}{21}7 \qquad (\%) \tag{7.2}$$

$$\Delta GT_{red,reg} = 100 - GT_{reg} \qquad (\%); \tag{7.3}$$

where $\theta_{v,i}$ represents each vertical vanes angle, and $\theta_{h,i} = 0$ has been applied, since for all the cases in this chapter $\theta_{h,i} = 0$. Note that the division of the test section in four regions results in two columns of vanes

being assigned to each region.

Definition of subobjectives
It has been mentioned that the goal of this analysis is to address differences in convergence for different gust designs. This goal can be more precisely stated as a set of subobjectives:

- Evaluate the influence of grid transparency reduction in convergence.
- Evaluate the influence of grid transparency reduction differently distributed spanwise in convergence.
- Evaluate the influence of other regions on a region's convergence.
- Compare open-loop and closed-loop performance.
- Evaluate the precision of the tool in designing predefined profiles.

These objectives are matched to the analyzed cases in Table 7.1

Table 7.1: **Static gust objectives and analyzed cases.** Analyzed cases, corresponding to a combination of the profile types described, are dealt with in this chapter in the order presented, from left to right.

Objectives	Uniform OL	Non-uniform Saturated OL	Non-uniform Saturated CL	Non-uniform UNsaturated CL	Non-uniform UNsaturated OL
Effect of ΔGT_{red} magnitude	**X**				
Effect of ΔGT_{red} distribution spanwise		**X**			
Influence of other regions		**X**			**X**
Open-loop vs closed-loop performance		**X**	**X**	**X**	**X**
Precision of the tool in designing predefined profiles				**X**	**X**

Different sets of data are used to address each of the cases shown in Table 7.1. The experimental procedure to obtain them is described in the following section: input settings are defined, as well as the main parameter to compare their performance. Once the experimental procedure is described, results for each case are presented in separate sections, drawing conclusions at the end of each section. After analyzing the different cases, conclusions for the whole analysis are gathered in the last section of the chapter.

7.2. Experimental procedure

The wind sensor array is used in the design of these static gusts, with a sampling frequency of 40Hz and set up as described in Chapter 3. The wind tunnel speed is set to 5m/s and the temperature in the test section is controlled and fixed to 20ºC. A 4-region closed-loop controller is used to reach in each region the desired flow speed value (see Figure 7.1). The controller's parameters for K_c and δt are the ones derived from the tuning in Chapter 6.

Input settings
For the uniform profiles in open-loop, a sequence of steps with amplitudes from 90 to 10deg is inputted, and each P state was kept for 20s (see Figure 5.19a). This set of data has been used in Chapter 6 and Chapter 5; the focus is placed now on the evolution of the profiles in deceleration.

For the non-uniform profiles, the P inputs used (for OL cases) and $\hat{U}_{ref}$ inputs (for CL ones), for each case, are presented in Table 7.2. For each non-uniform case, data is gathered at the wind sensors array for a total sampling time of 90s. Open-loop unsaturated inputs (in vanes angular position P) are determined as the last vane position registered in the corresponding closed-loop unsaturated cases.

Definition of t_{RMS} parameter
In order to compare the convergence performance across all the analyzed cases, a time parameter t_{RMS} is defined. It quantifies the time it takes until the generated profile and the steady state profile have a root-mean-square error $e_{RMS} \leqslant 0.05$. This parameter has already been introduce in subsection 5.4.1; its computation is now described in further detail. It is obtained as follows:

1. *Selection of wind profiles*: the relevant set of continuous wind profiles, each made up of 16 points of data, is selected.

Table 7.2: **Input settings at each region for non-uniform profiles.** Regions are indicated with roman numerals. For open-loop cases inputs are the vanes angular position at each region. For closed-loop cases, inputs are $\hat{U}_{ref}$ at each region.

	Non-uniform profiles 90s at each configuration																
	Open-Loop Input: P (deg)								**Closed-Loop** Input: $\hat{U}_{ref}$								
	SAT				UNSAT				SAT				UNSAT				
	I	II	III	IV	I	II	III	IV	I	II	III	IV	I	II	III	IV	
Step	90	90	0	0	90	90	25	21	0	0	1	1	0.3	0.3	0.7	0.7	Step
Shear	90	90	19.5	0	90	51	18	0	0.25	0.5	0.75	1	0	0.4	0.6	0.8	Shear
Jet	90	0	0	90	90	15	6	78	0	1	1	0	0.4	0.8	0.8	0.4	Jet
Wake	0	90	90	0	1	71	86	6	1	0	0	1	0.8	0.4	0.4	0.8	Wake
Sawtooth	90	0	90	0	71	0	57	0	0	1	0	1	0.6	0.9	0.6	0.9	Sawtooth

2. *Outliers removal*: outliers in sensor measurements are removed. Note that low-cost wind sensors are used to prove their ability to measure mean flow speeds and control gust design; so outliers are expected. First, profiles with extreme sensor readings are identified by evaluating the mean value across the profile. Then, the measurements of the affected sensors are substituted by the average between the measurement of the same sensor one timestep before and one timestep after (timestep between measurements is 0.025s).
3. *Postprocessing*: each 16-measurements profile is resampled, through interpolation, to 32 points. Data is later smoothed using a moving average over the span of one region. For the 4-region controller, this corresponds to eight points after resampling. This is done in order to reduce noise in the data and for a better assessment of the profile evolution and error.
4. *Determination of steady-state profile*: the steady-state profile is defined as the average profile over the last 1/6 of the postprocessed profile samples.
5. *Determination of t_{RMS}*: the parameter t_{RMS} is obtained as the time instant at which the first profile presents a root-mean-square error with the steady-state profile less or equal to 0.05.

For the uniform open-loop profiles $t = 0$ is considered after removing an observed deadtime (already commented in Chapter 5, subsection 5.4.3). For the closed-loop cases $t = 0$ is taken when the controlled loop is started. Particularities and specific parameters derived for each case are discussed in the corresponding *Results* sections.

7.3. Results

The results for each of the cases considered are presented and discussed below. At the end of each section a brief conclusion summarizes the main observations. Main takeaways from all cases are gathered in the final *Conclusions* section.

7.3.1. Uniform profiles in open-loop

The objective with the analysis of uniform profiles in open-loop is to look into the effect of an instant reduction on grid transparency (of different amplitudes), on the profiles' convergence time. To do so, a certain vertical vanes angular position P is inputted and the convergence of the uniform profiles generated downstream is observed.

Flow deceleration mechanisms

In Chapter 5 and 6, the main mechanisms affecting the flow dynamics when the grid transparency is suddenly reduced have been commented. The first one is a deceleration mechanism, from the pressure waves caused when the fluid upstream the active grid is suddenly forced to stop, and from the turbulence induced, causing losses in the flow's kinetic energy. The pressure wave leads to an effect similar to the "water hammer effect" that takes place on incompressible flows when suddenly a valve is closed. As commented in Chapter 5, section 5.5, the intensity of this pressure wave is proportional to the induced change in speed (from the momentum equation applied to the wavefront). A second mechanism is the convective term, or inertia in the flow, which opposes changes in the fluid's state of motion and is larger for a larger change in momentum. Another opposing mechanisms would be due to viscous losses. The Reynolds number in the flow Re gives us an estimation of the importance of inertial forces relative to viscous ones. With fully-open grid $Re = \frac{\rho UL}{\mu} \sim 3.4 \cdot 10^5$, with kinematic viscosity of air $\mu = 1.789 \cdot 10^{-5}$, flow speed $U = 5m/s$ and characteristic length scale (wind tunnel width) $L = 1m$ assuming sea level conditions. The dominant mechanisms are therefore identified to be deceleration, through the pressure waves and turbulent losses, and the convective term. For a larger grid transparency reduction, the strength of the pressure wave will be larger, but also the opposing inertial force, since a larger change in momentum is induced. The aim is to look into how both mechanisms interact and with them explain differences in convergence times with varying grid transparencies reductions.

Convergence of uniform open-loop profiles

To analyze this effect, flow speed data from the open-loop sequence shown in Chapter 5, Figure 5.19a is looked into. A qualitative assessment was presented in that chapter. The focus is now placed on the profiles and on the time to decelerate the flow. The data acquisition is done in two sequences, inputting steps with amplitude 90 to 50deg in the first sequence, and 50 to 40deg in the second one.

When analyzing this set of data in Chapter 5, an increasing deadtime with the position of the step in the sequence was identified. The goal now is to compare the time to decelerate, due to the different decelerating slopes induced by the different step amplitudes. Thus, for a comparable analysis the response is considered when the flow starts to react to the step input ΔP.

To do so, step responses are smoothed over a span of 0.5s (Figure 7.3) and three deadtime estimators are computed, aiming for a close match to the point where the response starts to react. These parameters are a variation of the ones introduced earlier for other sets of data. The results obtained for these parameters, for the different steps are shown in Figure 7.5; further details on their computation can be found in Appendix F. It can be seen indeed that the value in all estimators increases with the position of the step in the sequence; (compare deadtimes for $\Delta P = 50deg(1)$ inputted at the end of the first sequence and $\Delta P = 50deg(1)$ inputted at the beginning of the second one, in Figure 7.5). Thus the deadtime is removed, taking as deadtime value the one given by the slope_{th} parameter (dot marker in Figure 7.3), which seems to match the change of slope more closely. Figure 7.4 shows the $\hat{U}_{med}$ responses with the deadtime value removed.

Taking the profiles from the end of the deadtime until the end of the sample, the t_{RMS} is computed as explained in the previous section. The profiles evolution in time is shown in Figures 7.6 and 7.7, where the steady-state profile and the profile at t_{RMS} are also indicated. Note that the vanes angle sense of rotation also affects the shape of the profiles obtained as mentioned in Chapter 4. The values of the t_{RMS} parameter

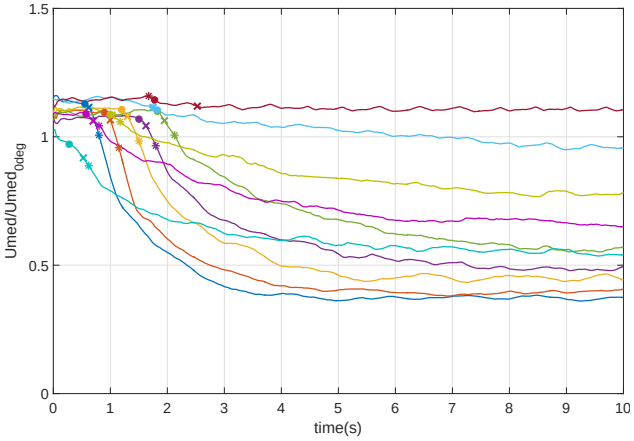

Figure 7.3: **Response $\hat{\mathbf{U}}_{\mathbf{med}}$ to the different steps in P**. Markers correspond to the following points in time: $DB_{2\%}$ (cross) is the point that differs with deadband value in 2%; slope_{th} (dot) is the point that differs with previous one more than a certain threshold, chosen from analyzing the smoothed slope (-0.003); slope_{max} (star) is the point that differs the most with the previous one. More details about these parameters can be found in Appendix F.

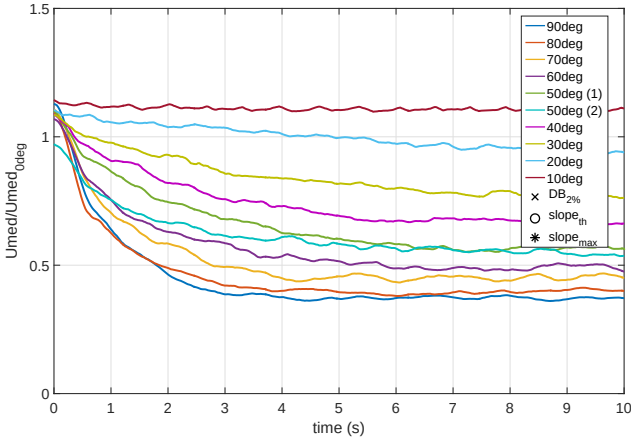

Figure 7.4: **Response $\hat{\mathbf{U}}_{\mathbf{med}}$ to the different steps in P with deadtime removed**. The slope_{th} parameter (dot marker in Figure 7.3) is used as the most representative for the deadtime value.

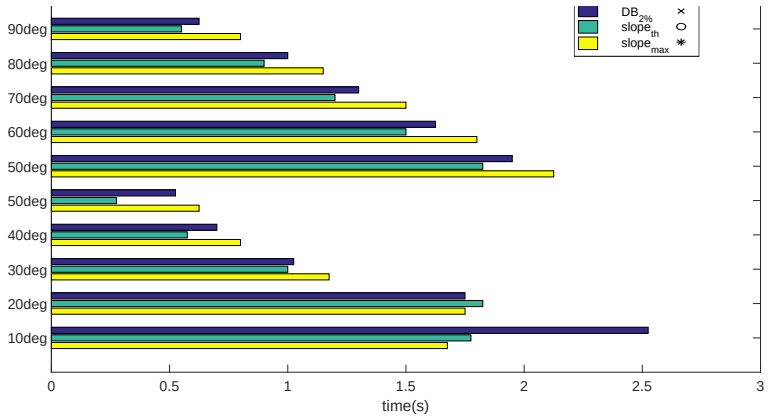

Figure 7.5: **Deadtime parameters for open-loop sequence.** Results are shown for all three parameters used to estimate the deadtime value., for steps in sequence 1 (90deg to 50deg (1)) and 2 (50deg (2) to 10deg). Notice how deadtime value increases with progress in the sequence; compare step 50deg (1) and (2), given at the end of first sequence and at the beginning of the second respectively).

for each case are gathered and compared in Figure 7.8. Note that both $\Delta P = 50deg$ steps, from first and second sequence, give a very similar value for t_{RMS} which confirms an adequate deadtime removal.

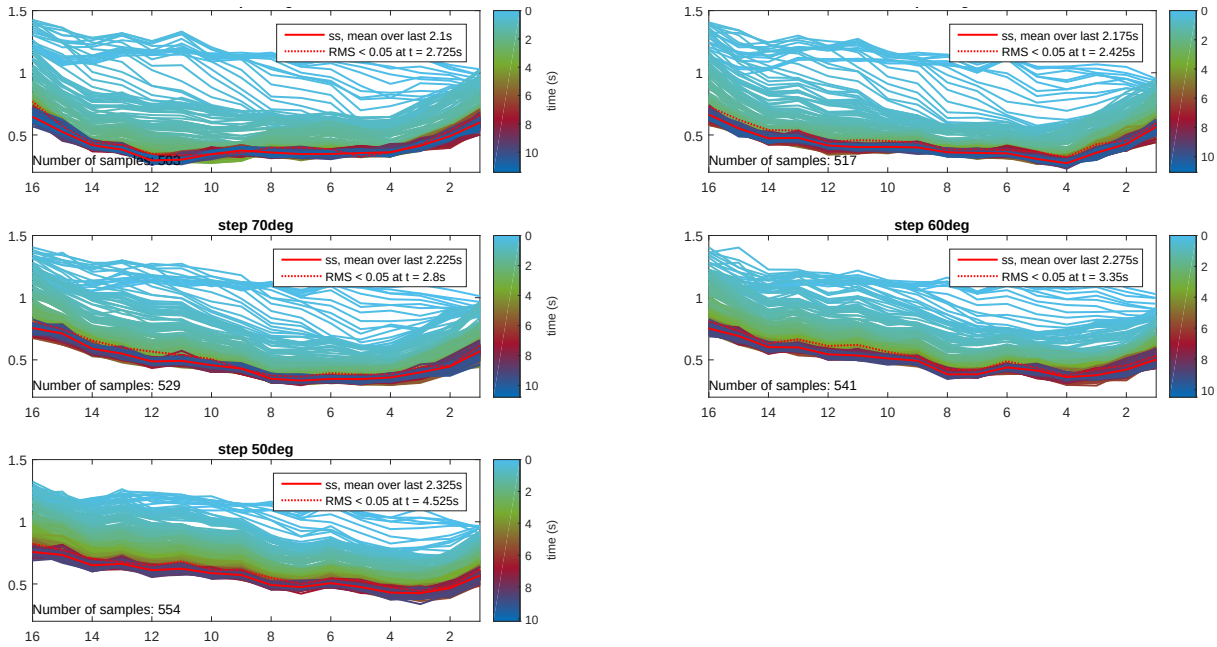

Figure 7.6: **Evolution of uniform flow profiles in open-loop, with deadtime removed,** for the different steps in vanes angles in sequence 1. Profiles result from plotting and smoothing point measurements of $\hat{U} = U/U_{med}$. Sensors' identifying number is indicated in the x-axis; these numbers correspond to their spanwise location as indicated in Figure 3.13. Timestep between profiles: 0.025s

Results in Figure 7.8 show that for initial fully-open grid, the larger the grid transparency change, the faster the convergence to steady-state. This may indicate that the deceleration induced by the pressure wave and turbulence losses due to partial closure of the grid is larger for larger changes in grid transparency. From steps 90 to 50deg, (which correspond to grid transparency reductions from 38% up to 29%), time t_{RMS} increases around 0.46s per 10deg increase in the input step ΔP. For steps from 50deg until 20deg however, t_{RMS} parameter varies -0.1s per 10deg increase in the input step (see trend lines in Figure 7.9). It seems that for these smaller reductions in grid transparency the deceleration is not as effective in overcoming the inertia in the flow at fully-open grid. Note that the step to 10deg induces a very small variation in the flow downstream the grid and its computed t_{RMS} value is 0. This matches the observations on grid's effectiveness of previous chapters.

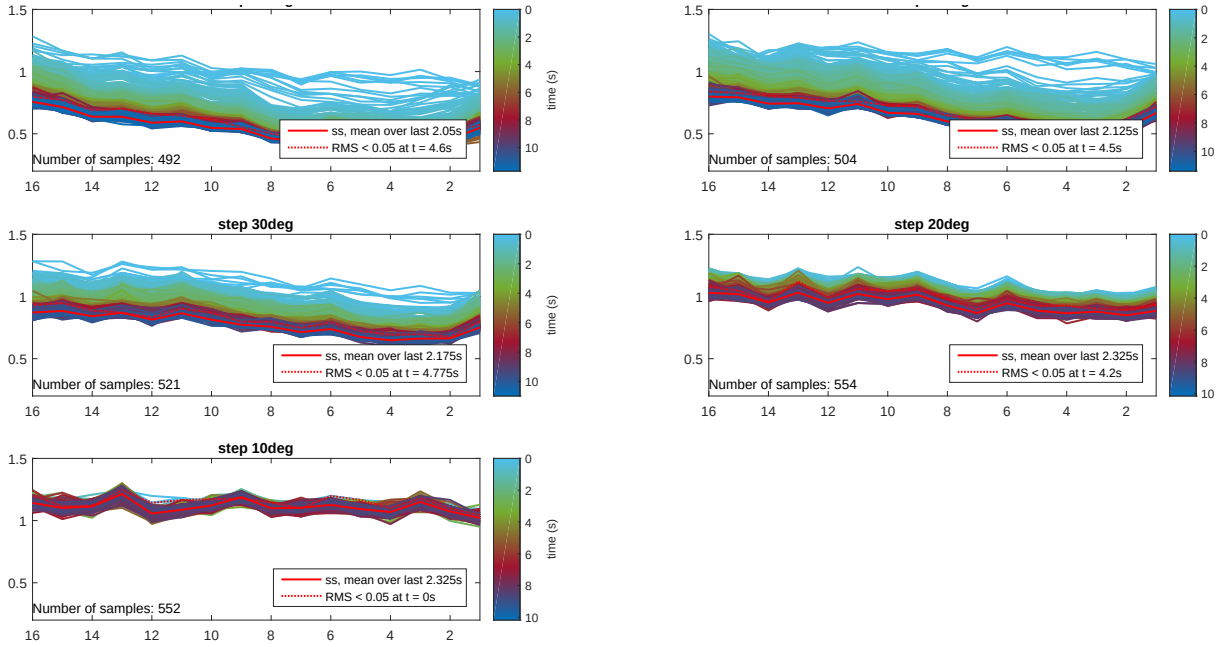

Figure 7.7: **Evolution of uniform flow profiles in open-loop, with deadtime removed,** for the different steps in vanes angles in sequence 2. Profiles result from plotting and smoothing point measurements of $\hat{U} = U/U_{med}$. Sensors' identifying number is indicated in the x-axis; these numbers correspond to their spanwise location as indicated in Figure 3.13. Timestep between profiles: 0.025s

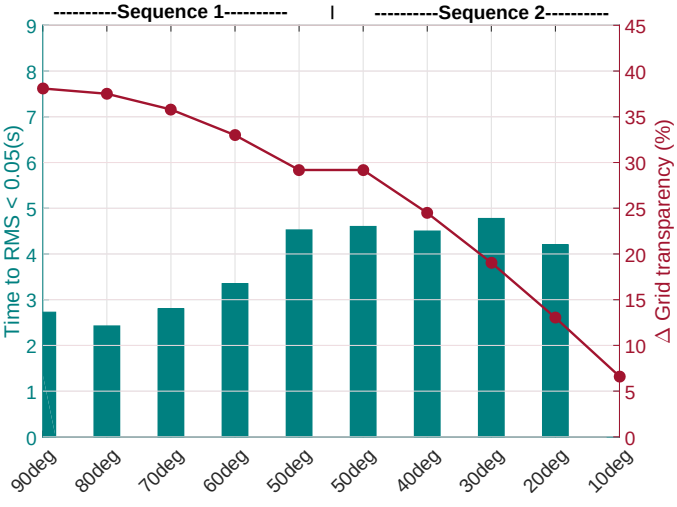

Figure 7.8: **Uniform open-loop profiles convergence and grid transparency reduction.** Parameters t_{RMS} (bars) and grid transparency reduction (red plot) shown for the different input steps ΔP.

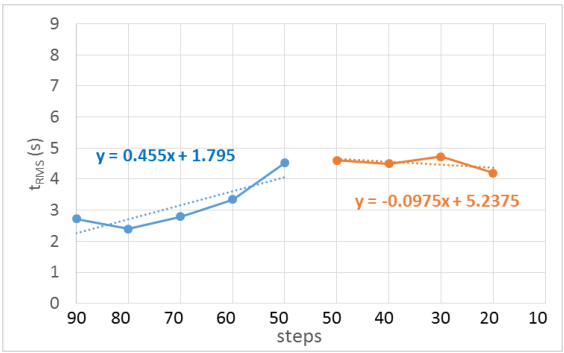

Figure 7.9: **Slope for t_{RMS} values vs grid transparency reduction**

.

7.3.2. Non-uniform saturated profiles in open-loop

Having analyzed the effect of reducing grid transparency uniformly along the span, it is now examined how different spanwise distributions of grid transparency affect the profiles' convergence, and how flow in neighbouring regions affect each other.

Advantages of non-uniform saturated profiles

To vary grid transparency in each region, while keeping the overall grid transparency value constant, vertical vanes in each region are set to one of the two saturated values, 90 or 0deg. It is expected that these angular positions deviate the flow the least (they yield the most symmetrical uniform profiles downstream, see Figure 7.6 and 4.4). They are also convenient for the later comparison between open-loop and closed-loop performance. Five gust designs are defined: *step, shear, jet, wake* and *sawtooth* (see vane angle inputs for each region P_i in Table 7.3). Note that the shear gust design is included for the sake of comparison later with closed-loop performance; its grid transparency reduction is slightly higher than the rest of designs and thus will not be considered for now.

Table 7.3: **Vane angles inputs per region $\mathbf{P_i}$**, for generation of non-uniform saturated profiles (open-loop). The vane angle for *shear* profile, region III is determined from the last value obtained in the corresponding closed-loop (covered in the next section).

	Region I P_I	Region II P_{II}	Region III P_{III}	Region IV P_{IV}
Step	90	90	0	0
Shear	90	90	19.5	0
Jet	90	0	0	90
Wake	0	90	90	0
Sawtooth	90	0	90	0

Deadtime and $\hat{U}_{med}$ evolution

For each gust design data is gathered at the wind sensors array for a total sampling time of 90s. With no sequence in vanes angles applied and with longer sampling times, the deadtimes now are expected to be comparable. Thus removal is not required to compare between the different cases. This can be confirmed in Figure 7.10 which shows the evolution of $\hat{U}_{med}$ in time for the five gust designs considered. Note that for the same overall grid transparency reduction (i.e., for cases *step, jet, wake, sawtooth*), flow response $\hat{U}_{med}$ decelerates to similar values as expected. Additionally, Figure 7.11 shows the evolution of $\hat{U}_{med}$ per region. In both figures it can be seen that the deadtime is similar for all cases. Note as well in Figure 7.10 the comparison between $\hat{U}_{med}$ for the uniform case (red dashed line) and non-uniform ones: the uniform case yielding a slightly higher flow speed downstream may indicate an increased dynamic pressure loss due to turbulent losses in the non-uniform cases.

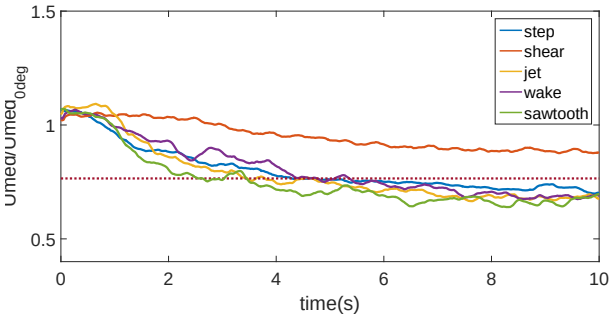

Figure 7.10: **Evolution of $\hat{U}_{med}$** in time for the five gust designs. Dashed line represents the steady-state $\hat{U}_{med}$ value for the same grid transparency reduction as cases *step, jet, wake* and *sawtooth*, applied uniformly across the span. Median computed on raw data and smoothed with moving average over 15s samples.

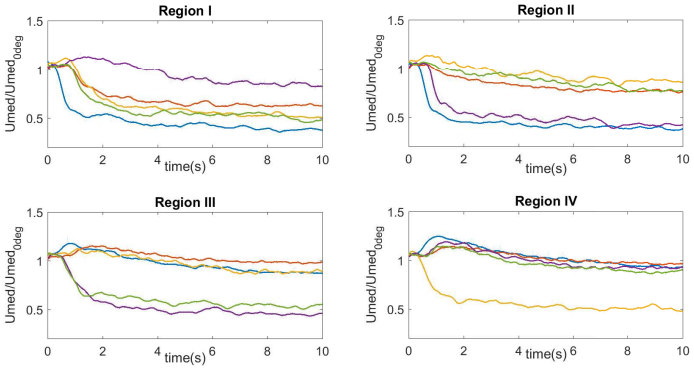

Figure 7.11: **Evolution of $\hat{U}_{med}$ in time, per region** for the five gust designs. Four measurement points are located in each region. Median computed on raw data and smoothed with moving average over 15s samples.

Evolution of profiles in time and t_{RMS}

Figure 7.12 shows the evolution of the flow profiles in time; note that profiles are plotted with a timestep of 1s between them. With the whole sets of profiles the same analysis as before is repeated and the t_{RMS} parameter computed. Results obtained are shown in Figure 7.13.

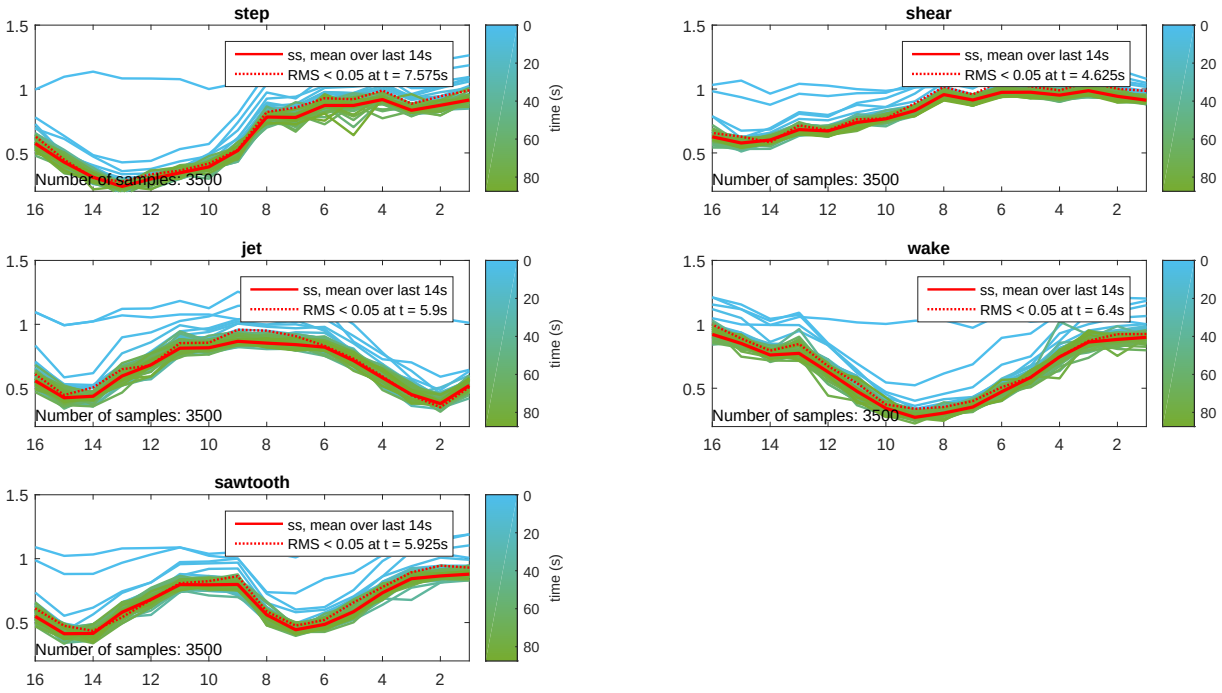

Figure 7.12: **Evolution in time of non-uniform saturated profiles in open-loop**, $\hat{U}_{med}$ vs sensors, smoothed data. Profiles are plotted with a timestep of 1s. Sensors' identifying number is indicated in the x-axis.

From the t_{RMS} results in Figure 7.13 it can be seen that the *shear* profile, which involves a larger change in grid transparency, presents a faster convergence to steady-state. This is in line with what has been seen for uniform profiles. For the rest of the cases with equal overall grid transparency change, convergence times are fairly similar ($\sim 6s$), except for the *step* gust ($7.575s$). This may be due to the flow recirculation and deviation induced by its distribution of blockage spanwise. Indeed, the two slowest configurations, *step* and *wake*, present their maximum blockage regions (i.e., regions with vanes at 90deg) side-by-side. The flow deviated may generate a recirculation region between them that delays convergence. On the other hand, the fastest results come from *jet* and *sawtooth* configurations, which both have their maximum blockage regions not contiguous. The deviation of part of the flow to the neighbouring regions may lead to faster convergence times overall (see Figure 7.14). A more gradual flow deviation spanwise seems to also benefit the *shear* profile (see vanes disposition in *shear* compared to *step* in Figure 7.16); however this case also presents a larger grid transparency reduction. However differences between the analyzed cases are small, and the suggested trend will be verified with the next experiments.

Influence of neighbouring regions

Finally the influence of neighbouring regions is assessed, comparing $\hat{U}_{med}$ values reached per region and assessing the effect on the profiles shape.

Figure 7.15 compares for each profile design, the steady-state $\hat{U}_{med}$ value reached in each region, to the steady-state $\hat{U}_{med}$ value reached for the same grid transparency reduction, but applied uniformly across all the span. For the cases with same overall grid transparency (i.e.,*step, jet, wake, sawtooth*), it can be seen that neighbouring regions "degrade" the flow speed values reached: lower median flow speed values are increased whereas higher ones are decreased.

Regarding the effect of neighbouring regions on the profile shape, Figure 7.16 shows the steady-state profiles for the analyzed cases. First, it can be seen that the *sawtooth* profile (green) matches closely with the *jet*

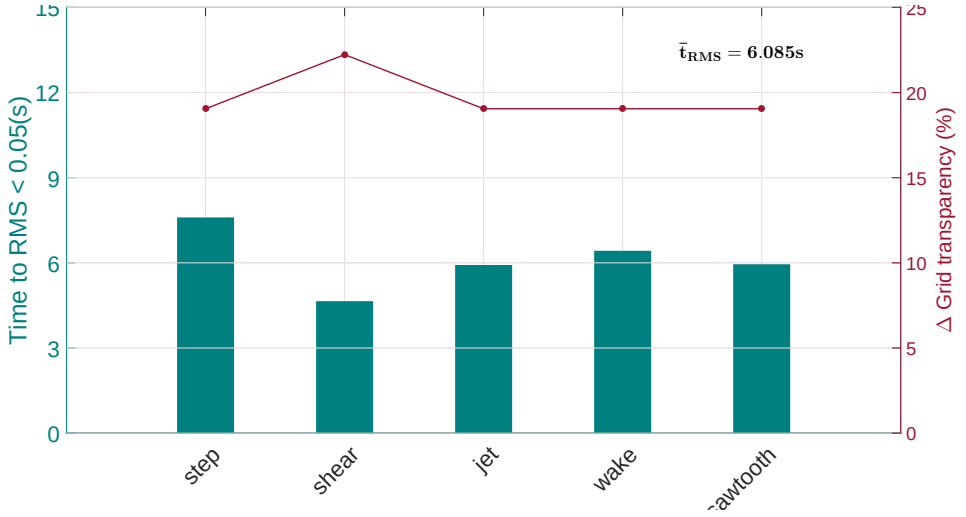

Figure 7.13: **Non-uniform saturated profiles convergence in open-loop, and grid transparency reduction.** Parameter t_{RMS} (bars) and grid transparency reduction (red plot) shown for the different cases analyzed.

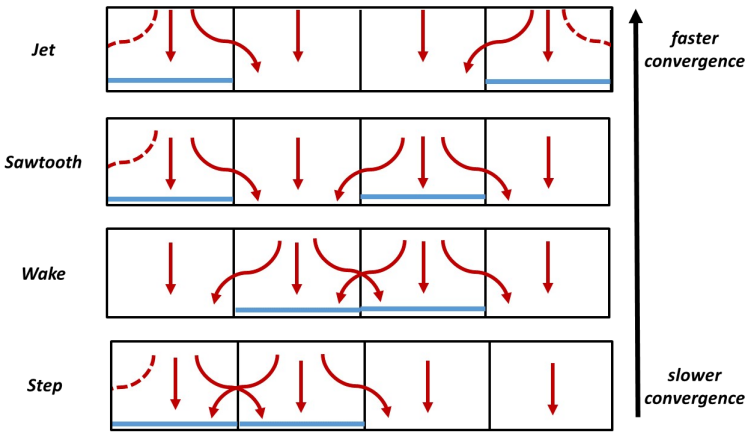

Figure 7.14: **Schematic for the flow deviation in the non-uniform saturated profiles with equal grid transparency reduction**. Horizontal blue lines represent regions with vanes at 90deg. Cases are ordered from top to bottom from faster to slower convergence. Solid red lines represent the direction of the incoming flow; dashed lines represent spillage near the walls.

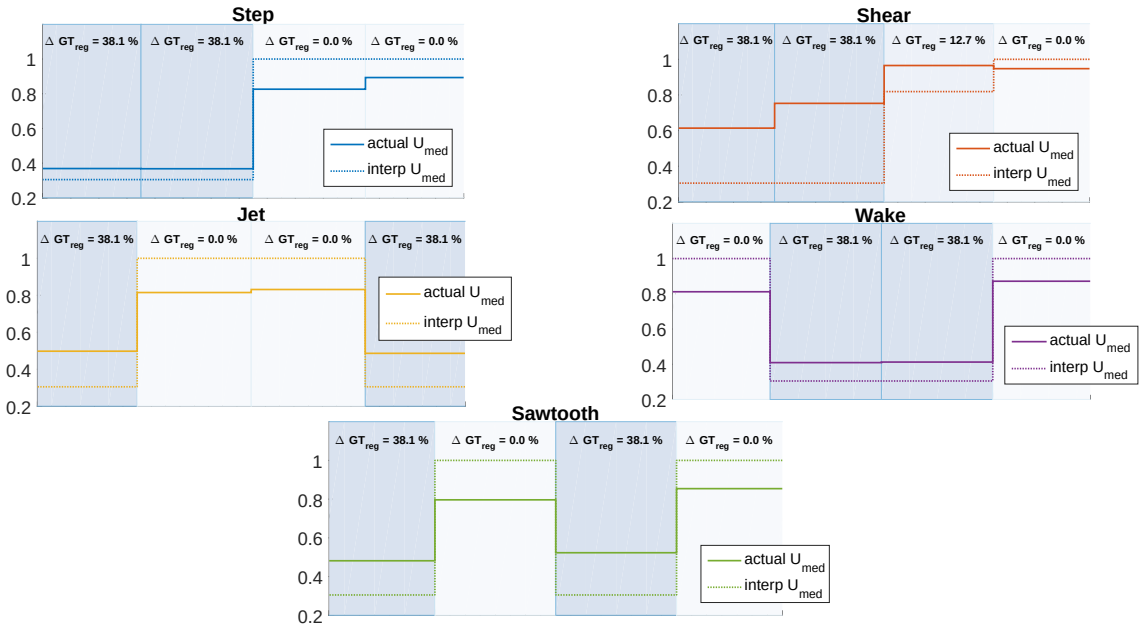

Figure 7.15: **Comparison $\hat{U}_{med}$ and grid transparency reduction ΔGT_{red}%, per region and uniformly spanwise.** Median values per region for each profile design are shown ($\hat{U}_{med}$ vs sensors). Solid line represents $\hat{U}_{med}$ in each region, dashed line represents $\hat{U}_{med}$ value when that same grid transparency reduction is applied uniformly spanwise. The difference between both lines gives an indication of the influence of one region on the neighbouring ones. For each region, grid transparency reduction is indicated on top, and regions are blue-shaded according to their grid transparency. X-axis represents spanwise direction in the test section.

profile (yellow) in regions I and II, and with the *wake* one (purple) in regions III and IV. It seems then that the region of influence of one region extends up to its contiguous one, and that it has almost no impact in further regions. However this seems only true for the saturation positions for the vanes (i.e. vanes at either 0 or 90deg). Analyzing profiles for *step* (blue) and *shear*, it can be seen that, although their vanes' disposition only differ in region III, their profiles don't match as closely. The unsaturated vane angle in region III (at 19.5deg) seems to influence strongly the profile shape in regions I and II for the *shear* case. So it seems that for the saturated cases the region of influence extends up to the contiguous region, but when considering other vane angles the interaction across regions increases, due to flow deviation. This will be looked further into for the case of unsaturated profiles.

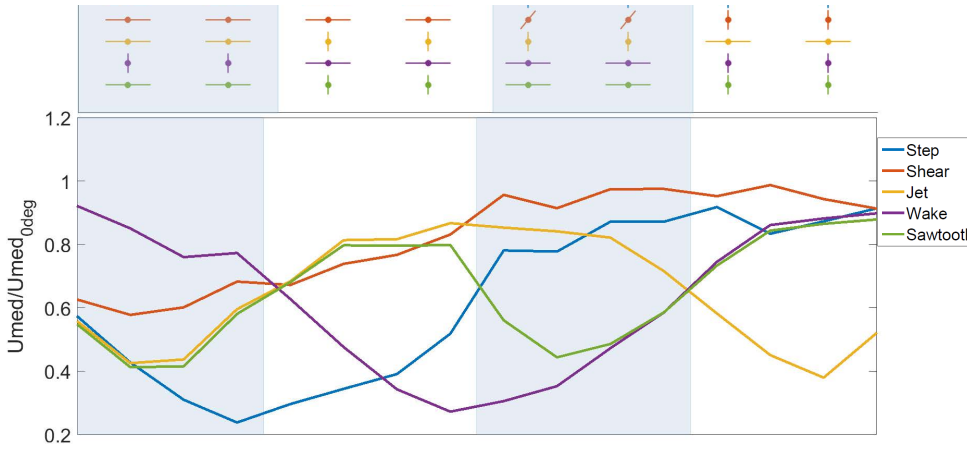

Figure 7.16: **Steady-state profiles for non-uniform saturated profiles in open-loop.** Although the *shear* profile does not present the common grid transparency reduction, it s included for comparison. X-axis represents spanwise direction. Plot on top shows the vanes position for each of the steady-state profiles.

7.3.3. Non-uniform saturated profiles in closed-loop

The open-loop analysis of uniform and non-uniform saturated profiles has given us some insight into the phenomena taking place in the profiles' convergence to steady-state. Now, the same non-uniform saturated profiles are replicated in closed-loop, using the 4-region closed-loop controller. The aim is to address to what extent this phenomena are still relevant for the closed-loop response. Note that in closed-loop the grid transparency reduction occurs gradually, at a rate that depends on the flow response (through the error, 1.08deg per 0.1 error). In contrast in the open-loop case, vanes' angles are instantly changed.

Evolution of profiles in time and profiles for steady-state

Table 7.4 summarizes the inputs used for the 4-region closed-loop controller in the design of the saturated profiles. Saturation is forced by inputting $\hat{U}_{ref} = 0$ and $\hat{U}_{ref} = 1.5$. The evolution of the flow profiles for each case is shown in Figures 7.18 to 7.22, where the left graph shows the raw data from the 16 sensors array, and the right graph the smoothed data (as described in section 7.2). The timestep between plotted profiles is 1s. The steady-state profile and the profile at $t = t_{RMS}$ are also shown (red solid and dashed line respectively). The procedure to determine the t_{RMS} parameter was repeated for this set of data. As an additional information, Figure 7.17 shows some more details regarding the steady-state profile determination.

Table 7.4: $\hat{U}_{ref}$ inputs per region for the generation of non-uniform saturated profiles (open-loop)

	Region I $U_{ref,I}$	Region II $U_{ref,II}$	Region III $U_{ref,III}$	Region IV $U_{ref,IV}$
Step	0	0	1	1
Shear	0.25	0.5	0.75	1
Jet	0	1	1	0
Wake	1	0	0	1
Sawtooth	0	1	0	1

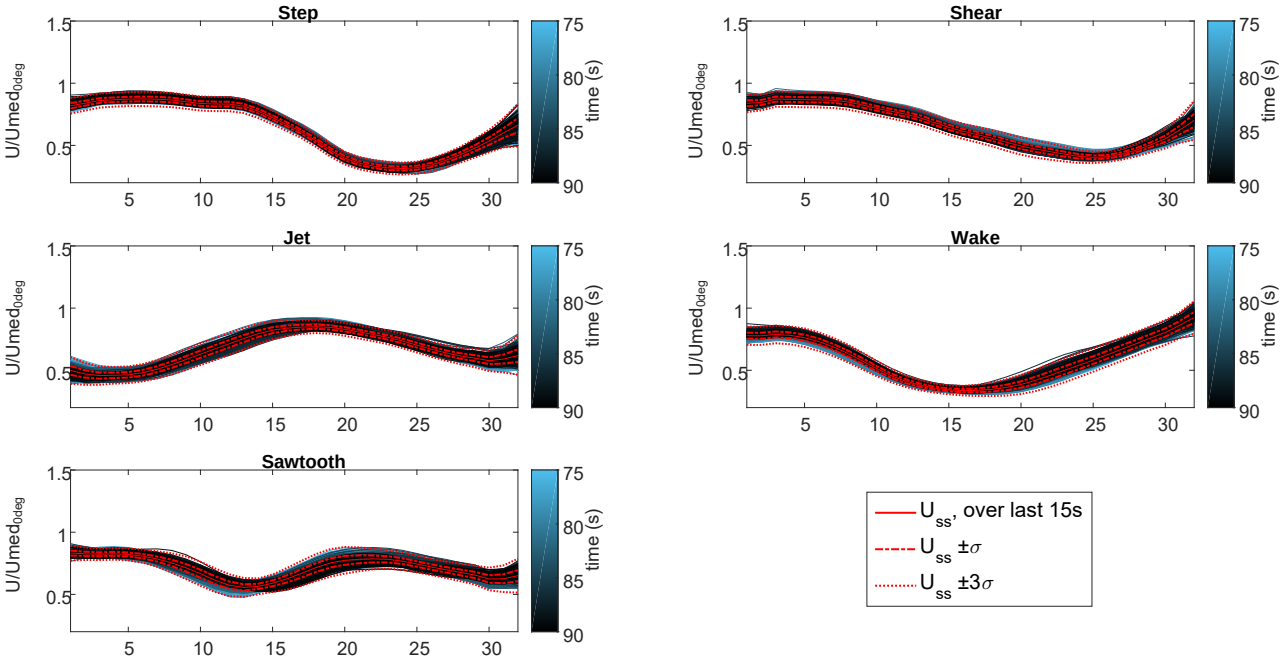

Figure 7.17: **Profiles for steady-state profile determination, for non-uniform saturated profiles in closed-loop.** The last 15s over a sample of 90s are considered to compute the steady-state profile.

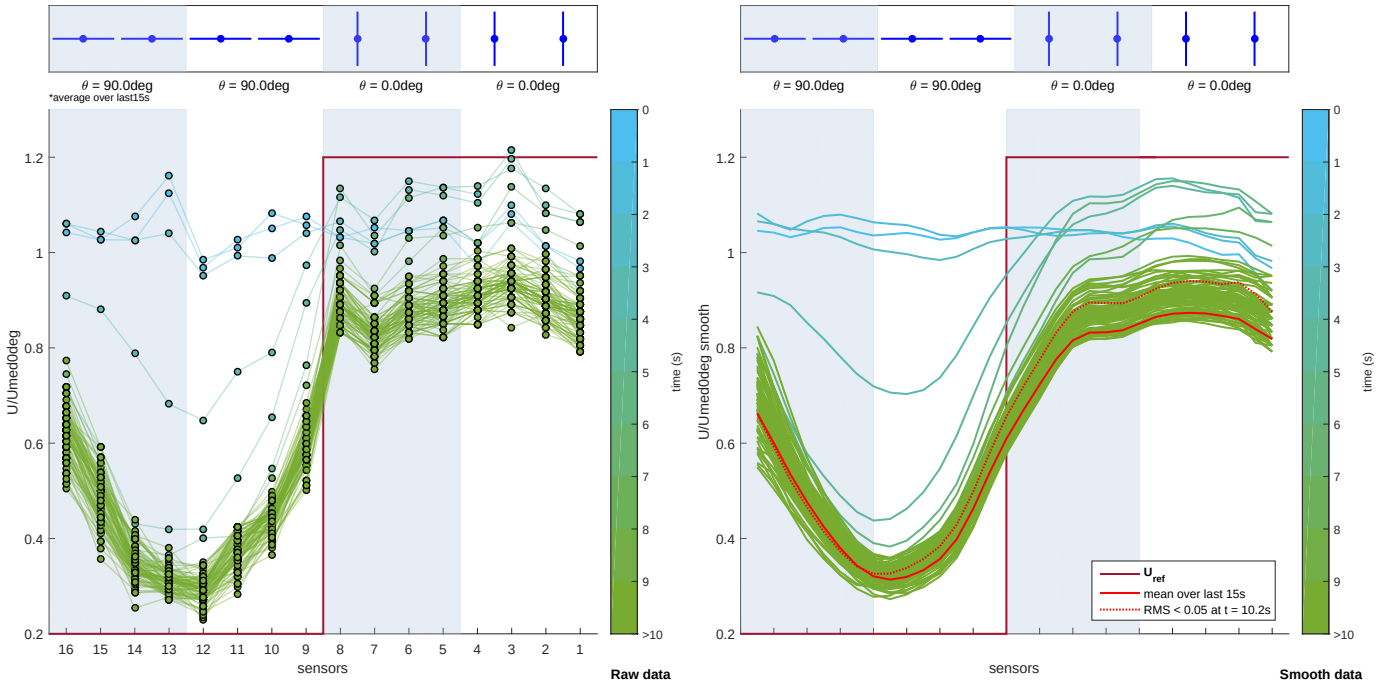

Figure 7.18: **Closed-loop saturated step profile evolution in time.** For a clearer visualization in the figure $\hat{U}_{ref} = 0$ and $\hat{U}_{ref} = 1.5$ have been plotted as $\hat{U}_{ref} = 0.2$ and $\hat{U}_{ref} = 1.2$ respectively.

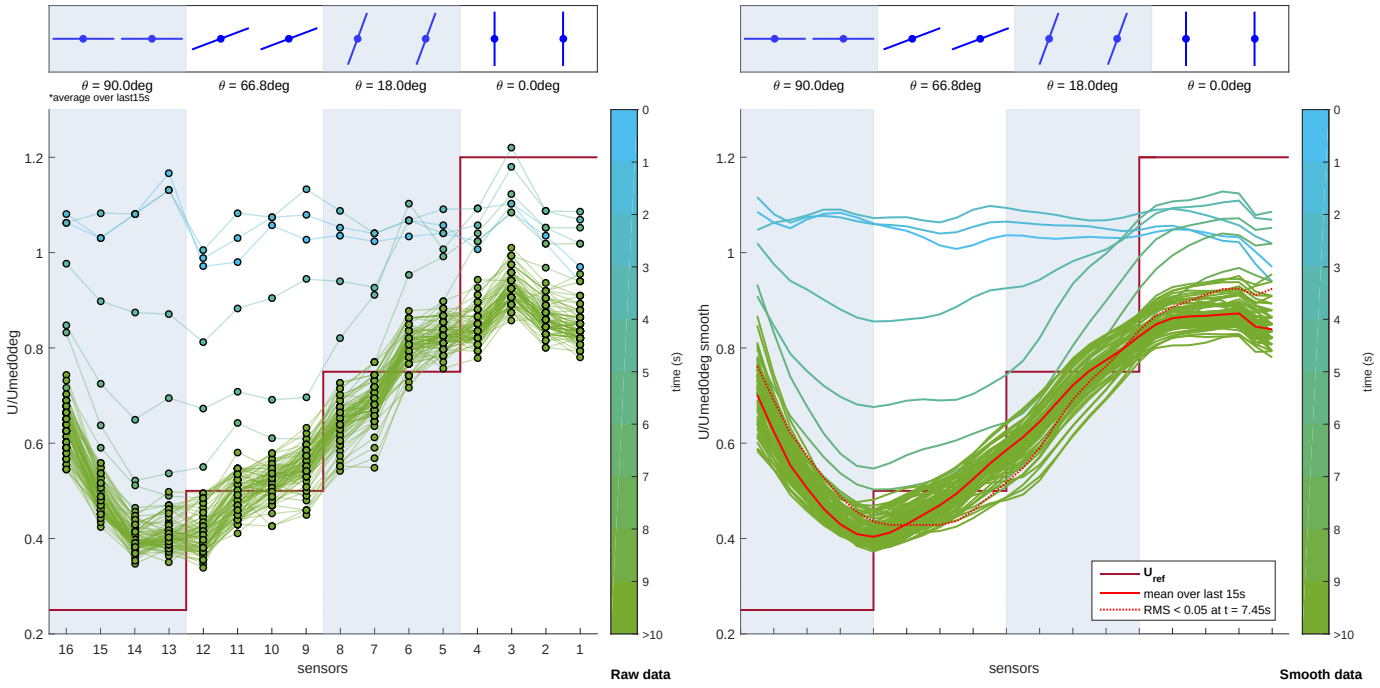

Figure 7.19: **Closed-loop saturated shear profile evolution in time.** For a clearer visualization in the figure $\hat{U}_{ref} = 0$ and $\hat{U}_{ref} = 1.5$ have been plotted as $\hat{U}_{ref} = 0.2$ and $\hat{U}_{ref} = 1.2$ respectively.

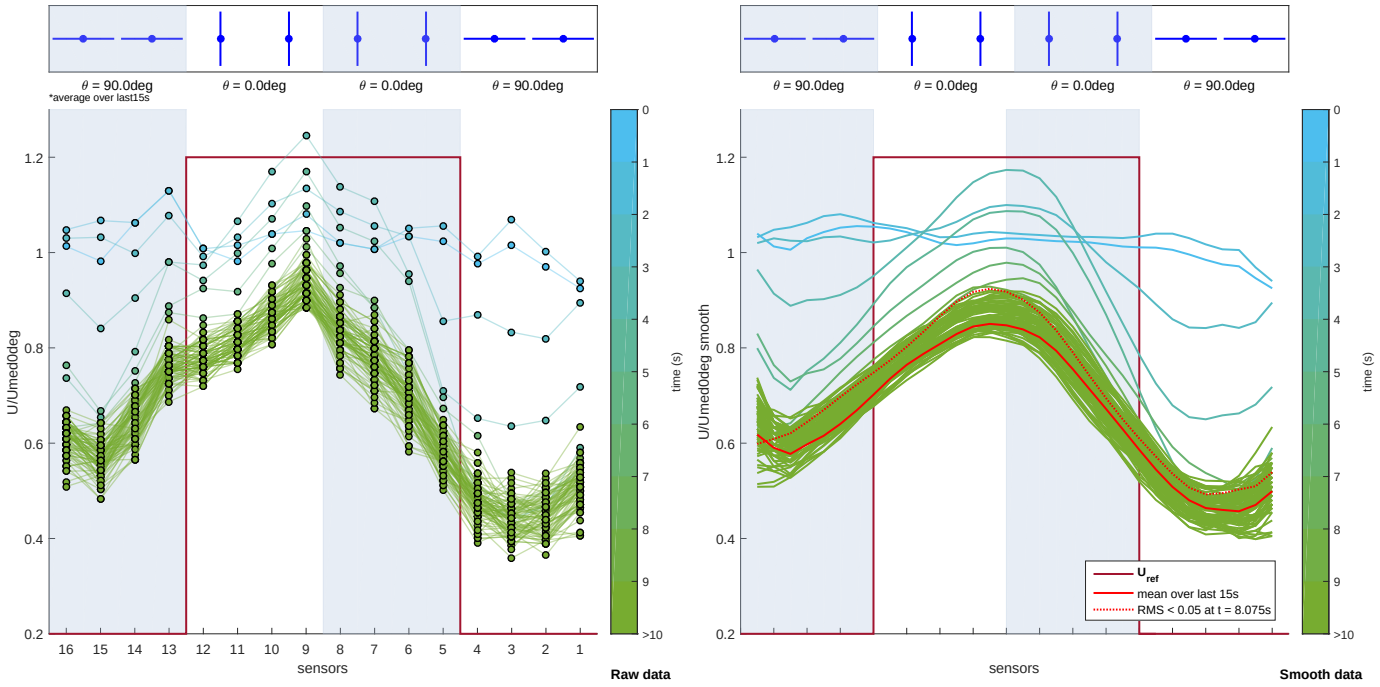

Figure 7.20: **Closed-loop saturated jet profile evolution in time.** For a clearer visualization in the figure $\hat{U}_{ref} = 0$ and $\hat{U}_{ref} = 1.5$ have been plotted as $\hat{U}_{ref} = 0.2$ and $\hat{U}_{ref} = 1.2$ respectively.

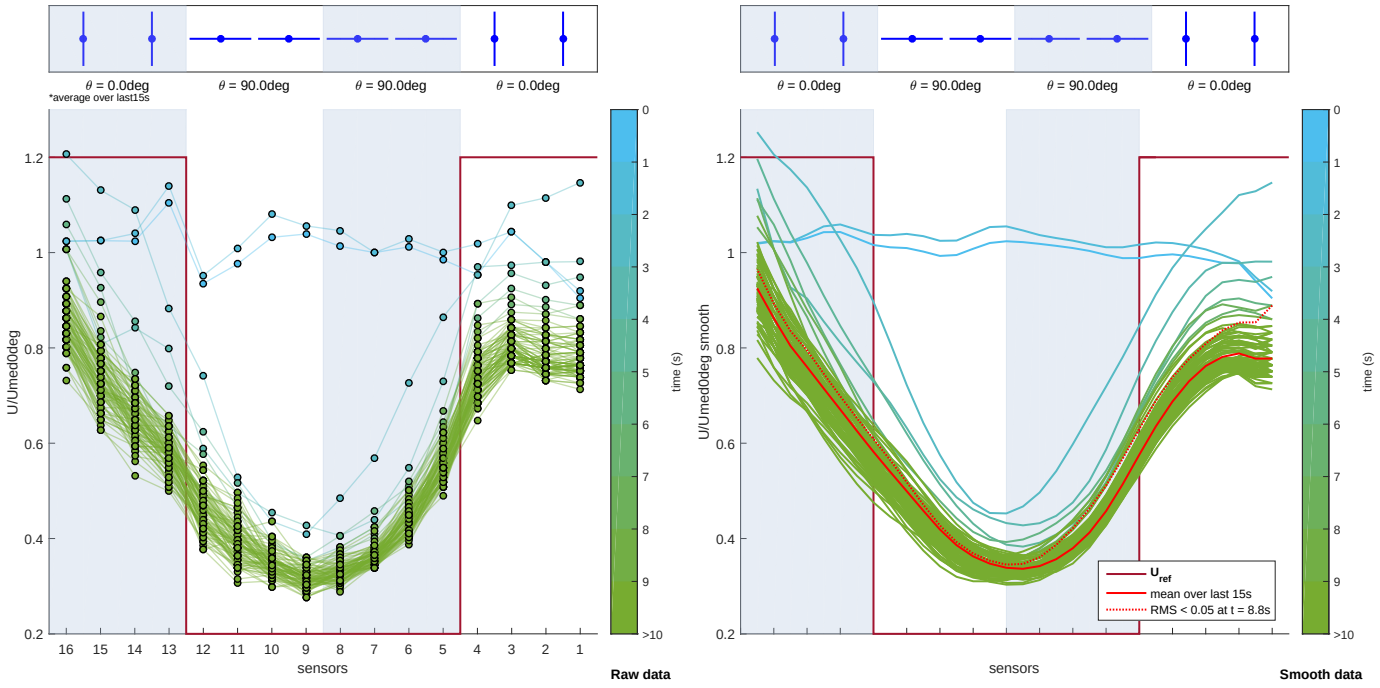

Figure 7.21: **Closed-loop saturated wake profile evolution in time.** For a clearer visualization in the figure $\hat{U}_{ref} = 0$ and $\hat{U}_{ref} = 1.5$ have been plotted as $\hat{U}_{ref} = 0.2$ and $\hat{U}_{ref} = 1.2$ respectively.

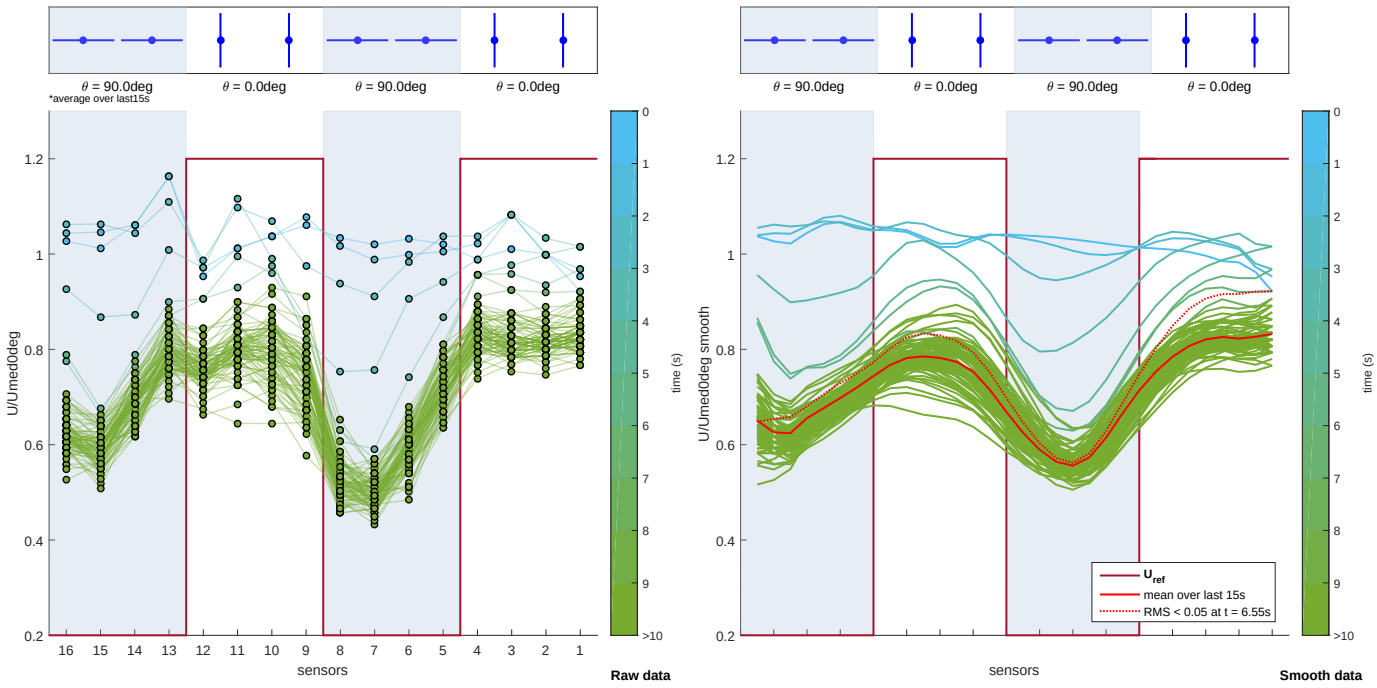

Figure 7.22: **Closed-loop saturated sawtooth profile evolution in time.** For a clearer visualization in the figure $\hat{U}_{ref} = 0$ and $\hat{U}_{ref} = 1.5$ have been plotted as $\hat{U}_{ref} = 0.2$ and $\hat{U}_{ref} = 1.2$ respectively.

Results for t_{RMS} and comparison with open-loop

From the t_{RMS} results shown in Figure 7.23 it can be seen a similar trend to the one observed for the open-loop cases, but differences across gust types are more abrupt. Whereas in the open-loop case, *sawtooth* and *jet* profiles presented similar t_{RMS} values, in the closed-loop case the *sawtooth* profile converges 25% faster. Again *step* presents the longest time to steady-state convergence. This makes sense considering that the controller speed is a function of the error, and thus it follows the flow response. It can be concluded that the main mechanism explaining differences in t_{RMS} in closed-loop saturated profiles is also flow recirculation and deviation, as in the equivalent open-loop cases.

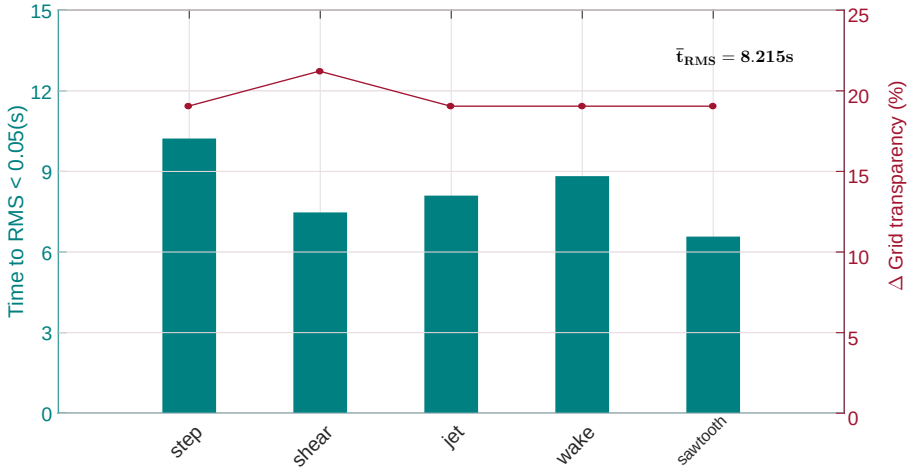

Figure 7.23: **Non-uniform saturated profiles convergence in closed-loop, and grid transparency reduction.** Parameter t_{RMS} (bars) and grid transparency reduction (red plot) shown for the different cases analyzed.

A comparison with open-loop t_{RMS} results, for the same gust designs is shown in Table 7.5. Cases of same grid transparency average $\bar{t}_{RMS} = 8.4s$ (including the *shear* profile $\bar{t}_{RMS} = 8.215s$). An average increase of 36% is observed in t_{RMS}, in closed-loop with respect to open-loop.

Table 7.5: Comparison of performance for non-uniform saturated profiles, in open-loop and closed-loop

Increase in t_{RMS}, for CL with respect to OL
34.65 %
61.08 %
36.86 %
37.50 %
10.55 %

7.3.4. Non-uniform unsaturated profiles in closed-loop

The design of unsaturated profiles in closed-loop is now assessed, using the 4-region closed-loop controller. The objective is to evaluate the capabilities of the tool and the error with respect to the reference settings. The same gust types analyzed until now are reproduced, now with unsaturated values (i.e., with input values that do not force the vanes' angles saturation). Only one $\hat{U}_{ref}$ input value forced saturation in region I, for the *shear* profile, aiming to reproduce a sharp slope. All the input $\hat{U}_{ref}$ values are summarized in Table 7.6. Figures 7.25 to 7.29 show the wind profiles evolution in time as in the previous section. As before, the profiles used to define the steady-state profile are shown in Figure 7.24.

Table 7.6: $\hat{U}_{ref}$ inputs per region for the generation of non-uniform unsaturated profiles (closed-loop)

	Region I $U_{ref,I}$	Region II $U_{ref,II}$	Region III $U_{ref,III}$	Region IV $U_{ref,IV}$
Step	0.3	0.3	0.7	0.7
Shear	0	0.4	0.6	0.8
Jet	0.4	0.8	0.8	0.4
Wake	0.8	0.4	0.4	0.8
Sawtooth	0.6	0.9	0.6	0.9

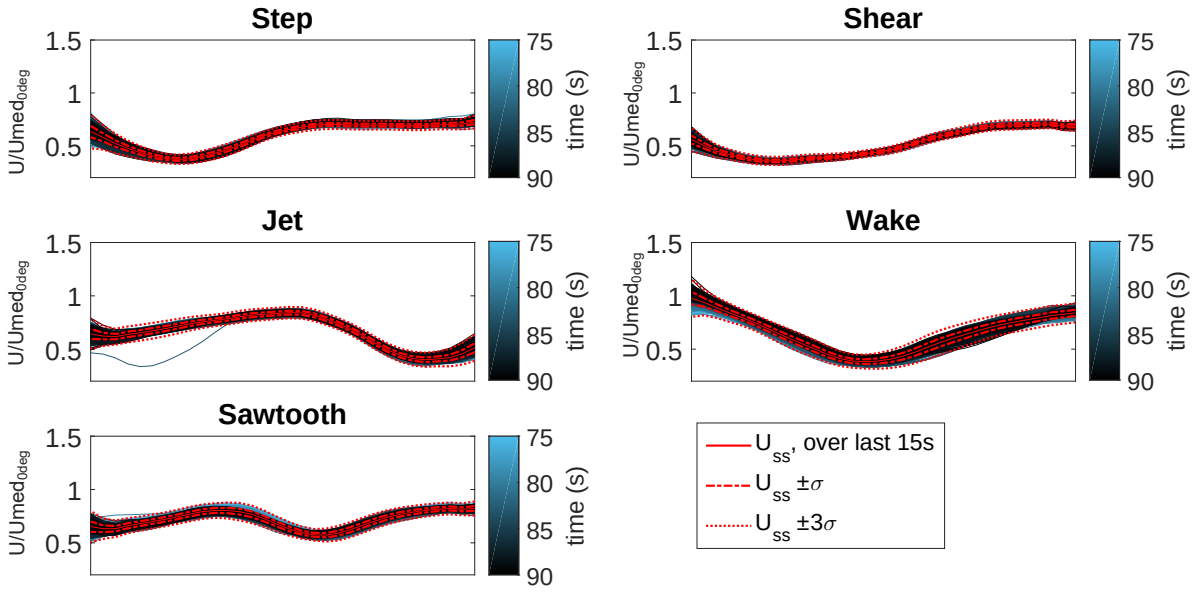

Figure 7.24: **Profiles for steady-state determination, for closed-loop unsaturated profiles.** The last 15s over a sample of 90s are considered to compute the steady-state profile.

The analysis for determining the time parameter t_{RMS} is carried out for this set of profiles, and results are presented in Figure 7.30.

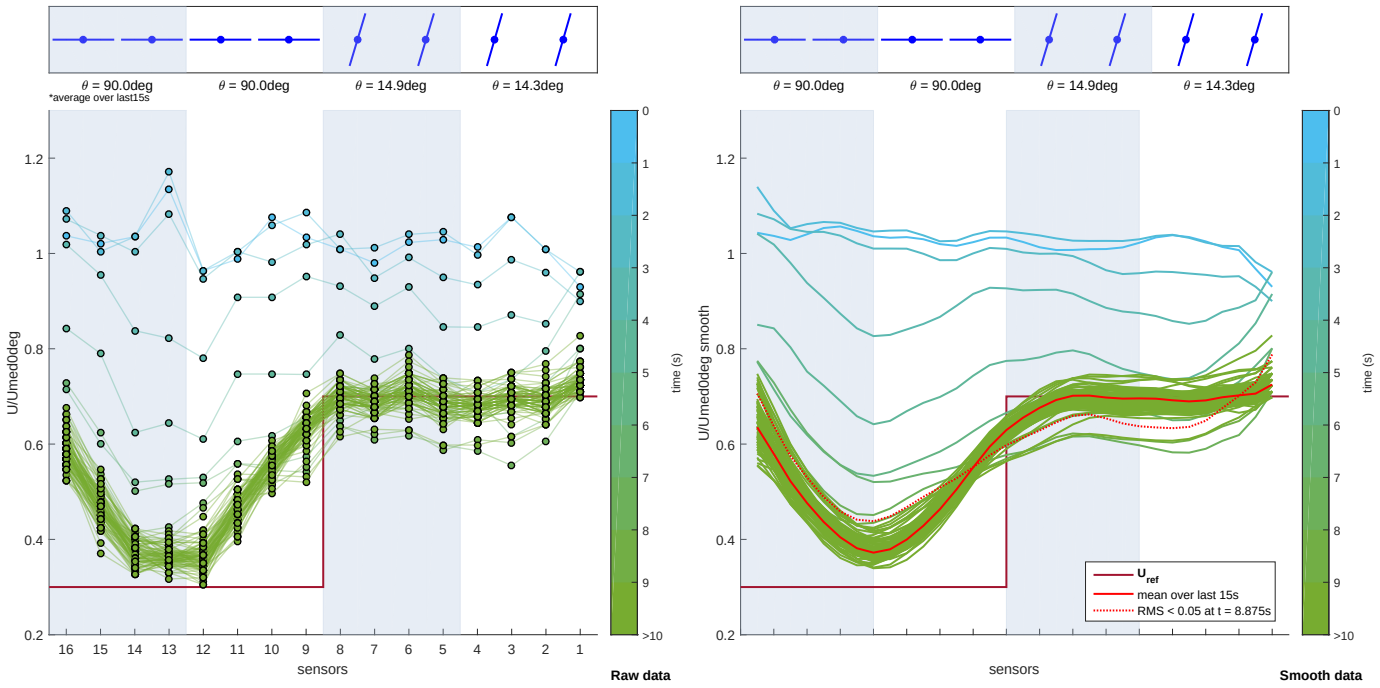

Figure 7.25: **Closed-loop unsaturated step profile evolution in time.**

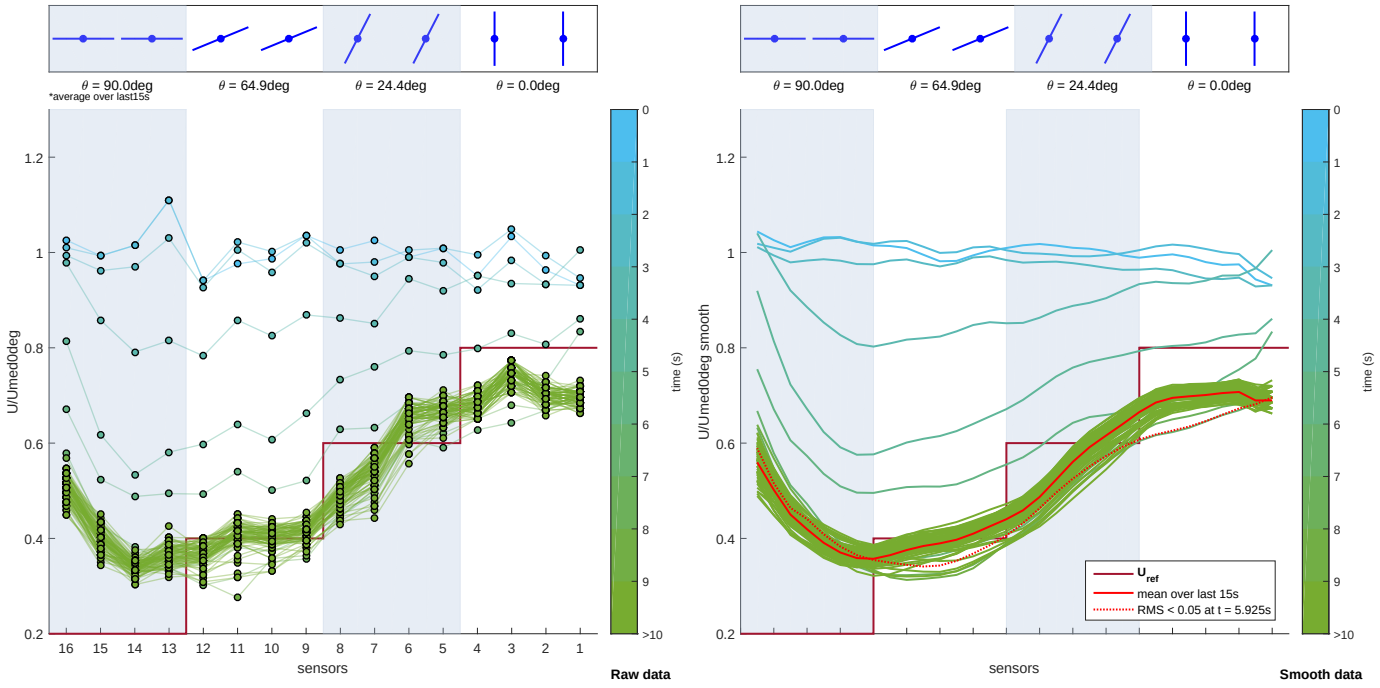

Figure 7.26: **Closed-loop unsaturated shear profile evolution in time.**

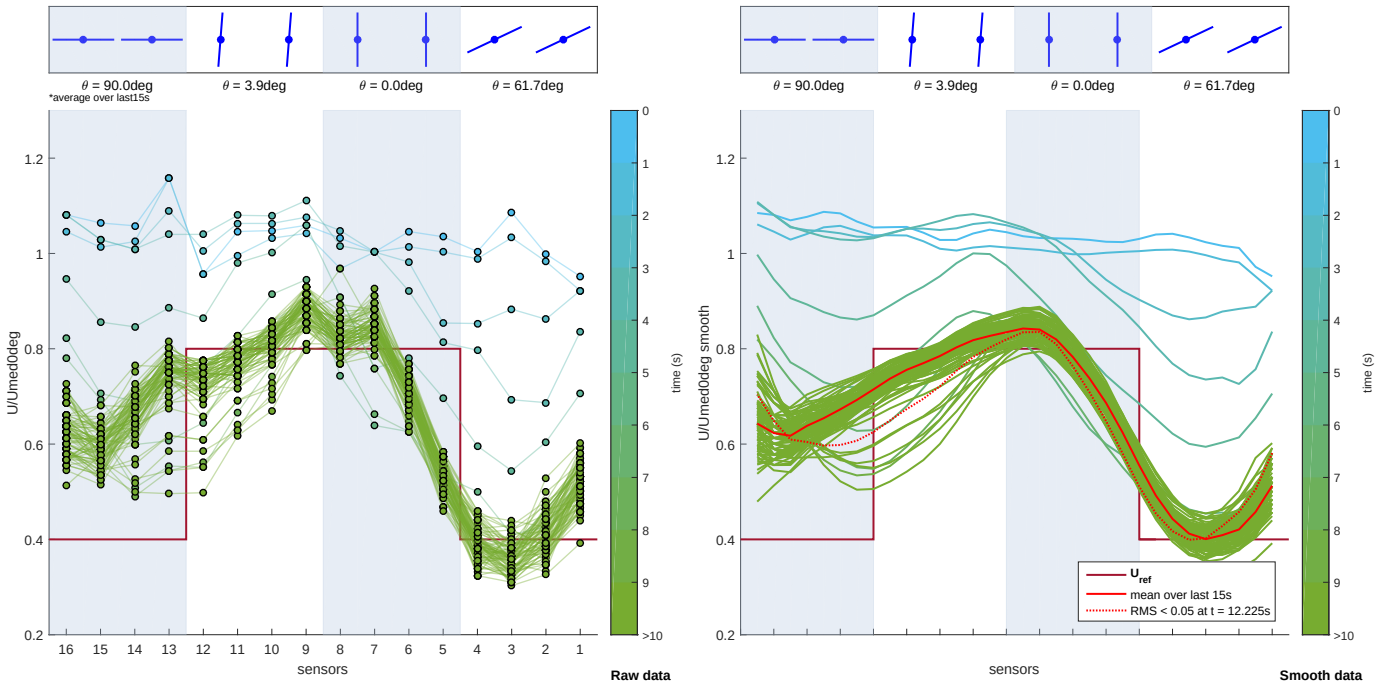

Figure 7.27: **Closed-loop unsaturated jet profile evolution in time.**

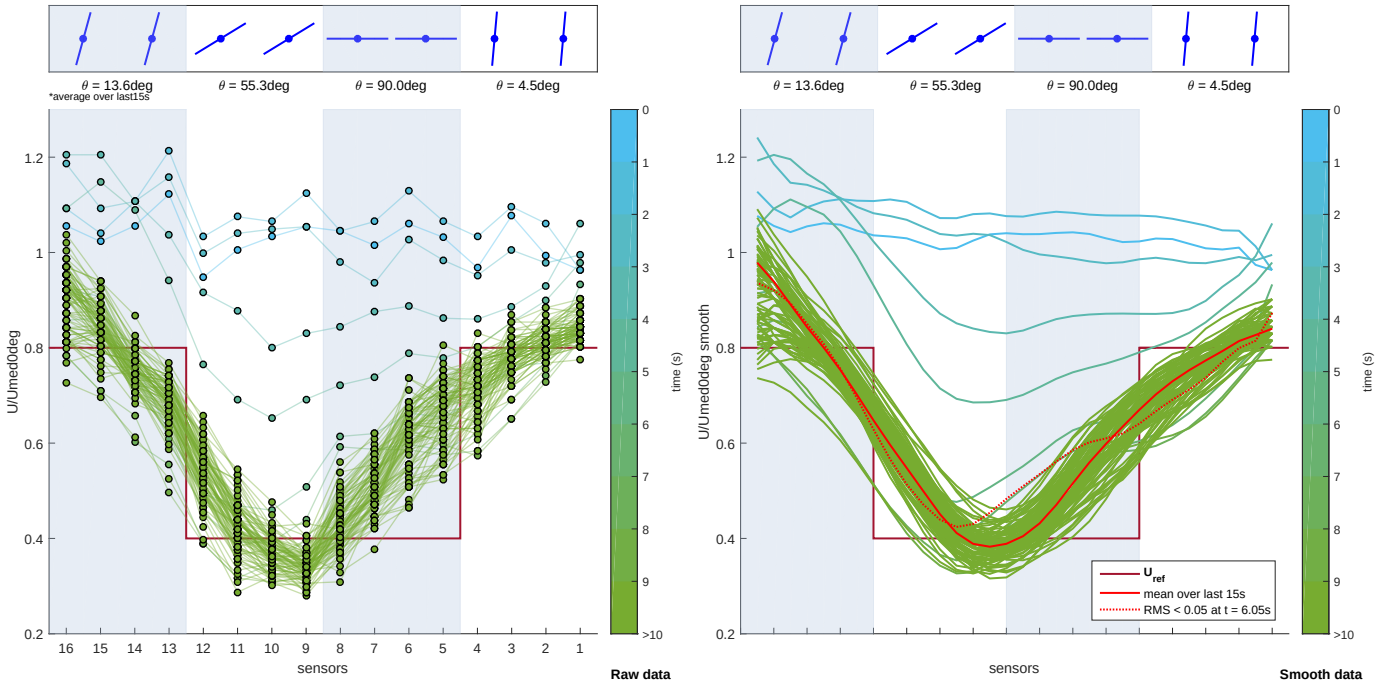

Figure 7.28: **Closed-loop unsaturated wake profile evolution in time.**

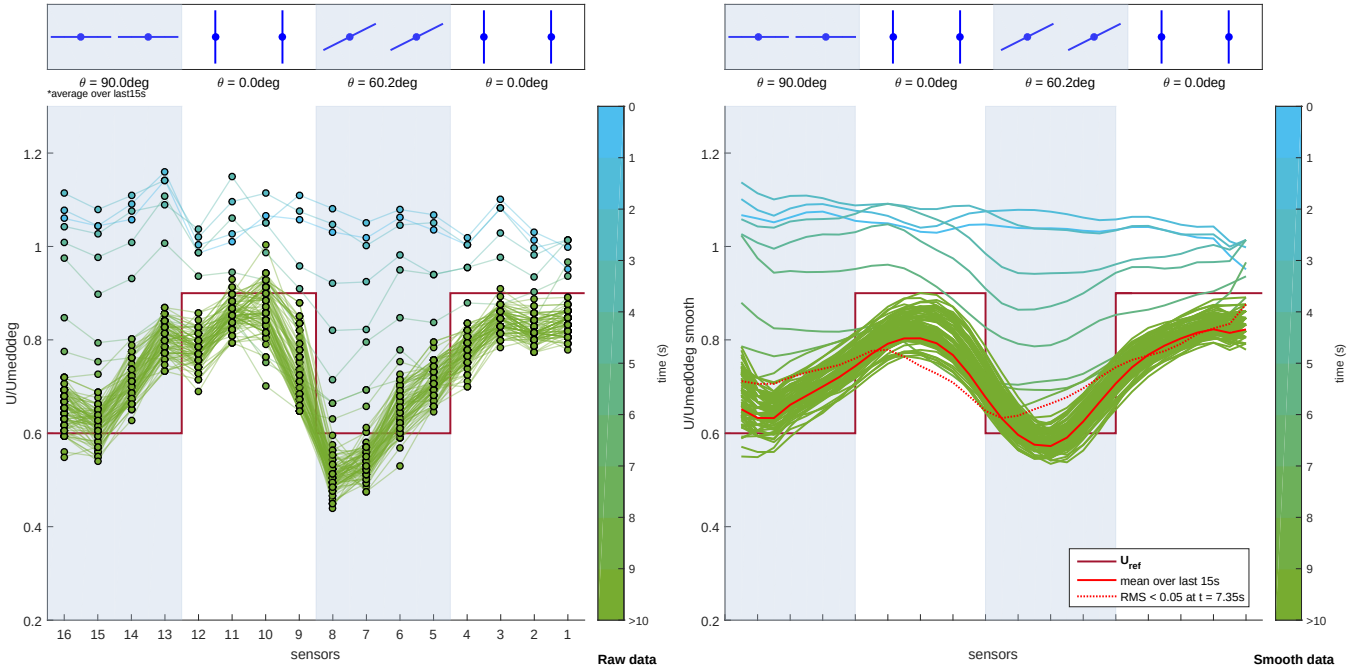

Figure 7.29: **Closed-loop unsaturated sawtooth profile evolution in time.**

Results for t_{RMS} and influence of neighbouring regions

Results for the t_{RMS} parameter are shown in Figure 7.30. Larger grid transparency changes seem to enhance convergence for *wake* and *shear*, but the variation in results suggest that the effects commented on earlier (flow recirculation, deviation and influence of neighbouring regions, gradual grid transparency change) also play an important role in convergence. A striking difference with the trends seen before is the result for the *jet* profile: its large time to converge may indeed indicate the importance of deviated flow for that design, which make the steady-state profile less stable. This can be seen analyzing *jet* profiles evolution in Figure 7.27. In it it can be seen that regions further to the left have more fluctuations. This would lead to higher t_{RMS} values and may explain the significantly higher time to converge to the steady-state profile for the *jet* profile. Note as well that it is expected that unsaturated settings present larger mutual interference between regions, since their vanes present different angles than the saturated values.

However flow deviation of one region may benefit the convergence in the neighbouring one, as it seems to occur for the *shear* and the *wake* profile. The opposite seems to occur for the *step* gust design, in which the low-speed side of the step is clearly influenced by the deviated flow from the other two regions (Figure 7.25). A "spillage" effect, due to the half-vane wide openings in the laterals of the grid frame that can't be blocked, can also result beneficial or detrimental for some designs (compare extreme regions for *jet* design in Figure 7.27 and *wake* in Figure 7.28).

Error in the profiles design

Finally the error in the profiles design is assessed. To further look into the interference of neighbouring regions and to evaluate closeness to reference inputs, two measures of error are defined. First, $\mathbf{e_{RMS}}$ the overall root-mean-square error for the steady-state profile with respect to the reference profile is computed. This is indicated for each case in the top color boxes in Figure 7.31. Then, an equivalent measure for each of the regions $\mathbf{e_{RMS,reg}}$ is determined; values are shown at the top of each region in Figure 7.31. The area between the reference values $\hat{U}_{ref}$ and the corresponding steady-state profile is filled to give an indication of the error. It can be seen that the profiles fairly match the reference ones, particularly the *shear* profile (the overall error value is large due to forcing saturation in region I, to guarantee a sharp slope). This can be very interesting for the design of wind profiles with a predefined gradient. Average values overall and per region are $\bar{e}_{RMS} = 0.2$ and $\bar{e}_{RMS,reg} = 0.1$, respectively.

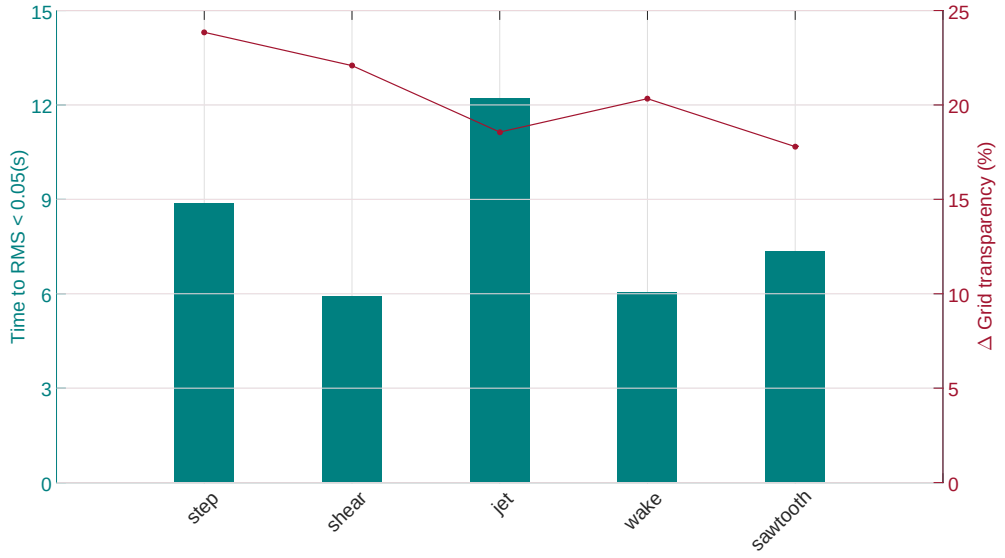

Figure 7.30: **Non-uniform unsaturated profiles convergence in closed-loop, and grid transparency reduction.** Parameter t_{RMS} (bars) and grid transparency reduction (red plot) shown for the different cases analyzed.

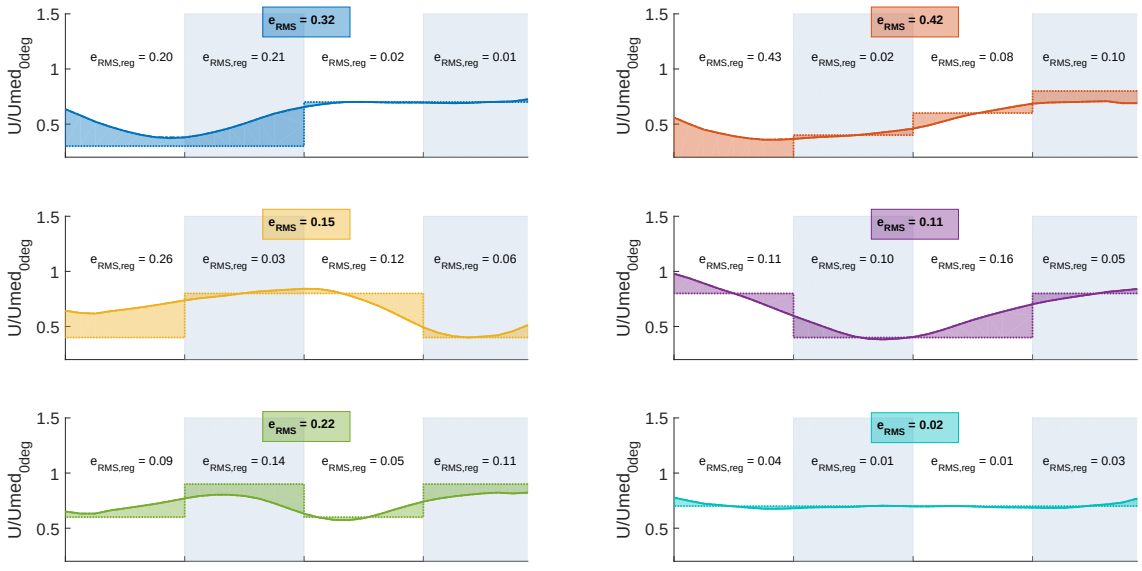

Figure 7.31: **Overall root-mean-square error spanwise and per region,** for the unsaturated gust designs considered. The error for a uniform profile at $\hat{U}_{ref} = 0.7$ is shown for reference.

7.3.5. Non-uniform unsaturated profiles in open-loop

As a final comparison, the unsaturated profiles described in the previous section are replicated in open-loop, inputting to the grid the last vanes angular position reached by the 4-region closed-loop controller. Again, the main objective with the analysis of open-loop profiles is to better assess the physical phenomena that result in faster convergence of one or other profile. Inputs to vanes angular positions in each region are summarized in Table 7.7.

Table 7.7: Vane angles inputs per region P_i (deg) for generation of non-uniform unsaturated profiles (open-loop)

	Region I P_I	Region II P_{II}	Region III P_{III}	Region IV P_{IV}
Step	90	90	25	21
Shear	90	51	18	0
Jet	90	15	6	78
Wake	1	71	86	6
Sawtooth	71	0	57	0

Profiles analyzed for these cases are shown in Figure 7.32 and the results for the t_{RMS} determination are presented in Figure 7.33.

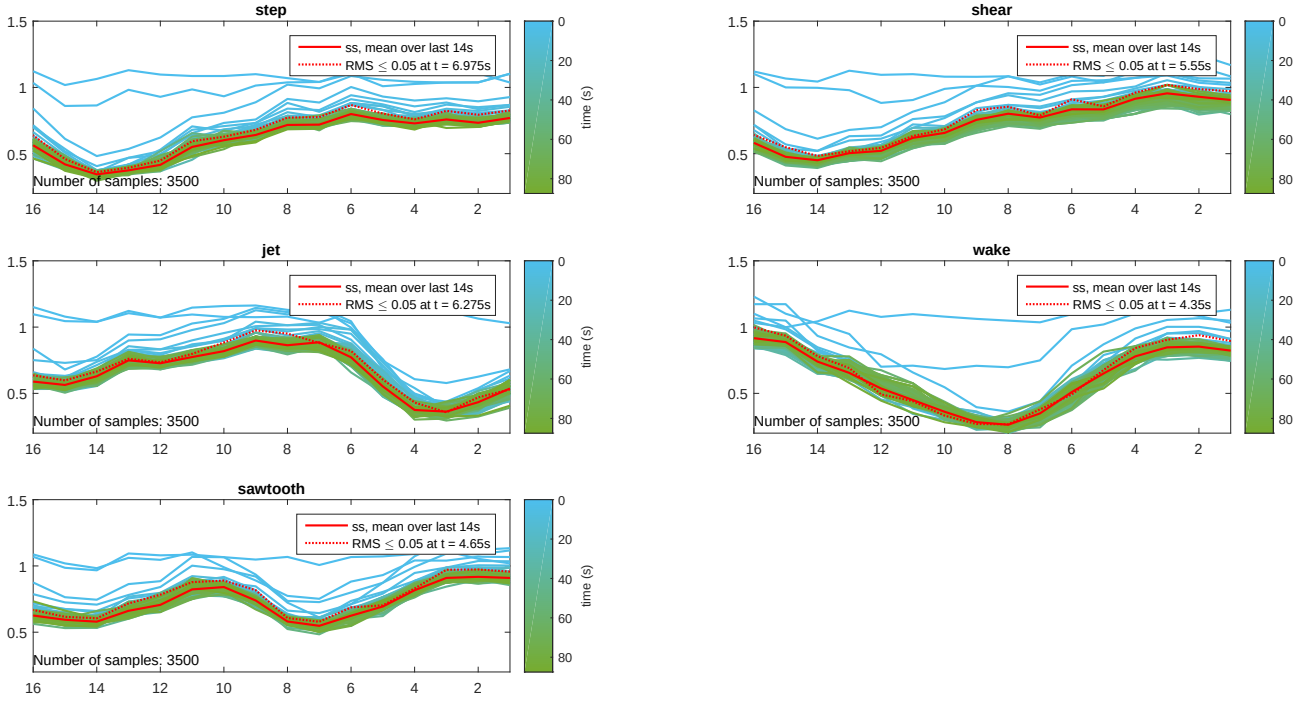

Figure 7.32: **Evolution in time of non-uniform unsaturated profiles in open-loop,** $\hat{U}_{med}$ vs sensors, smoothed data. Profiles are plotted with a timestep of 1s. Sensors' identifying number is indicated in the x-axis.

Results for t_{RMS}

As in the previous comparison open- and closed-loop, it can be seen as well that for unsaturated profiles the different time values for t_{RMS} across gust designs are lower. However, the trend across the designs does maintain, and the *step* and *jet* design are again the ones with longer convergence times (see Figure 7.33); this seems to confirm the importance of blockage distribution in convergence. It can also be seen that grid transparency reduction plays a less relevant role: there does not seem to be a strong link between large grid transparency reduction and smaller t_{RMS} values. This may be due to the fact that reductions are all in the same range of grid effectiveness data. It appears that flow deviation is the main mechanism accounting for differences in convergence for unsaturated profiles, when grid transparency changes are belo 30%. This

would be in line with what has been shown in subsection 7.3.1, Figure 7.8.

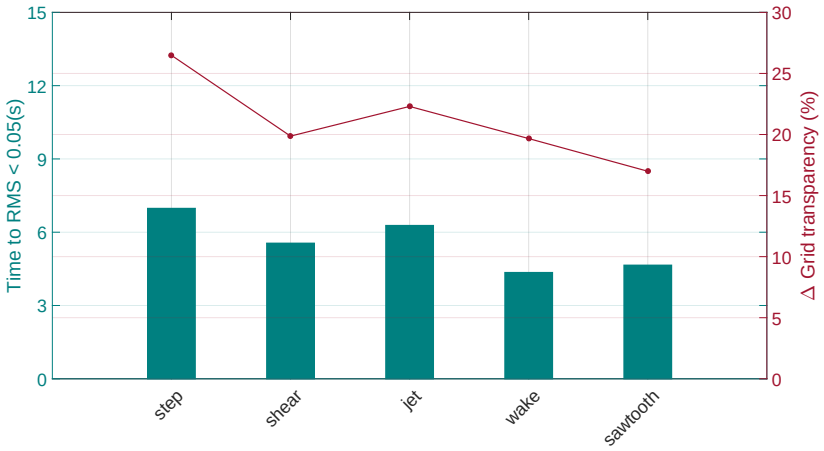

Figure 7.33: **Non-uniform unsaturated profiles convergence in open-loop, and grid transparency reduction.** Parameter t_{RMS} (bars) and grid transparency reduction (red plot) shown for the different cases analyzed.

Influence of neighbouring regions

Regarding influence between regions, a comparison analogous to the one presented for non-uniform saturated profiles in open-loop is included. It can be seen on Figure 7.34 that by using vanes angular positions different from the saturated values, the median flow speed value reached is generally most degraded (with respect to uniformly applied grid transparency case) in the left-most regions. The vanes angular position on top are included to clarify the point.

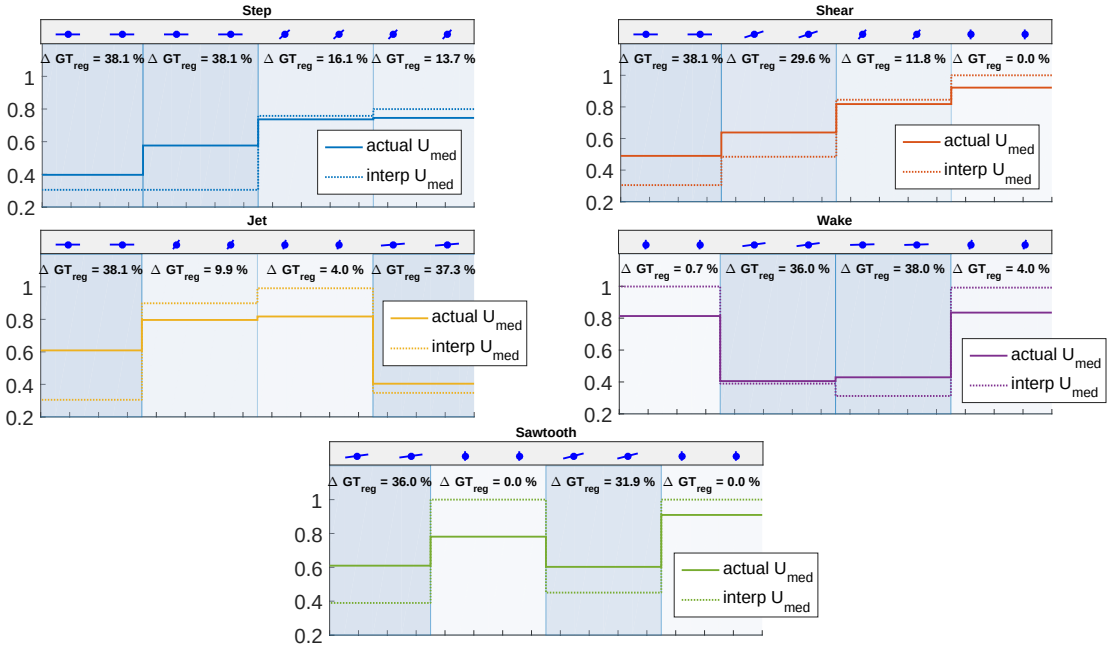

Figure 7.34: **Comparison $\hat{U}_{med}$ and grid transparency reduction ΔGT_{red}%, per region and uniformly spanwise.** Median values per region for each profile design are shown ($\hat{U}_{med}$ vs sensors). Solid line represents $\hat{U}_{med}$ in each region, dashed line represents $\hat{U}_{med}$ value when that same grid transparency reduction is applied uniformly in the whole span. The difference between both lines gives an indication of the influence of one region on the neighbouring ones. For each region, grid transparency reduction is indicated on top, and regions are blue-shaded according to their grid transparency. Sensors' identifying number is indicated in the x-axis.

7.4. Conclusions

The analysis of the static gust design presented in this chapter has provided further insight into the physical response of the system when inputting grid transparency reductions of different amplitude and spatial distribution. In order to assess these effects, different types of profiles were analyzed and suggestions for the mechanisms driving convergence were given in each case. Saturated profiles (generated with vanes positions either at 90deg or 0deg) and unsaturated profiles (generated with all vane positions considered) were considered, both in closed-loop and open-loop. Note that in closed-loop the grid closure is gradual, whereas in open-loop vanes move to the desired position immediately; this is expected to cause a different flow response. The main conclusions from the static gust analysis are summarized in this section.

- The analysis starts looking at the flow response when designing **uniform profiles in open-loop**. This is done by inputting grid transparencies reductions of different amplitude, but uniformly distributed in the spanwise direction. For these cases the convergence time was found to be related to the amplitude of the grid transparency reduction, matching the previous observations on varying time constant (see Chapter 6 and Chapter 5). For initial fully-open grid, the **larger the grid transparency reduction, the faster the convergence to steady-state**, assessed by t_{RMS} parameter (Figure 7.8). It is suggested this faster deceleration is due to the higher intensity of the pressure waves generated and the increase in turbulent losses, for a larger closure of the grid. From steps 90 to 50deg, (which correspond to grid transparency reductions from 38% up to 29%), t_{RMS} parameter increases $\sim 0.46s$ per 10deg increase in the input step ΔP. However for steps from 50deg until 20deg, the t_{RMS} parameter reaches a pleateau, varying around $-0.1s$ per 10deg increase in the input step (see Figure 7.9). This seems to indicate that for smaller reductions in grid transparency the lower intensity of the decelerating effects are not as effective in overcoming the inertia in the flow.

- **Non-uniform saturated profiles generated in open-loop** were assessed next. Different profile types were generated using only 0deg or 90deg vane positions. The *shear* profile, with slightly larger grid transparency reduction, presented the lowest time to convergence ($t_{RMS} = 4.625s$). This is in line with what was shown for uniform profiles. The rest of the cases presented equal grid transparency reduction, but differently distributed spanwise: in them convergence times were similar, averaging $\bar{t}_{RMS} = 6.45s$. Within these, the *step* profile presented the largest t_{RMS} value; this seemed to be due to the **blockage distribution** spanwise. Profiles with distributions in which maximum blockage regions are separated present slightly lower convergence times (*jet, sawtooth* and *wake*, from faster to slower convergence). Larger times to reach steady-state are then suggested to be consequence of a larger flow recirculation and less flow deviation, when blockage regions are contiguous. The **influence of neighbouring regions** is also assessed, comparing median flow speed reached in each region, to the value reached for the same grid transparency uniformly distributed across the whole span. For the cases with same overall grid transparency (i.e.,*step, jet, wake, sawtooth*), it was observed that neighbouring regions degrade performance: lower median flow speed values are increased whereas higher ones are reduced, with respect to equivalent full span values.

- The **non-uniform saturated profiles** analyzed in open-loop (*step, shear, jet, wake and sawtooth*) are now reproduced **in closed-loop** using the 4-region controller. Note that the integral controller will lead to a gradual reduction in grid transparency, as opposed to the instantaneous one in open-loop. From the **time to convergence** results, considering all sources of delay, the average convergence time is $\bar{t}_{RMS} = 8.215s$, higher than in open-loop case. It can be seen that the controller accentuates the differences across gust designs, but the trend is similar to the one seen in open-loop. This is coherent with the controller speed being a function of the error between current flow speed and set value, resulting in the controller following the flow response. For the cases with equal grid transparency change (*step*, (*jet, sawtooth* and *wake*) t_{RMS} values average $8.41s$. It is suggested that differences in t_{RMS} in closed-loop saturated profiles are also linked to blockage distribution spanwise, as in the equivalent open-loop cases. The gradual closure of the grid versus the instantaneous one in open-loop may also explain differences in performance between closed-loop and open-loop; it seems that a gradual closure may be advantageous for some profile designs such as *sawtooth*, that presents the smallest increase in time to converge with respect to open-loop.

- Once the different mechanisms affecting convergence have been evaluated for saturated profiles, the capabilities of the controller to design static **unsaturated profiles** are tested. Larger grid transparency

changes seem to enhance convergence for *wake* and *shear*, but the variation in results suggest that the effects commented on earlier (flow recirculation, flow deviation from neighbouring regions and gradual grid transparency change) also play an important role in convergence. A striking difference with the trends seen before is the large time to converge for the *jet* profile, which may reflect the importance of recirculating and deviated flow for that design, which make the steady-state profile less stable. Indeed analyzing the profiles evolution for *jet* gust design (Figure 7.27), it can be seen that regions further to the left have more fluctuations in flow speed. This would lead to higher t_{RMS} values and explain the significantly higher time to converge to the steady-state profile. The **error with respect to the reference input profile**, per region and overall is also evaluated. Error values average $\bar{e}_{RMS} = 0.2$ overall, and $\bar{e}_{RMS,reg} = 0.1$ per region. The tool shows a good capability of reproducing tailored slopes in the wind profile, even with only 4-region resolution.

- Finally, the **non-uniform unsaturated profiles** analyzed in closed-loop are reproduced **in open-loop** to compare the effect of using the controller. Again the open-loop approach presents a similar trend to the one observed for the same gust designs in closed-loop, with less differences across gust types. The unsaturated *step* and *jet* designs are again the ones with longer convergence times (Figure 7.33). This seems to confirm the importance of **blockage distribution** in convergence also in open-loop. There does not seem to be a strong link between large grid transparency reduction and reduced t_{RMS} values. This may be due to grid transparency reductions being all in the **plateau** region mentioned in the open-loop uniform profiles cases (from 5 to 30% grid transparency reduction approximately). It is therefore suggested that flow deviation is the main mechanism accounting for differences in convergence for unsaturated profiles. Additionally, the **influence across regions** with vanes in unsaturated positions is assessed and compared to the previous saturated analysis. Results seem to indicate that angles different to 0deg or 90deg result in left-most regions being the most degraded in performance, with respect to uniformly applied grid transparency case.

The static gusts study has enabled to analyze the influence of grid transparency reductions differently distributed spanwise and thus assess the potential benefit of certain gust designs for use in real-time experiments. From previous chapters the amplitude of the grid transparency reduction has been linked to time to convergence; now for equal grid transparency changes across the span it has been shown that differences exist depending on how the blockage is distributed. Moreover, for grid transparency reductions below ~ 30%, the benefit of a larger reduction seems to decrease. *Step* profiles which have contiguous blockage regions are generally slower to converge, whereas *shear* and *sawtooth* have shown in most cases a faster response. These differences are amplified in closed-loop, with convergence times increasing overall. The closed-loop controller has shown to allow a careful tailoring of profiles, with good results even with only 4-regions resolution. This confirms the closed-loop approach as a good option for profile design; in the next dynamic gust designs, the closed-loop 4-region controller will be turned into a 8-region tool.

8

Dynamic gusts with 8-region controller

The static gust analysis carried out in the previous chapter has provided useful insight into the convergence of different profile designs. In this chapter, similar flow profiles are analyzed, adding the *dynamic gust* approach: by including a motion capture system in the loop, it is possible to generate profiles that follow the position of a moving objective (i.e., flying animal or robot). Figure 8.1 shows the concept for dynamic gusts and the analyzed approaches.

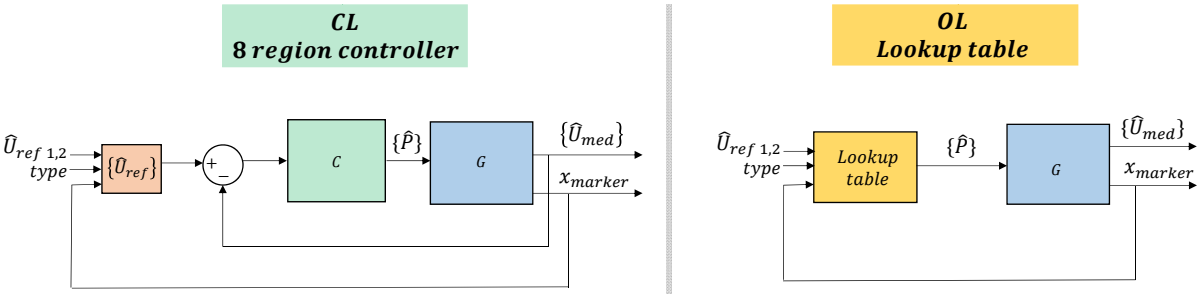

Figure 8.1: **Dynamic gust design approaches**. Block diagrams of the two approaches followed (closed-loop and open-loop Lookup table) are presented. Note that the system G now includes the motion tracking equipment. In both cases the marker's position given by the motion tracking system is fed back, constituting a closed-loop; however this closed-loop is not included in the controllers name for clarity. Note as well that the input to the system $\hat{P}$ does not necessarily apply to all outputs (e.g., x_{marker}). Curly brackets indicate the quantity is a row vector.

First, an 8-region closed-loop controller is built, based on the 4-region one developed in the previous chapter. The motion tracking equipment is added to the loop as a proof of a double closed-loop setup (in the profile design and in the motion tracking) in a wind tunnel. However, the main objective of this ***closed-loop*** (CL) controller is to serve as a design tool, for populating a lookup table. Indeed the final aim of the project is to define a non-linear controller based on a lookup table, for the design of dynamic gusts. With the 8-region closed-loop approach the required vane positions for a range of profile designs are determined, and thus the lookup table is defined. Since the table is used in open-loop, this approach is called the ***open-loop Lookup table*** approach (OL-Lookup), in contrast to the *closed-loop* approach of the 8-region closed-loop controller. In this chapter the construction of each of them is explained, and their performance is compared in terms of speed of response and error. Note that in both cases the marker's position given by the motion tracking system is fed back, constituting a closed-loop; however this closed-loop is not included in the controllers name for clarity (see Figure 8.1). Workflows for each approach are further explained in the following section.

8.1. Chapter overview

The two approaches considered for the dynamic gust design are shown in Figure 8.1. The closed-loop approach guarantees a compensation of disturbances, whereas the open-loop looses this capability, in favour of an increased speed of response. Note that in both cases, the information provided by the motion tracking system is used to define the reference, conferring in this way the tracking capability.

The first approach presented is the ***closed-loop*** one (CL) and it consists on adding the motion capture system to an 8-region controller, analogous to the 4-region one described in the previous chapter. With this new division each region is comprised of one vane and the two wind speed sensors directly downstream (see Figure 1.9); this allows a closer match of the marker's lateral coordinate with a region in the test section. The motion tracking system provides information of the marker's lateral position, and this data is used to define the reference profile to which the controller converges. This approach is expected to present the lowest deviations with respect to the reference profile (since the controller is continuously acting to minimize them), but also the slowest response, since it is limited by the controller's convergence speed. In this CL approach four gust types are analyzed: *step*, *shear*, *jet* and *wake*. Differences between profile designs are also looked into. In principle *jet* and *wake* should involve smaller variations in grid transparency when moving the profile along the spanwise direction in the test section, which may be beneficial for convergence.

The second approach, ***open-loop Lookup table*** (OL-Lookup), aims to reduceconvergence time by making use of a lookup table. This lookup table is generated in closed-loop with the 8-region controller. Using as inputs the current position of the retroreflective marker, and the user-defined flow speed parameters, the table provides the vanes angular position. The table is generated for the *step* type of gust only, out of practicality, but the same approach can be easily translated to any other type of gust. Note that by using the lookup table the vanes change position instantly, as opposed to the closed-loop approach, in which grid transparency varies gradually, at a rate imposed by the controller and the flow response (1.08deg per 0.1 error). This is expected to cause a difference in convergence. Larger errors with respect to the reference profile than those obtained in closed-loop are also expected, since there is no longer a feedback control.

The performance of both controllers presented is analyzed in terms of their speed of response and measures of error. Regarding the first one, it should be highlighted that most benefit is expected to come from reducing the computational delay. However and as it has been shown in previous chapters (Chapter 7, Chapter 5, Chapter 6), the main limitation to the system's response time is the mass flow acceleration and deceleration. Another aspect that is looked into is the differences in the system's response when changing between gusts of similar grid transparency values: most grid transparency changes in the dynamic gusts analysis present amplitude below 10%, whereas in the static gusts analysis, grid transparency changes were around 20%-25%). Note that in this chapter both grid transparency reductions and increases are considered (whereas on the *static gusts* analysis on Chapter 7, only grid transparency reductions were looked into). Therefore the parameter used is now the grid transparency change ΔGT as:

$$\Delta GT = GT_{final} - GT_{initial} \qquad (\%); \tag{8.1}$$

In the following section the experimental setup is described and the construction of both approaches is further detailed. Then, the experiments carried out to compare their performance are introduced. Results are shown first for the CL approach, then for the OL-Lookup one, and lastly a comparison between the two is presented. Finally, the main conclusions for the dynamic gusts analysis are drawn in the last section.

8.2. Experimental setup and procedure

The main addition to the experimental setup in this chapter is the QualiSys motion tracking system. It consists on four infrared cameras (Qualisys Oqus 7+), which are set around the test section as shown in Figure 8.3, and a half-spheric retroreflective marker of 3mm diameter. This marker is fixed to the tip of a thin balsa wood rod covered with black tape, to avoid undesired reflections. The cameras are calibrated following the manufacturer's instructions (Qualisys Motion Capture Systems, 2011). The reference frame for the calibration is set such that the axis of reference has its origin in the mid-spanwise position at the grid test section, with the x-axis pointing to the right and the y-axis pointing downstream (for an observer looking

upstream, see Figure 8.2). Position data streaming rate was set to 1000Hz. Before performing the experiments, it was verified that the cameras covered the required volume by accessing the test section from the downstream trapdoor and moving laterally the rod with the marker.

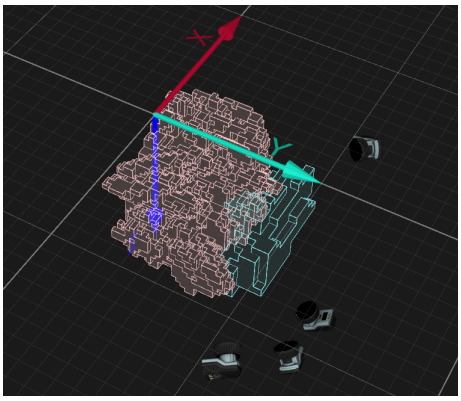

Figure 8.2: **Snapshot of the QualiSys software QTM 2.11 showing the volume covered by the tracking cameras.** The reference axis for calibration and tracking waiinside and at mid-spanwise position.

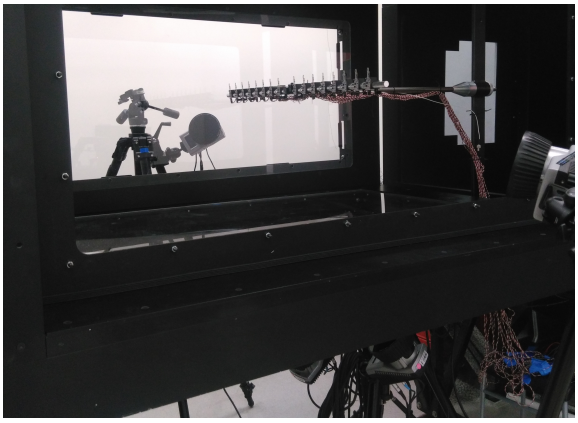

Figure 8.3: **Position of the infrared motion capture cameras.** Two cameras are located below the test section and two on the sides. Accessing from the trapdoor downstream, the thin rod with the marker is translated spanwise the test section in the volume covered by the cameras. Note that the acrylic side panel of the test section was removed when taking the picture, but this was not the situation when performing the experiments.

In the following sections particularities of the setup for each controller approach are briefly explained. After, the experimental procedure for the comparison data is described.

8.2.1. Closed-loop approach

The 8-region controller used in the closed-loop approach is built analogously to the 4-region one developed in Chapter 7. In this case eight controllers are set in parallel with the same tuning parameters as those obtained for the 1-region closed-loop controller developed in Chapter 6. As a result each vane's position is now linked to the measurements of the two sensors directly downstream. The further subdivision of the space enables an increased spatial resolution for the gust designs, required to follow the marker more closely. The motion tracking system is incorporated as an additional loop. The motion capture system outputs the marker's lateral coordinate x_{marker}, which is assimilated to the closest region in the test section. The region the marker is at is added to the user-defined parameters (gust type, $\hat{U}_{ref,1}$ and $\hat{U}_{ref,2}$) to determine the reference profile for the controller (see Figure 8.4a). Note that not only the marker's lateral position, but also the rest of parameters can be modified by the user any time.

8.2.2. Open-loop Lookup table approach

The open-loop Lookup table approach determines the required vanes position for a certain user-defined profile by making use of a closed-loop generated lookup table. In the generation of the table, eight possible positions for the marker are considered, corresponding to each one of the eight regions, and values for $\hat{U}_{ref}$ from 0.3 to 1 are inputted, resulting in a total of 512 vertical vanes configurations. To ensure that steady-state has been reached, each profile design is kept for 20s, and the average over the last 5 vanes angular positions is added to the table. For our study a lookup table for a *step* gust design is generated, but the same approach can be followed for the other types of gusts.

Once the lookup table is defined, the open-loop controller is set up. Due to the lookup table implementation in Labview being limited to a maximum of 3 inputs and 1 output, it is built as follows. The real-time position of the marker (given by the motion tracking system) and the two extreme flow speed values defined by the user constitute the inputs to the lookup table, which outputs a configuration number (1-512). This configuration number corresponds to the row of a matrix of size 512x8, containing the eight vanes angular

positions corresponding to each configuration. The workflow for this approach is shown in Figure 8.4b.

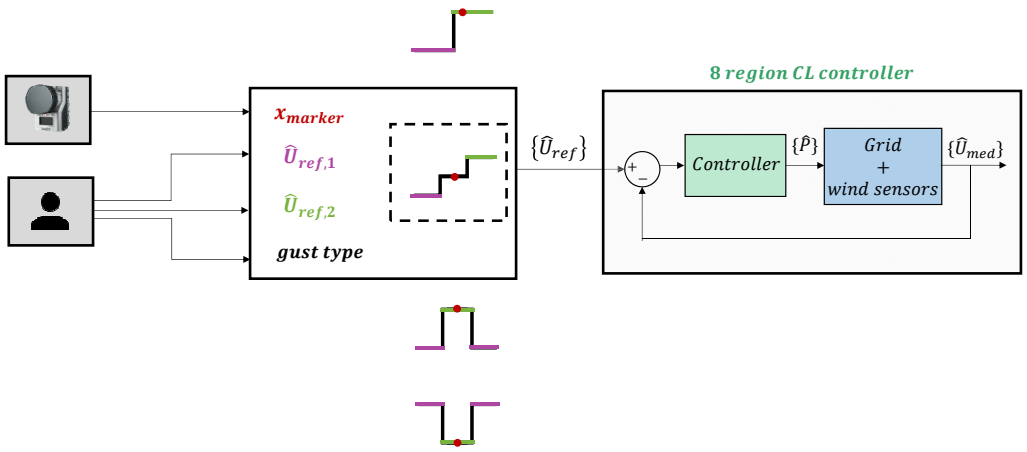

(a) **Workflow for the 8-region CL approach.** The motion tracking system provides the spanwise coordinate of the marker, which is used to define the reference profile for the controller, alongside the flow speed inputs set by the user. The curly brackets around $\hat{U}_{ref}$, $\hat{P}$ and $\hat{U}_{med}$ indicate that they are row vectors of eight components, corresponding to the eight regions defined and the eight vertical vanes. The reference profiles for four sample gust designs (*step*, *shear*, *jet* and *wake*) are shown.

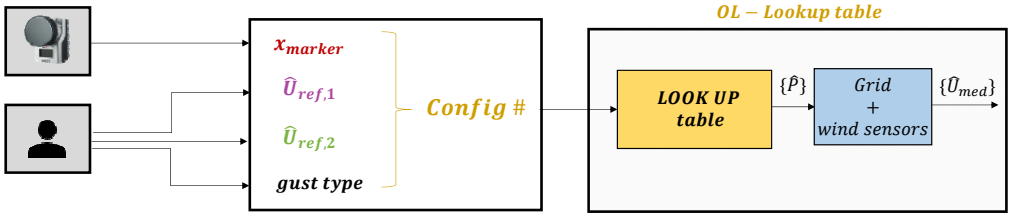

(b) **Workflow for the OL-Lookup table approach.** The motion tracking system provides the spanwise coordinate of the marker, which is used alongside the flow speed inputs set by the user to define the configuration number to lookup in the table. The output of the lookup table is directly the angular position of the eight vertical vanes. The curly brackets around $\hat{U}_{ref}$, $\hat{P}$ and $\hat{U}_{med}$ indicate that they are row vectors of eight components, corresponding to the eight regions defined and the eight vertical vanes.

Figure 8.4: **Workflows for the two approaches considered for dynamic gusts design.**

8.2.3. Experimental procedure

For all cases the wind tunnel setpoint speed was set to 5m/s and the temperature is kept to 20ºC. The $U_{med,0deg}$ value is obtained at the beginning of each test, taking the median over 200 U_{med} values acquired with the trapdoor closed. After the value is determined, the system is set to "Start Moving". The trapdoor is then opened and the marker is introduced in the test section, initially setting it at mid-spanwise position. The marker is then translated laterally across different stations in a sequence, as shown in Figure 8.5, staying in each station for approximately 5s (all final stations timespan values are within 2s and 7s, excluding the initial and final stations). Nine stations are considered for each approach. The evolution of the profiles is analyzed at each of the stations. The objective is to capture the transition between stations in the flow response, and assess the speed at which the flow adapts to the new condition.

Table 8.1 summarizes the types of gusts considered for each approach. In the closed-loop approach, *step*, *shear*, *jet* and *wake* gusts were considered, whereas for the open-loop approach only *step* gusts were analyzed. Figure 8.6 shows the procedure used to define the reference profile $\{\hat{U}_{ref}\}$, taking as inputs the marker position and the flow speed user-defined parameters. The same definition was used in the lookup table generation.

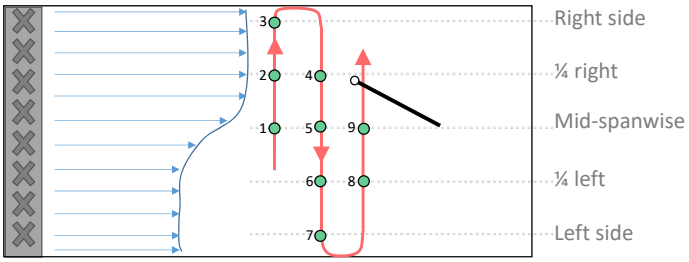

Figure 8.5: **Stations considered for dynamic gusts analysis**. The marker is moved along the red path and kept static at each station (green dots) for approximately 5s at each station (green dots). Stations are numbered in the order they are visited in time. The stations are based in five spanwise locations in the test section, which approximately correspond to mid-spanwise position, 1/4 from the right, furthermost right, 1/4 from the left and furthermost left.

Table 8.1: **Gust types considered for each dynamic gust approach**. The numeric values indicate the reference flow speed values $\hat{U}_{ref,1}/\hat{U}_{ref,2}$ (left/right for *step* and *shear* gusts, inner/outer for *jet* and *wake* gusts).

CL approach		**OL-Lookup approach**	
Gust type	$\hat{\mathbf{U}}_{\mathbf{ref,1}}/\hat{\mathbf{U}}_{\mathbf{ref,2}}$	**Gust type**	$\hat{\mathbf{U}}_{\mathbf{ref,1}}/\hat{\mathbf{U}}_{\mathbf{ref,2}}$
Step	0.3/0.7	Step	0.9/0.5
Shear	0.6/0.9	Step	0.3/0.7
Jet	0.8/0.4	Step	0.4/0.8
Wake	0.5/0.9		

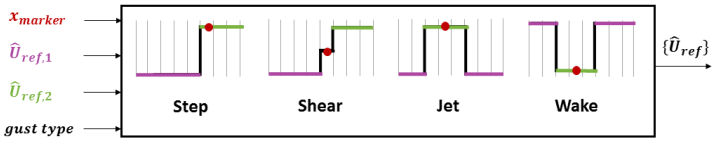

Figure 8.6: **Definition of reference profile $\{\hat{\mathbf{U}}_{\mathbf{ref}}\}$.** The user-input flow speed values $\hat{U}_{ref,1}$ and $\hat{U}_{ref,2}$ determine the extreme values of the profile: left and right for *step* and *shear*, inner and outer for *jet* and *wake*. The marker's position defines the area in which $\hat{U}_{ref} = \hat{U}_{ref,2}$: for the *step* gust, it extends from the marker's current region to the one most to the right in the test section; for the *jet* and *wake* ones it extends from the marker's current region to one region outwards, in left and right direction; for the *shear* gust it extends over the regions to the right of the marker's current region. The rest of regions are set to $\hat{U}_{ref,1}$, except in the *shear* gust case, in which the marker's region is set to the average value between $\hat{U}_{ref,1}$ and $\hat{U}_{ref,2}$. Grey vertical lines indicate regions limits.

8.3. Results

The results obtained for both closed-loop and open-loop approaches are detailed in the following two sections. A comparison between approaches is presented afterwards, with a focus on the effect of the grid transparency change.

8.3.1. Closed-loop approach

In the closed-loop approach, four types of gusts are considered, as indicated in Table 8.1. Figure 8.7 shows the evolution of the marker's lateral coordinate in time; the selected end limits for the nine stations considered are indicated with a dot marker. Profiles at each station are analyzed with a similar approach to the one applied to static gusts in chapter 7. The objective is to analyze the transition across profiles when moving the marker.

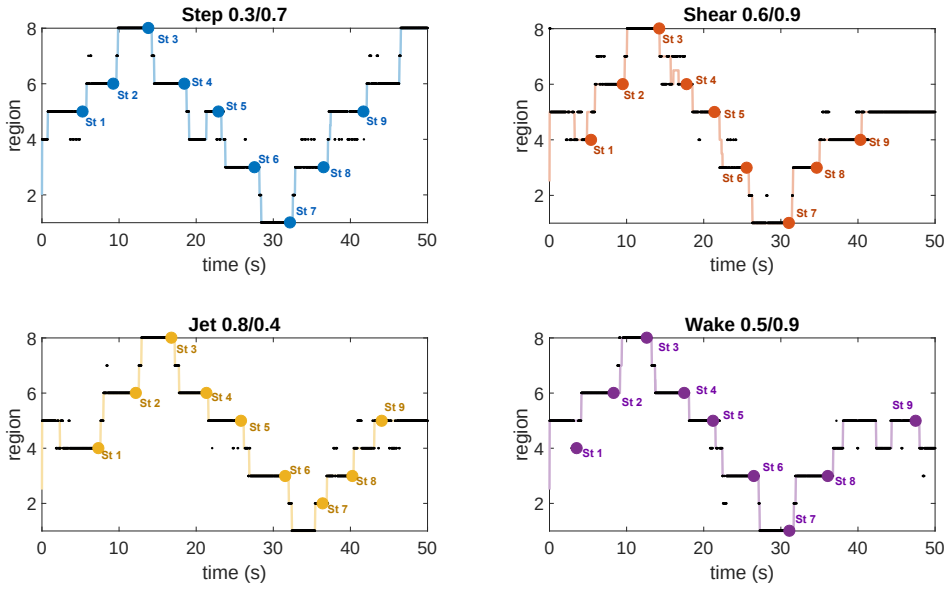

Figure 8.7: **Marker's lateral coordinate and region position in time, for closed-loop cases.** Colors correspond to different gust types. Markers indicate the end of each of the stations. Only the first 9 stations are considered for the analysis.

Figures 8.8 to 8.11 show the **evolution of the profiles in time at each station**, for each of the gust types considered in closed-loop. Point measurements from the sensors are postprocessed by resampling to 32 points and smoothing with a moving average over the span of one region (8 resampled points). To remove outliers, first outlying profiles are identified (thoe with negative mean or mean above 1.5); within them, outlying sensor readings are located with the same bound criteria; outlier sensor readings are substituted by the mean of the readings of the same sensor, one instant ahead and after. The figures include data regarding the overall grid transparency change at each station (between the first and last vanes angular positions). Additionally, on the x-axis, the initial and final position of the marker are plotted, in light and dark blue respectively. Intermediate positions occupied by the marker during the station timespan are also plotted, following the colorbar for time progression in the profiles.

The **steady-state profile** is defined as in the static case, taking the average over the last 1/6 samples in the station. Note however that steady-state is not reached within the time frame of the each station (being these around 5s), and that this profile evaluates the average final profile shape reached at the end of the station. As for the $\mathbf{t_{RMS}}$ **profile**, this one is now defined with a lower threshold, as the first profile with a root-mean-square deviation of the steady-state one less or equal than 0.025. This is done because dynamic profiles involve lower changes in grid transparency and thus lower deviations are expected (a root-mean-square error of 0.05 is reached too early in the station time frame).

From a preliminary analysis of the profiles evolution, some trends in the response can already be extracted.

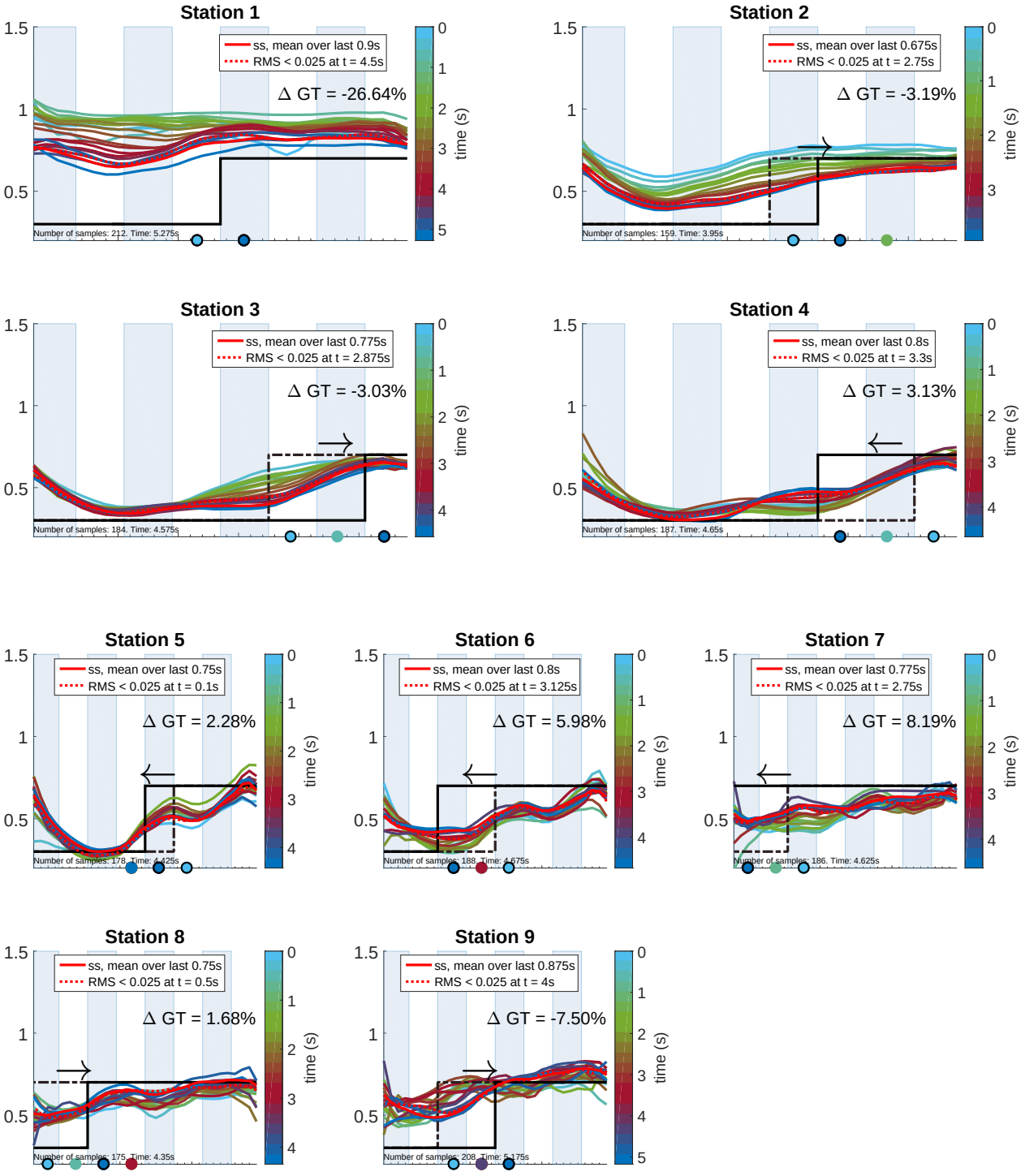

Figure 8.8: **Profiles evolution in time, for closed-loop dynamic gust Step 0.7/0.3, from stations 1 to 9.** Profiles are plotted with 0.25s timestep and colored with their progression in time as indicated by the colorbar. The reference profile at the start of the station (black dashed line) and at the end of the station (black solid line) are shown. Grid transparency change at the station is also included, obtained as the difference between final and initial grid transparency values at the station. Profile plotted in solid red line represent steady-state profile; profile in dotted red line indicates the profile at rms < 0.025. Note that the eight regions considered are alternatively shaded. Marker's position throughout the station is plotted on the x-axis as a colored dot, following the same color scheme as the profiles. Initial and final marker's position are contoured in black.

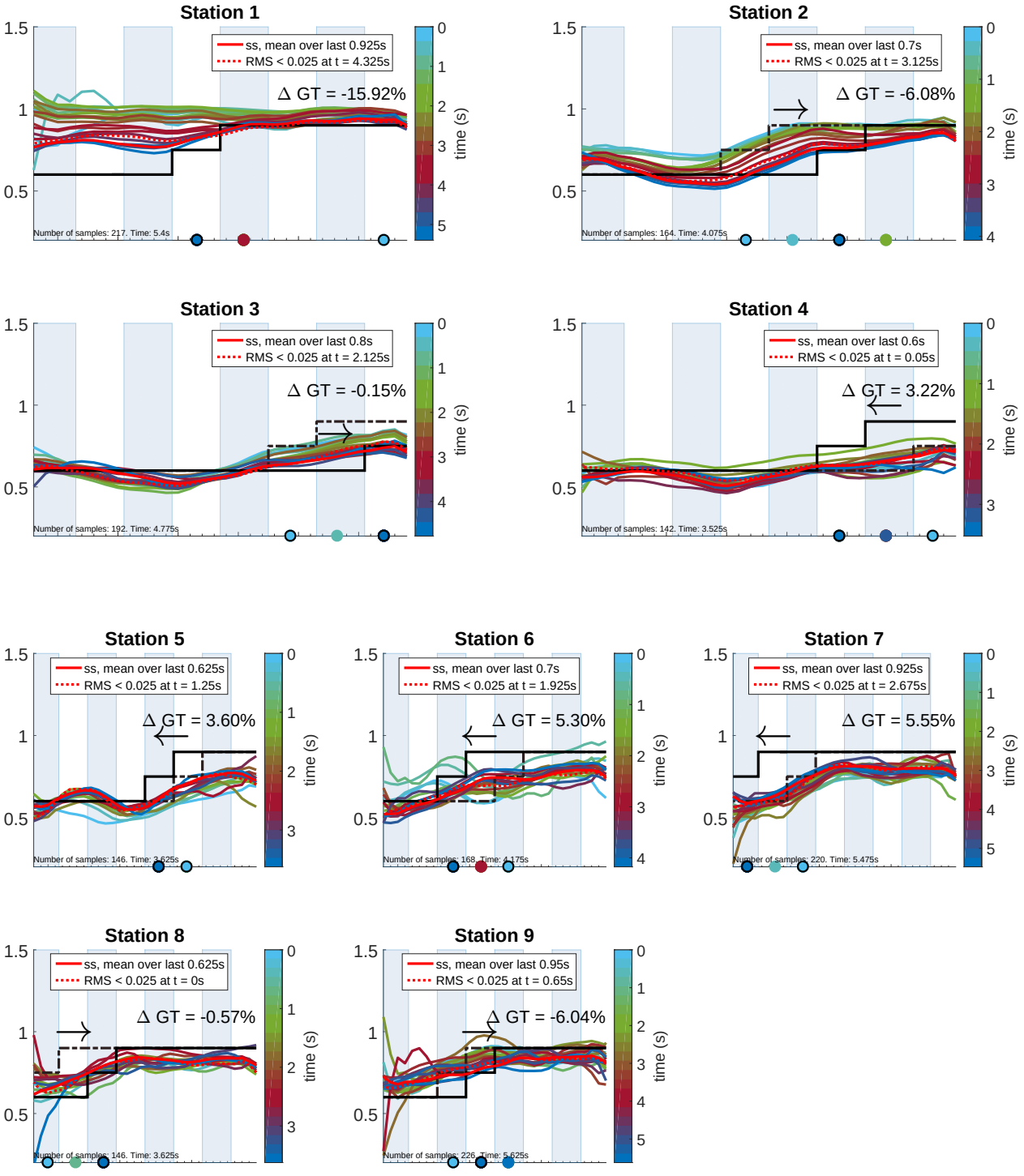

Figure 8.9: **Profiles evolution in time, for closed-loop dynamic gust Shear 0.6/0.9, from stations 1 to 9.** Profiles are plotted with 0.25s timestep and colored with their progression in time as indicated by the colorbar. The reference profile at the start of the station (black dashed line) and at the end of the station (black solid line) are shown. Grid transparency change at the station is also included, obtained as the difference between final and initial grid transparency values at the station. Profile plotted in solid red line represent steady-state profile; profile in dotted red line indicates the profile at rms < 0.025. Note that the eight regions considered are alternatively shaded. Marker's position throughout the station is plotted on the x-axis as a colored dot, following the same color scheme as the profiles. Initial and final marker's position are contoured in black.

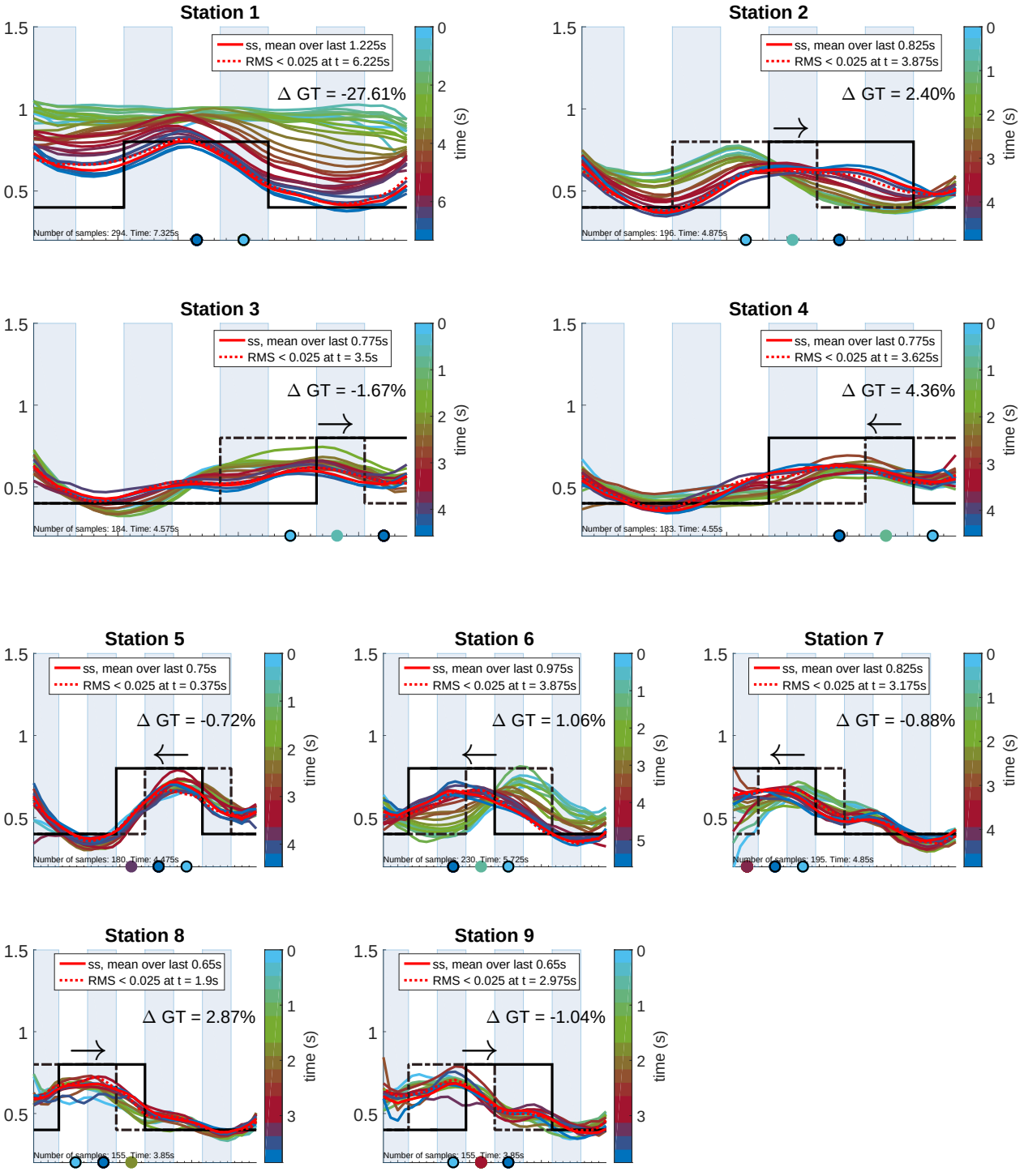

Figure 8.10: **Profiles evolution in time, for closed-loop dynamic gust Jet 0.8/0.4, from stations 1 to 9.** Profiles are plotted with 0.25s timestep and colored with their progression in time as indicated by the colorbar. The reference profile at the start of the station (black dashed line) and at the end of the station (black solid line) are shown. Grid transparency change at the station is also included, obtained as the difference between final and initial grid transparency values at the station. Profile plotted in solid red line represent steady-state profile; profile in dotted red line indicates the profile at rms < 0.025. Note that the eight regions considered are alternatively shaded. Marker's position throughout the station is plotted on the x-axis as a colored dot, following the same color scheme as the profiles. Initial and final marker's position are contoured in black.

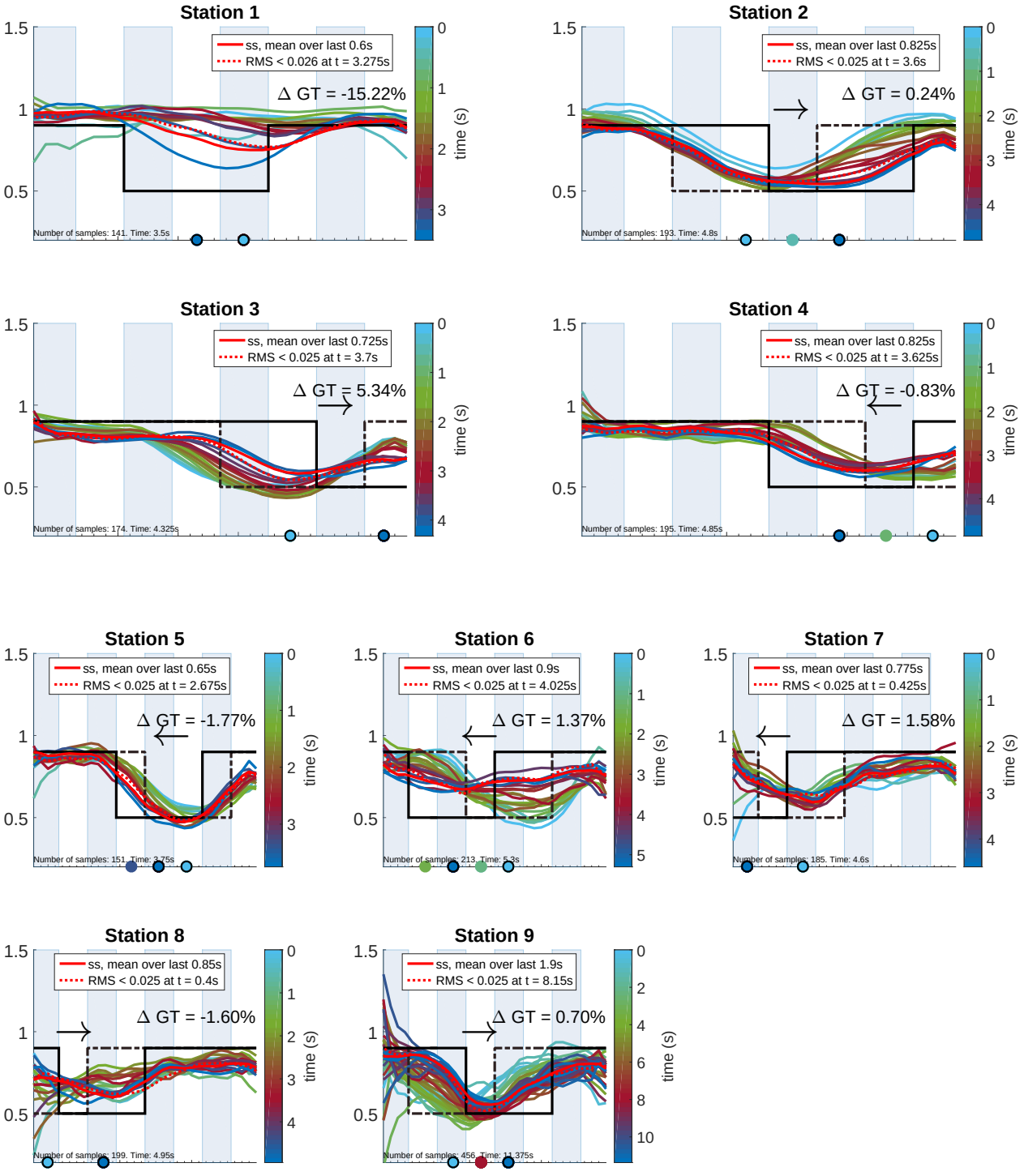

Figure 8.11: **Profiles evolution in time, for closed-loop dynamic gust Wake 0.5/0.9, from stations 1 to 9.** Profiles are plotted with 0.25s timestep and colored with their progression in time as indicated by the colorbar. The reference profile at the start of the station (black dashed line) and at the end of the station (black solid line) are shown. Grid transparency change at the station is also included, obtained as the difference between final and initial grid transparency values at the station. Profile plotted in solid red line represent steady-state profile; profile in dotted red line indicates the profile at rms < 0.025. Note that the eight regions considered are alternatively shaded. Marker's position throughout the station is plotted on the x-axis as a colored dot, following the same color scheme as the profiles. Initial and final marker's position are contoured in black.

Some **differences between accelerating and decelerating** transitions can be observed especially in the *step* and *shear* gusts, which involve larger grid transparency changes. For example comparing the profile shape change at decelerating station 3 and accelerating station 4, for both *step* and shear, it can be seen that decelerating station 3 presents a larger change in shape. For *jet* and *wake* gusts, differences between accelerating and decelerating stations are not as evident, possibly because transitions between stations for these gust types involve lower changes in grid transparency.

For all gust types it can be seen that there are more **fluctuations in the measurements** in the later stations (compare stations 1-4 with 5-9 in all cases). It is expected that this more turbulent conditions at the start of the later stations degrade the flow adaptation to the new reference profile. Turbulence due to flow deviation may also be increased in some cases due to the vanes sense of rotation. Since these rotate clockwise for increasing angles, it is expected that they deviate flow further to the left, and thus profiles with decreasing flow speeds on the sections most to the left would be affected negatively. This may be the case for the *step* gust in station 9, the *jet* gust at stations 3, 8 and 9 or the *wake* gust at station 6.

To gain further insight into the **rate of change in the profile shape** at each station, some new parameters are defined. A reference profile is defined, profile 1, as the average over the first 1/6 profiles in the station. The parameter $e_{\text{RMS 1,ss}}$ is defined as the root-mean-square error between this profile 1 and the steady-state profile. In this way this parameter estimates the "amount of change" between the average first and average last profile. Dividing over the time at the station t_{station}, the **average rate of change** in the profile $\mathbf{e_{RMS\ 1,ss}/t_{station}}$ is obtained. To analyze the possible relation between this average rate of change and the overall grid transparency change, the values obtained for the $e_{\text{RMS 1,ss}}/t_{\text{station}}$ parameter (for each gust type and station) are plotted against ΔGT in Figure 8.12. In Appendix G, further data regarding the relation between the $e_{\text{RMS 1,ss}}/t_{\text{station}}$ parameter and t_{RMS} can be found.

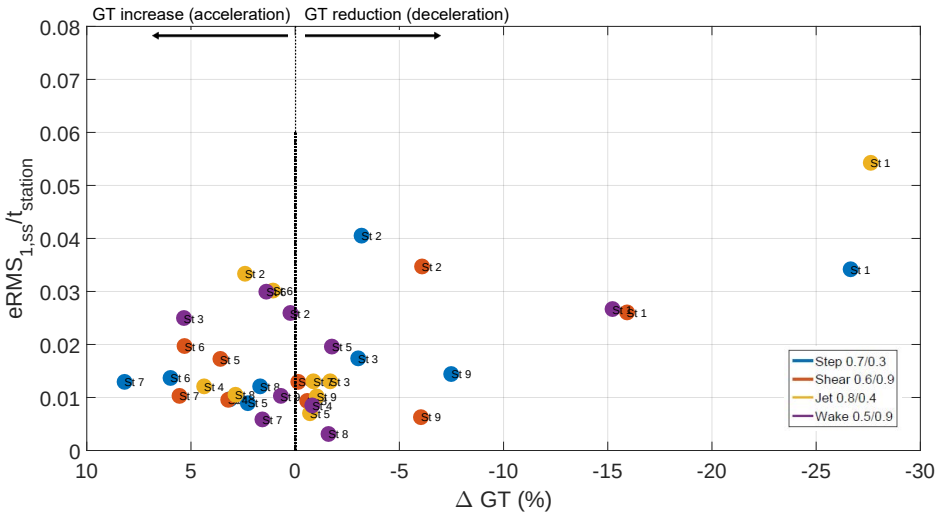

Figure 8.12: **Rate of change for all gust types and stations considered in closed-loop approach, against grid transparency change ΔGT.** Markers are colored according to gust types and labeled with the corresponding station.

In order to assess the **relation between grid transparency change and rate of change**, values for each station and gust type in closed-loop are plotted in Figure 8.12. Note that the x-axis, indicating overall grid transparency change, is inverted, showing deceleration cases to the right and acceleration cases to the left. This is done to agree with previous chapters considering grid transparency reductions ($\Delta GT < 0\%$); these are expected to present faster rates of change. That seems to be the case for the station 1 cases plotted. Comparing them for all gust cases, it can be seen that the rate of change increases for larger ΔGT reductions; this is in agreement with what has been shown in previous chapters.

In Figure 8.12 there seems to be differences in the data distribution for each gust type. Data is separated in two cases for a clearer visualization in Figures 8.13a and 8.13b. This division responds to the assumption that *step* and *shear* profiles would in principle involve larger grid transparency changes when translating

spanwise; whereas lower values would be expected for *jet* and *wake*.

For ***step* and *shear* gusts** (red and blue markers, Figure 8.13a) it can be seen that, in accelerating transitions ($\Delta GT > 0\%$), all of the cases lie around a rate of change of approximately $0.015s^{-1}$. In decelerating cases however, rate of change values for similar grid transparency changes are more spread. Particularly station 2 presents larger rates of change than the rest, in both gust types. This may be because of the flow being in a less turbulent state than in the rest of stations, but already quite decelerated. Note as well that similar performance is found, in terms of rate of change, for both gust designs, for the same stations.

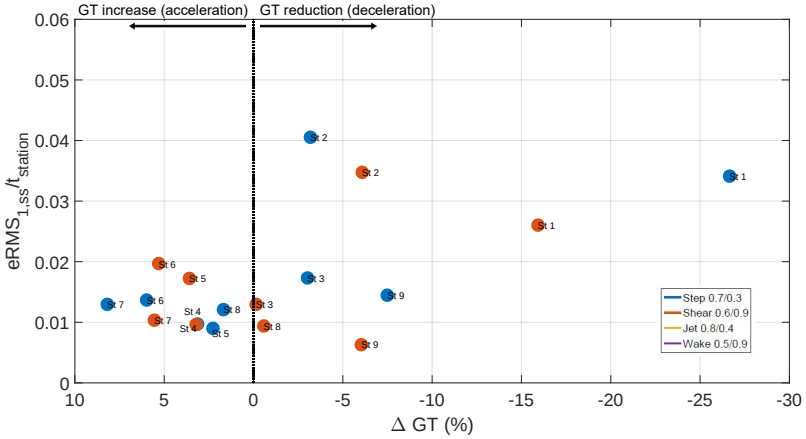

(a) **Rate of change for *step* and *shear* gust types in closed-loop, for every station analyzed, against grid transparency change ΔGT.** Markers are colored according to gust types (step, blue markers; shear, red markers) and labeled with the corresponding station.

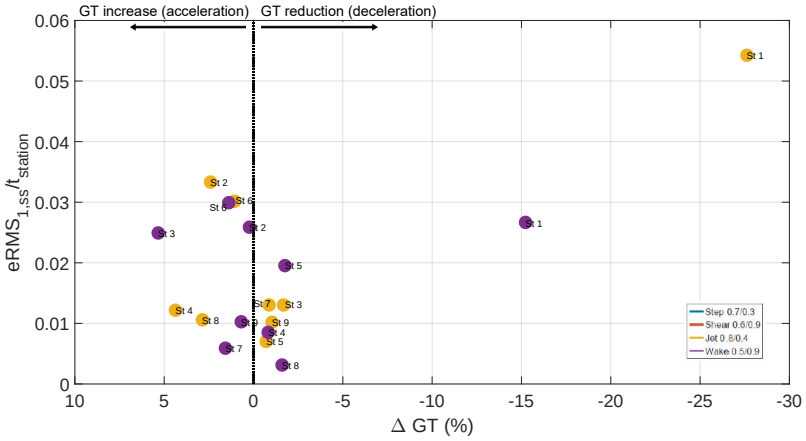

(b) **Rate of change for *jet* and *wake* gust types in closed-loop, for every station analyzed, against grid transparency change ΔGT.** Markers are colored according to gust types (jet, yellow markers; wake, purple markers) and labeled with the corresponding station.

Figure 8.13: **Rate of change for all gust types and stations considered in closed-loop approach, against grid transparency change ΔGT., plotted separately.** Markers are colored according to gust types and labeled with the corresponding station.

For the case of ***jet* and *wake* gusts** (purple and yellow markers, Figure 8.13b), it can be seen that moving the gusts across all stations implies smaller grid transparency changes (at or below 5% amplitude for all except station 1, which converges from fully-open grid). Results for the $e_{RMS1,SS}/t_{\text{station}}$ parameter seem to be slightly more spread, from $0.005s^{-1}$ to around $0.035s^{-1}$ (excluding station 1), especially for the *wake* gust type (purple). Indeed for *jet* gust most stations present values around $0.01s^{-}1$, with only stations 2 and 6 presenting larger values. For the *wake* gust stations half of the sample lie around $0.025s^{-}1$ and the other half around $0.01s^{-}1$. The *wake* gust may be able to reach higher rates of change due to the half vane distance to the test section that is open to the flow (see the higher flow speed values in the extremes of 90deg uniform profiles, Figure 4.4 in Chapter 4. This may enhance the convergence to higher speeds in the outer regions.

The same effect may promote more turbulence in the outer regions of the *jet* gusts and thus limit their rate of change. In both *jet* and *wake* cases station 6 shows a high rate of change, which may be due to the gust translating in the center, far from the extremes . A favorable translation with respect to the vanes sense of rotation (which deviate flow to the left with increasing angles) may benefit the performance of *wake* in station 6.

Regarding the **differences across gust types** in closed-loop it should be highlighted that in view of the many effects taking place in the translation of dynamic gusts, it results challenging to explain the differences in convergence and in speed of response across the different gust types. A larger sample would be required to derive stronger conclusions. However, from the data presented preliminary conclusions can be extracted. Results suggest there is a lower limit imposed by the controller to the profile rate of change (around $0.01 s^{-1}$). Additionally, it seems that flow deviation and the turbulence generated play a relevant role in faster or slower convergence. Stations with larger rates of change seem to be those starting from a less turbulent and less decelerated flow (station 2), or resulting from a translation across the central regions (station 6 for *jet* and wake). Turbulence may be enhanced with vanes deviation of the flow and with the successive accelerations and decelerations. Note that fluctuations in the measurements may also be due to a degradation in the sensors performance with time. It also seems that *jet* and *wake* gusts may enable faster shape changes than *step* and *shear* gusts, for similar grid transparency changes.

As for the **error with respect to the reference profile**, the parameter $\mathbf{e_{RMS,ss}}$ is evaluated, as the root-mean-square error of the steady-state profile with the reference profile. This is the same as defined in the static gust case (see Chapter 7). The error for these dynamic gusts designs in closed-loop lies around $e_{RMS} = 0.15$, as seen in Figure 8.14; this value is within the same range of the 4-region static gust cases (see Figure 7.31, overall average on 0.2). Note that, although in the dynamic gust analysis the time given at each station is lower than the time given for each static gust design, grid transparency changes are also lower. It can be also seen that the *shear* profile presents the lowest error values, being more realistic regarding flow deviation than the other designs. Additionally, no significant differences are found in the error for larger station time t_{station}. Most station sampling times stay within 3.5 and 6s (excluding initial and final stations, 1 and 9).

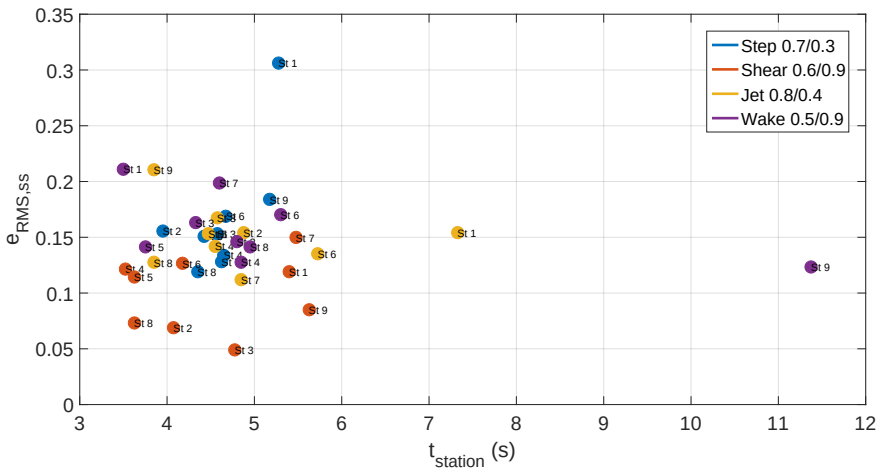

Figure 8.14: **Root-mean-square error between steady-state profile and reference profile, for closed-loop cases.** Increasing station times do not lead to deacreasing error.

8.3.2. Open-loop Lookup table approach

For the open-loop Lookup approach, an open-loop controller based on a closed-loop generated lookup table is used. Since the lookup table is only generated for *step* gust cases, these are the designs analyzed in the open-loop approach, with three different combinations of flow speed values. An interesting aspect to address with these cases is the effect of the vanes sense of rotation. A comparison across *step* gusts with different flow speed reference values may provide further insight on this. Additionally, the use of a lookup table gives a fixed vane configuration for each gust design; this will help analyze the differences in grid transparency changes of same amplitude but different sign. Note that this didn't occur in closed-loop because vane configurations converged each time.

Figure 8.15 shows the regions across which the marker moves during the three trials, as well as the end limits for each station. Station limits are selected far from noise areas in the marker's region. This is more relevant in this open-loop case than in the closed-loop one, since noise in the marker's position affects the response to a larger extent (Appendix G shows vanes angular position evolution in closed-loop). In closed-loop fast changes in the marker's position could not be sensed by the flow, and if they were, there was a continuous correction, whereas in open-loop every marker movement, even fast ones, will lead to a change in configuration. Since the marker moves faster than the accessing to the lookup table, this can lead to mismatches between the current marker's position and the current configuration, leading to grid transparency changes that are not representative of what occurred in most of the station.

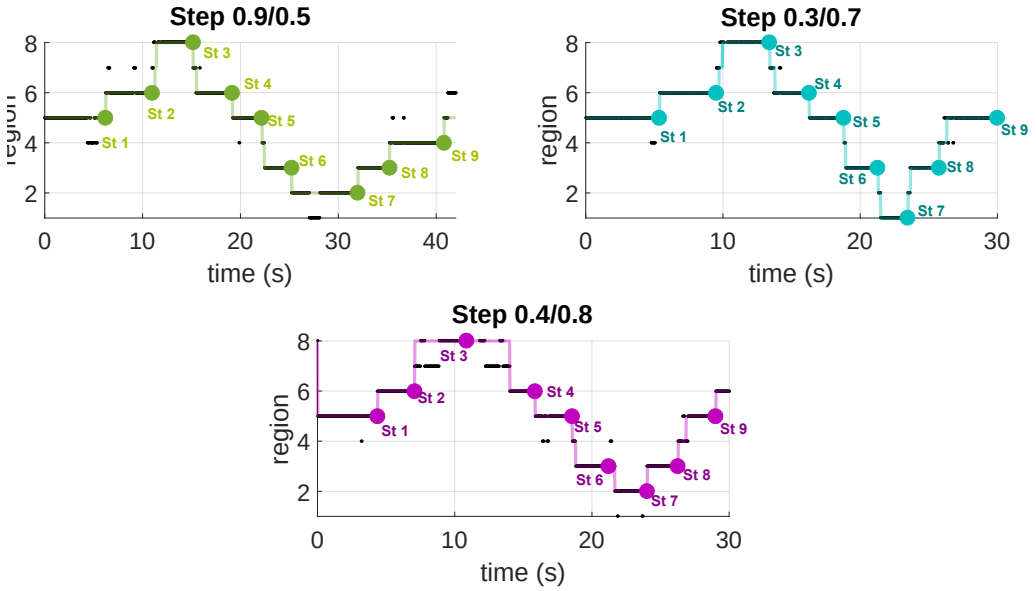

Figure 8.15: **Marker's position in time, for open-loop Lookup table cases.** Colors correspond to different gust types. Colored dots indicate the end of each of the stations. Only the first 9 stations are considered for the analysis.

The **evolution of the profiles in time**, for the three *step* gusts analyzed, across the nine stations considered, are shown in Figures 8.16 to 8.18. The same analysis is carried out as in the previous section. Note that in this case vanes angular position does not change gradually but instantly with the marker's position, and that there is no continuous correction since there is no feedback control.

The **effect of vanes sense of rotation** can be seen by observing the profiles evolution. Particularly, comparing the second (*step* 0.3/0.7) and third (*step* 0.4/0.8) cases with the first (*step* 0.9/0.5), when moving the marker (or the step profile transition point) to the left (stations 4, 5, 6, 7). When moving to and while in stations 6 and 7, it is especially evident that the *step* gusts with a lower reference flow speed value to the left (*step* 0.3/0.7 and *step* 0.4/0.8), present little shape change and show larger deviation from the reference. This is probably due to the flow deviation from the vanes to the right to the left regions, preventing from further reducing the flow speed. Note that for the *step* 0.4/0.8, the one with higher reference flow speed to the left, there is a closer match with the reference profile when moving the marker to the left extreme. In order to

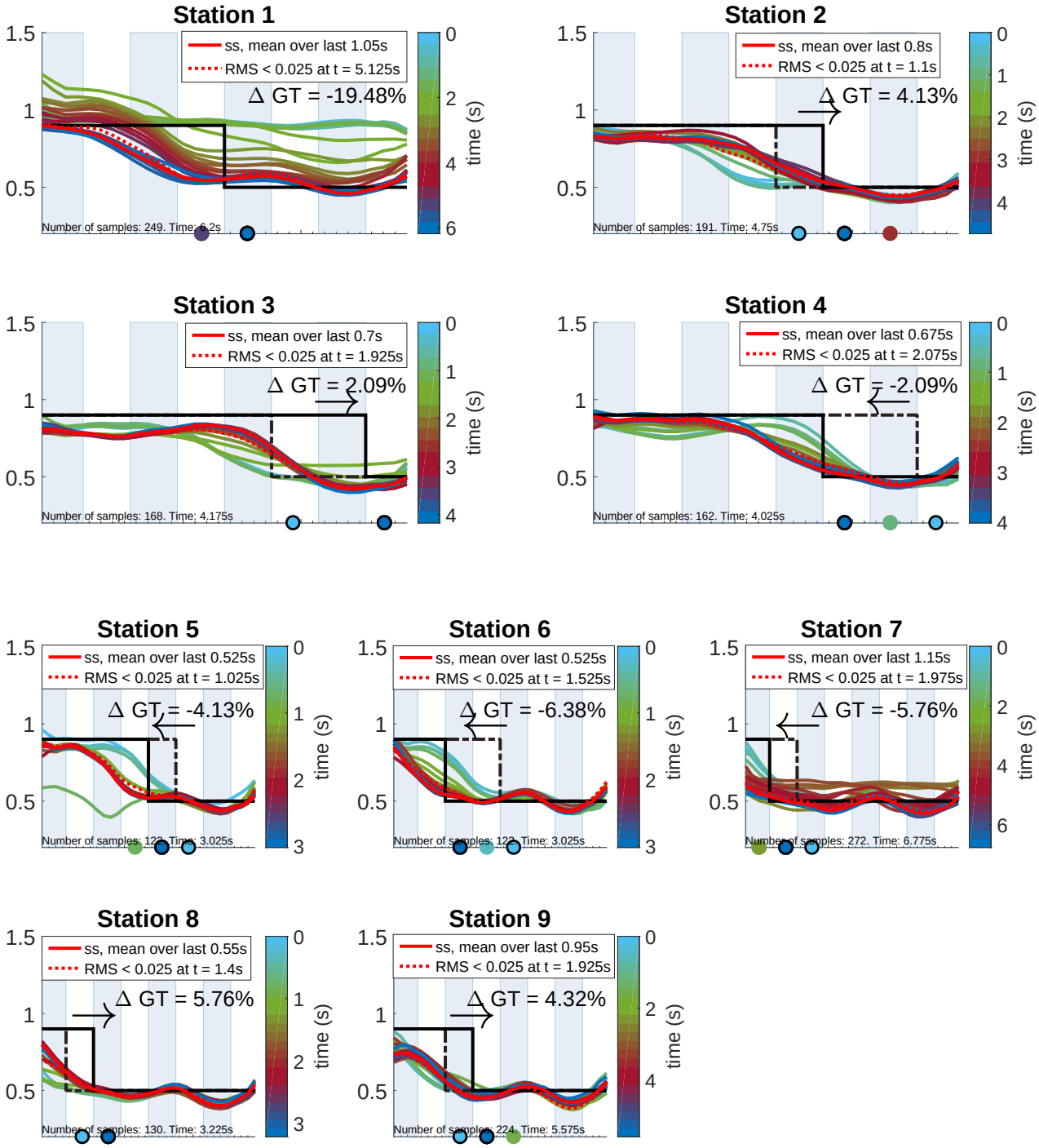

Figure 8.16: **Profiles evolution in time, for open-loop Lookup table dynamic gust Step 0.9/0.5, from stations 1 to 9.** Profiles are plotted with 0.25s timestep and colored with their progression in time as indicated by the colorbar. The reference profile at the start of the station (black dashed line) and at the end of the station (black solid line) are shown. Grid transparency change at the station is also included, obtained as the difference between final and initial grid transparency values at the station. Profile plotted in solid red line represent steady-state profile; profile in dotted red line indicates the profile at rms < 0.025. Note that the eight regions considered are alternatively shaded. Marker's position throughout the station is plotted on the x-axis as a colored dot, following the same color scheme as the profiles. Initial and final marker's position are contoured in black.

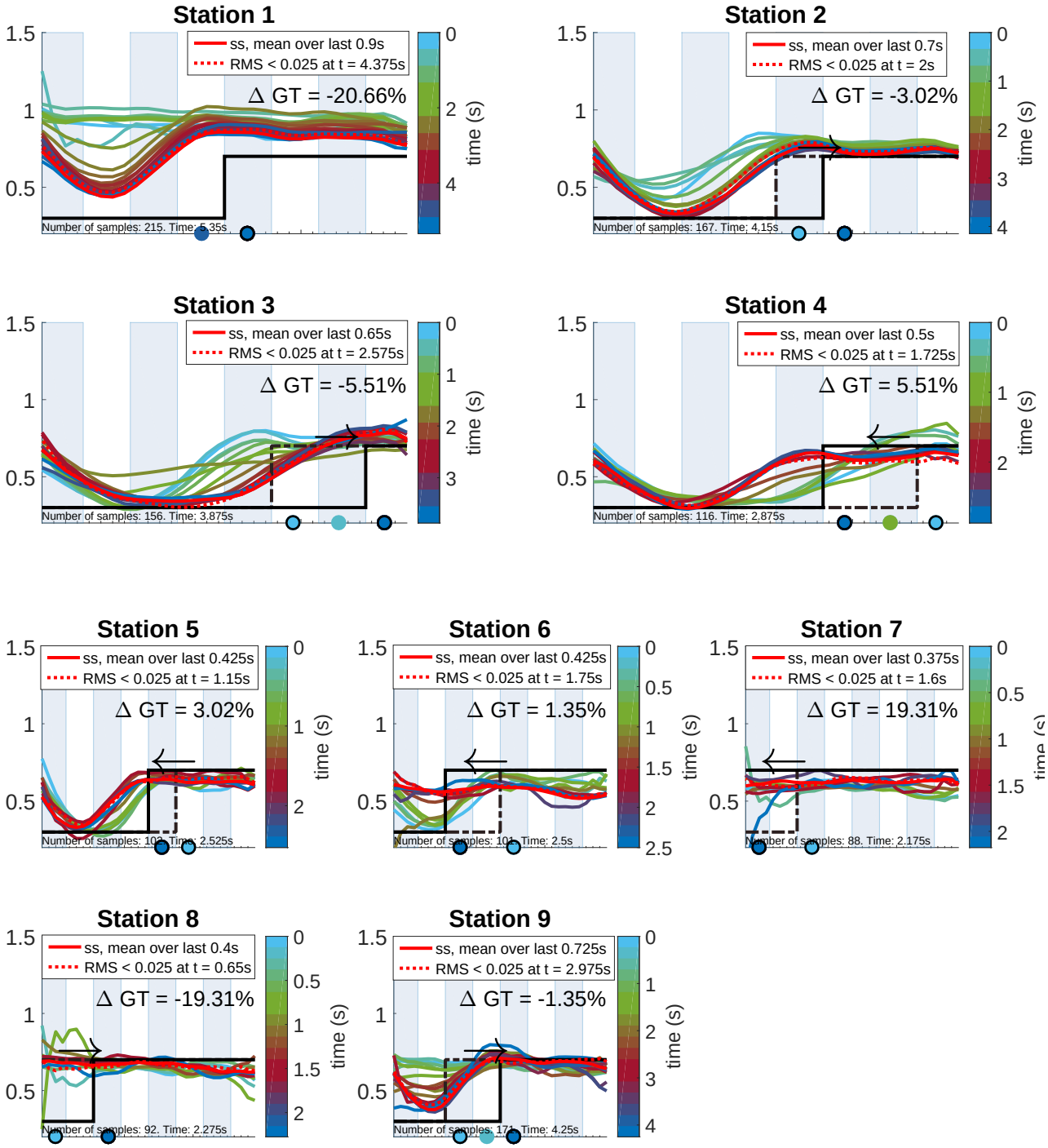

Figure 8.17: **Profiles evolution in time, for open-loop Lookup table dynamic gust Step 0.3/0.7, from stations 1 to 9.** Profiles are plotted with 0.25s timestep and colored with their progression in time as indicated by the colorbar. The reference profile at the start of the station (black dashed line) and at the end of the station (black solid line) are shown. Grid transparency change at the station is also included, obtained as the difference between final and initial grid transparency values at the station. Profile plotted in solid red line represent steady-state profile; profile in dotted red line indicates the profile at rms < 0.025. Note that the eight regions considered are alternatively shaded. Marker's position throughout the station is plotted on the x-axis as a colored dot, following the same color scheme as the profiles. Initial and final marker's position are contoured in black.

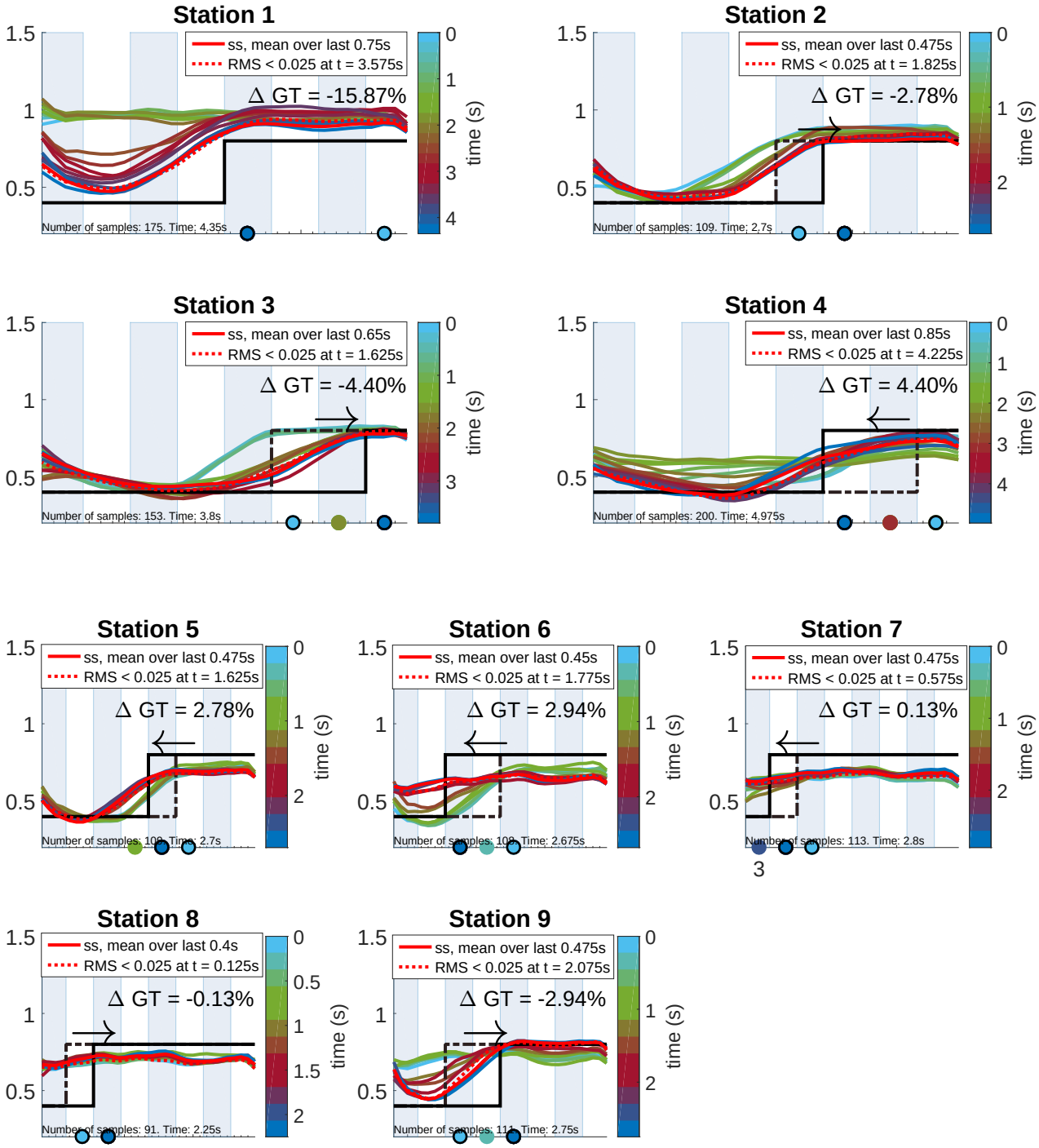

Figure 8.18: **Profiles evolution in time, for open-loop Lookup table dynamic gust Step 0.4/0.8, from stations 1 to 9.** Profiles are plotted with 0.25s timestep and colored with their progression in time as indicated by the colorbar. The reference profile at the start of the station (black dashed line) and at the end of the station (black solid line) are shown. Grid transparency change at the station is also included, obtained as the difference between final and initial grid transparency values at the station. Profile plotted in solid red line represent steady-state profile; profile in dotted red line indicates the profile at rms < 0.025. Note that the eight regions considered are alternatively shaded. Marker's position throughout the station is plotted on the x-axis as a colored dot, following the same color scheme as the profiles. Initial and final marker's position are contoured in black.

assess the differences quantitatively, the average rate of change in profile shape at each station is again evaluated, making use of the $e_{\text{RMS 1,ss}}/t_{\text{station}}$ parameter.

Figure 8.19 compares the values obtained for **rate of change** at each station, with the corresponding grid transparency changes. A first look reveals larger spread of values than those obtained in closed-loop. This seems to be in accordance with this approach changing grid transparency instantly and not gradually. Regarding differences between accelerating ($\Delta GT > 0\%$) and decelerating cases ($\Delta GT < 0\%$), most difference is found in step 0.9/0.5 (green dots) and step 0.4/0.8 (pink dots). For these cases, values for rate of change in deceleration, for similar grid transparency changes, appear slightly larger than corresponding acceleration ones. This is in accordance to what has been seen in previous chapters 5 and chapter 6. In contrast with these observed behaviours, step 0.3/0.7 (light blue dots) presents less variation in the computed rate of change for the different grid transparency changes, averaging around 0.035. Since this step presents the lower values for $\hat{U}_{ref,1}$ and $\hat{U}_{ref,2}$ of the analyzed set, it may be that accelerating (pressure gradient generated with each grid transparency change) and decelerating forces (mainly flow inertia) are of similar order. The symmetrical step to 0.3/0.7 has been analyzed in the closed-loop case, also showing little correlation with grid transparency. A more detailed comparison between approaches is discussed in the next section.

The use of a lookup table results in **symmetric grid transparency changes**; that is, grid transparency changes of equal amplitude but opposite sign. It can be seen from the profile plots (Figures 8.16 to 8.18) that stations 3 and 4, 7 and 8, and 2 and 5 present this kind of "symmetric" grid transparency changes. In Figure 8.19, step 0.9/0.5 (green) and step 0.3/0.7 (blue) show a rate of change similar for all symmetric pairs. This matches the symmetric behaviour seen for uniform profiles for small grid transparency changes (see Figure 5.22 in Chapter 5). However, step 0.4/0.8 (pink) shows a larger difference between symmetric pair values, with decelerating cases presenting larger rates of change. This may be due to a larger difference between accelerating and decelerating forces, maybe due to the turbulence induced by the particular vanes movement between both flow speed references, although this can only be speculative and more data would be required to extract definite conclusions on this.

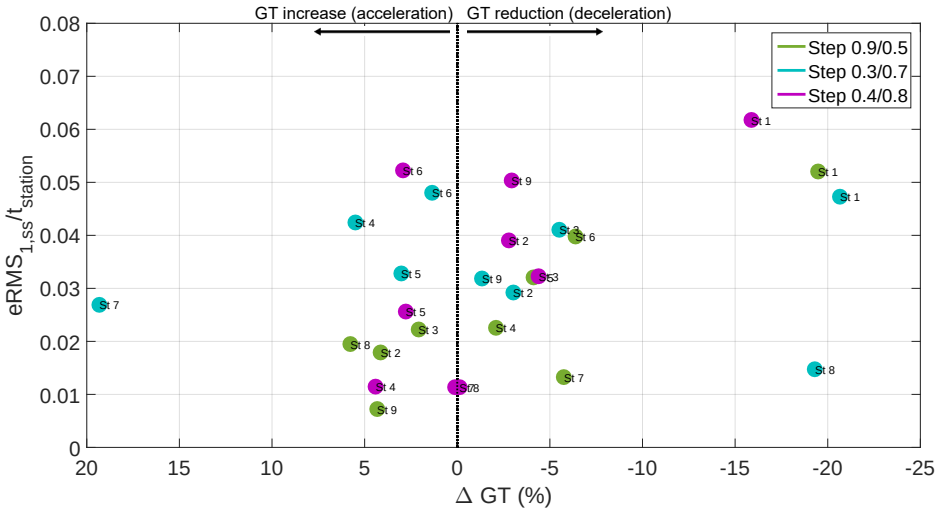

Figure 8.19: **Rate of change for all gust types and stations considered in open-loop Lookup approach, against grid transparency change ΔGT.** Markers are colored according to gust types and labeled with the corresponding station.

Finally regarding the **error between the steady-state profile and the reference profile**, it can be seen that similar values to the closed-loop case are reached, averaging around ~ 0.15 and with not much variation with increasing station timespan (Figure 8.20). It can thus be concluded that although there is no feedback control with this approach, the use of a closed-loop generated lookup table yields a similar range of error with respect to the reference profile than the closed-loop one. No particular benefit is found for *step* 0.9/0.5 (green), with higher flow speed at the left .

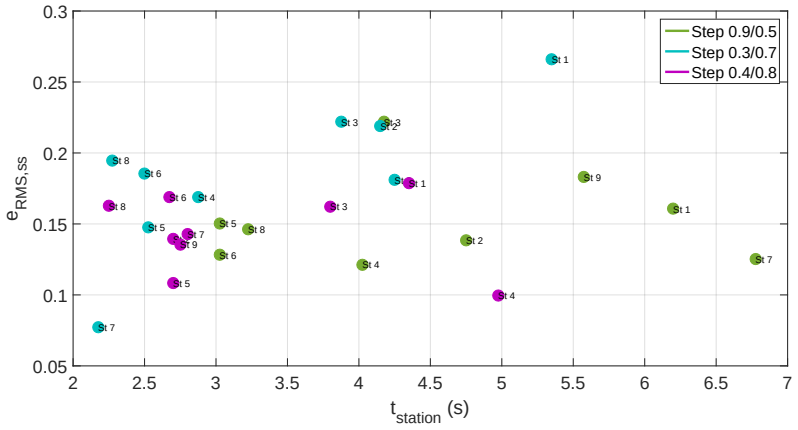

Figure 8.20: **Rate of change for all gust types and stations in open-loop Lookup table, against grid transparency change ΔGT.** Markers are colored according to gust types and labeled with the corresponding station.

8.3.3. Comparison of approaches

The speed of response results and the error obtained for the approaches considered are now compared. Figure 8.21 shows the results for the **rate of change parameter** for all the gust cases analyzed in closed-loop and open-loop. It can be seen that for the closed-loop case the average rate of change for each gust type is similar, with a mean value of $0.018s^{-1}$. For the open-loop case it can be seen that by reducing the delay for the controller's convergence and substituting the gradual change in vanes position with an instant one, a 72% higher average rate of change is obtained. Note as well that the open-loop approach presents a larger spread in the data, with a 36% higher standard deviation.

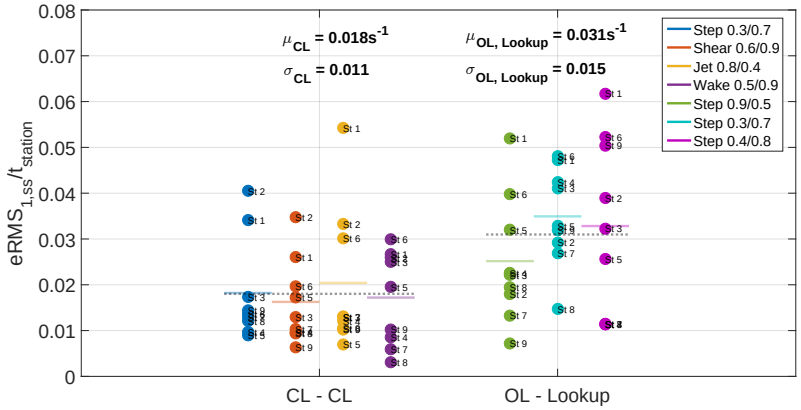

Figure 8.21: **Comparison of rate of change in profile shape across approaches.** Markers are colored according to gust types and labeled with the corresponding station. Average values for each gust type are indicated with horizontal colored lines. The average over each approach is plotted as a gray dotted line. Mean μ and standard deviation σ values for each approach are included at the top of the figure.

The numerator and denominator for the rate of change, $\mathbf{e_{RMS}}$ and $\mathbf{t_{station}}$, are looked into, to verify that the parameter is providing useful insight in the system's response. In Figure 8.22 it can be seen that the open-loop approach presents a range of values for e_{RMS} similar to the closed-loop results, but for stations with a timespan equal or lower than the closed-loop ones. This indicates that, overall, the change in profile shape occurs at a faster rate for the open-loop approach.

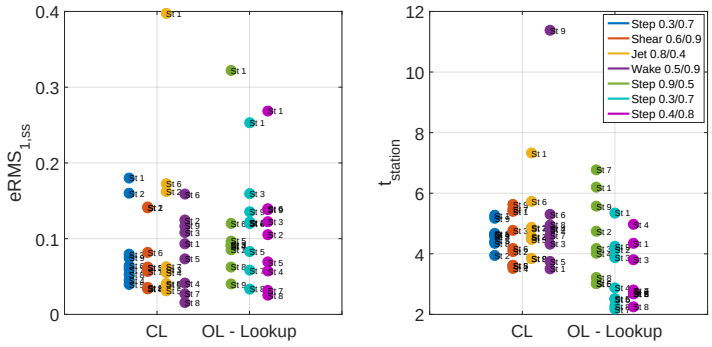

Figure 8.22: **Comparison across approaches of change in profile shape (left) and time at each station (right).** Markers are colored according to gust types and labeled with the corresponding station.

Regarding the **influence of grid transparency change ΔGT on the rate of change**, results from both approaches are shown in Figure 8.23a. At a first sight it can be seen that closed-loop values seem more limited to the lower region, compared to the open-loop ones; indeed standard deviation of open-loop cases is 36% larger, as mentioned). Correlation coefficients ρ and least-square linear fits, for each gust type and approach, are determined to analyze the relation between both parameters. The former are obtained following Pearson's definition, as the ratio between the covariance of the two variables over the product of their standard deviations. The value of ρ indicates how much of a linear dependency exists between the

variables, and the sign of their relation. Thus the coefficient's value ranges from -1 to 1, with ±1 indicating purely linear relation (increasing or decreasing) and 0 indicating no correlation.

From the linear fit trend lines shown on Figure 8.23a it seems that larger and more decelerating grid transparency changes lead to increased rates of change. However the correlation coefficients computed for each case show a large disparity of results, as shown in the figure. Considering all the data points a value $\rho = -0.4521$ is obtained. If results from stations 1 are removed (Figure 8.23b), lower grid transparency changes can be analyzed separately. In this case lower correlation coefficients are obtained for all cases, except for *wake 0.5/0.9* and *step 0.3/0.7*, and an overall $\rho = -0.1138$. Linear fit lines keep their slope sign, except for the closed-loop cases of *jet* and *wake* and the open-loop *step* 0.3/0.7. It can be concluded that for low grid transparency variations there is little correlation between grid transparency change and rate of profile change, in accordance to what has been discussed in the previous sections. Note however that the sample sizes considered are quite small, which increases the error in the computed coefficient.

Finally when analyzing the **error comparison**, it can be seen in Figure 8.24 that by using a closed-loop generated lookup table the level of error is reasonably kept, with just an increase of the average error value of ~ 11%. It should be highlighted that in closed-loop, *shear* gusts present a lower average error across all stations than the rest of gusts, which can be a valuable asset for designing dynamic gusts for experiments. Also worth commenting is the fact that the difference in *jet* and *wake* is not as large as expected, and thus the flow deviation due to the vanes does not result in a large error finally for the closed-loop approach. Regarding the spread of the error data, it can be seen again that using the lookup table generated in closed-loop results advantageous also in this aspect, since the standard deviation is ~ 90% of the closed-loop value.

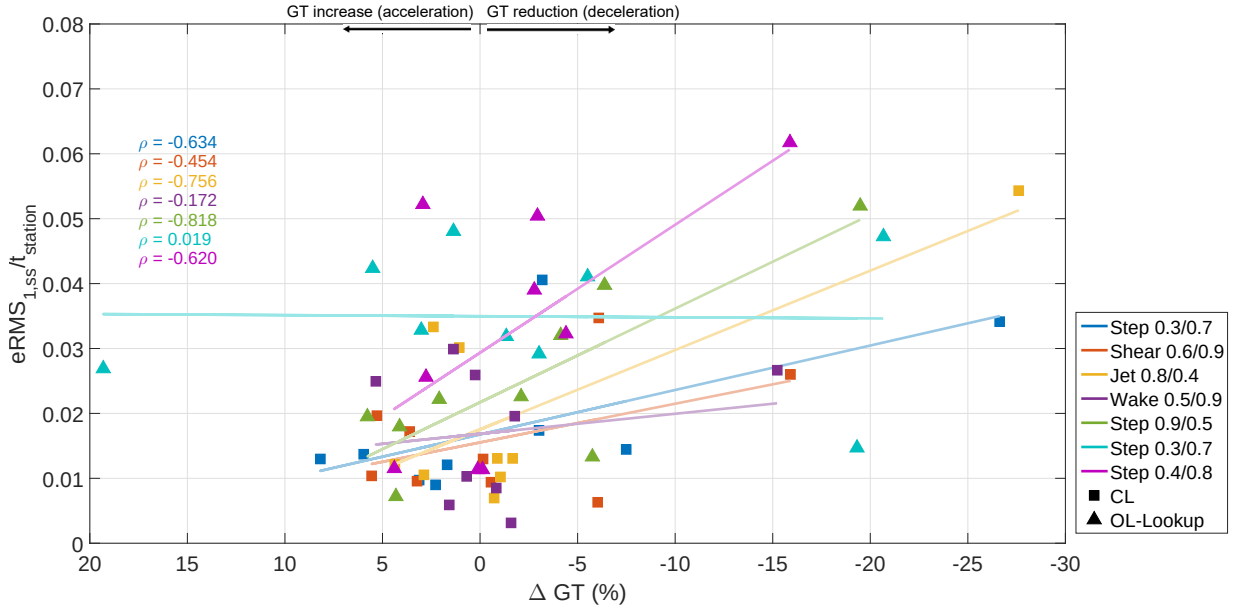

(a) **Rate of change for all gust types and stations, for all approaches, against grid transparency change ΔGT.** Marker shape indicates approach: square for closed-loop and diamond for open-loop. Colors correspond to gust types. Correlation coefficients and linear fit trend lines are included for reference, with the same color scheme. Closed-loop cases appear more limited to the lower part of the plot. Except for step 0.3/0.7, the rest of the cases show an increase in rate of change with larger GT reduction ($GT < 0$). However a large spread is found in the correlation coefficients rho obtained. Note that the sample is quite small for an accurate rho computation.

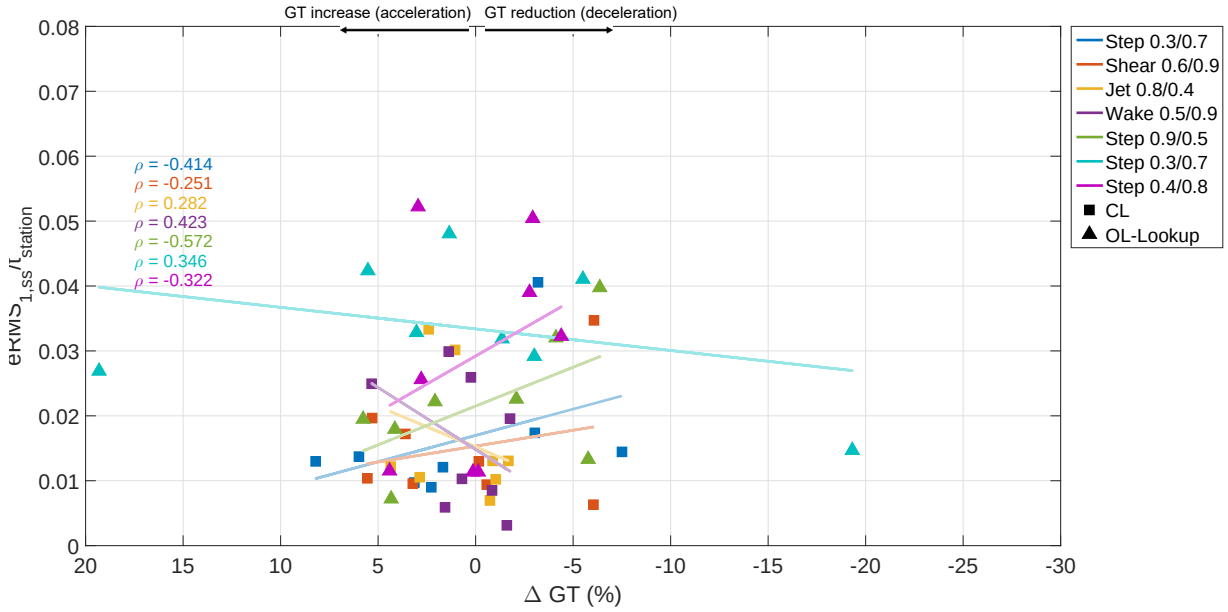

(b) **Rate of change for all gust types and stations, EXCEPT stations 1, for all approaches, against grid transparency change ΔGT.** Marker shape indicates approach: square for closed-loop and diamond for open-loop. Colors correspond to gust types. In this analysis stations 1 have not been considered. Correlation coefficients and linear fit trend lines are included for reference, with the same color scheme. Values shown correspond to lower grid transparency changes; for these cases there seems little correlation between both parameters. Note that some linear fit lines change slope sign when removing station 1 cases.

Figure 8.23: **Rate of change for all gust types and stations considered in open-loop and closed-loop approach, against grid transparency change ΔGT** Marker style corresponds to the approach type; color corresponds to gust type.

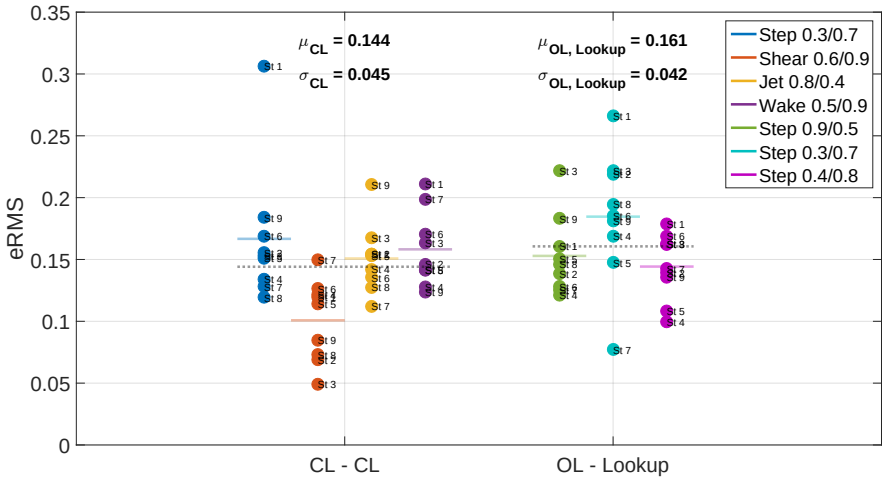

Figure 8.24: **Root-mean-square error between steady-state profile and reference profile, for all approaches.** Markers are colored according to gust types and labeled with the corresponding station. Average values for each gust type are indicated with horizontal colored lines. The average over each approach is plotted as a gray dotted line. Mean μ and standard deviation σ values for each approach are included in the top of the figure.

8.4. Conclusions

The objective of the dynamic gusts analysis is to demonstrate the capability of designing gusts which are able to follow a moving objective. The performance of the two approaches considered is compared in terms of speed of response and error, and the effect of small changes in grid transparency is looked into. Note that with respect to the static gust cases, grid transparency changes are now smaller in amplitude, include positive values of grid transparency changes, and start from an initial flow state which is not always fully-open grid (only for station 1 cases).

Regarding the comparison in terms of **speed of response**, the open-loop approach is an attempt to apply a nonlinear controller for the dynamic gusts designs, based on a Lookup table. Compared to the closed-loop approach (used mainly to populate said lookup table), the open-loop approach is expect to reduce computational delay (the desired vanes angular position is reached earlier). From the results shown in Figure 8.21, it can be seen that indeed a higher mean rate of change in the wind profile shape is observed in open-loop.

Note that the open-loop approach may also affect the speed of **flow response**, since as seen in previous chapters, the response varies when inputting vanes angles gradually (as with the discrete integral controller) or instantly (as with the lookup table). However, the difference on the flow response is expected to be small, since the grid transparency changes involved in translating dynamic gusts are low and thus an instant change in the vanes angular position will be similar to the gradual change imposed by the controller (which changes vanes angle at a rate 1.08deg per 0.1 difference between $\hat{U}_{ref}$ and $\hat{U}_{med}$, see Chapter 6). This seems to be the case when analyzing the results: with the open-loop approach an improvement on the average rate of change in the profile is obtained, but the improvement seems to be still limited by the flow's slow response. For the open-loop case it can also be seen a further spread in the data (see Figure 8.21); this may be because in closed-loop the controller speed is a function of the current error, and thus it follows if the flow response is fast (as with station 1 cases for example), but for most cases in which the gust is translated spanwise, the controller limits potentially faster rates of change.

As for the **error**, it has been shown that the open-loop Lookup table approach provides an error in the range of the closed-loop one (see Figure 8.24). This good resultis a consequence of the Lookup table being generated in closed-loop, with an integral controller. Note however that with no feedback signal the ability to correct for disturbances is lost.

Regarding the influence of the **grid transparency change** on the rate of change in the profile shape, the initial hypothesis assumed that the larger the grid transparency change, the larger the change in momentum in the flow, and thus the larger pressure gradient and accelerating force. However it seems, as seen in Chapter 6, that it is the relation between the accelerating force generated and the decelerating one what determines a faster or slower rate of change. It is not only relevant how much change of momentum is introduced in the flow through the grid transparency change, but also what was the initial state of the flow. This seems to be the case for the dynamic gust stations: large grid transparency changes at large initial flow speed conditions present large rates of change (station 1 cases). Cases with small grid transparency changes, which occur at initial states with lower inertia than fully-open grid ones, do not show a clear trend between rate of change and grid transparency amplitude. Note that the non-uniformity of the profiles makes the qualitative analysis quite challenging, and that other factors such as increased turbulence due to flow recirculation and consecutive accelerations/decelerations of the regions may play important roles.

Finally **differences across gust types** are also looked into for the closed-loop case, considering the decelerating contribution of the turbulence and flow recirculation induced by the profiles translation. From the analysis carried out it appears that *jet* and *wake* gusts enabled faster changes in the profile shape for small variations in grid transparency. Additionally, performance seem especially faster when translating them in the central regions. This may point them as good candidates for use in real time experiments. It was also observed that the *shear* gust profile presented low error values, probably due to being a more realistic reproduction of a *step* gust. However it is interesting to highlight the capability of designing tailored wind profiles with sharp slopes in this way.

8.4.1. Additional results: firing a gust demo and switching with $\Delta GT = 0$

As shown, the dynamic gust tool, limited mostly by a slow flow response, is not fast enough to follow fast maneuvering birds or drones. For lovebirds these are estimated to be in the order of 0.1s. However with the open-loop approach presented the dynamic gust tool could be used (as it is or with slight modifications) in some stability experiments, as it will be later developed on Chapter 9.

Two follow-up demos were carried out, and are outlined here as a proof of the potential of the presented tool. Both of them look into practical applications of the developed tool in real-time experiments.

The first one consists on a demo for a **firing a gust** approach. With small modifications on the dynamic gust setup, a simplified approach was built in which a gust is fired at the position of the retroreflective marker (when pushing the space bar in a wireless keyboard linked to the Labview PC). For this demo, initially all horizontal vanes were open and all vertical vanes were closed; upon "firing the gust" the vertical column of vanes at the marker's position opened to 90deg. Further developments could easily include different gust designs.

The next approach aimed for a faster flow response, by analyzing the switch from uniform to *jet* and to *wake* saturated profiles, with **no grid transparency change**, at a mean speed of 10m/ (with fixed fan speed). In this way the deceleration time was reduced to $\sim$ 2s, a large improvement but still too slow for real-time following of a bird's or MAV's fast maneuvers. An interesting next step would be to include the wind tunnel fan speed in the loop, to compensate the pressure loss across the grid and other sources of deceleration in order to increase the wind profile convergence time.

9

Conclusions and recommendations

A wind-tunnel Gust Design Tool with tracking capability has been developed at the level of proof-of-concept, for application in MAVs testing and animal flight stability studies. The presented tool is, to our knowledge, the first manipulated-stimuli approach built in a wind-tunnel. As such, the study has provided valuable guidelines for the construction of follow-up controllers or more sophisticated manipulated-stimuli setups. The final conclusions from the analysis are presented below, as well as recommendations for further developments. Suggestions for possible short and long term applications are also included.

9.1. Final conclusions

To set up the proposed Gust Design Tool, with the ability to follow a moving objective, a nonlinear controller has been suggested based on a closed-loop generated lookup table. To populate this lookup table and develop this nonlinear controller, different controllers have been built. In parallel, the flow response in the wind tunnel has been looked into and supporting theory has been provided to explain the different mechanisms observed. The analysis has been driven by two main goals: first, to assess the performance of the developed tool; second, to derive recommendations for follow-up controllers with a fast enough response for real-time fast bird maneuvers.

The main conclusions from the different sections addressed are summarized below.

- in the **open-loop analysis**, the flow response is found to be very slow and non-linear with the vanes angular position. The step response has been the main focus: its different characteristics have been analyzed and theory has been suggested to explain them. However, further exploration with more precise measurements is suggested, especially for the deadtime characterization, which seems to be related to flow phenomena. Since the system is nonlinear, a nonlinear controller is proposed for the design of dynamic gusts. This is based on a lookup table, that is populated making use of a closed-loop controller. This closed-loop controller is built in progressive steps, based initially on one, then four and finally eight regions.

- in the **manual tuning of the 1-region controller**, a discrete integral architecture for the controller is chosen, being the simplest solution for a zero steady-state error requirement in the profiles design. A dependency of the chosen parameter δt with the deadtime seems to exist and a loss of damping is found, linked to the increased time constant at low grid transparency states. This aspect could be fixed by choosing grid transparency as a manipulated variable in the controller. After manually tuning the controller parameters, its performance is found satisfactory to proceed with the 4-region design.

- in the **static gusts design with the 4-region controller**, different gust designs are looked into to assess potential benefits of certain profiles. It is found that profiles in which maximum blockage regions are separated perform better, for the same grid transparency reduction overall. The *shear* and *sawtooth* designs appeared particularly favourable, probably due to a good combination between flow deviation and blockage regions distribution. *Jet* gust design also presented potential advantage, although performance degraded for unsaturated cases, seemingly due to unfavourable flow deviation. The closed-loop approach is found useful for the design of the profiles, but the open-loop led to shorter times to convergence, supporting the next open-loop approach presented for dynamic gusts.

- in the **dynamic gust design**, the open-loop approach using the nonlinear controller, yields promising results. The performance of this controller, based on a closed-loop generated lookup table, is compared to the closed-loop approach used to populate the table. An improvement in convergence time is obtained, with similar error to the closed-loop approach. However the speed of response is not enough for following birds' or drones' fast maneuvers, mainly due to the slow flow response (6-10s to decelerate the flow, versus bird fast maneuvers estimated to be in the order of 0.1s). Two ways of improving this are additionally looked into to: first, a firing a gust demo was considered, which presented a practical implementation of the tool in a stability experiment context; however the response was still limited by the slow flow response. Another approach, from continuing work on the project, suggests switching from *uniform* to *jet* and *wake* profiles without grid transparency change . This approach, performed at a higher mean speed (10m/s) reduced decelerating time to convergence to around $\sim 2s$. Further recommendations on the next strategies to follow are detailed in the next section.

Possible current applications of the presented tool, with zero or little further development, are now discussed:

- the static gust setup presented could already be used to analyze the response of a hovering bird or flying robot to a destabilizing profile, of increasing intensity. The animal could be kept in hovering by feeding it from an artificial flower (as done in the works by Ortega-Jimenez et al. (2014b) and Ravi et al. (2015) with hummingbirds, and in the works by Ravi et al. (2013) and Crall et al. (2017) with bumblebees). It might be relevant to compare the progression of the wind profile with the progression of the main wingbeat kinematic variables (wingbeat frequency, wingbeat amplitude, stroke plane angle or body pitch, for example).

- the dynamic gust approach could be used in biomechanical studies and MAV testing to look into a stabilization in slow lateral translation. For experiments with animals, it might be useful to translate a feeder with a retroreflective marker and make the dynamic gust slowly follow

- the firing a gust demo can be applied as a step pitch input to the flying robot or bird; this approach may simplify the derivation of flight dynamics models. An interesting application would be to use it to compare the response of different ornithopter geometries: for example, comparing the response in yaw of configurations with and without tail.

9.2. Recommendations for follow-up designs

With the knowledge acquired on this exploratory study, the following guidelines are proposed. These summarize the suggested next steps for further development of this setup, ordered from short- to longer-term implementation:

- Regarding the **open-loop response**, a more detailed characterization of the dynamics of the system can be carried out with a more rigorous system identification approach. A good understanding of the system dynamics, with a realistic modeling of the flow mechanisms taking place, may help design more efficient controllers and understand the behaviour of the system in other operating conditions.

- As for the **controller for dynamic gust designs**, closed-loop approaches should be further looked into. Here, we proposed a nonlinear controller in open-loop, to fulfill requirements over the whole operating range. However, faster closed-loop controllers can be built, and a good performance can be obtained in the whole range by linearizing around different operating points. The use of grid transparency as manipulated variable should be looked into in these cases, since it is close to linear

with flow speed in steady-state. An architecture worth considering, for both profile design in closed-loop and dynamic gusts applications, is one that simultaneously combines an open-loop and closed-loop approach. By feeding forward the vane's position (derived for example from the third-order polynomial relation observed in steady-state Figure 4.2), and adding a discrete integral controller for corrections (similar to the one presented), a good precision in the design is expected with an improvement in the convergence speed. A further development would be to include the wind tunnel flow speed control in the loop, to compensate the loss of momentum when modifying grid transparency.

- From the additional results presented in 8.4.1, an increase in converging speed was observed for **switching profiles with zero grid transparency change** across them. On the other hand, results from open-loop uniform profiles in section 7.3.1, Figure 7.8, seemed to indicate that above a certain threshold (around 30% grid transparency reduction), larger grid transparency reductions led to faster convergences. Both approaches are recommended to look further into, and evaluate which one is more convenient. For reaching larger grid transparency changes, horizontal vanes can be included along to vertical ones to manipulate grid transparency, similarly to what is done in Roadman and Mohseni (2009a).

- Horizontal vanes can also be added as **turbulence injectors** with random flapping motions, separating in this way vertical vanes for gusts generation and horizontal vanes for turbulence injection. Switching these roles, horizontal vanes can also be added to recreate a scaled atmospheric boundary layer (ABL), while vertical vanes are used to inject turbulence in the flow. It would be very interesting to construct a controller for these applications; these controllers can be very similar to the one proposed here. This approach would generate conditions that are more realistic, closer to what is found in the ABL. This has been similarly done, with an open-loop approach, in the work by Cekli and van de Water (2010).

- In the static gust analysis, the *sawtooth* profile often presented faster convergence times than designs with equal grid transparency change but different distribution spanwise. The reason seemed to be a good combination of **blockage distribution and favourable flow deviation**. Although it was not considered in this study, a dynamic *sawtooth* gust may have a fast response and its recreation would be interesting as a spatial wave of gusts.

- The static gust designs proposed in space could be instead be inputted in time, similarly as done in the work by Chirarattananon et al. (2017). Another interesting **incorporation of time-variation** could be to consider changing gusts at a certain frequency; applied to a *step* gust might be a good way of recreating vortex shedding behind an obstacle (as done for example in the work by Ortega-Jimenez et al. (2014b)).

- Regarding more sophisticated manipulated-stimuli setups, some interesting applications could be to link the animal's or flying robot's response (and not just its position) to the stimuli presented. For example, if body pitch angle increases, then increase the intensity of the gust; or if wingbeat frequency increases, then increase the turbulence intensity injected.

The tool presented sets the first steps towards covering a current niche in both MAV testing and in studies on stability mechanisms in animal flight. For the first one, it allows the replication of relevant destabilizing effects in a wind tunnel, contributing to more rigorous testing and more robust designs. As for the second one, the tool aims to independently trigger some of the different mechanisms observed in birds, and proves a manipulated-stimuli approach implemented in a wind tunnel. This would facilitate the extraction of models for each case, resulting in a further understanding of biomechanics of flight, and in a easier translation of the observed mechanisms to new flying robots designs.

Bibliography

Abdulrahim, M., Watkins, S., Segal, R., Marino, M., and Sheridan, J. (2010). Dynamic sensitivity to atmospheric turbulence of unmanned air vehicles with varying configuration. *Journal of Aircraft*, 47(6):1873–1883.

Altshuler, D. L., Bahlman, J. W., Dakin, R., Gaede, A. H., Goller, B., Lentink, D., Segre, P. S., and Skandalis, D. A. (2015). The biophysics of bird flight: functional relationships integrate aerodynamics, morphology, kinematics, muscles, and sensors. *Canadian Journal of Zoology*, 93(12):961–975.

Badger, P. (2014a). New Rev P Wind Sensors | Modern Device. [Web Page]. Retreived on 2017-01-22, from, https://moderndevice.com/uncategorized/new-rev-p-wind-sensors/.

Badger, P. (2014b). Wind Sensor Rev. P - Low Cost Anemometer | Modern Device. [Web Page]. Retrieved on 2017-01-22, from, https://moderndevice.com/product/wind-sensor-rev-p/.

Beatus, T., Guckenheimer, J. M., and Cohen, I. (2015). Controlling roll perturbations in fruit flies. *Journal of The Royal Society Interface*, 12(105):20150075.

Brundrett, E. (1993). Prediction of pressure drop for incompressible flow through screens. *Journal of Fluids Engineering*, 115:239–242.

Caetano, J. V., de Visser, C. C., de Croon, G. C. H. E., Remes, B., Wagter, C. D., Verboom, J., and Mulder, M. (2013a). Linear aerodynamic model identification of a flapping wing MAV based on flight test data. *International Journal of Micro Air Vehicles*, 5(4):273–286.

Caetano, J. V., de Visser, C. C., Remes, B. D., De Wagter, C., Van Kampen, E. J., and Mulder, M. (2013b). Controlled flight maneuvers of a flapping wing micro air vehicle: a step towards the Delfly II identification. In *AIAA Atmospheric Flight Mechanics (AFM) Conference, 19-22 August 2013, Boston, Massachusetts*, number AIAA 2013-4843.

Caetano, J. V., Percin, M., Oudheusden, B. W. V., Remes, B., Wagter, C. D., Croon, G. C. H. E. D., and Visser, C. C. D. (2015). Error analysis and assessment of unsteady forces acting on a flapping wing micro air vehicle: free flight versus wind-tunnel experimental methods. *Bioinspiration & biomimetics*, 10(5):056004.

Cebeci, T. (2004). *Analysis of Turbulent Flows - 2nd Revised Edition*. Elsevier. Online version available at:. http://app.knovel.com/hotlink/toc/id:kpATFREE01/analysis-turbulent-flows/analysis-turbulent-flows.

Cekli, H. E. (2011). *How to stir turbulence*. PhD thesis, Eindhoven University of Technology.

Cekli, H. E. and van de Water, W. (2010). Tailoring turbulence with an active grid. *Experiments in Fluids*, 49(2):409–416.

Chirarattananon, P., Chen, Y., Helbling, E. F., Ma, K. Y., Cheng, R., and Wood, R. J. (2017). Dynamics and flight control of a flapping- wing robotic insect in the presence of wind gusts. *Interface Focus*, 7(1):20160080.

Combes, S. A. and Dudley, R. (2009). Turbulence-driven instabilities limit insect flight performance. *Proceedings of the National Academy of Sciences*, 106(22):9105–9108.

Comte-Bellot, G. and Corrsin, S. (1966). The use of a contraction to improve the isotropy of grid-generated turbulence. *Journal of Fluid Mechanics*, 25(04):657–682.

Corrsin, S. and Gad-El-Hak, M. (1974). Measurements of the nearly isotropic turbulence behind a uniform jet grid. *Journal of Fluid Mechanics*, 62(01):115.

Craig, K. (2002). Mechatronics course: control of a First-Order Process with Dead Time. [PDF document]. Retrieved on 2017-01-22 from NYU Engineering, Mechatronics Control Lab website at, http://engineering.nyu.edu/mechatronics/Control_Lab/Criag/Craig_RPI/2002/Week2/First-Order_Process_Time_Delay_2002.pdf.

Crall, J. D., Chang, J. J., Oppenheimer, R. L., and Combes, S. A. (2017). Foraging in an unsteady world: bumblebee flight performance in field- realistic turbulence. *Interface Focus*, 7(1):20160086.

Dantec Dynamics (2013a). Constant Temperature Anemometry (CTA) measurement principles | Dantec Dynamics. [Web Page]. Retrieved on 2017-01-22, from, http://www.dantecdynamics.com/measurement-principles-of-cta.

Dantec Dynamics (2013b). Hot-wire and Hot-film probe technical references | Dantec Dynamics. [Web Page]. Retrieved on 2017-01-22, from, http://www.dantecdynamics.com/hot-wire-and-hot-film-probes-technical-reference.

Dantec Dynamics (2013c). MiniCTA Measurement System | Dantec Dynamics. [Web Page]. Retrieved on 2017-01-22, from, http://www.dantecdynamics.com/minicta-system.

Dantec Dynamics (2013d). Single-sensor miniature wire probes | Dantec Dynamics. [Web Page]. Retrieved on 2017-01-22, from, http://www.dantecdynamics.com/products-and-services/single-sensor-miniature-wire-probes.

Davis, G. d. V. (1964). The flow of air through wire screens. In *Proceedings of the First Australasian Conference on Hydraulics and Fluid Mechanics, University of Western Australia, 6-13 December, Nedlands, Australia*, pages 191–212. Elsevier.

de Croon, G., Groen, M., De Wagter, C., Remes, B., Ruijsink, R., and van Oudheusden, B. W. (2012). Design, aerodynamics and autonomy of the DelFly. *Bioinspiration & biomimetics*, 7(2):025003.

de Wagter, C., Koopmans, A., de Croon, G., Remes, B., and Ruijsink, R. (2013). Autonomous wind tunnel free-flight of a flapping wing MAV. *Advances in Aerospace Guidance, Navigation and Control. Springer Berlin Heidelberg*, pages 603–621.

Di Luca, M., Mintchev, S., Heitz, G., Noca, F., and Floreano, D. (2016). Bioinspired morphing wings for extended flight envelope and roll control of small drones. *Interface Focus*, 7(1):20160092.

Donely, P. (1939). An experimental investigation of the normal acceleration of an airplane model in a gust. Technical Report No. 706, National Advisory Committee for Aeronautics.

Fisher, A., Ravi, S., Watkins, S., Watmuff, J., Wang, C., Liu, H., and Petersen, P. (2016). The gust-mitigating potential of flapping wings. *Bioinspiration & Biomimetics*, 11(4):046010.

Floreano, D. and Wood, R. J. (2015). Science, technology and the future of small autonomous drones. *Nature*, 521(7553):460–466.

Fritzing (2017). Fritzing software download. [Web Page]. Retrieved on 2017-01-2,2 from:, http://fritzing.org/download/.

Gutierrez, E., Quinn, D. B., Chin, D. D., and Lentink, D. (2016). Lift calculations based on accepted wake models for animal fl ight are inconsistent and sensitive to vortex dynamics. *Bioinspiration & Biomimetics*, 12(1):1–15.

Hedrick, T. L. (2011). Damping in flapping flight and its implications for manoeuvring, scaling and evolution. *Journal of Experimental Biology*, 214(24):4073–4081.

Ingimundarson, A. (2000). *Robust tuning procedures of dead-time compensating controllers*. Master thesis, Lund Insitute of Technology.

Irwin, H. (1981). A simple omnidirectional sensor for wind-tunnel studies of pedestrian-level winds. *Journal of Wind Engineering and Industrial Aerodynamics*, 7(3):219–239.

Keennon, M., Klingebiel, K., Won, H., and Andriukov, A. (2012). Tailless flapping wing propulsion and control development for the nano hummingbird micro air vehicle. In *50th AIAA Aerospace Sciences Meeting including the New Horizons Forum and Aerospace Exposition, 9-12 January 2012, Nashville, Tennessee*, number AIAA 2012-0588.

Knebel, P., Kittel, A., and Peinke, J. (2011). Atmospheric wind field conditions generated by active grids. *Experiments in Fluids*, 51(2):471–481.

Kress, D., van Bokhorst, E., and Lentink, D. (2015). How lovebirds maneuver rapidly using super-fast head saccades and image feature stabilization. *PLoS one*, 10(6):e0129287.

Laws, E. and Livesey, J. (1978). Flow through screens. *Annual Review of Fluid Mechanics*, 10(1):247–266.

Lentink, D. and Dickinson, M. H. (2009). Biofluiddynamic scaling of flapping, spinning and translating fins and wings. *Journal of Experimental Biology*, 212(16):2691–2704.

Lentink, D., Haselsteiner, A. F., and Ingersoll, R. (2015). In vivo recording of aerodynamic force with an aerodynamic force platform: from drones to birds. *Journal of The Royal Society Interface*, 12(104):20141283.

Lentink, D., Jongerius, S. R., and Bradshaw, N. L. (2009). The scalable design of flapping micro-air vehicles inspired by insect flight. In *Flying insects and robots*, chapter 14, pages 185–205. Springer Berlin Heidelberg.

LentinkLab (2016). Engineering Methods | LentinkLab. [Web Page]. Retrieved on 2017-01-22, from, http://lentinklab.stanford.edu/welcome/engineering_methods.

Ma, K. Y., Chirarattananon, P., Fuller, S. B., and Wood, R. J. (2013). Controlled flight of a biologically inspired, insect-scale robot. *Science*, 340(6132):603–607.

Makita, H. (1991). Realization of a large-scale turbulence field in a small wind tunnel. *Fluid Dynamics Research*, 8(1-4):53–64.

Manglik, R. (1997). Heat Transfer Fluid Flow Data Books - 406.4 Water Hammer. In *Heat Transfer and Fluid Flow Data Books*, pages 406.4.1–406.4.19. Genium Publishing Corporation, Amsterdam, NY (USA).

McMaster-Carr (2016). McMaster-Carr. [Web Page]. Retrieved on 2017-01-22, from, https://www.mcmaster.com/.

Microchip (2016). Low-Power Linear Active Thermistor ICs Datasheet - MCP9700/9700A MCP9701/9701A. [PDF Document]. Retrieved on 2017-01-22, from, http://ww1.microchip.com/downloads/en/DeviceDoc/20001942G.pdf.

Mohamed, A., Abdulrahim, M., Watkins, S., and Clothier, R. (2016). Development and flight testing of a turbulence mitigation system for micro air vehicles. *Journal of Field Robotics*, 33(5):639–660.

Mohamed, A., Massey, K., Watkins, S., and Clothier, R. (2014a). The attitude control of fixed-wing MAVS in turbulent environments. *Progress in Aerospace Sciences*, 11(1):37–48.

Mohamed, A., Watkins, S., Clothier, R., and Abdulrahim, M. (2014b). Influence of turbulence on MAV roll perturbations. *International Journal of Micro Air Vehicles*, 6(3):175–191.

Moya, R. and Prohasky, D. (2014). Tutorial – Mini Airflow Tunnel Project. [Web Page]. Retrieved on 2017-01-22, from, https://miniwindtunnel.wordpress.com/tutorial/.

Moya, R., Prohasky, D., Watkins, S., Ding, Y., and Burry, J. (2014). Aerodynamic strategy applied in an urban shelter design - Simulation and analysis of aerodynamic phenomena in an urban context. In *eCAADe 2014: Fusion-data integration at its best, Northumbria University, Newcastle upon Tyne, 10-12 September 2014*, volume 1, pages 137–144. Association for Computer Aided Design in Architecture.

Mydlarski, L. and Warhaft, Z. (1996). On the onset of high-Reynolds-number grid-generated wind tunnel turbulence. *Journal of Fluid Mechanics*, 320(1):331–368.

National Instruments (2017). LabVIEW System Design Software - National Instruments. [Web Page]. Retrieved on 2017-01-22 from, http://www.ni.com/labview/.

Ogata, K. (2002). *Modern Control Engineering - 4th Edition*. Pearson Education International, Prentice Hall, Upper Saddle River, New Jersey.

Ortega-Jimenez, V. M., Greeter, J. S. M., Mittal, R., and Hedrick, T. L. (2013). Hawkmoth flight stability in turbulent vortex streets. *Journal of Experimental Biology*, 216(24):4567–4579.

Ortega-Jimenez, V. M., Mittal, R., and Hedrick, T. L. (2014a). Hawkmoth flight performance in tornado-like whirlwind vortices. *Bioinspiration & Biomimetics*, 9(2):025003.

Ortega-Jimenez, V. M., Sapir, N., Wolf, M., Variano, E. A., and Dudley, R. (2014b). Into turbulent air: size-dependent effects of von Kármán vortex streets on hummingbird flight kinematics and energetics. *Proceedings of the Royal Society of London B: Biological Sciences*, 281(1783):20140180.

Paranjape, A. A., Dorothy, M. R., Chung, S.-j., and Lee, K. D. (2012). A flight mechanics-centric review of bird-scale flapping flight. *International Journal of Aeronautical and Space Sciences*, 13(3):267–281.

Pete, A. E., Kress, D., Dimitrov, M. A., and Lentink, D. (2015). The role of passive avian head stabilization in flapping flight. *Journal of The Royal Society Interface*, 12(110):20150508.

Pinker, R. A. and Herbert, M. V. (1967). Pressure loss associated with compressible flow through square-mesh wire gauzes. *Journal of Mechanical Engineering Science*, 9(I):11–23.

Prohasky, D., Moya, R., Watkins, S., and Burry, J. (2014). Wind sensing with real-time visualisations for Designers - An approach to understanding wind phenomena for pedestrian comfort using low cost wind sensors. In *eCAADe 2014: Fusion-data integration at its best, Northumbria University, Newcastle upon Tyne, 10-12 September 2014*, pages 165–171. Association for Computer Aided Design in Architecture.

Prohasky, D. and Watkins, S. (2014). Low Cost Hot-element Anemometry Verses the TFI Cobra. In *19th Australasian Fluid Mechanics Conference, Melbourne, Australia, 8-11 December 2014*.

Qualisys Motion Capture Systems (2011). QTM Qualisys Track Manager - User Manual. [Web Page]. Retrieved on 2017-01-22, from, http://fy.chalmers.se/~f7xiz/TIF081C/QTM-usermanual.pdf.

Quinn, D. B., Watts, A., Nagle, T., and Lentink, D. (2015). A new low-turbulence wind tunnel for animal and small vehicle flight experiments. [Manuscript submitted for publication].

Ravi, S., Crall, J. D., Fisher, A., and Combes, S. A. (2013). Rolling with the flow: bumblebees flying in unsteady wakes. *Journal of Experimental Biology*, 216(22):4299–4309.

Ravi, S., Crall, J. D., McNeilly, L., Gagliardi, S. F., Biewener, A. A., and Combes, S. A. (2015). Hummingbird flight stability and control in freestream turbulent winds. *The Journal of experimental biology*, 218(9):1444–1452.

Reeh, A. D. (2014). *Natural laminar flow airfoil behavior in cruise flight through atmospheric turbulence*. PhD thesis, Technische Universität Darmstadt.

Roach, P. E. (1987). The generation of nearly isotropic turbulence by means of grids. *International Journal of Heat and Fluid Flow*, 8(2):82–92.

Roadman, J. M. and Mohseni, K. (2009a). Gust characterization and generation for wind tunnel testing of micro aerial vehicles. In *47th AIAA Aerospace Sciences Meeting Including The New Horizons Forum and Aerospace Exposition, 5-8 January 2009, Orlando, Florida*, number AIAA 2009-1290.

Roadman, J. M. and Mohseni, K. (2009b). Large scale gust generation for small scale wind tunnel testing of atmospheric turbulence. In *39th AIAA Fluid Dynamics Conference, 22-25 June 2009, San Antonio, Texas*, number AIAA 2009-4166.

SmallRig (2017). Professional camera accessories | SmallRig. [Web Page]. Retrieved on 2017-01-22, from, http://www.smallrig.com/.

Taylor, G. K., Bacic, M., Bomphrey, R. J., Carruthers, A. C., Gillies, J., Walker, S. M., and Thomas, A. L. R. (2008). New experimental approaches to the biology of flight control systems. *Journal of Experimental Biology*, 211(2):258–266.

Turbulent Flow Instrumentation (2016). Products: Cobra probe. [Web Page]. Retrieved on 2017-01-22, from, http://www.turbulentflow.com.au/Products/CobraProbe/CobraProbe.php.

Ulrich, E. R. (2012). *Design, developement, analysis and control of a bio-inspired robotic samara rotorcraft*. PhD thesis, University of Maryland, College Park.

van Halder, Y. (2015). Turbulence Grid Manual. [PDF Document]. Retrieved on 2016-03-01, from LentinkLab private wiki site, aviary.stanford.edu.

Warwick, K. and Rees, D. (1988). *Industrial digital control systems*. Number 37. Peter Peregrinus Ltd. on behalf of the Institution of Electrical Engineers, London, UK.

Watkins, S., Abdulrahim, M., Thompson, M., Shortis, M., Loxton, B. J., Segal, R., Bil, C., and Watmuff, J. (2009). An overview of experiments on the dynamic sensitivity of MAVs to turbulence. In *AIAA Guidance, Navigation, and Control Conference, 10-13 August 2009, Chicago, Illinois*, number AIAA 2009-5906.

Watkins, S., Fisher, A., Mohamed, A., Marino, M., Thompson, M., Clothier, R., and Ravi, S. (2013). The turbulent flight environment close to the ground and its effects on fixed and flapping wings at low Reynolds number. In *5th European Conference for Aeronautics and Space Sciences (EUCASS), Munich, Germany, 1–5 July 2014*, pages 1–10.

Watkins, S., Milbank, J., Loxton, B. J., and Melbourne, W. H. (2006). Atmospheric winds and their implications for microair vehicles. *AIAA Journal*, 44(11):2591–2600.

Watkins, S., Thompson, M., Loxton, B., and Abdulrahim, M. (2010). On Low Altitude Flight Through The Atmospheric Boundary Layer. *International Journal of Micro Air Vehicles*, 2(2):55–68.

Williams, C. D. and Biewener, A. A. (2015). Pigeons trade efficiency for stability in response to level of challenge during confined flight. *Proceedings of the National Academy of Sciences*, 112(11):3392–3396.

Williams, M., Moya, R., Prohasky, D., Khorasgani, M. L., Watkins, S., Burry, M., Burry, J., and Belesky, P. (2015). A physical and numerical simulation strategy to understand the impact of the dynamics in air for the design of porous screens. In *Proceedings of the Symposium on Simulation for Architecture and Urban Design SimAUD 2015, 12-15 April 2015, Alexandria, Virginia*, pages 1085–1092. Society for Modeling and Simulation International.

Wyngaard, J. and Clifford, S. (1977). Taylor's hypothesis and high-frequency turbulence spectra. *Journal of Atmospheric Sciences*, 34(6):922–929.

Zbrozek, J. (1960). The relationship between the discrete gust and power spectra presentations of atmospheric turbulence, with a suggested model of low-altitude turbulence. Technical Report 3216, HM Stationery Office. Aeronautical Research Council Reports and Memoranda.

A

Experimental setup additional information

Wind sensor array in wind tunnel

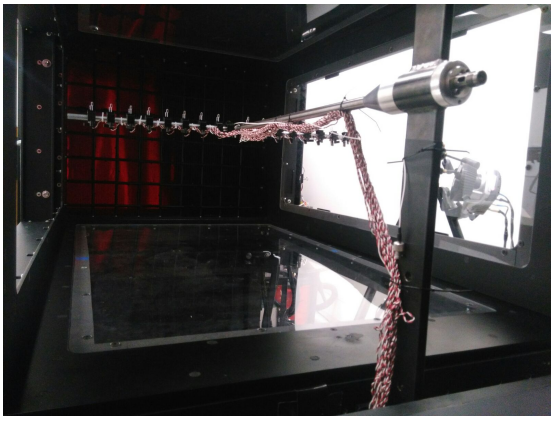

Figure A.1: Array in wind tunnel, view from downstream (1).

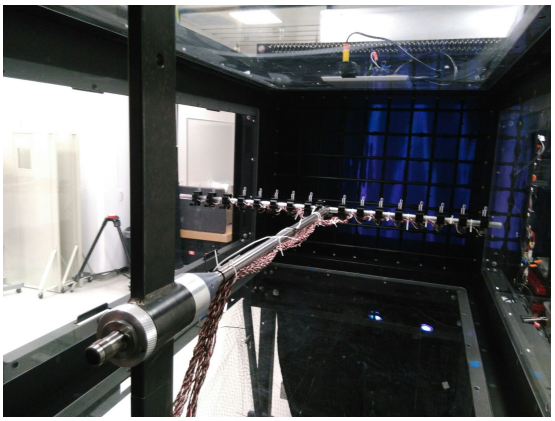

Figure A.2: Array in wind tunnel, view from downstream (2)

Figure A.3: Motion capture cameras

Figure A.4: Labview PC and USB dongle with XBee module

Figure A.5: Array wiring to Arduino board and XBee module.

Labview VIs screenshots

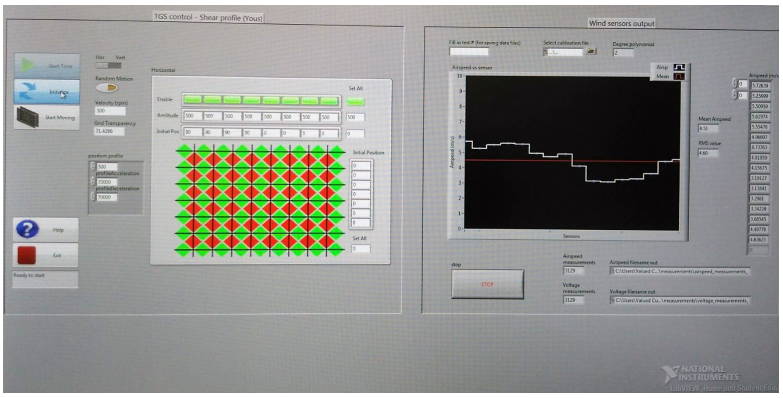

Figure A.6: Open-loop Labview VI: grid controls to the left (developed by Yous van Halder), wind sensor array readings to the right

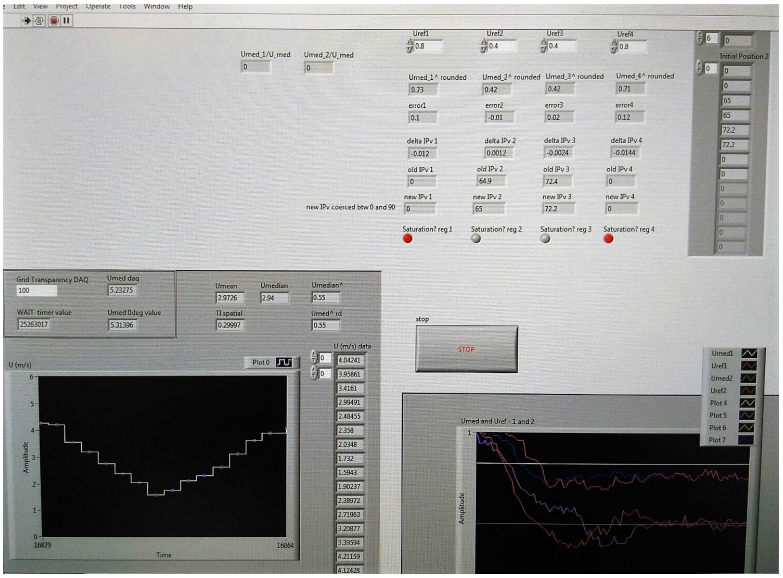

Figure A.7: Labview VI user screen for 4-region closed-loop controller designing *wake* gust.

Clamps array setup

Figure A.8: Types of clamps used for the array setup. Left and center show the clamps used to hold sensors (wind sensors and hotwire probe); right shows the rectangular clamp used to attach the array to the wind tunnel traverse. Images from SmallRig (2017).

B

Open-loop steady state: additional results

Fit for relation flowspeed - vane angle

Equation of fit:

$$U = p_1\hat{P}^3 + p_2\hat{P}^2 + p_3\hat{P} + p_4 \tag{B.1}$$

with $\hat{P} = P/90$ and $p_1 = 0.4943, p_2 = -0.2528, p_3 = -0.963, p_4 = 1.042$. Goodness-of-fit parameters: $SSE = 0.0083$, $R^2 = 0.9922$, $R_{adj} = 0.9907$, $RMSE = 0.0235$.

TI spatial

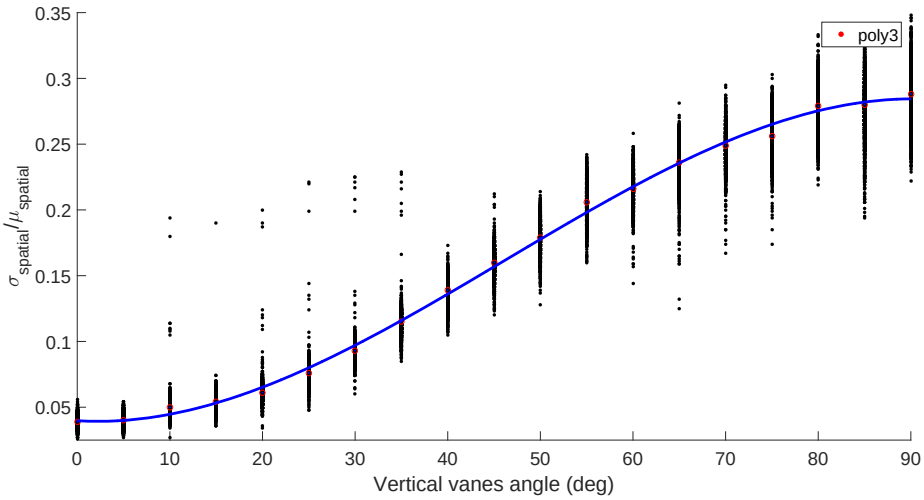

Figure B.1: Turbulence intensity parameter computed spatially $\sigma_{\text{spatial}}/\mu_{\text{spatial}}$

C

Open-loop transient: additional results

Wind sensors + Hotwire, 5s step: profiles evolution in time

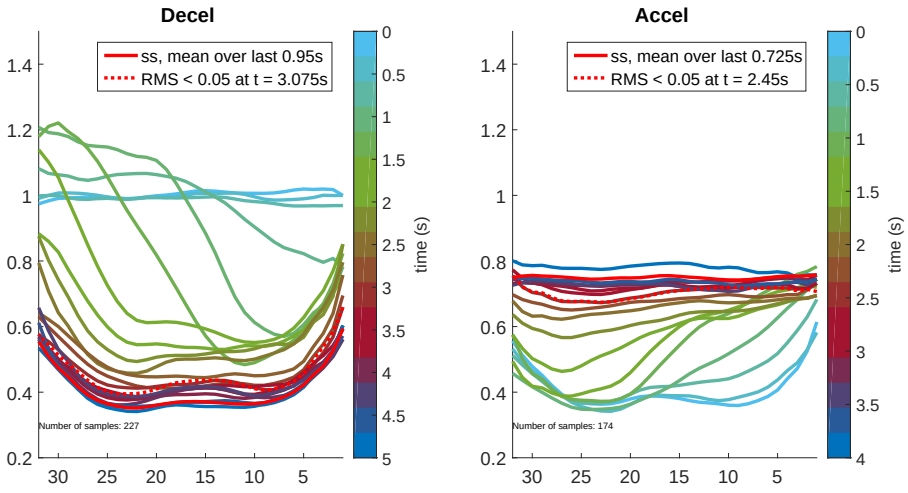

Figure C.1: Profiles evolution in time for decelerating 90deg step (right) and accelerating (left).

Staircase response

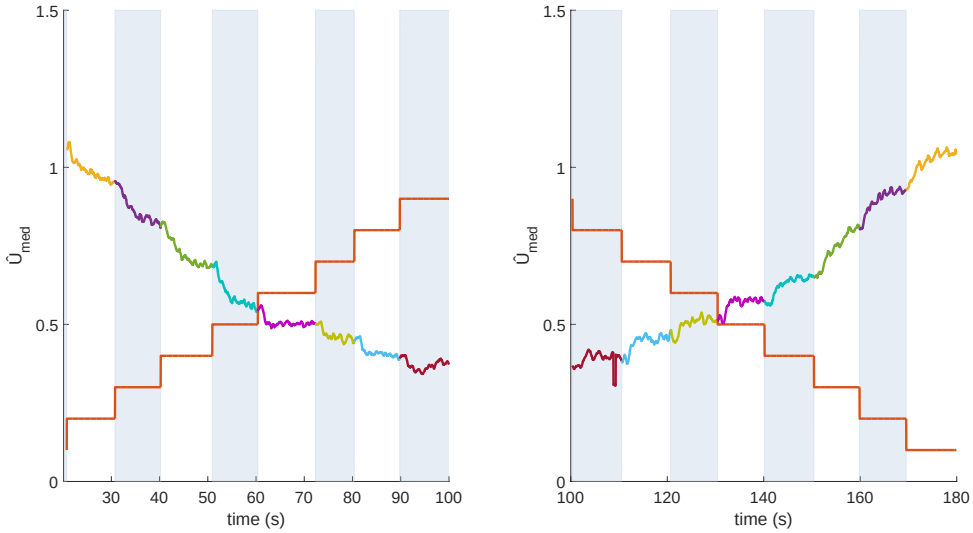

(a) Staircase response: separation decelerating and accelerating steps; each step is 10deg.

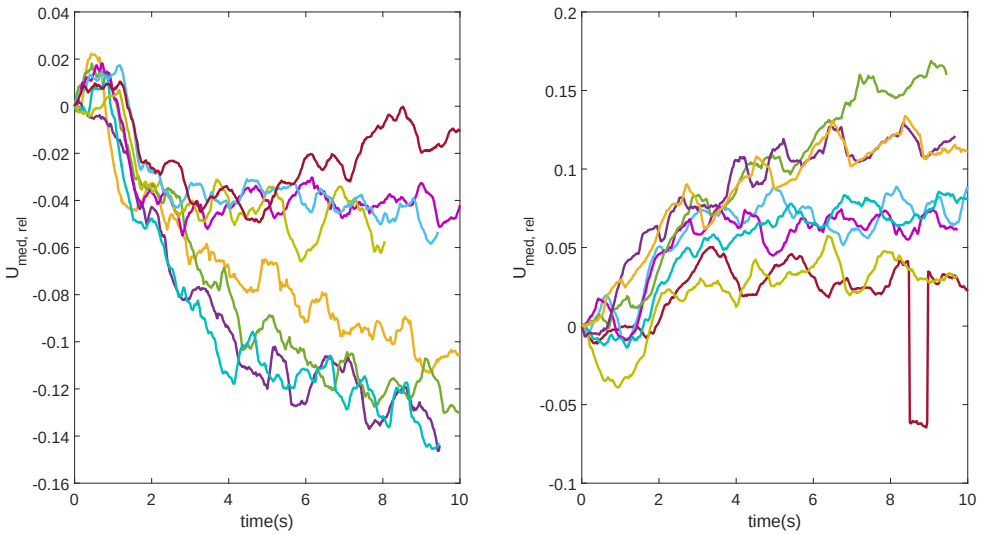

(b) Staircase response: comparison of responses decelerating and accelerating steps; note responses are referred to initial step value

D

Linear models

First order model

A first order model between input vanes angle and output median flow response can be derived:

$$G(s) = \frac{\hat{U}_{med}(s)}{\hat{P}(s)} = \frac{K}{\tau s + 1} = \frac{-0.765}{1 + 3.65s} \tag{D.1}$$

where K is the system's gain and τ the system's time constant. The fit to estimation data with this model is of 73.39%, MSE (mean-square error) = 0.006808.

First order + deadtime model

The next step would be to include the dead time in the model. If we model the dead-time element as shown in Figure D.1, input and output signals in the time domain can be related as follows:

$$y(t) = x(t - \tau_{DT}) \cdot H(t - \tau_{DT}) \tag{D.2}$$

where $x(t)$ and $y(t)$ are input and output signals and H is the Heaviside function on τ_{DB}:

$$H(t - \tau_{DB}) = \begin{cases} 1 & \text{if } t \geq \tau_{DB} \\ 0 & \text{if } t < \tau_{DB} \end{cases} \tag{D.3}$$

Taking the Laplace transform in equation D.2:

$$\mathscr{L}\{y(t)\} = \mathscr{L}\{x(t - \tau_{DT}) \cdot H(t - \tau_{DT})\} \tag{D.4}$$

It results for the Laplace domain:

$$Y(s) = e^{-\tau_{DB}s} \cdot X(s) \tag{D.5}$$

Thus, the dead-time element is equivalent to a block $e(s)^{-\tau_{DB}s}$ and the transfer function for this first order system with dead time would be:

$$G(s) = \frac{\hat{U}_{med}(s)}{\hat{P}(s)} = \frac{K \cdot e^{-\tau_{DB}s}}{\tau s + 1} \tag{D.6}$$

Figure D.1: **Block diagram for dead time element.** Input and output time signals, $x(t)$ and $y(t)$ are shown

E

Wind sensor yaw measurements

Wind sensor yaw measurements

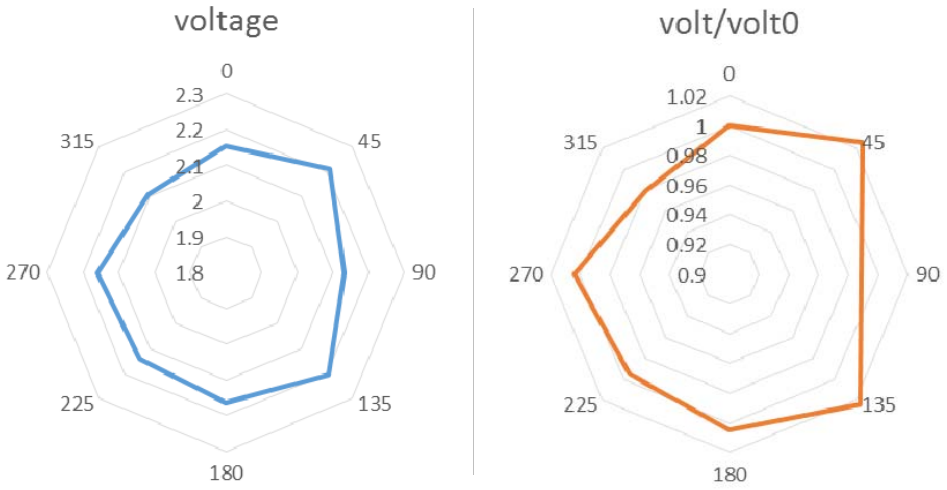

Figure E.1: Yaw dependance in term of voltage for one of the wind sensors. Left plot: absolute values; right plot: values relative to voltage at 0deg.

Static gusts: additional results

OL Uniform profiles, deadtime determination: response and parameters

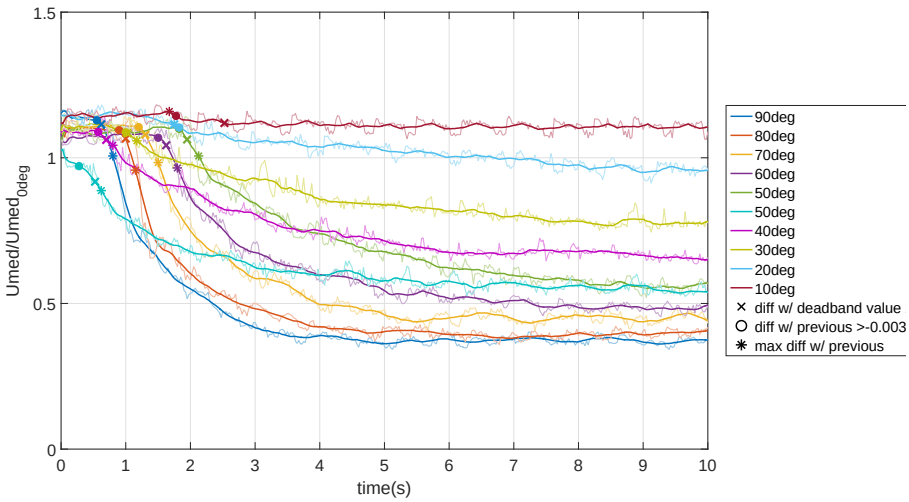

Figure F.1: Median flow response for open-loop decelerating steps in vanes angle. Data smoothed with a moving average over 20 samples (raw data plotted in a thinner line); deadband value computed as mean over first 20 samples. Slope threshold for $slope_{th}$ determined by observing the slope evolution, aiming to match the instant it starts to increase

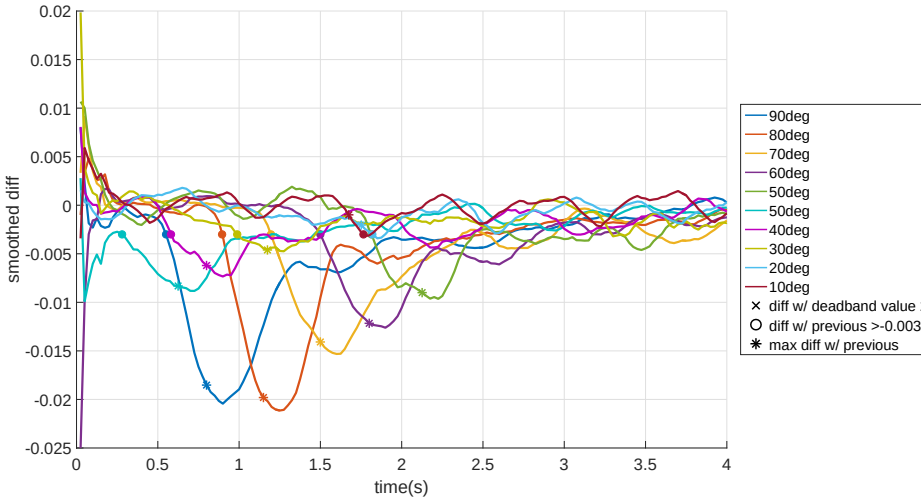

Figure F.2: Static gusts open-loop uniform profiles, deadtime determination: slope in decelerating steps. Slope threshold determined from the slope evolution, trying to match the instant it starts to increase; a value of -0.003 is selected. Star marker indicates maximum slope within a window from 0.1 to 5s

G

Dynamic gusts: additional results

Closed-loop approach

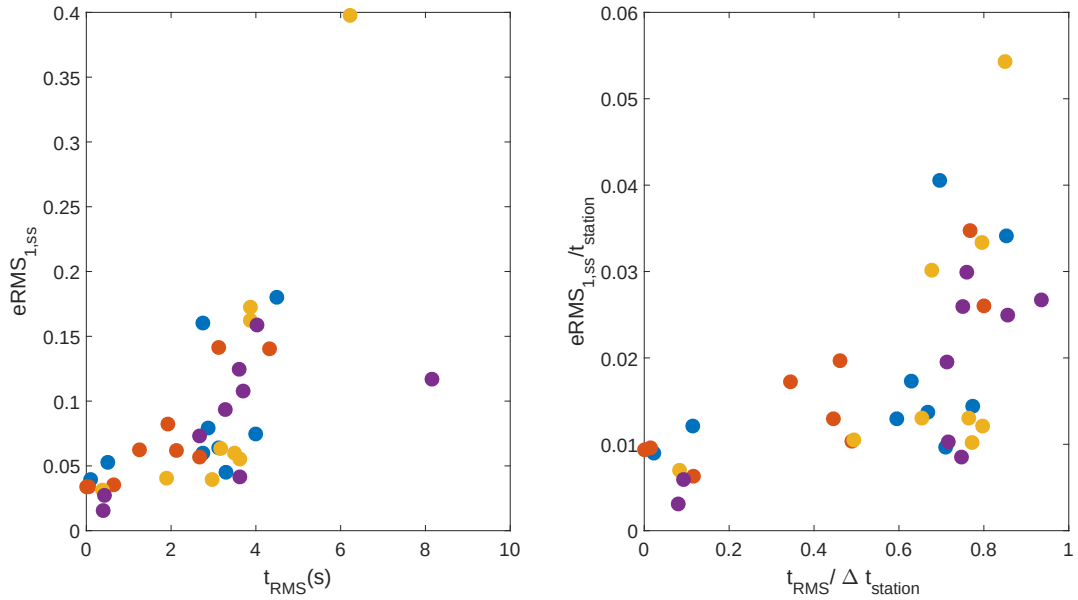

Figure G.1: Left: $e_{RMS1,ss}$ vs t_{RMS} for dynamic gusts cases in closed-loop approach. Note the close to linear relation between both parameters. Right plot shows the same parameters divided by $t_{station}$.

Open-loop Lookup table approach

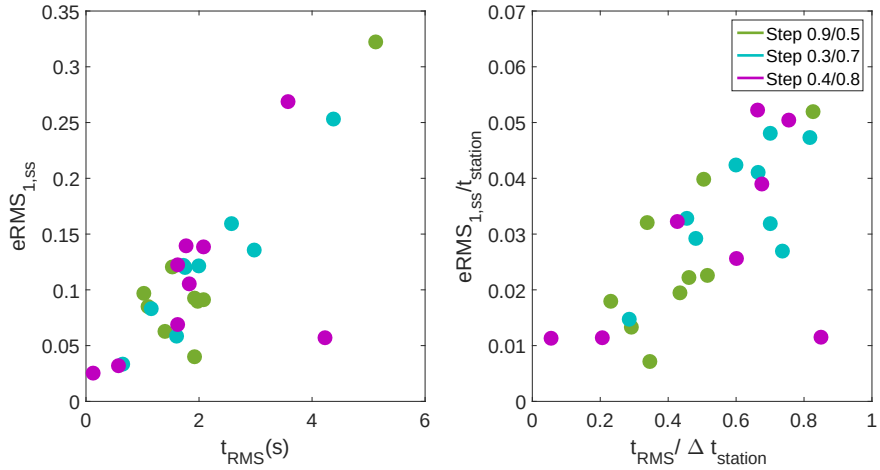

Figure G.2: Left: $e_{RMS1,ss}$ vs t_{RMS} for dynamic gusts cases in open-loop approach. Note the close to linear relation between both parameters. Right plot shows the same parameters divided by $t_{station}$.

Closed-loop approach: progression in vanes angle

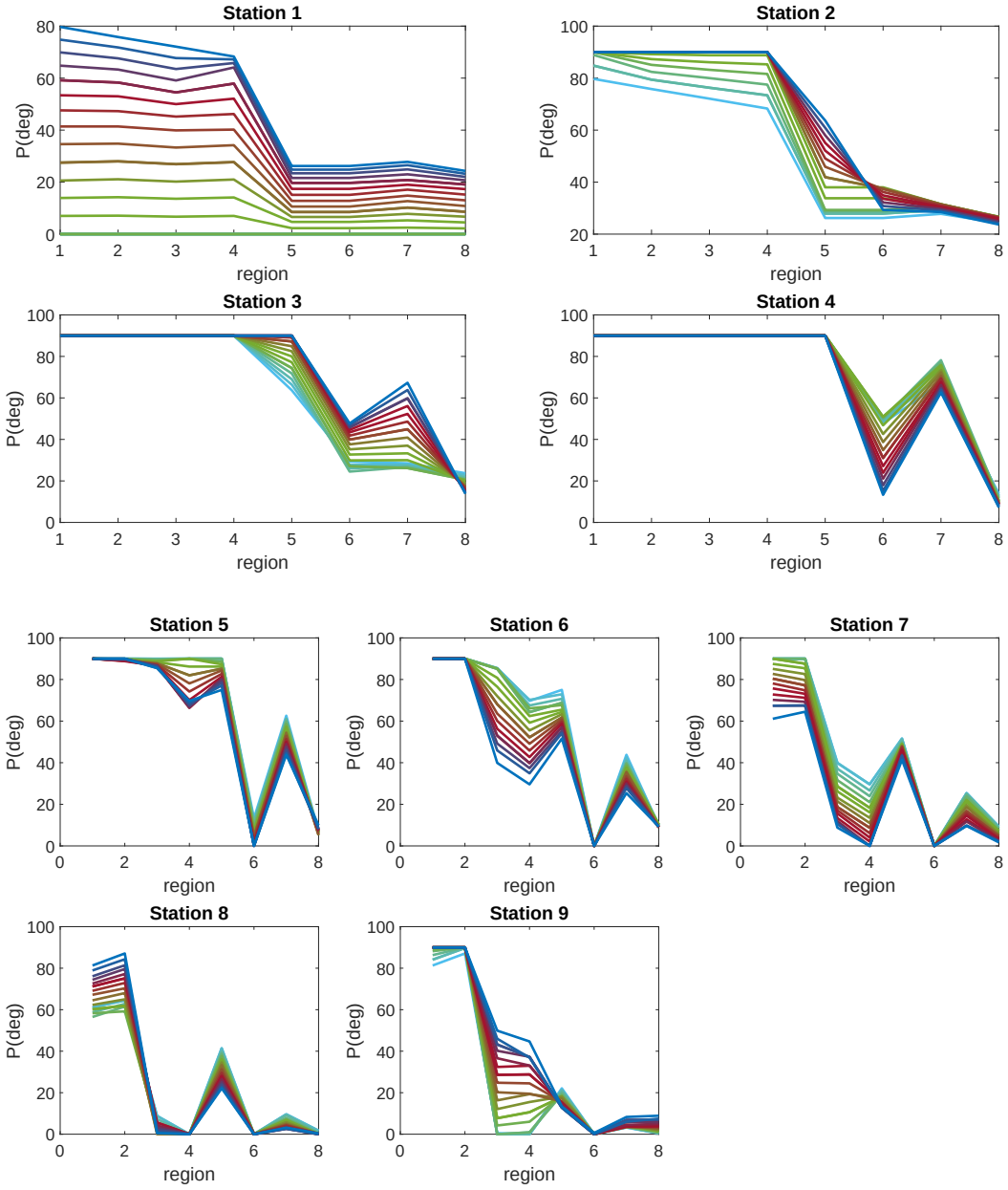

Figure G.3: Progression in vanes angular position, for *Step* dynamic gust in closed-loop approach. Since its obtained with the 8-region controller, each region corresponds to a vane

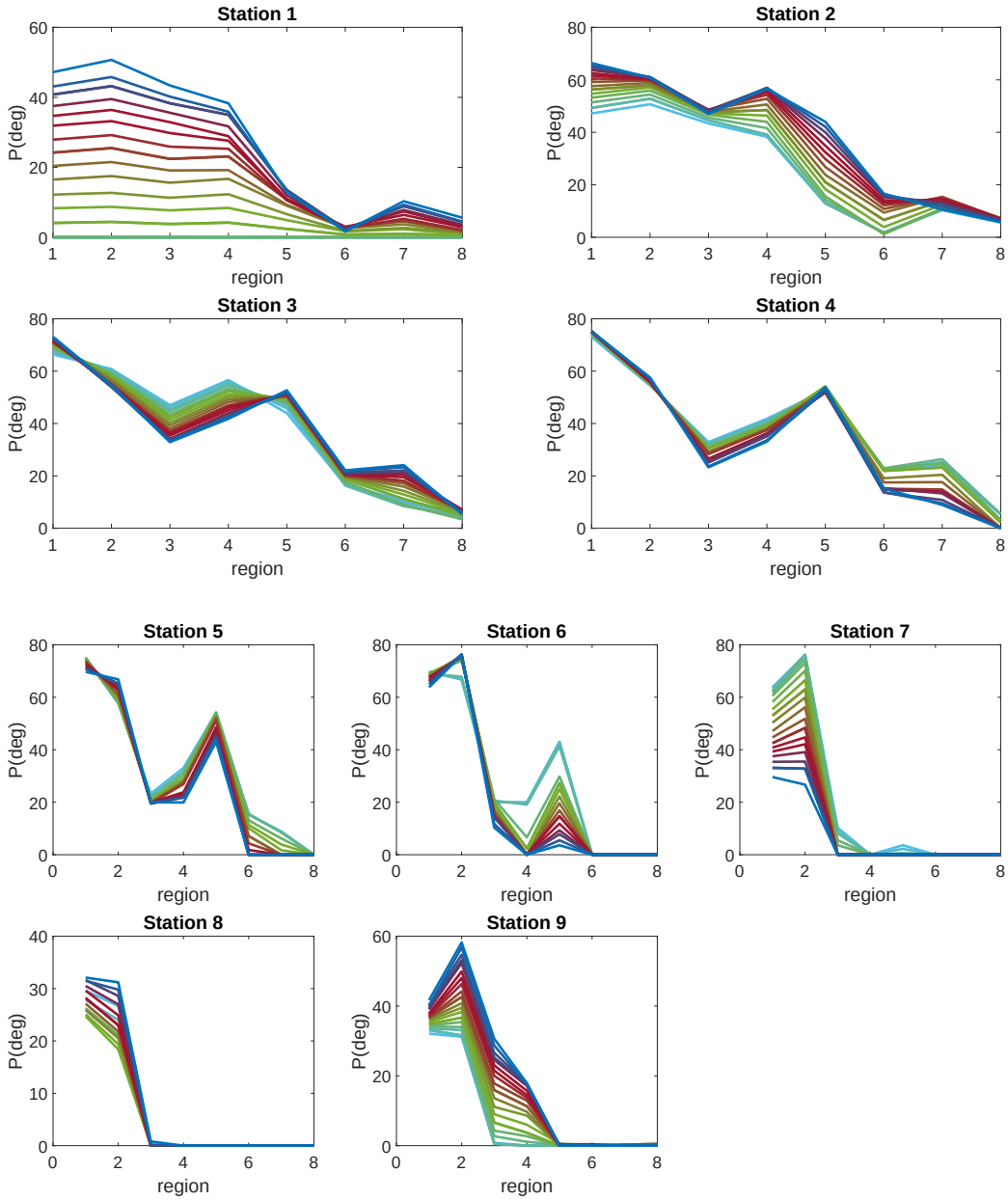

Figure G.4: Progression in vanes angular position, for *Shear* dynamic gust in closed-loop approach. Since its obtained with the 8-region controller, each region corresponds to a vane

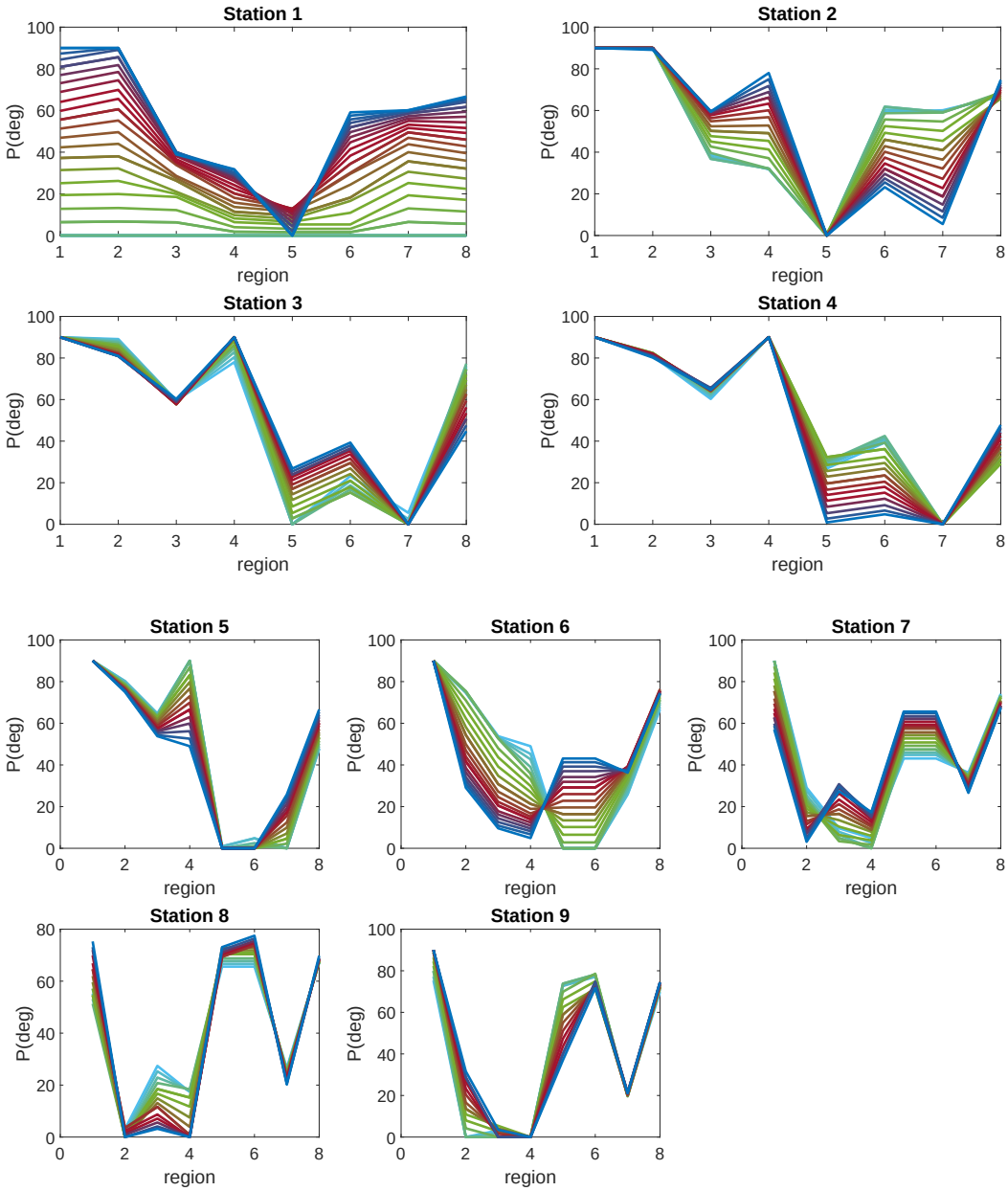

Figure G.5: Progression in vanes angular position, for *Jet* dynamic gust in closed-loop approach. Since its obtained with the 8-region controller, each region corresponds to a vane

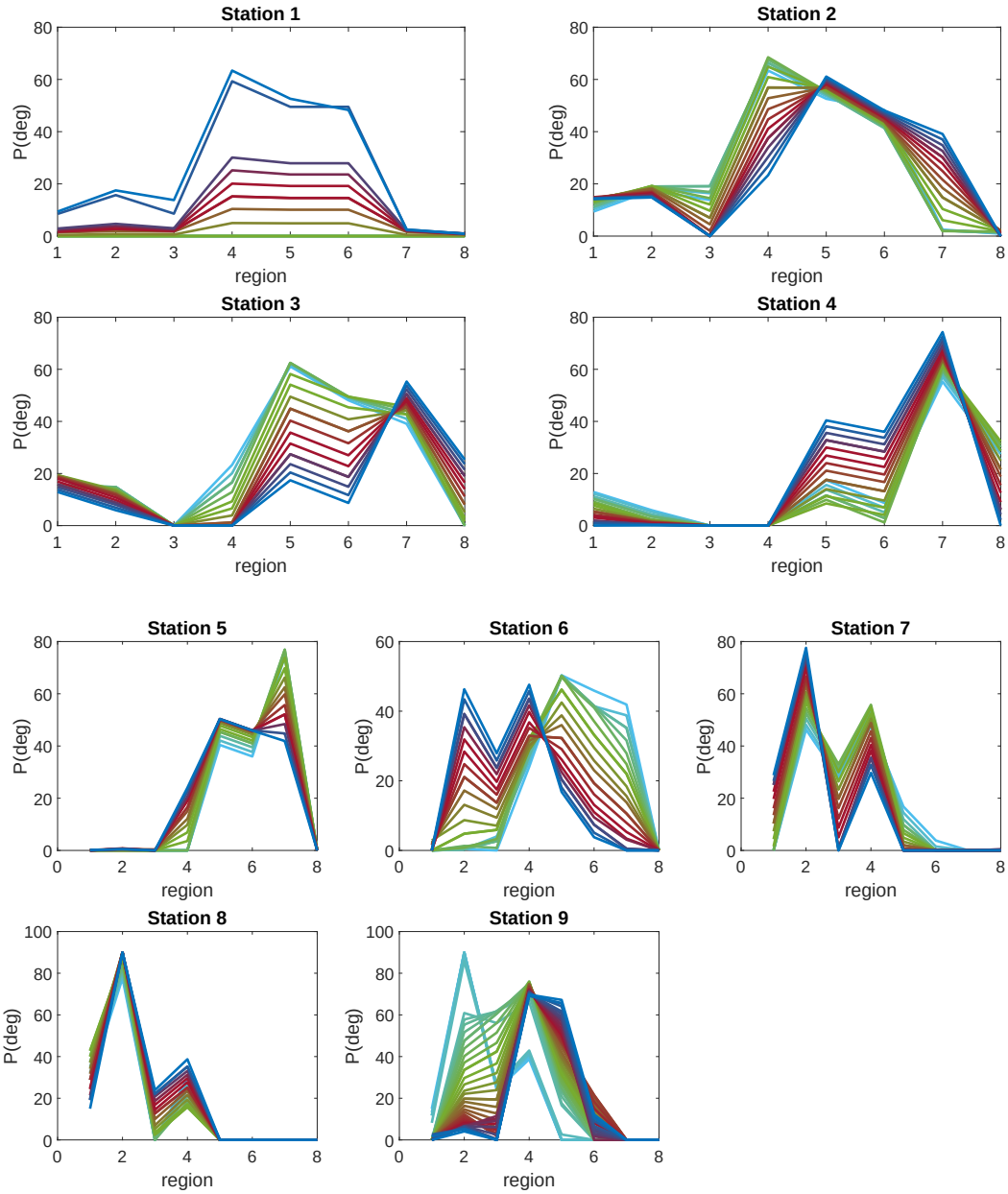

Figure G.6: Progression in vanes angular position, for *Wake* dynamic gust in closed-loop approach. Since its obtained with the 8-region controller, each region corresponds to a vane